Title

Exploration of Power Laws in and Development of Analytical Tools for the Study of Stem Cell-derived Cardiomyocytes

Author

Dunham, Christopher Stuart

Publication Date

2022

UNIVERSITY OF CALIFORNIA

Los Angeles

Exploration of Power Laws in and Development of Analytical Tools for the Study of Stem Cell-derived Cardiomyocytes

A dissertation submitted in partial satisfaction of the requirements for the degree Doctor of Philosophy in Chemistry

by

Christopher Dunham

2022

ABSTRACT OF THE DISSERTATION

Exploration of Power Laws in and Development of Analytical Software for Two-Dimensional Stem Cell-derived Cardiomyocyte Cultures

by

Christopher Dunham
Doctor of Philosophy in Chemistry
University of California, Los Angeles, 2022
Professor James K. Gimzewski, Chair

Human embryonic and induced pluripotent stem cell-derived cardiomyocytes (hESC-CM and hiPSC-CM, respectively) have held considerable scientific interest for their potential applications in the fields of drug screening, disease modeling, and tissue engineering. One of the most significant roadblocks currently hindering the use of hESC-CMs and hiPSC-CMs concerns their inability to achieve cellular phenotypic maturity. This roadblock is referred to as the “maturation block” problem: cardiomyocytes derived from stem cells are known to experience limitations in phenotypic expression, in which the cells demonstrate characteristics analogous to late fetal stage cells, rather than adult cells. If hESC-CM and hiPSC-CM cultures are to achieve their full potential in pharmacology and regenerative medicine applications, the maturation block problem must be resolved.

This dissertation sought to improve upon the current understanding of the mechanisms involved in stem cell-derived cardiomyocyte maturation. Here, analysis of microelectrode array (MEA) recordings of hESC-CM and hiPSC-CM cultures revealed that the pacemaker region often moves (translocates) across the MEA. The variable length of the quiescent period between translocation events was found to obey a power law probability distribution. Such distributions are a characteristic of critical systems, or systems that demonstrate complex spatiotemporal dynamics and emergent properties. The power law exponent obtained for pacemaker translocation quiescent periods ($\alpha = -1.58$) closely mirrors the power law exponent observed in several critical systems ($\alpha = -1.5$), indicating that critical dynamics may play a crucial role in the development of a stable pacemaker region in the cardiomyocyte culture.

The computational tools developed for cardiomyocyte power law analysis were expanded to investigate a variety of cardiomyocyte properties, including local activation time and conduction velocity, as well as spatial relationships between the pacemaker region and cardiomyocyte electrical properties. This led to the development of Cardio PyMEA, a free and open source, graphical user interface-based program that was written in Python for the analysis of MEA cardiomyocyte data. Cardio PyMEA was made available on Github for any interested individual to use for MEA-based cardiomyocyte analysis and could serve as an evolving platform for such analyses in the future.

The dissertation of Christopher Dunham is approved.

Joseph Ambrose Loo

Atsushi Nakano

Emil Reisler

James K. Gimzewski, Committee Chair

University of California, Los Angeles

2022

I dedicate this dissertation to my parents, Alfred and Sharon, and my grandparents, Walter and Dolleen. You are, and were, the true heroes in my life.

TABLE OF CONTENTS

LIST OF FIGURES

Chapter 2:

Chapter 3:

Chapter 4:

Chapter 5:

Chapter 6:

Chapter 7:

LIST OF TABLES

Chapter 4:

Chapter 6:

ACKNOWLEDGMENTS

This degree was only possible thanks to the wonderful and talented people in my life who helped me get here. My journey to a career in chemistry can be directly attributed to three college professors early in my academic life: Amy Kudrna, my general chemistry instructor at Grand Rapids Community College; Kathleen Nolta, my organic and biochemistry professor at the University of Michigan, Ann Arbor; and Dominika Zgid, my physical chemistry professor and undergraduate research mentor at the University of Michigan, Ann Arbor. It is exceedingly improbable that I would've taken, much less succeeded on, this path in my life if not for these three gifted teachers and mentors.

I was incredibly fortunate to have a true force-of-nature, James (Jim) K. Gimzewski, as my mentor for this doctoral degree. I am not sure what I would have done without his creativity, guidance, and occasional prodding. I am extremely grateful to have received additional mentorship from Adam Z. Stieg of the California NanoSystems Institute. Jim and Adam both helped me to realize my potential as a research scientist throughout this adventure.

I want to thank the members of my committee, Joseph Loo, Atsushi Nakano, and Emil Reisler, for their support. I especially appreciate Joe's patience over the last few years in handling the affairs of Chemistry 184 and the trials and tribulations associated with our ICP-MS project.

Additionally, I wish to thank the undergraduate students who have worked with me over the last few years, namely Michelle Phi, Madelynn Mackenzie, and Alexis Kim for their contributions, and for providing me with a sounding board to help reign in the chaos. I want to emphatically thank Wonhyeuk Jung and Katie Perrotta for being the best collaborators I could ever ask for while working together on the ICP-MS project.

I am grateful to all of the professors I've taught for, but two in particular stand out for special thanks. Thank you, Jim, for letting me build and teach Chemistry 103 - Environmental Chemistry with you for the last 5 years. I am exceedingly proud of what we were able to accomplish with that class. Thank you, Richard "Dick" Weiss, for letting me teach biochemistry with you so many times and for helping me grow as an educator.

This degree would not have been possible without the support of my friends and family who have supported me over these past several years. Above all, I dedicate this PhD to my parents, Alfred and Sharon Dunham. Thank you for always being there for me.

Chapter 2 is an adaptation of "Glucose inhibits cardiac muscle maturation through nucleotide biosynthesis" and was written by the following authors: Haruko Nakano, Itsunari Minami, Daniel Braas, Herman Pappoe, Xiuju Wu, Addelynn Sagadevan, Laurent Vergnes, Kai Fu, Marco Morselli, Christopher Dunham, Xueqin Ding, Adam Z Stieg, James K Gimzewski, Matteo Pellegrini, Peter M Clark, Karen Reue, Aldons J Lusis, Bernard Ribalet, Siavash K Kurdistani, Heather Christofk, Norio Nakatsuji, and Atsushi Nakano. This article appeared in the journal eLife in 2017 and carries with it the following acknowledgments: Authors thank Jinghua Tang and the BSCRC stem cell core, the BSCRC FACS core, and the metabolomics core for technical support. This work was supported by the Oppenheimer Foundation (AN), the Center for DMD at UCLA (AN), NIH NIAMS P30AR057230 (Musculoskeletal Core

Center, AN), the National Center for Research Resources Grant S10RR026744 (KR), NIH DK094311 (AJL), NIH CA178415 (SKK), NIH HL126051 (AN), and NIH HL124503 (AZS, JKG, AN). XD is supported by a fellowship from the Chinese Scholarship Council of Chemistry and Chemical Engineering, Hunan University, Changsha, PR China.

Chapter 3 is an adaptation of “Nanoscale neuromorphic networks and criticality: a perspective” and was written by the following authors: Christopher S Dunham, Sam Lilak, Joel Hochstetter, Alon Loeffler, Ruomin Zhu, Charles Chase, Adam Z Stieg, Zdenka Kuncic, and James K Gimzewski. This article appeared in the Journal of Physics: Complexity in 2021 and carries with it the following acknowledgments: The authors wish to thank members of the California NanoSystems Institute (CNSI) Integrated Systems Nanofabrication Cleanroom (ISNC) and Nano and Pico Characterization Lab (NPC) for their support for this project. A special thanks is given to Masakazu Aono of the International Center for Materials Nanoarchitectonics (MANA), National Institute of Materials Science (NIMS), in Tsukuba, Japan. ZK acknowledges support from the Australian-American Fulbright Commission. The authors also wish to thank Hirofumi Tanaka and Takumi Kotooka at the Research Center for Neuromorphic AI Hardware, Kyushu Institute of Technology, Kitakyushu, Fukuoka, Japan, for their technical advice and inspiration for the design of silver selenide nanowire networks. JKG would like to acknowledge Dante Chialvo and the late Walter Freeman III for inspirational discussions on criticality.

Chapter 4 is an adaptation of “Pacemaker translocations and power laws in 2D stem cell-derived cardiomyocyte cultures” and was written by the following authors: Christopher S. Dunham, Madelynn E. Mackenzie, Haruko Nakano, Alexis R. Kim, Michal B. Juda, Atsushi Nakano, Adam Z. Stieg, and James K. Gimzewski. This article appeared in the journal PLoS ONE in 2022 and carries with it the following acknowledgments: CSD would like to acknowledge the work of Michelle (Nguyen) Phi, at the time an undergraduate biochemistry student at UCLA, in the early stages of this project. Her contributions to the codebase, early analysis, and troubleshooting were essential in pushing this project to its present state.

Chapter 5 is an adaptation of “Cardio PyMEA: A user-friendly, open-source Python application for cardiomyocyte microelectrode array analysis” and was written by the following authors: Christopher S. Dunham, Madelynn E. Mackenzie, Haruko Nakano, Alexis R. Kim, Atsushi Nakano, Adam Z. Stieg, and James K. Gimzewski. This article is currently in press in the journal PLoS ONE and carries with it the following acknowledgments: CSD would like to acknowledge the work of Michelle (Nguyen) Phi, at the time an undergraduate biochemistry student at UCLA, for providing invaluable assistance to MEA software development during the earliest stages of this project. Her contributions to the original codebase were essential in advancing this project.

Chapter 6 is an adaptation of “Optimizing Methods for ICP-MS Analysis of Mercury in Fish: An Upper-division Chemistry Laboratory” and was written by the following authors: Wonhyeuk Jung*, Christopher S. Dunham*, Katie A. Perrotta*, Yu

Chen, James K. Gimzewski, and Joseph A. Loo. This article is currently under review at the Journal of Chemical Education and carries with it the following acknowledgments: The authors wish to thank Dr. Chonghyun Chang at the ICP-MS facility, UC Center for Environmental Implications of Nanotechnology, for his support for this project. The authors are thankful for the wonderful contributions made by the students of the Chemical Instrumentation class. The authors wish to thank Kevin Koshiro for being the ultimate team player while assisting in troubleshooting and operational exercises. We acknowledge Biorender as the software used for figure generation. Finally, support from the US National Science Foundation (CHE-1808492 to JAL) and UCLA educational improvement grant (IIP #20-12) is acknowledged.

Chapter 7 is an adaptation of “Spoken Digit Classification by In-Materio Reservoir Computing With Neuromorphic Atomic Switch Networks” and was written by the following authors: Sam Lilak, Walt Woods, Kelsey Scharnhorst, Christopher Dunham, Christof Teuscher, Adam Z. Stieg, and James K. Gimzewski. This article appeared in the journal Frontiers in Nanotechnology in 2021 and carries with it the following acknowledgments: The authors gratefully acknowledge past group members: Cristina Martin-Olmos, Henry Sillin and Audrius V. Avizienis for their foundation work in chip fabrication, LabView programming and crystal growth, respectively. Physical ASN chips were fabricated in the UCLA Nanofabrication Laboratory at the California Nanosystems Institute (CNSI). Instruments used in this study were operated and maintained by the Molecular Instrumentation Center at the Department of Chemistry and Biochemistry at UCLA.

VITA

Education & Degrees:

2016	B.S. Chemistry, University of Michigan, Ann Arbor
2018	M.Sc. Chemistry - Analytical, University of California, Los Angeles

Publications:

Jung W*, Dunham CS*, Perrotta KA*, Chen Y, Gimzewski JK, Loo JA. Optimizing Methods for ICP-MS Analysis of Mercury in Fish: An Upper-division Chemistry Laboratory. J Chem Ed (Under Review). 2022.

Dunham CS, Mackenzie ME, Nakano H, Kim AR, Nakano A, Stieg AZ, Gimzewski JK. Cardio PyMEA: A user-friendly, open-source Python application for cardiomyocyte microelectrode array analysis. PLoS ONE (Under Review). 2022.

Dunham CS, Mackenzie ME, Nakano H, Kim AR, Juda MB, Nakano A, Stieg AZ, Gimzewski JK. Pacemaker translocations and power laws in 2D stem cell-derived cardiomyocyte cultures. PLoS ONE. 2022;17(3): e0263976. doi: 10.1371/journal.pone.0263976

Dunham CS, Lilak S, Hochstetter J, Loeffler A, Zhu R, Chase C, Stieg AZ, Kuncic Z, Gimzewski JK. Nanoscale Neuromorphic Networks and Criticality: A Perspective. J Phys Complex. 2021;2: 042001. doi: 10.1088/2632-072X/ac3ad3

Lilak S, Woods W, Scharnhorst K, Dunham C, Teuscher C, Stieg A, Gimzewski J. Spoken Digit Classification by In-Materio Reservoir Computing with Neuromorphic Atomic Switch Networks. Front Nanotechnol. 2021. doi: 10.3389/fnano.2021.675792

Aguilera R, Scharnhorst K, Lilak SL, Dunham CS, Aono M, Stieg AZ, Gimzewski JK. (2020) Atomic Switch Networks for Neuroarchitectonics: Past, Present, Future. In: Aono M. (eds) Atomic Switch. Advances in Atom and Single Molecule Machines. Springer, Cham. doi: 10.1007/978-3-030-34875-5_11

Nakano H, Minami I, Braas D, Pappoe H, Wu X, Sagadevan A, Vergnes L, Fu K, Morselli M, Dunham C, Ding X, Stieg AZ, Gimzewski JK, Pellegrini M, Clark PM, Reue K, Lusis AJ, Ribalet B, Kurdistani SK, Christofk H, Nakatsuji N, Nakano A. Glucose Inhibits Cardiac Muscle Maturation Through Nucleotide Biosynthesis. eLife. 2017;6:e29330. doi: 10.7554/eLife.29330

Chapter 1. Overview

Structure of the dissertation

The works contained within this dissertation primarily address three topics: 1) elucidation of the mechanisms underlying the maturation of stem cell-derived cardiomyocytes as a means of overcoming the cardiomyocyte maturation block, 2) development of analytical software to facilitate cardiomyocyte analysis and expand access of scientific tools to researchers, and 3) improvement of the educational outcomes of undergraduate chemistry students through development and implementation of an advanced analytical chemistry laboratory exercise. Topic (1) is explored in Chapters 2, 3, and 4. Topic (2) is explored in Chapter 5 and Topic (3) is explored in Chapter 6. The context and scientific importance of each topic is discussed in the following sections.

The cardiomyocyte maturation block

One of the most exciting fields in medicine today is regenerative medicine. Arising from the discovery of stem cells and subsequent advancements in our understanding of stem cell biology, regenerative medicine refers to the growth and cultivation of stem cells for the production of tissue grafts and/or organs for facilitating organ repair and, perhaps eventually, transplantation [1-2]. Embryonic and other pluripotent stem cells are critical for regenerative medicine applications due to their ability to be programmed into any somatic cell type in the body [1-3].

Thanks to the development of induced pluripotent stem cells, select cells can be derived from the patient (autologous) or donor (allogeneic) and converted into stem cells, which can be subsequently differentiated into the target tissue cell type [3]. This approach (used in conjunction with mesenchymal stem cells in the case of an allogeneic donor) could bypass issues concerning the immune system response and organ rejection that are inherent to traditional tissue graft and organ transplant protocols [4-5]. Furthermore, the potential to produce organs from scratch – e.g. growing a whole heart from stem cells – would alleviate significant supply constraints affecting donor organ availability. Currently, the number of waitlisted patients awaiting an organ donor significantly exceeds supply, leading to some patients succumbing to organ failure before a donor becomes available [6-8]. Regenerative medicine using stem cells offers the tantalizing potential for overcoming transplant supply constraints and may improve patient outcomes for a variety of diseases, e.g. lung disease, Crohn’s Disease, and neurological disorders [9-11]. However, there are many challenges impeding full clinical implementation of stem cell therapies [12].

One such challenge concerning the heart involves limitations affecting the maturation of cardiomyocytes derived from stem cells. Cardiomyocytes derived from stem cells are affected by a problem commonly referred to as the “maturation block”. The maturation block refers to the inability of the cells to generate phenotypic traits associated with healthy, functional adult cells [13-15]. Therefore, such cells are neither suitable nor safe for transplant, as they do not possess the requisite properties for incorporation into an adult human [13, 16]. For cardiomyocytes specifically, those cells that are derived from stem cells exhibit characteristics more closely associated with a late fetal phenotype rather than an adult phenotype cardiomyocyte. These characteristics include: expression of genetic markers (e.g. switching from gene *MYL7* to *MYL2*, which express the regulatory light chain of myosin in sarcomere development); morphological differences (e.g. round vs oblong cell shape); electrophysiological differences (e.g. decreased action potential amplitude and duration, lower conduction velocity); and biomechanical differences (e.g. decreased contractile force) [13-14, 17]. The cardiomyocyte maturation block problem significantly limits applications of stem cell-derived cardiomyocytes in regenerative medicine applications. Additionally, the inability to achieve an adult phenotype imposes limitations on the use of these cardiomyocytes for drug screening and disease modeling applications [13].

Chapter 2 presents further context and insight regarding the stem cell-derived cardiomyocyte maturation problem through an exploration of the role of the central metabolite glucose in the maturation process. The chapter describes a highly interdisciplinary study to investigate the cardiomyocyte maturation block from metabolic, genetic, electrophysiological, biomechanical, and morphological perspectives. In short, glucose was found to have a significant effect on stem cell-derived cardiomyocyte maturation via the pentose phosphate pathway and nucleotide biosynthesis. These results illuminate the role that select metabolites may play in either promoting or inhibiting cardiomyocyte maturation and provide some indication regarding the complex system dynamics underlying the maturation process.

Critical dynamics in biotic and abiotic systems

Critical dynamics is one field that became of particular focus to the works presented herein. Critical dynamics, also commonly referred to as criticality, is a term used to describe complex systems with nonlinear spatiotemporal dynamics that exhibit a select set of characteristics. These characteristics include: power law relationships between events and their probabilities with a power law exponent of $\alpha = -1.5$, long-range spatiotemporal correlations, finite size scaling of correlation length and order parameter susceptibility (i.e. distribution cut-offs diverge with system size), shape (or data) collapse, mathematical relationships between power law exponents among different system parameters, and tunability, among others [18-19].

Chapter 3 presents a broad overview of critical dynamics in both abiotic and biotic systems. Furthermore, Chapter 3 offers a perspective on critical dynamics in a fully synthetic abiotic system: silver selenide (Ag_2Se) nanowire networks. The networks highlighted in this chapter demonstrate select attributes characteristic of critical systems, including power laws and avalanche dynamics [18-19]. These properties suggest that silver selenide nanowire networks could serve as a synthetic model, or biologically-adjacent analog, system for studying critical phenomena in both abiotic and biotic systems.

Chapter 4 provides some tantalizing evidence that critical dynamics may be involved in the progression and establishment of the pacemaker region in cardiomyocytes. This work showed that pacemaker translocations (instability of the pacemaker region by which it moves from one position to another) obey a doubly truncated power law distribution. Importantly, the results showed that the power law exponent $\alpha \cong -1.5$, is similar to the value of α demonstrated in several known or suspected critical systems [20].

Democratizing scientific software

Most of the work presented in Chapter 4 relied on code and programs that were developed within the Gimzewski group. Improving accessibility to cardiomyocyte MEA data analysis was an initial developmental goal during this work in order to reduce the learning curve necessary to get new students acclimated to performing the analysis. Initially this meant adapting MATLAB scripts to a graphical user interface (GUI) in order to provide the user with a more intuitive operational scheme. Eventually, limitations presented by MATLAB's licensing paradigm provided motivation to convert the existing code to Python. Such a migration would also enable the incorporation of additional analytical tools.

These goals inspired the development of Cardio PyMEA, which is discussed thoroughly in Chapter 5. In short, Cardio PyMEA was designed to utilize the completely free and readily accessible Python programming language and its object-oriented design principles for the purpose of generating user-friendly software for cardiomyocyte MEA analysis. The application uses the PyQt5 framework for its graphical elements (called "widgets"). One of the primary benefits of PyQt5 is that it makes use of the computer's operating system's design scheme when displaying windows and widgets. In other words, any software written using PyQt5 for their GUI demonstrates a native appearance, regardless of the operating system they are deployed on.

Aside from improving GUI compatibility between devices, Cardio PyMEA utilizes basic object oriented programming (OOP) design principles. These design principles make Cardio PyMEA much easier to modify, allowing a moderately-skilled (or even a knowledgeable beginner) to add new calculations and operations to the application. Overall, these development choices – free of licensing, readily modifiable and extensible, and accessible to anyone with an internet connection – improve accessibility to and contribute toward the democratization of cardiomyocyte MEA analysis.

A special focus on education in analytical chemistry

An equally important component of this dissertation concerns pedagogy. Over the duration of this PhD, the author has taught numerous courses in biochemistry, environmental chemistry, and analytical chemistry, with particular focus paid to identifying ways to improve the educational outcomes of university students. A tangential example of these efforts to improve undergraduate education at UCLA is provided in Chapter 6. Chapter 6 describes an educational paper whose primary focus is to provide students with a practical, real-world experiment that highlights the methods and practices employed in food safety studies for the purposes of method validation and parameter optimization. The experiment utilizes inductively coupled plasma mass spectrometry (ICP-MS), which utilizes a plasma gas to ionize and atomize samples for elemental analysis [21]. It is a method that is frequently used for trace elemental analysis, e.g. lead (Pb) in drinking water [21-22]. For our educational protocol, this method was applied to the analysis of mercury (Hg) in fish samples to evaluate whether fish Hg content fell within Food and Drug Administration (FDA) consumer safety levels. Fish samples were prepared via microwave digestion using the instrument from the Center for Environmental Implications of Nanotechnology at the California NanoSystems Institute at UCLA. The ICP-MS instrument itself was housed in the Molecular Instrumentation Center at UCLA.

Students were tasked with evaluating the effects of different digestion matrices (nitric acid + hydrogen peroxide vs nitric acid + hydrogen peroxide + hydrochloric acid), kinetic energy discrimination (KED) voltages, and gas modes (no gas vs helium) on method performance. An earlier study found that Hg analysis using a sample digestion matrix containing hydrochloric acid gives the best results [23]. The presence of Cl^- helps mitigate what is known as the mercury memory effect. The mercury memory effect occurs because reduced Hg more readily sublimes than oxidized mercury. The sublimation occurs in the nebulizer, and the sublimated mercury then enters the plasma torch, where it is next transported into the quadrupole system along with the sample. The result is that the detector falsely reports that there is a significantly higher concentration of Hg in the sample [24]. The addition of HCl and other chloride-containing compounds significantly reduces this effect. This phenomenon is likely attributable to reduction-oxidation (redox) chemistry between Hg^{2+} and Cl^- ions [24]. Another potential complication that can be mitigated for mercury analysis is polyatomic interference. Polyatomic interference refers to the presence of small molecules whose atomic masses overlap with the mass of the analyte, e.g. $Poly^{201+}$ and Hg^{201+} [25]. The presence of polyatomic species can result in the artificial inflation of the analyte signal, i.e. a false positive, thereby complicating analysis [25].

These polyatomic species, if present, can be mitigated through the application of a KED voltage barrier. The concept is simple: a barrier of chosen strength (voltage) is applied at the end of a collision cell. Non-reactive atoms (e.g. He) flow into the cell, colliding with the species inside. Larger species (i.e. $Poly^{201+}$) will experience greater kinetic energy loss than smaller species (i.e. Hg^{201+}) [25]. If the kinetic energy loss experienced by $Poly^{201+}$ is too great to overcome the voltage barrier, then $Poly^{201+}$ will be prevented from reaching the detector. Meanwhile, the analyte Hg^{201+}, which has experienced less kinetic energy loss, will pass the barrier – provided, of course, that the voltage barrier is not set too high to also exclude the analyte. Therefore, it is important to empirically determine an optimal KED voltage for a given set of experimental conditions. Evaluation of the KED voltage is performed by comparing signal performance and method validation across no gas (i.e. no collisional gasses will flow into the cell) and He instrument modes.

Ultimately, students were tasked with determining whether the application of a KED voltage yielded superior instrument performance. This was done, in part, through method validation techniques, specifically the utilization of a standard reference material (SRM). Students were required to evaluate different KED voltages, in no gas and helium gas modes, for different matrices, to select an optimal method that could then be used to analyze the mercury content in their fish samples. The manuscript and protocol were developed in conjunction with two (current/former) UCLA graduate students, Wonhyeuk Jung and Katie Perrotta, and the experiment was successfully implemented to positive student reception during the Winter 2022 quarter for the class Chemistry 184 - Chemical Instrumentation, which was taught by Dr. Joseph A. Loo.

References

1. Mimeault M, Hauke R, Batra SK. Stem cells: a revolution in therapeutics - recent advances in stem cell biology and their therapeutic applications in regenerative medicine and cancer therapies. Clin Pharmacol Ther. 2007;82(3): 252-264. doi: 10.1038/sj.clpt.6100301
2. Rajabzadeh N, Fathi E, Farahzadi R. Stem cell-based regenerative medicine. Stem Cell Investig. 2019;6(18). doi: 10.21037/sci.2019.06.04
3. Wu SM, Hochedlinger K. Harnessing the potential of induced pluripotent stem cells for regenerative medicine. Nat Cell Biol. 2011;13: 497-505. doi: 10.1038/ncb0511-497

4. Barreca MM, Cancemi P, Geraci F. Mesenchymal and induced pluripotent stem cells-derived extracellular vesicles: the new frontier for regenerative medicine? Cells. 2020;9: 1163. doi: 10.3390/cells9051163
5. Yoshida S, Miyagawa S, Toyofuku T, Fukushima S, Kawamura T, Kawamura A, et al. Syngeneic mesenchymal stem cells reduce immune rejection after induced pluripotent stem cell-derived allogeneic cardiomyocyte transplantation. Sci Rep. 2020;10: 4593. doi: 10.1038/s41598-020-58126-z
6. Kwong AJ, Mannalithara A, Heimbach J, Prentice MA, Kim WR. Migration of patients for liver transplantation and waitlist outcomes. Clin Gastroenterol Hepatol. 2019;17(11): 2347-2355.e5. doi: 10.1016/j.cgh.2019.04.060
7. Edgar L, Pu T, Porter B, Aziz JM, La Pointe C, Asthana A, et al. Regenerative medicine, organ bioengineering and transplantation. Br J Surg. 2020;107(7): 793-800. doi: 10.1002/bjs.11686
8. Roest S, Kaffka genaamd Dengler SE, van Suylen V, van der Kaaij NP, Damman K, van Laake LW, et al. Waiting list mortality and the potential of donation after circulatory death heart transplantations in the Netherlands. Netherlands Heart J. 2021;29: 88-97. doi: 10.1007/s12471-020-01505-y
9. Panés J, García-Olmo D, Assche GV, Colombel JF, Reinisch W, Baumgart DC, et al. Long-term efficacy and safety of stem cell therapy (Cx601) for complex perianal fistulas in patients with Crohn's Disease. Gastroenterol. 2018;154(5): 1334-1342.e4. doi: 10.1053/j.gastro.2017.12.020
10. Cruz FF, Rocco PRM. The potential of mesenchymal stem cell therapy for chronic lung disease. Expert Rev Respir Med. 2020;14(1): 31-39. doi: 10.1080/17476348.2020.1679628
11. Nguyen H, Zarriello S, Coats A, Nelson C, Kingsbury C, Gorksy A, et al. Stem cell therapy for neurological disorders: a focus on aging. Neurobiol Dis. 2019;126: 85-104. doi: 10.1016/j.nbd.2018.09.011
12. Kwon SG, Kwon YW, Lee TW, Park GT, Kim JH. Recent advances in stem cell therapeutics and tissue engineering strategies. Biomater Res. 2018;22: 36. doi: 10.1186/s40824-018-0148-4

13. Karbassi E, Fenix A, Marchiano S, Muraoka N, Nakamura K, Yang X, et al. Cardiomyocyte maturation: advances in knowledge and implications for regenerative medicine. Nat Rev Cardiol. 2020;17: 341-359. doi: 10.1038/ s41569-019-0331-x.
14. Guo Y, Pu WT. Cardiomyocyte maturation: New phase in development. Circ Res. 2020;126: 1086-1106. doi: 10.1161/CIRCRESAHA.119.315862.
15. Ahmed RE, Anzai T, Chanthra N, Uosaki H. A brief review of current maturation methods for human induced pluripotent stem cells-derived cardiomyocytes. Front Cell Dev Biol. 2020;8: 178. doi: 10.3389/fcell.2020.00178.
16. Scuderi GJ, Butcher J. Naturally Engineered Maturation of Cardiomyocytes. Cell Front Cell Dev Biol. 2017;5: 50. doi: 10.3389/fcell.2017.00050.
17. Machiraju P, Greenway SC. Current methods for the maturation of induced pluripotent stem cell-derived cardiomyocytes. World J Stem Cells. 2019;11(1): 33-43. doi: 10.4252/wjsc.v11.i1.33
18. Beggs JM, Timme N. Being critical of criticality in the brain. Front Physiol. 2012;3(163). doi: 10.3389/fphys.2012.00163
19. Friedman N, Ito S, Brinkman BAW, Shimono M, DeVille REL, Dahmen KA, et al. Universal critical dynamics in high resolution neuronal avalanche data. Phys Rev Lett. 2012;108: 208102. doi: 10.1103/PhysRevLett.108.208102
20. Muñoz MA. Colloquium: Criticality and dynamical scaling in living systems. Rev Mod Phys. 2018;90: 031001. doi: 10.1103/RevModPhys.90.031001
21. Ammann AA. Inductively coupled plasma mass spectrometry (ICP MS): a versatile tool. J Mass Spectrom. 2007;42: 419–427. doi: 10.1002/jms.1206
22. Abdul RM, Mutnuri L, Dattatreya PJ, Mohan DA. Assessment of drinking water quality using ICP-MS and microbiological methods in the Bholakpur area, Hyderabad, India. Environ Monit Assess. 2012;184(3): 1581-1592. doi: 10.1007/s10661-011-2062-2
23. Krata A, Bulska E. Critical evaluation of analytical performance of atomic absorption spectrometry and inductively coupled plasma mass spectrometry for mercury determination. Spectrochim Acta B: At Spectrosc. 2005;60: 345-350. doi: 10.1016%2Fj.sab.2004.11.011

24. Parikh Y, Lang H, Mahmoud S, Lallo J. Sample preparation method for mercury analysis in reagent chemicals by ICP-OES. Spectrosc. Supp. 2015;30(11): 8-17.
25. Yamada N. Kinetic energy discrimination in collision/reaction cell ICP-MS: Theoretical review of principles and limitations. Spectrochim Acta B: At Spectrosc. 2015;110: 31–44. doi: 10.1016/j.sab.2015.05.008

Chapter 2. Glucose inhibits cardiac muscle maturation through nucleotide biosynthesis.

Abstract

The heart switches its energy substrate from glucose to fatty acids at birth, and maternal hyperglycemia is associated with congenital heart disease. However, little is known about how blood glucose impacts heart formation. Using a chemically defined human pluripotent stem-cell-derived cardiomyocyte differentiation system, we found that high glucose inhibits the maturation of cardiomyocytes at genetic, structural, metabolic, electrophysiological, and biomechanical levels by promoting nucleotide biosynthesis through the pentose phosphate pathway. Blood glucose level in embryos is stable in utero during normal pregnancy, but glucose uptake by fetal cardiac tissue is drastically reduced in late gestational stages. In a murine model of diabetic pregnancy, fetal hearts showed cardiomyopathy with increased mitotic activity and decreased maturity. These data suggest that high glucose suppresses cardiac maturation, providing a possible mechanistic basis for congenital heart disease in diabetic pregnancy.

Introduction

Congenital heart disease (CHD) is the most common type of birth defect affecting 0.8% of human live births (Fahed et al., 2013). Although genetic factors play a significant role in the development of CHD, current genomic technologies, including exome sequencing and SNP arrays, have provided a genetic diagnosis for only 11% of the probands (Gelb et al., 2013), highlighting the crucial role of non-genetic contributors.

Among the non-genetic factors that influence the fetal heart, maternal hyperglycemia is the most common medical condition, associated with a 2-5-fold increase in CHD independent of genetic contributors (Centers for Disease Control, 1990; Simeone et al., 2015; Yogev and Visser, 2009). Diabetic pregnancy is often accompanied by maternal complications including vasculopathy, neuropathy, and insulin resistance, which potentially affect fetal cardiac formation indirectly. These systemic complications are often subclinical, hindering the dissection of the pathomechanism of CHD in diabetic pregnancy. Thus, despite the established association between maternal hyperglycemia and malformation of the fetal heart, little is known about how glucose levels impact cardiomyocyte development and how hyperglycemia affects heart formation in diabetic pregnancy (Gaspar et al., 2014).

The metabolic environment is one potential non-genetic determinant of cell proliferation and differentiation. Cells display distinct metabolic characteristics depending on their differentiation stage (Carey et al., 2015; Tohyama et al., 2016; Wang et al., 2009), and the fuel type used by the cells serves not merely as a source of energy but also as a critical regulator of self-renewal and differentiation of stem or progenitor cells (Harris et al., 2013; Oburoglu et al., 2014; Shiraki et al., 2014; Shyh-Chang et al., 2013). However, little is known about the mechanism. Cardiomyocytes shift their energy substrate during late embryonic and neonatal stages (Makinde et al., 1998). Glucose is the major energy source during the early developmental stages. Oxidative phosphorylation is low until E10.5 of developing rodent hearts and rapidly increases between E10.5 and E14.5 (Cox and Gunberg, 1972). This coincides with the rapid maturation of the mitochondrial structure in embryonic cardiomyocytes (Mackler et al., 1971). Shortly after birth, fatty acid oxidation becomes the predominant source of ATP production to meet the high energy demand of the maturing heart (Warshaw and Terry, 1970). These metabolic changes occur as a consequence of changes in the expression of metabolic enzymes and transporters. However, it remains unclear whether and how these metabolic changes, in turn, regulate the cardiac differentiation program.

Here, we describe the use of *in vitro* human embryonic stem cell-derived cardiomyocytes (hESC-CMs) and an *in vivo* murine diabetic model to show that glucose not only induces cardiomyocyte proliferation but also inhibits cardiomyocyte maturation. Glucose can be metabolized in multiple catabolic and anabolic pathways, including glycolysis, oxidative phosphorylation, the pentose phosphate pathway (PPP) and the hexosamine biosynthesis pathway. Our chemical screening revealed that the pro-mitotic and anti-maturation effect of high glucose is regulated by glucose-derived deoxynucleotide biosynthesis through PPP. *In vivo* measurement of ^{18}F-FDG accumulation revealed that glucose uptake is drastically suppressed during the late gestational and early postnatal stages. Exposure to high blood glucose in a murine model of diabetic pregnancy resulted in higher mitosis and delayed maturation of fetal cardiomyocytes *in vivo*. Together, our data uncover how the dynamics of glucose metabolism impact late embryonic cardiogenesis.

Results

Glucose reduction promotes hESC-CM differentiation

hESC-CMs were differentiated in monolayer in a chemically defined condition, reproducibly yielding ~90% of MF20$^+$ cardiomyocytes at day 14 with multiple cell lines including WA09 (H9) and UCLA4 hESCs (Figure 1A–C) (Arshi et al., 2013; Minami et al., 2012). hESC-CMs start to beat synchronously at around day 6–7 in our system. To characterize the differentiation stages, mRNA expression profiles from H9 hESC-CMs were serially examined by RNA-seq at five distinct stages (GSE84815): undifferentiated hESC (day 0); mesodermal precursor stage (hMP, day 2); cardiac progenitor stage (hCP, day 5); immature cardiomyocyte (hCM14); and hESC-CMS differentiated for 14 additional days (hCM28). The expression data were analyzed using signatures collected from MSigDB, a body atlas and primary cell atlas (Mabbott et al., 2013; Su et al., 2004; Subramanian et al., 2005). As expected, the stem cell signature decreases during these five stages, while signatures associated with heart and smooth muscle increase, further suggesting that our protocol leads to a high degree of enrichment for cardiomyocytes (Figure 1D and E). This differentiation course is comparable to that reported in previous publications (Paige et al., 2012; Wamstad et al., 2012).

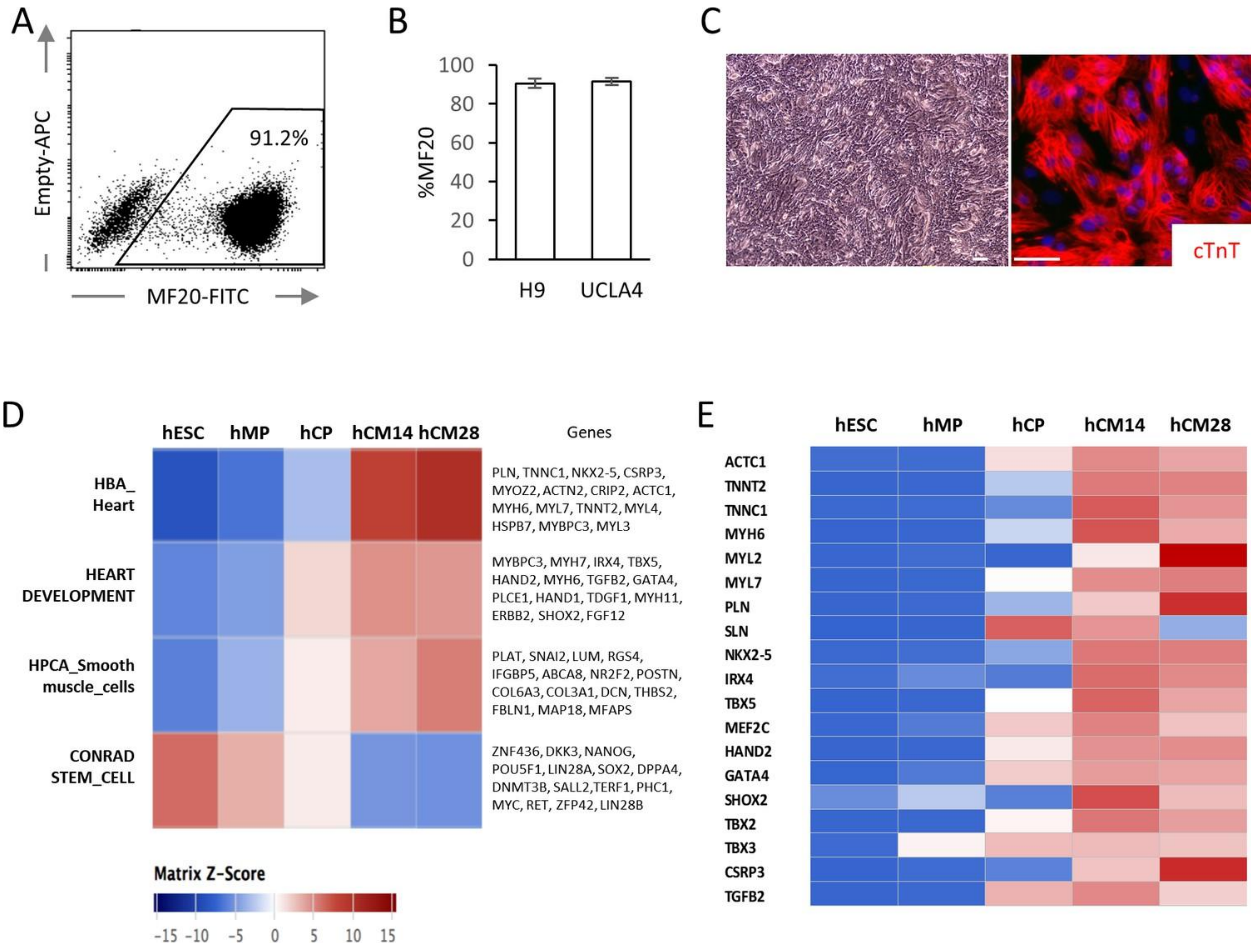

Figure 1. High yield hESC-CMs derived under chemically defined conditions recapitulate developmental time course. (A) Representative flow cytometry analysis of a cardiac marker, MF20 (myosin) in hESC-CMs (H9) at day 14. (B) Bar chart of the percentage of MF20$^+$ cardiomyocytes in hESC-CMs generated from H9 (n = 8) and UCLA4 cells (n = 3, mean ± SD), as determined by flow cytometry analysis. (C) Images of phase-contrast and Tnnt2 (cTnT: cardiac Troponin T) immunofluorescent staining of hESC-CMs at day 28. Scale bar = 50 mm. (D) The time course of the gene expression profile obtained by RNA-seq using MSigDB is shown as a heatmap (n = 3). hCM14 or hCM28, human ESC-derived cardiomyocyte differentiation day 14 or 28; hCP, human cardiac progenitor; hESC, human embryonic stem cell; hMP, human mesodermal

precursor. (E) Heatmap of representative cardiac genes from (D), showing progressive upregulation over the time.

To examine the impact of glucose levels on cardiac differentiation, hESC-CMs were cultured in media containing various concentrations of glucose, starting at the hCM14 stage when cells are already differentiated to immature cardiomyocytes (Figure 2A). The basal differentiation medium contains 25 mM glucose, 0.9 mM pyruvate, essential and nonessential amino acids, and human albumin (G25 medium). Interestingly, glucose dose-dependently suppressed the expres- sion of TNNT2 (a cardiac marker), NKX2-5 (a cardiac marker), and PPARGC1A (a mitochondrial marker) (Figure 2B). Gene expression profiling by RNA-seq revealed that genes that are related to cardiac muscle and function are enriched in hESC-CMs in low glucose medium, and that genes that are associated with mitosis and cell cycle are enriched in the high-glucose group genome-wide (Figure 2C). These data suggest that low glucose after day 14 induces the differentiation and suppresses the cell cycle of hESC-CMs.

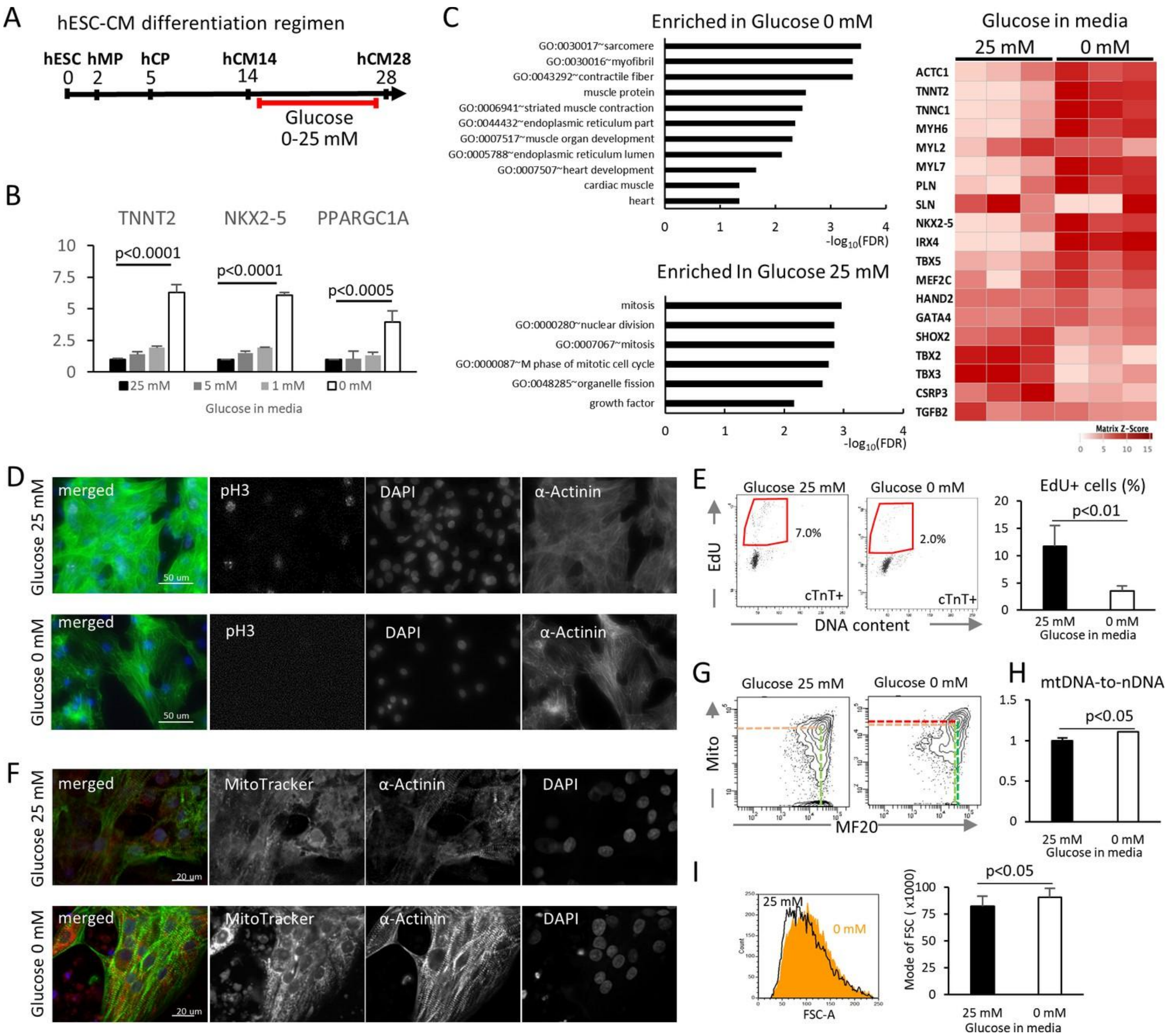

Figure 2. Glucose reduction promotes maturation of hESC-CMs. (A) Experimental regimen. hESC-CMs are differentiated in the medium containing 25 mM glucose until day 14, when ~ 90% of the cells are already MF20$^+$. Cells are analyzed at day 28 unless otherwise specified. (B) Relative mRNA expression of TNNT2, NKX2-5, and PPARGC1A as determined by qPCR. All these markers are upregulated in hESC-CMs in glucose-deprived conditions (n = 3, mean ± SD, p-value by one-way ANOVA test). (C) Pathway analysis of differentially expressed genes in 0 mM glucose (top left panel), and of differentially expressed genes enriched in hESC-CMs in 25 mM glucose (bottom left)

based on RNA-seq data. The heatmap (right panel) shows the relative expression of representative cardiac genes compared between hESC-CM cultured with 25 mM glucose or without glucose. (D) Assessment of mitotic activity by pH3 immunostaining. Representative images of three independent experiments. (E) Assessment of mitotic activity. Representative data from EdU flow cytometry (left) and quantitation of %EdU$^+$ cardiomyocytes (right) are shown. (n = 3, mean ± SD, $p<0.01$ by t-test.) (F) Assessment of the maturity of cardiomyocytes by MitoTracker (mitochondrial content) and α-actinin staining. Representative images of three independent experiments. (G) Assessment of the maturity of cardiomyocytes by flow cytometry for MF20 and MitoTracker. Representative images of at least three independent experiments are shown. (H) Assessment of mitochondrial DNA contents obtained by quantitative PCR for mitochondrial and nuclear DNA (n = 4, mean ± SD, $p<0.05$ by t-test). (I) Assessment of the cell size by forward scatter (FSC) from flow cytometry data. At least 10,000 cells were measured for each sample. Representative histogram from three flow cytometry data for each group (left) and the geometrical means of FSC (right).
(n = 3, mean ± SD, $p<0.05$ by t-test.)

To validate these results, hESC-CM proliferation was analyzed by pH3 staining and EdU flow cytometry analysis. Low glucose decreased mitotic activity at day 28 without affecting the viability of hESC-CMs (Figure 2D,E). In addition, hESC-CMs in low glucose medium showed more robust staining of α-actinin, although the sarcomere length did not significantly change (Figure 2F). MitoTracker staining and flow cytometry analyses revealed that hESC-CMs cultured in low glucose media have increased mitochondrial contents and inter-myofibrillar distribution of mitochondria, characteristic of differentiated cardiomyocytes (Figure 2F and G). Addition of 2-DG (2-deoxy-D-glucose), a competitive inhibitor of glucose phosphorylation, induced higher levels of MitoTracker and MF20 expression even in the presence of 5 mM or 25 mM glucose, suggesting that the effect is specific to glucose and not to changes in osmotic pressure. Consistently, flow cytometry showed a significant increase in cell size under glucose-restricted conditions (Figure 2I). Together, these results demonstrate that glucose dose- dependently suppresses the maturation of cardiomyocyte cellular architecture and the upregulation of cardiac genes in hESC-CMs.

Glucose reduction promotes functional maturation of hESC-CMs

We next compared the metabolic and functional maturity of hESC-CMs cultured in the presence and absence of glucose by six methods. First, hESC-CMs were stained with JC-1, a green fluorescent dye that generates red fluorescence upon formation of aggregates in active mitochondria. The level of red fluorescence is often used as an indicator of mitochondrial membrane potential and, therefore, mitochondrial activity. Immunofluorescent staining revealed that mitochondria in glucose-reduced hESC-CMs are more elongated (Figure 3A), and flow cytometry analysis revealed that the level of JC-1 aggregation is significantly higher in glucose-reduced hESC-CMs cultured in both regular 0.9 mM and 10 mM pyruvate conditions. (Figure 3B). These data suggest that high glucose inhibits the functional maturation of mitochondria.

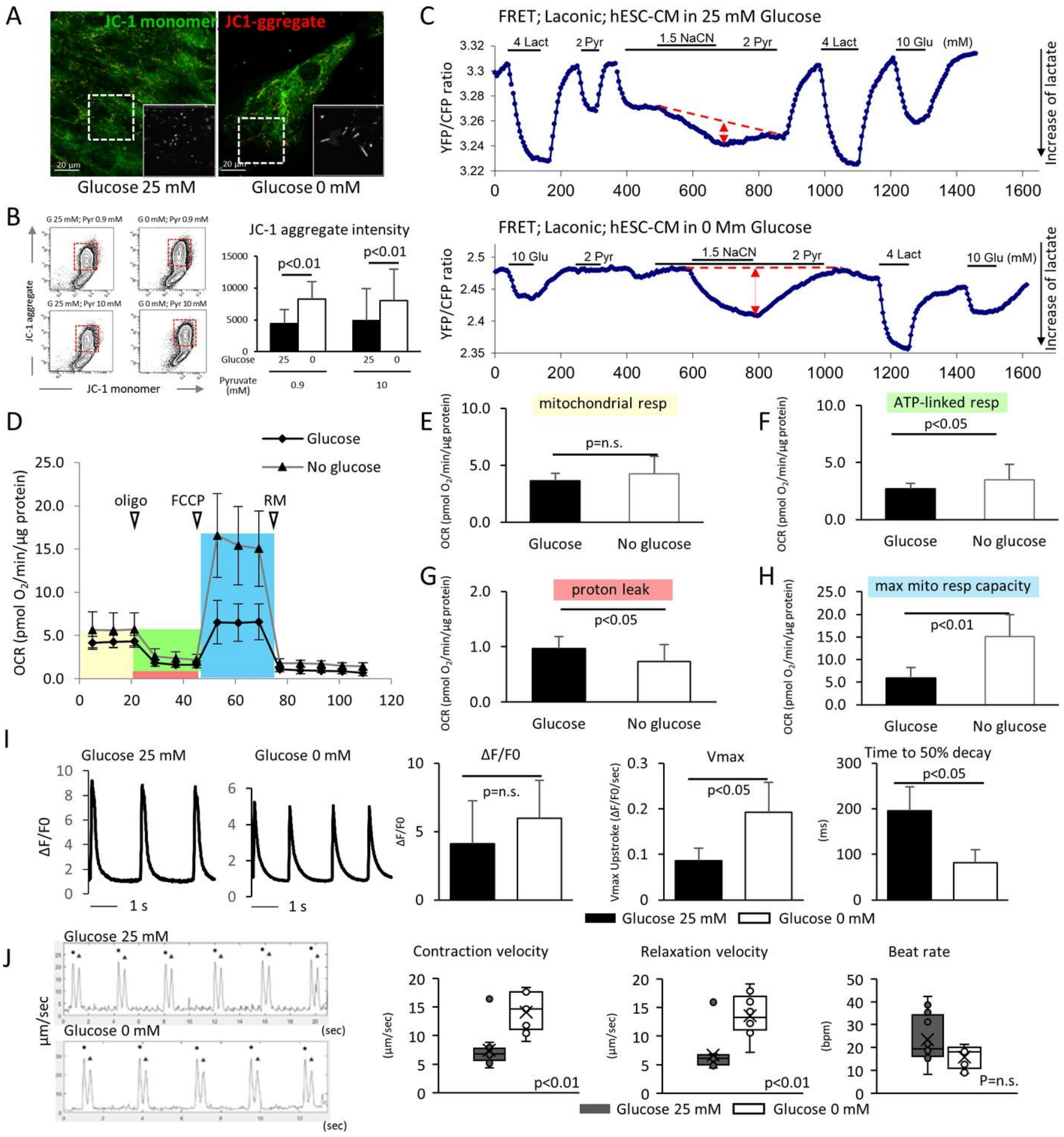

Figure 3. Glucose deprivation promotes the functional maturation of hESC-CM. (A) Representative images of mitochondrial membrane potential assay using JC-1 dye in hESC-CMs cultured in the presence (left) and absence (right) of glucose. Note the elongated mitochondria in the hESC-CMs cultured in 0 mM glucose. (B) Flow cytometry analyses of JC-1of hESC-CMs cultured in different concentrations of glucose and

pyruvate. Representative flow cytometry profile (left) and the quantitation of the intensity of JC-1 aggregates (right). (Mean intensity ± SD, $p<0.01$ by one-way ANOVA test.) (C) Changes in intracellular lactate level measured as YFP/CFP ratio with Laconic, a fluorescence resonance energy transfer (FRET)-based biosensor of lactate, in hESC-CMs cultured in the presence (upper panel) or absence (lower panel) of glucose. Increase in intracellular lactate level is indicated by a downwards shift in the trace. Note that, in hESC-CMs cultured in the absence of glucose, the addition of pyruvate (Pyr) does not lead to an increase in intracellular lactate. Data are representative of two independent experiments. (D–H) Oxygen consumption rate (OCR) measured with a Seahorse analyzer (D). ESC-CMs cultured in the absence of glucose show comparable mitochondrial respiration (E), but greater ATP-linked respiration (F), and maximum mitochondrial respiration capacity (H) with slight difference in proton leak (G), suggesting that glucose-deprivation potentiates OXPHOS. (n = 19, each; mean ± SD, $p<0.01$ by t-test.) (I) Calcium transient assay of hESC-CMs cultured in the presence or absence of glucose. Representative waves, V_{max}, $\Delta F/F0$, and time to 50% decay are shown. (n = 10 (G25) and 11 (G0), p values by t-test.) (J) Motion speed analysis by digital image correlation. The first (.) and the second peak (~) of the duplex represent the contraction and the relaxation speed, respectively (left). Contraction velocity, relaxation velocity, and beat rate are shown. (n = 12 (G25) and 9 (G0); mean ± SD, p values by t-test.)

Second, intracellular lactate levels of hESC-CMs were measured using Laconic, a fluorescence resonance energy transfer (FRET)-based lactate nanosensor (San Martı´n et al., 2013). After glucose deprivation, the Laconic construct was introduced into hESC-CMs via adenovirus as described previously (John et al., 2008). In hESC-CMs differentiated in standard 25 mM glucose, bath-applied lactate (4 mM) caused a rapid increase in intracellular lactate (measured as a decrease FRET ratio), demonstrating the efficacy of the probe. Subsequent addition of pyruvate evoked a similar but smaller elevation of intracellular lactate. Under these conditions, inhibition of mitochondrial respiration with sodium cyanide (NaCN) had only a minor effect on the intracellular lactate level. This result suggests that hESC-CMs that are differentiated in standard 25 mM glucose do not actively metabolize pyruvate (Figure 3C, upper panel). By contrast, addition of 4 mM pyruvate to glucose-reduced hESC-CMs did not cause intracellular lactate accumulation, and addition of NaCN in the presence of pyruvate resulted in a substantial increase in lactate level. This result is consistent with pyruvate utilization by mitochondria (Figure 3C, lower panel). Together, these data suggest that mitochondria metabolize pyruvate in hESC-CMs that are cultured in glucose-reduced conditions, but not in the presence of glucose.

Third, we assessed cellular respiration of hESC-CM using the XF24 Extracellular Flux Analyzer (Seahorse Bioscience), in which oxygen consumption rate (OCR) was measured in real time in a basal state and in response to oligomycin (an ATP synthase inhibitor), FCCP (carbonilcyanide p-triflouromethoxyphenylhydrazone, a mitochondrial uncoupler), and rotenone or myxothiazol (complex I or III inhibitors, respectively) (Figure 3D). Although base-line mitochondrial respiration was not changed (Figure 3E), ATP-linked respiration was elevated in the no glucose condition (Figure 3F and G). Glucose-reduced hESC-CMs also demonstrated substantially larger maximum respiration capacity, as indicated by the response to FCCP (Figure 3H). These results corroborate the increased capacity of cellular respiration in hESC-CMs cultured under low glucose conditions.

Fourth, the Ca^{2+} kinetics of hESC-CMs were assessed using a Ca^{2+} transient assay (Shimizu et al., 2015). Although the peak amplitude of the transient ($\Delta F/F0$) did not show a significant difference, the maximum upstroke (V_{max}) was significantly faster and the time to 50% decay was significantly shorter in the glucose-reduced group (Figure 3I). This pattern is consistent with the previous report demonstrating the role of thyroid hormone on hiPSC-CM maturation (Yang et al., 2014), and suggestive of an inhibitory role of high glucose on hESC-CM maturation.

Fifth, taking advantage of our monolayer culture system, we examined electrophysiological properties, using a multi-electrode array (MEA) culture plate as reported previously (Zhu et al., 2017). Maximum upstroke velocity (dV/dt_{max}) of field potential is a reliable parameter for approximating the electrophysiological maturity of cardiomyocytes derived from pluripotent stem cells (Haase et al., 2009; Ma et al., 2011; Zhang et al., 2009). Compared with hESC-CMs cultured in 25 mM glucose, those hESC-CMs cultured in the absence of glucose displayed a significant increase in dV/dt_{max} (Figure 3).

Finally, the monolayer culture method allowed us to measure cell contractility by digital image correlation using the MotionGUI program (Huebsch et al., 2015). Both average maximum contraction speed and average maximum relaxation speed were higher in those hESC-CMs cultured in 0 mM glucose (Figure 3J). Together, these data suggest that glucose reduction promotes the functional maturation of hESC-CMs at the metabolic, electrophysiological, and biomechanical levels.

Glucose blocks cardiac maturation through the pentose phosphate pathway

Having determined that glucose reduction induces cardiac maturation at morphological, genetic metabolic, and functional levels, we next sought to analyze the mechanism by which glucose blocks cardiac maturation. Glucose is metabolized by multiple pathways involving both catabolic reactions (anaerobic glycolysis and the aerobic TCA cycle) and anabolic reactions (PPP, the hexosamine pathway, etc.). We first examined the impact of glucose reduction on the global metabolomics signature. Mass spectrometry revealed that glucose deprivation resulted in a significant decrease in the levels of the metabolites in purine metabolism, pyrimidine metabolism, the PPP, the hexosamine pathway, and glycolysis, whereas lipid precursors, amino acids, glutamine, and glutamate, as well as urea cycle metabolites, were not significantly affected (Figure 4A). ATP levels were not significantly different under glucose-restricted conditions (Figure 4B), neither were any specific stress pathways significantly increased when examined by RNA-seq, suggesting that the cells were not energy-starved in the absence of glucose in the cell culture media.

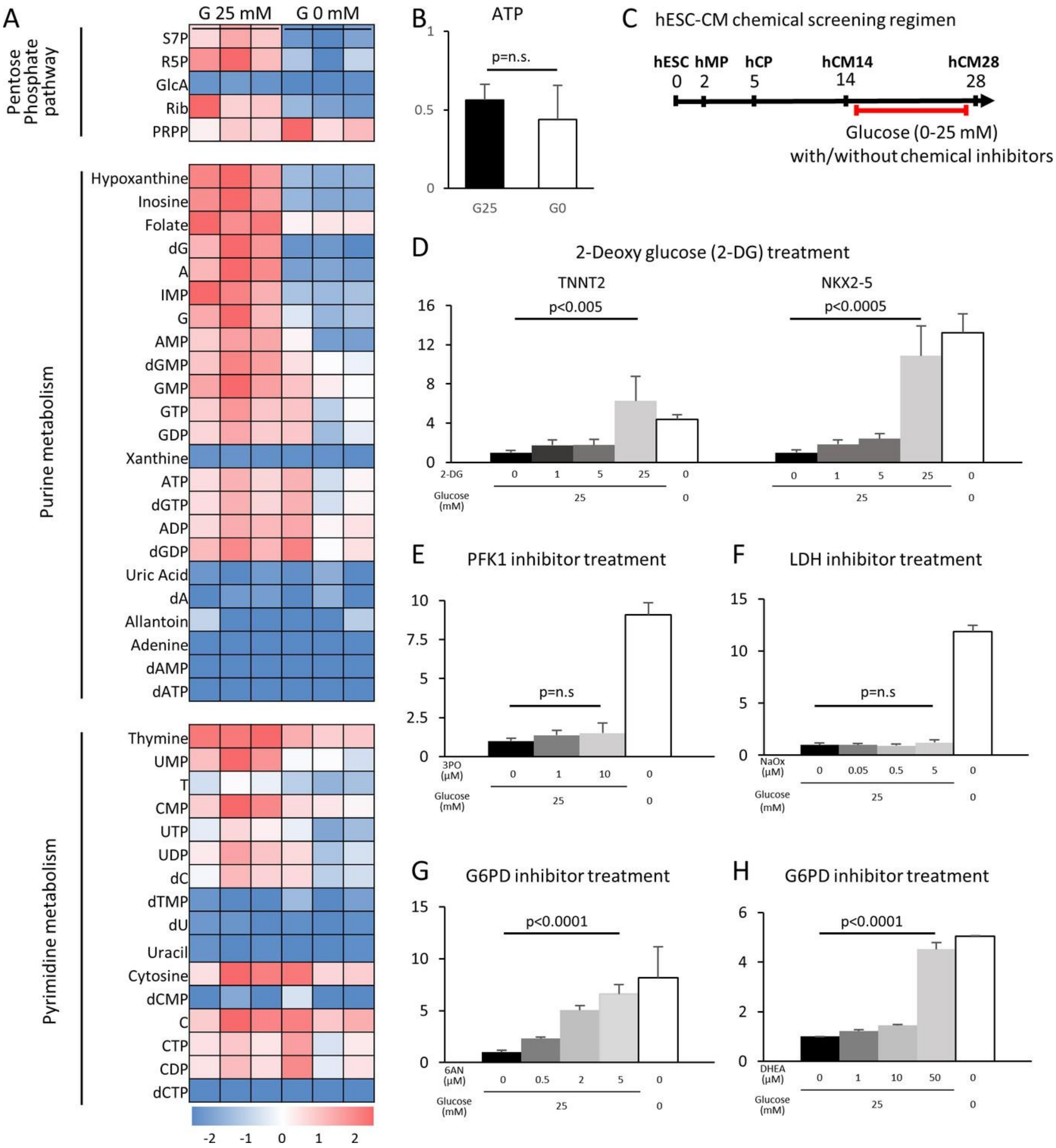

Figure 4. The pentose phosphate pathway inhibits cardiac maturation. (A) Heatmap presentation of the metabolomics analysis of hESC-CMs cultured in the presence or absence of glucose. Note the decrease in the metabolites in purine metabolism, pyrimidine metabolism and the pentose phosphate pathway (PPP) in

glucose-deprived conditions (n = 3, each). GlcA, glucuronic acid; R5P, ribose 5-phosphate; Rib, ribose; PRPP, phosphoribosyl pyrophosphate; S7P, sedoheptulose-7-phosphate. (B) ATP levels of hESC-CMs in 25 mM glucose medium (G25) and glucose-depleted medium (G0) (n = 3, mean ± SD, p = n.s. by t-test.) (C) Experimental regimen for chemical inhibition of glucose metabolic pathways. hESC-CMs are cultured in the medium containing four different glucose levels and different chemical inhibitors. (D) Relative mRNA expression of TNNT2 and NKX2-5 in different concentrations of glucose and 2-DG, a competitive inhibitor of glucose. 2-DG restored cardiac maturation in the presence of glucose. (E–H) Relative mRNA expression of TNNT2 in 0–25 mM glucose and with different chemical inhibitors of the glucose metabolic pathways: 0–10 mM 3PO (3-(3-pyridinyl)-1-(4-pyridinyl)-2-propen-1-one, a phosphofructokinase [PFK] inhibitor) (E); 0–5 mM sodium oxamate (NaOX; a lactate dehydrogenase [LDH] inhibitor) (F); 0–5 mM 6AN (6-aminonicotinamide, a glucose 6-phosphate dehydrogenase [G6PD] inhibitor) (G); and 0–50 mM DHEA (dehydroepiandrosterone, a G6PD inhibitor) (H). (n = 3, each. mean ± SD; p-value by one-way ANOVA)

To identify the metabolic pathway responsible for the improved cardiac maturation by glucose reduction, we conducted a systematic screening using chemical inhibitors for the various glucose metabolic pathways in the monolayer 384-well format (Figure 4C). Consistent with flow cytometry for MitoTracker and MF20, 2-DG dose-dependently abolished the glucose-dependent inhibition of TNNT2 and NKX2-5 mRNA levels in hESC-CM (Figure 4D). 3PO (3-[3-pyridinyl]-1-[4-pyridinyl]-2-propen-1-one), an inhibitor of the phosphofructokinase

PFKFB3 (which is a regulator of PFK1), did not affect the level of hESC-CM maturity at any concentration of glucose (Figure 4E). The failure of 3PO to recapitulate the effect of glucose deprivation suggests that glucose metabolites downstream of PFK1 are not essential for the glucose-dependent inhibition of cardiac maturation. Consistently, sodium oxamate (a lactate dehydrogenase [LDH] inhibitor) did not block the inhibitory effect of glucose (Figure 4F). Interestingly, however, 6AN (6-[cyclohexa-2,5-dien-1-ylideneamino] naphthalene-2-sulfonate) and DHEA (didehydroepiandrosterone), both inhibitors of glucose-6-phosphate dehydrogenase (G6PD) in the oxidative arm of the PPP, recapitulated glucose reduction (Figure 4G and H). As summarized in Figure 4, our chemical inhibitor screening suggests that the PPP plays a critical role in the inhibition of cardiac maturation and that blocking this pathway by either use of chemical inhibitors or glucose deprivation induces cardiac maturation. Although mitochondria are a major source of reactive oxygen species (ROS) and physiological levels of ROS pro- mote cellular differentiation (Crespo et al., 2010), the level of ROS measured by DCFDA (dichlorodihydrofluorescein diacetate) did not increase in the absence of glucose and neither did ROS inhibition had a significant impact on TNNT2 expression level, suggesting that the increase in ROS is not responsible for the induction of cardiac maturation.

Nucleotide metabolism regulates cardiomyocyte maturation

The oxidative arm of the PPP generates two major products: reducing power in the form of NADPH and 5-carbon sugars that supply the backbone for nucleotide biosynthesis. To test whether glucose level impacts cardiac maturation by affecting nucleotide biosynthesis, we rescued nucleotide synthesis by adding uridine to hESC-CMs cultured in low glucose media. Under glucose starvation, supplementation of uridine is known to rescue the growth of bacteria, yeast, and malignant cells (Linker et al., 1985). In our hESC-CM culture system, uridine restored cell proliferation even in low-glucose conditions (Figure 5A and B). Interestingly, uridine dose-dependently reduced the level of TNNT2 even in glucose-deprived conditions (Figure 5C), suggesting that glucose-mediated inhibition of cardiac maturation is dependent on the supply of nucleotides and not of NADPH.

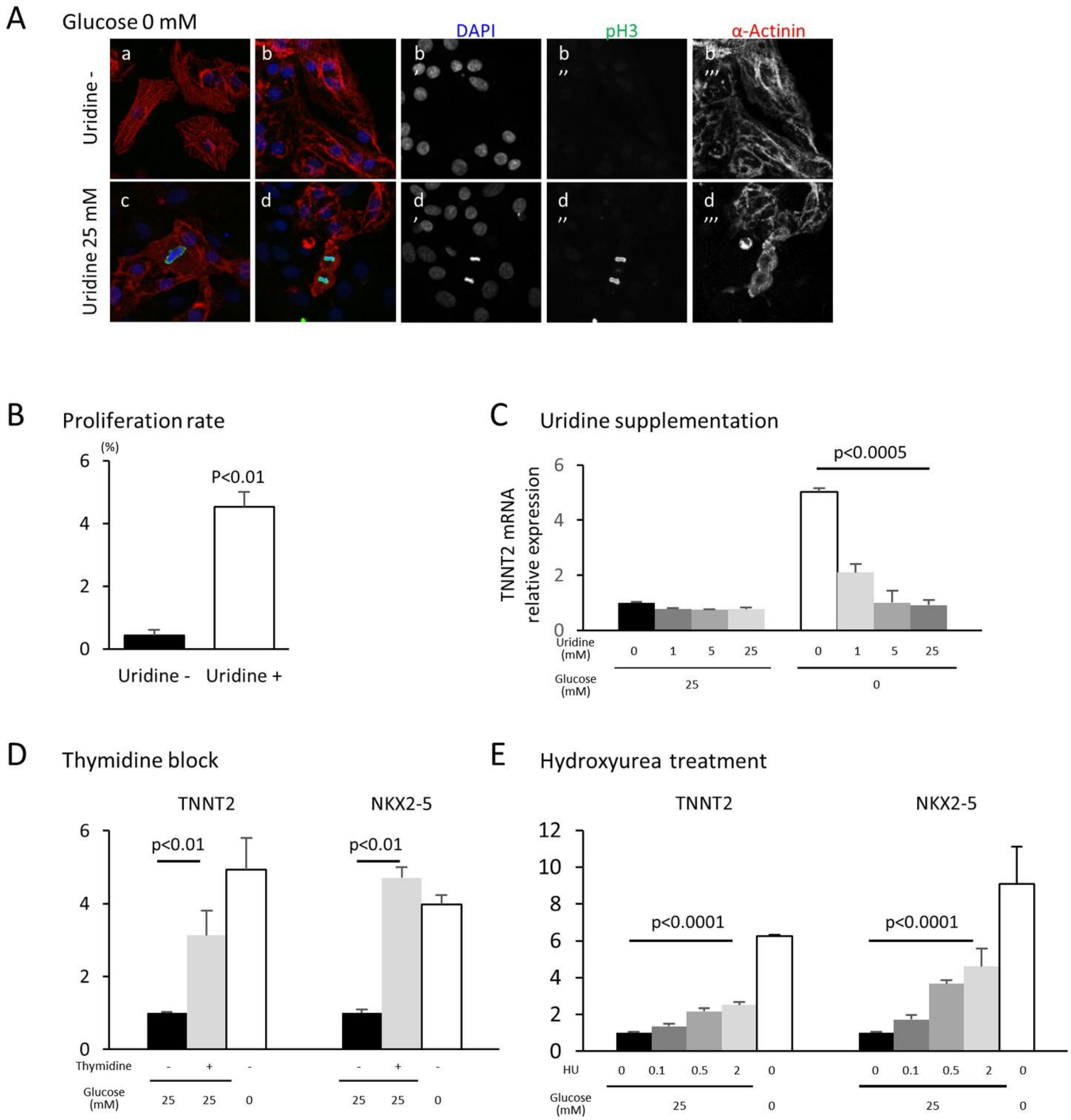

Figure 5. Nucleotide metabolism regulates cardiomyocyte maturation. (A) Glucose-deprived hESC-CMs are cultured in the absence (a, b) or presence (c, d) of 25 mM uridine, and stained for pH3 (a mitosis marker). The addition of uridine restored proliferative activity even in the absence of glucose. Data are representative of three independent experiments. (B) Proliferation rate, presented as number of $pH3^+$

cells/α-actinin$^+$ cells, seen in the stained images of Figure 5A. (n = 3, mean ± SD, p<0.01 by t-test.) (C) Relative mRNA expression of TNNT2 in hESC-CMs in 25 mM or 0 mM glucose with 0 or 25 mM uridine. Uridine dose-dependently inhibited the TNNT2 expression level in glucose-deprived conditions. (n = 3, mean ± SD, p<0.0005 by one-way ANOVA test.) (D) Relative mRNA expression of TNNT2 and NKX2-5 in hESC-CMs cultured in 0–25 mM of glucose in the presence or absence of thymidine. Thymidine block increases the levels of TNNT2 and NKX2-5 (n = 3, mean ±SD, p<0.01 for a t-test comparing samples with or without 25 mM thymidine in 25 mM glucose. (E) Relative mRNA expression of TNNT2 and NKX2-5 in hESC-CMs cultured in 0–25 mM glucose and 0–2 mM hydroxyurea (HU, a ribonucleotide reductase inhibitor). HU dose-dependently induced the expression of TNNT2 and NKX2-5 at 1, 5, and 25 mM glucose. (n = 3, mean ± SD, p-value by one-way ANOVA test.)

In order to test whether nucleotides are necessary for the glucose-dependent inhibition of cardiac maturation, nucleotide biosynthesis was blocked by multiple methods. Addition of an excess amount of thymidine (unlike uridine) blocks the synthesis of DNA by inhibiting the formation of deoxycytidine (i.e., the thymidine block method), which is commonly used to synchronize the cell cycle (Reichard et al., 1960; Xeros, 1962). When excess thymidine was added to hESC-CMs, the expression of TNNT2 and NKX2-5 were increased (Figure 5D). To further confirm this effect, we blocked deoxynucleotide synthesis by hydroxyurea (HU), an inhibitor of ribonucleotide reductase (RNR) that catalyzes the formation of deoxyribo-nucleotides. Consistent with the results from thymidine block, HU dose-dependently induced the expression of TNNT2 and NKX2-5 (Figure 5E). RNAi-based knockdown of RRM2B, a key subunit of

RNR, also resulted in a significant increase in TNNT2 expression level, even in the presence of 25 mM glucose. Together, these gain- and loss-of- function data suggest that nucleotide biosynthesis is a key regulatory pathway of the pro-mitotic–anti-maturation effect of glucose.

Nucleotide deprivation, not cell cycle block, induces cardiomyocyte maturation

Nucleotide synthesis is a key step in DNA replication and thus cell cycling. Therefore, it is not clear whether the maturation of hESC-CMs that results from deprivation of glucose is due to the cell-cycle block in general or to the effects of nucleotides themselves. To examine whether cell-cycle arrest in general is an essential trigger for cardiac maturation, we blocked the mitotic activity of hESC-CMs by a CDK4/6 inhibitor and paclitaxel (Taxol; an inhibitor of microtubule breakdown), both of which block the cell cycle without directly inhibiting the nucleotide kinetics. Interestingly, neither CDK4/6 inhibitor nor paclitaxel induced cardiac maturation. Together, these data suggest that cell-cycle arrest by itself is not crucial for the promotion of cardiac maturation. Rather, nucleotide deprivation is a key mechanism for cardiac maturation.

Glucose uptake is progressively suppressed during physiological cardiogenesis in utero

These *in vitro* data suggest that glucose reduction promotes cardiac maturation while inhibiting cardiomyocyte proliferation. An intriguing possibility is that the same mechanism underlies cardiac maturation in the *in vivo* natural counterpart. During normal embryogenesis, however, the blood glucose level is primarily regulated by maternal metabolism and stays relatively stable in utero, leading us to hypothesize that cellular glucose uptake becomes restricted during late fetal stages. To test this possibility, we measured the glucose uptake in the fetal hearts using ^{18}F-labeled 2-deoxy-2-fluoroglucose (FDG). ^{18}F-labeled FDG was injected intravenously via the maternal tail vein at E10.5, E12.5, and E15.5 or intraperitoneally into P1 and P7 pups. After 2 hr, the mice were imaged by PET/CT, the hearts were dissected, and cardiac accumulation was measured quantitatively. Interestingly, the normalized cardiac accumulation progressively and rapidly decreased from E10.5 to P7, with 0.11% and 0.05% ^{18}F-FDG uptake in P1 and P7 hearts, respectively, compared to E10.5 hearts (Figure 6). These data suggest that cardiac glucose uptake becomes significantly restricted during late gestational and early postnatal stages, creating an intracellular glucose deprivation condition during natural *in vivo* development.

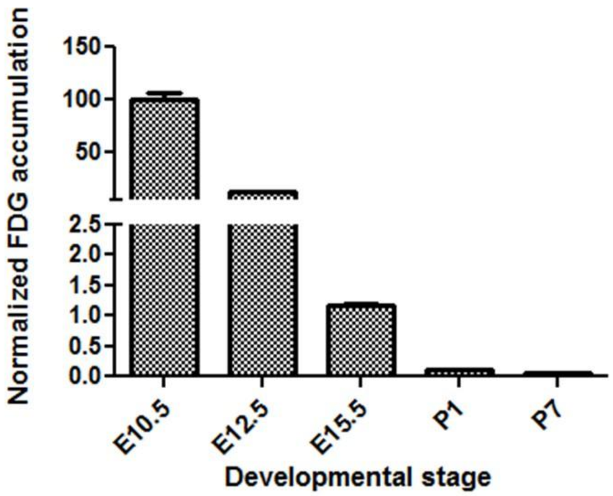

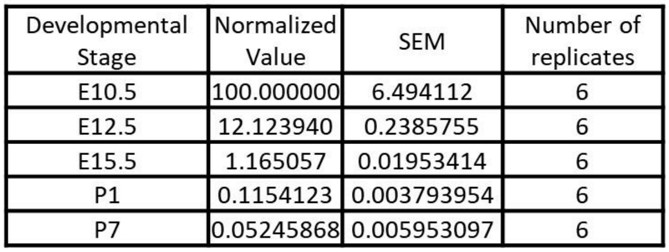

Developmental Stage	Normalized Value	SEM	Number of replicates
E10.5	100.000000	6.494112	6
E12.5	12.123940	0.2385755	6
E15.5	1.165057	0.01953414	6
P1	0.1154123	0.003793954	6
P7	0.05245868	0.005953097	6

Figure 6. Developmental time course of cardiac glucose uptake measured by ^{18}F-FDG accumulation. The radioactivity of the entire heart was measured by g-counter after tail vein i.v. (fetus) or i.p. (neonates) injections. Values were normalized to heart weight and total body signal (heart values/[heart weight * total body values]). Note a drastic decrease in glucose uptake during late gestational and neonatal stages (n = 6, each; $p<0.0001$ by one-way ANOVA test.)

Hyperglycemia promotes the proliferation and inhibits the maturation of cardiomyocytes in utero

We next tested whether hyperglycemia promotes the proliferation and inhibits the maturation of cardiomyocytes *in vivo* using fetuses and neonates from diabetic pregnancy. Akita heterozygous mice carry a single amino-acid substitution in the *Ins2* gene and exhibit multiple disorders associated with maturity-onset diabetes of the young (MODY) (Barber et al., 2005; Fujita et al., 2001; Wang et al., 1999; Yaguchi et al., 2003; Yoshioka et al., 1997). By crossing an Akita female with a wild-type male, we created a diabetic pregnancy condition in which wild-type fetuses (half of the pups in the litters) and their littermates are exposed to hyperglycemia (Figure 7A). In the C57BL/6 background, the average blood-glucose levels of the Akita mothers that we used were significantly higher than those of sex-matched control littermates (215 ± 84 vs 71 ± 12 mg/dl, respectively; $p<0.0005$). Fetal and neonatal Tnnt2^{+} cardiomyocytes from wild-type hearts from wild-type mothers and wild-type hearts from Akita mothers were examined for mitotic activity in an *in vivo* EdU incorporation assay at E16.5 and P0 stages, when cardiomyocytes are not yet multinucleated or multiploidic. As shown in Figure 7B and C, the number of cardiomyocytes in S phase was significantly higher at both E16.5 and P0 in the diabetes group. Histological analyses showed that the number of phosphorylated histone H3-positive cardiomyocytes ($pH3^+/Tnnt2^+$) is higher at E16.5 in the embryos from diabetic pregnancies (Figure 7D and E). These data suggest that fetal cardiomyocytes are more mitotic when exposed to maternal hyperglycemia.

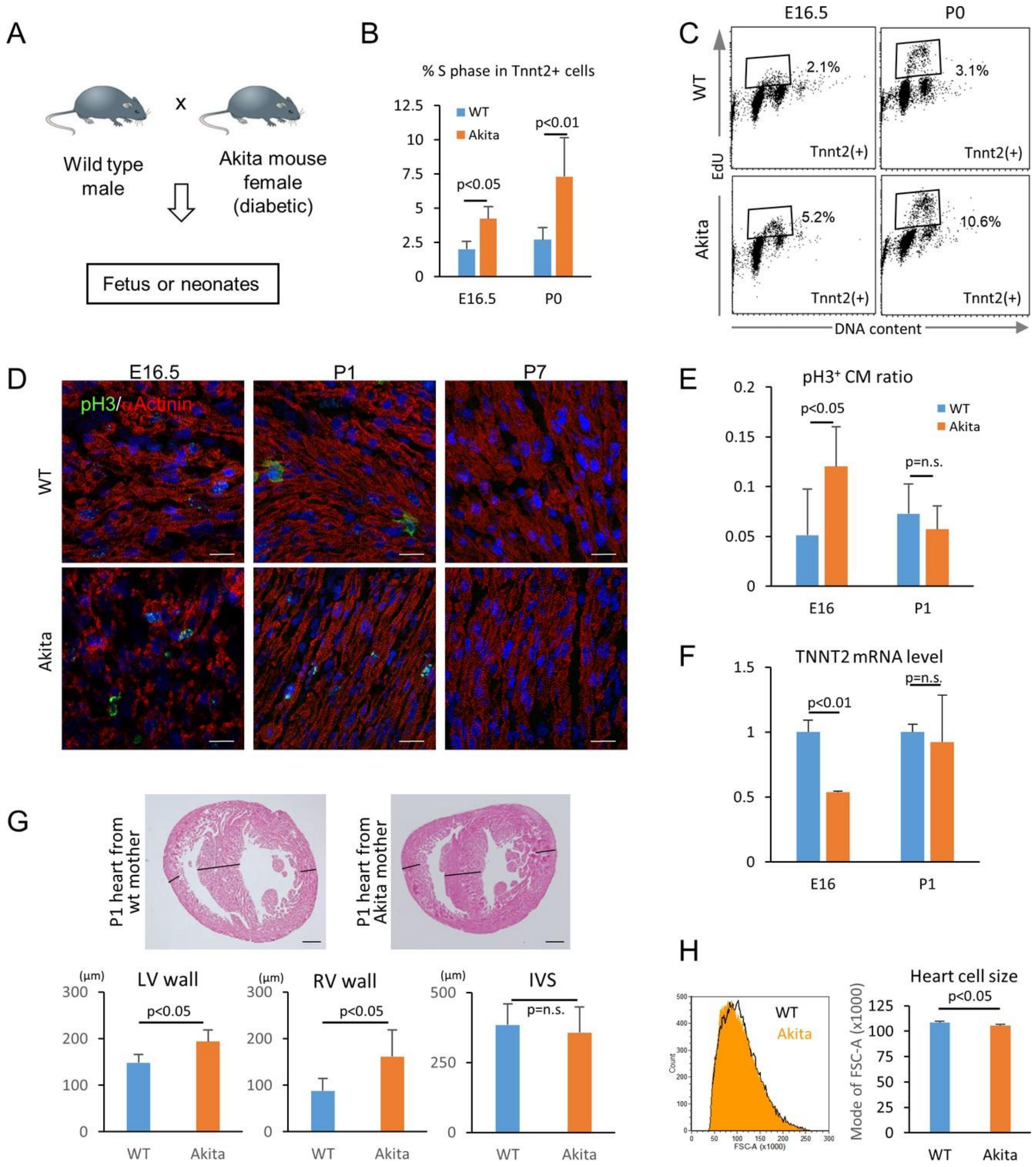

Figure 7. Hyperglycemia promotes the proliferation and inhibits the maturation of fetal cardiomyocytes in utero. (A) Diagram illustrating *in vivo* analysis of the impact of maternal hyperglycemia on fetal heart development using a diabetic mouse model (Akita). (B,C) Cell cycle analyses of fetal and neonatal cardiomyocytes from normal and

diabetic pregnancies. Tnnt2-positive cardiomyocytes from diabetic Akita mothers show a higher percentage of cells in S-phase at both E16.5 and P0. (n = 7, each; data shown are mean ± SD, p-value by t-test). (D,E) Double immunostaining for phospho-histone H3 (pH3, green) and α-actinin (red) of the heart from normal and diabetic pregnancies at E16.5, P1 and P7 (D). %pH3$^+$ cells within α-actinin$^+$ cardiomyocytes (CM) from normal (WT) and diabetic (Akita) pregnancies at E16.5 and P1 (E). At least 10,000 cardiomyocytes were counted for each of five hearts. (n = 7, each; mean ± SD, p-value by t-test.) (F) qPCR analysis for *Tnnt2* expression in hearts from normal and diabetic pregnancies. The expression level is normalized to control at each stage (n = 3, each; p-value by t-test.) (G) Histological analysis of P1 hearts from normal (WT) and diabetic (Akita) pregnancies. Ventricular wall thickness (RV, right ventricle; LV, left ventricle) and interventricular septum (IVS) thickness were analyzed histologically. Scale bar = 200 mm. (n = 5 and 4 for WT and Akita, respectively; data shown are mean ± SD, p-value by t-test). (H) Cell-size analysis of the cells isolated from P1 hearts from normal (WT) and diabetic (Akita) pregnancies using forward scatter by flow cytometry (FSC). At least 25,000 cells were measured per sample. Representative histogram from three flow cytometry measurements for each group (left) and the geometrical means of FSC (right). (n = 3, $p<0.05$ by t-test).

To examine whether hyperglycemia inhibits the maturation of fetal cardiomyocytes *in vivo*, we analyzed the fetal and neonatal hearts from diabetic pregnancies. The level of *Tnnt2* expression was significantly lower in the hearts from the diabetic pregnancies (Figure 7F). A hallmark of the congenital heart disease associated with diabetic pregnancy is asymmetric cardiac hypertrophy. Although heart weight/body weight ratio did not show a difference in our mouse model, the thickness of left and right ventricular free walls was significantly increased in the hearts from diabetic pregnancies at P1 (Figure 7G). Consistently, the cardiomyocyte size measured by flow cytometry was significantly smaller in the diabetic pregnancy group (Figure 7H). These data suggest that overproliferation and/ or delayed maturation underlie the pathological mechanism of cardiomyopathy associated with diabetic pregnancy.

Discussion

In summary, we investigated the role of glucose in cardiac formation, and discovered (1) that glucose dose-dependently inhibits cardiac maturation in hESC-CMs, (2) that the maturation-inhibitory effect is dependent on nucleotide biosynthesis via the PPP, (3) that the developing heart accomplishes intracellular glucose starvation by limiting glucose uptake in late gestational stages during normal embryogenesis, and (4) that perturbation of the environmental glucose level in diabetic pregnancy affects natural cardiomyocyte maturation *in vivo*.

Cardiomyocytes switch their main energy substrate from glucose (or other carbohydrates) to fatty acids shortly after birth. This metabolic switch has long been believed to be an adaptation of cardiomyocytes to facilitate more efficient production of ATP. However, our study has revealed that a drastic suppression of glucose uptake occurs during gestational stages, long before the metabolic switch after birth (Figure 5). Our *in vitro* hESC-CM glucose-deprivation experiments mimic this *in vivo* glucose starvation. The results suggest that glucose deprivation induces cardiac maturation at genetic, morphological, metabolic, electrophysiological and biomechanical levels (Figures 2 and 3), suggesting that glucose is a negative regulator of the maturation of fetal cardiomyocytes *in vitro* and *in vivo*, as well as a positive regulator of the mitotic activity of these cells. Perturbation of the natural glucose starvation results in higher mitotic activity and lower maturity of cardiomyocytes *in vivo* (Figure 7). Together, our results suggest that the metabolic switch during perinatal stages is necessary not only to meet the energy demand but also to induce the genetic program that facilitates the maturation of the cardiomyocytes *in vivo*. An important question that is yet to be answered is how the drastic suppression of intracellular glucose uptake is achieved in the fetal heart. As the fetal glucose environment is primarily determined by maternal metabolism and kept relatively constant in utero, one possibility is that the glucose uptake is limited at the glucose transporter level in fetal cardiomyocytes. In fact, the fetal heart switches its glucose transporter isoform at around this stage. Understanding how glucose regulates the genetic program and how the glucose uptake is regulated at the genetic level will be key to further dissecting the cross-talk between the genetic and non-genetic factors governing heart formation.

Nucleotide biosynthesis via the PPP as a key mechanism in balancing proliferation and maturation

Glucose is the most fundamental and commonly available nutrient for the cells. Hence, the activity of the glucose metabolic pathways is tightly regulated in cells. Glucose is broken down to extract energy through the glycolysis pathway and also shunts to supply 5-carbon sugars and NADPH through the PPP. In our study, chemical inhibition of glucose metabolic pathways in hESC-CMs revealed that it is not the catabolic breakdown of glucose to extract energy but rather the anabolic use of glucose to build nucleotides that is responsible for the glucose-dependent inhibition of cardiac maturation. Most of the proliferating cells synthesize nucleotides de novo from glucose, glutamine, and CO_2. In our hESC-CM experiments, blocking the PPP and nucleotide biosynthesis inhibited the glucose-mediated induction of mitosis and suppression of maturation, and supplementation of nucleotides was sufficient to recapitulate the effect of glucose (Figures 4 and 5). These data suggest that nucleotide biosynthesis via the PPP is the key regulator of the pro-mitotic/anti-maturation effect of glucose. Interestingly, cardiomyocyte maturation was not fully induced by blocking of the cell cycle with a CDK4/6 inhibitor or paclitaxel, neither of which directly impacted the nucleotide kinetics. Therefore, it is not the cell cycle in general but the nucleotides themselves that blocks the maturation. It is well documented that there is generally an inverse correlation between cell proliferation and differentiation during developmental stages (Ruijtenberg and van den Heuvel, 2016). Our data raise an intriguing possibility that nucleotide biosynthesis serves as a nodal point balancing cell proliferation and differentiation during development.

Hyperglycemia as a potential teratogen in the fetal heart

Clinically, maternal diabetes can accompany multiple complications including neuropathy, microvasculopathy, nephropathy, and insulin resistance. Although meta-analysis predicts that hyperglycemia itself is a major teratogen during diabetic pregnancy (Reece et al., 1996), it is often difficult to dissect the impacts of maternal complications on CHD as they are often subclinical. To our knowledge, our *in vitro* study is the first to demonstrate that environmental glucose itself, if excessive, directly impacts cardiac differentiation. The formation of the heart is regulated by both genetic and non-genetic factors, with the latter playing important roles particularly during late-stage cardiogenesis. An interesting aspect of the interaction between genetic and non-genetic mechanisms is that they seem to reinforce each other mutually. Our data suggest that the glucose metabolic environment is, on the one hand, a consequence of changes in cardiac genetic program, and on the other hand, a cause of the changes in cardiac gene expression.

Potential application to the translation

Understanding the metabolic signature of hESC-CMs will potentially open new methods for purifying these cells (Tohyama et al., 2016; Tohyama et al., 2013) or inducing their maturation (Drawnel et al., 2014). Considering that the inhibitors of the PPP and nucleotide biosynthesis have entered clinical trials for cancer treatment (Tennant et al., 2010; Vander Heiden, 2011), our data raise the possibility that manipulating this pathway may allow us to control the proliferation and maturation of cardiomyocytes for regenerative medicine.

With the advances in fetal diagnosis and surgical techniques, the number of CHD patients who survive childhood (and so have adult CHD) is growing rapidly by nearly 5% per year (Brickner et al., 2000). Maternal hyperglycemia is a common medical condition associated with a 2–5-fold increase in CHD (Centers for Disease Control, 1990; Simeone et al., 2015; Yogev and Visser, 2009). Currently, 60 million women of reproductive age (18–44 years old) worldwide and approximately 3 million in the U.S. have diabetes mellitus. This number is predicted to double by 2030, posing a huge medical and economic burden (Gabbay-Benziv et al., 2015). Our findings will lay a foundation for understanding how the glucose environment regulates cardiogenesis and how disturbance of non-genetic factors affects the genetic program during the pathological development of the heart.

Materials and methods

Mouse and cell lines

Wild-type and Akita mice were maintained on the C57BL/6 background according to the Guide for the Care and Use of Laboratory Animals published by the US National Institute of Health (NIH Publication No. 85–23, revised 1996). Housing and experiments were performed according to the Institutional Approval for Appropriate Care and Use of Laboratory Animals by the UCLA Institutional Animal Care and Use Committee (Protocol #2008-127-07). H9 (WA09) and UCLA4 (UCLA stem cell core) hESC lines were maintained as described before (Arshi et al., 2013). Authentication of hESCs was achieved by confirming the expression of pluripotency genes and protein markers. hESCs were routinely verified as mycoplasma-free using a PCR-based assay. hESCs were grown and differentiated in a chemically defined condition (Minami et al., 2012; Young et al., 2016; Zhu et al., 2017). Usage of all the human embryonic stem cell lines is approved by the UCLA Embryonic Stem Cell Research Oversight (ESCRO) Committee and the Institutional Review Boards (IRB) (approval #2009- 006-04).

RNA-seq and data analyses

For the RNA-seq analyses shown in Figures 1D, E and 2C, RNA was extracted from hESC, hMP, hCP, hCM14, hCM28, hCM28 (in 25 mM glucose) and hCM28 (in 0 mM glucose) using TRIZOL (ThermoFisher) and RNeasy kit (QIAGEN). 500 ng of DNaseI-treated RNA was used as input material for library preparation using the Illumina TruSeq mRNA kit (Illumina, RS-122–2001), according to manufacturer's instructions. Final libraries were sequenced as single-end 50 bp on the Illumina HiSeq2000 platform (GSE84814). Libraries for RNA-Seq shown in Figures 1D, E and 2C were prepared with the KAPA Stranded RNA-Seq Kit. The workflow consists of mRNA enrichment, cDNA generation, end repair, A-tailing, adaptor ligation, strand selection and PCR amplification. Different adaptors were used for multiplexing samples in one lane. Sequencing was performed on an Illumina HiSeq 3000 for a paired end 2 x 150 run (GSE84815). A data quality check was done on an Illumina SAV. De-multiplexing was performed with the Illumina Bcl2fastq2 v 2.17 program. Short read sequences generated from an Illumina Sequencer were aligned to the UCSC human reference genome hg19 downloaded from support.Illumina.com (http://support.illumina.com/sequencing/sequencing_software/igenome.html) using TopHat from the Tuxedo Tools. The average overall read mapping rate reached over 82 percent (average = 82.43 percent). The output was in the form of BAM (Binary Sequence Alignment/Map format) files. These outputs contain information for assigning location and quantifying the short-read alignments obtained from the RNA-seq samples. This is necessary for downstream analyses such as annotation, transcript abundance comparison and polymorphism detection. Counts or gene expression matrices were generated using HTSeq, which quantified the reads per transcript. The expression matrices were log transformed and normalized using the rlog function in the Deseq2 package. The normalized gene expression matrices were used as input for SaVanT (Signature Visualization Tools), which allowed for the visualization of molecular signatures directly related to heart development as seen in Figures 1D, E and 2C.

Flow cytometry

hESC-CMs and mouse embryonic hearts were washed three times with PBS and incubated at 37˚C in a dissociation enzyme solution with occasional pipetting to a single-cell suspension. The enzyme solution contained 1% penicillin/streptomycin (ThermoFisher, 15140–122), 10% fetal bovine serum (Hyclone), collagenase 2 mg/ml (Worthington, CLS-2), dispase 0.25 mg/ml (Gibco, 17105–041), and DNAase I (ThermoFisher) in PBS. The cells were analyzed with the following antibodies: MF20 (mouse, 1:100, Hybridoma Bank), Tnnt2 (rabbit, 1:250, Sigma-Aldrich), MitoTracker Orange CMTMRos (ThermoFisher), JC-1 (Abcam), and EdU (100 ml of 10 mM EdU solution per 10 g of mouse, ThermoFisher). For MF20 and Tnnt2, FITC-conjugated anti-mouse IgG secondary antibody (BD Biosciences) was used. Stained cells were analyzed by a flow cytometer (LSRII, BD Biosciences). Data analysis was performed using FACSDiva (BD Biosciences).

Immunocytochemistry and morphological analysis

Cells were fixed with 4% paraformaldehyde, blocked for an hour with 5% normal goat serum, and incubated with mouse α-actinin antibody (Sigma) followed by Alexa fluor 488-conjugated secondary antibody (ThermoFisher). Images were taken with Zeiss LSM780 confocal microscopy. Sarcomere lengths were analyzed using Zeiss Zen software.

mtDNA-to-nDNA ratio analysis

Total DNA including mtDNA was extracted from cells using the PureLink DNA kit (ThermoFisher), and DNA purity and quantity were determined using a spectrophotometer. To determine the ratio between mitochondrial and nuclear DNA, qRT-PCR was performed on a Roche Lightcycler 480 using SYBR Green dye.

Mitochondrial gene expression was corrected for nuclear gene expression values, and normalized to the value of the control group for each experiment as described before. Forward and reverse primer sequences are as follows: UUR forward, CAC CCA AGA ACA GGG TTT GT; UUR reverse, TGG CCA TGG GTA TGT TGT TA for mt DNA; B2-microglobulin forward, TGC TGT CTC CAT GTT TGA TGT ATC T; and B2-microglobulin reverse, TCT CTG CTC CCC ACC TCT AAG T.

Ca^{2+} transient assay

Ca^{2+} transient was measured as described (Shimizu et al., 2015). Briefly, hESC-CMs cultured in the presence or absence of glucose were loaded with 5 mM fluo-4 AM and imaged in Tyrode buffer con- taining 138.2 mM NaCl, 4.6 mM KCl, 1.2 mM MgCl, 15 mM glucose and 20 mM HEPES according to the manufacturer's instruction. Images were recorded on a Zeiss LSM 780 confocal microscope. Data analysis was carried out using the Zeiss Zen and ImageJ.

In vitro contractility assay

Contractility assessments were performed by utilizing a video-based technique with the UCSF Glad- stone-developed Matlab program MotionGUI (Huebsch et al., 2015). The videos were converted from .mts to .avi format at native resolution using commercially available software and loaded into the MotionGUI program. The conversion between pixels and real distance was performed within the MotionGUI program using a reference image with unit divisions of 100 um, taken under the same objective and video zoom settings as the cell videos, to yield a pixel size of 0.681125. This pixel size was used for all contractility assessments. Motion vectors were calculated and the data were evaluated upon completion. All samples were subjected to the same post-processing procedures in order to ensure consistency during comparative analysis. Each video sample was post-processed using neighbor-based cleaning with the vector-based cleaning criterion within the program. The threshold for this post-processing method was set to two for all samples and was adequate for improving the signal-to-noise ratio enough to identify peaks clearly corresponding to beating events in most samples. A small number of videos suffering from significant noise issues were separately subjected to fast Fourier transform (FFT) frequency domain cleaning with a cut-off frequency of 1 Hz. Only one post-processing method was applied to one video at one time. All other parameters of the MotionGUI program not outlined here were set to their respective default values.

Measurement of intracellular lactate level by Laconic

The lactate biosensor Laconic was a gift from Dr. Barros (San Martı´n et al., 2013). Overexpression of Laconic in hESC-CM was achieved using engineered adenoviruses encoding the construct. Expression of the construct was sufficiently high after 36–48 hr for FRET experiments or microscopy imaging. All cells were imaged live without fixation. Images (16 bit) were acquired using a microscope (Eclipse TE300; Nikon) fitted with a 60x (1.4 NA) oil immersion lens (Nikon) and equipped with a filter cube comprising a CFP bandpass excitation filter, 436/20b, together with a longpass dichroic mirror (455DCLP; Chroma Technology Corp). Two LEDs (Philips Lumileds), one emitting at 455 ± 20 nm (royal blue) and the other emitting at 505 ± 15 nm (cyan) were used as light sources. Ratiometric FRET measurements were obtained from the YFP and CFP images acquired simultaneously using a Dual View image splitter (Optical Insights) equipped with a 505 nm longpass dichroic filter to separate the CFP and YFP signals, a CFP emission filter (480/30), and a YFP emission filter (535/40) (John et al., 2008). Images were captured with a Cascade 512B digital camera (Photometrics). Reagents indicated in Figure 3C were added and followed by washing.

XF24 extracellular flux analyzer

hESC-CMs were seeded onto a matrigel-coated XF24 Cell Culture Microplate (Seahorse Bioscience) at 2–7.5 10^4 cells/well with or without glucose (25 mM glucose of cardiac differentiation media). Oxygen consumption rate (OCR) was measured using an XF24 Extracellular Flux Analyser (Seahorse Bioscience) in unbuffered DMEM assay medium supplemented with 1 mM pyruvate, 2 mM glutamine and with or without 25 mM glucose. OCR was measured before and after the sequential addition of 0.75 mM oligomycin, 0.5 mM FCCP and 0.75 mM of rotenone/myxothiazol. OCR was normalized to protein concentration using a Bradford assay (Bio-Rad). Mitochondrial respiration was calculated as the difference between total and rotenone/myxothiazol rates. Maximal respiration was the response to FCCP. ATP-linked respiration was represented by the oligomycin-sensitive respiration rate, whereas uncoupled respiration was represented by the difference between oligomycin and rotenone/myxothiazol rates.

Micro-electrode array

hESC-CMs at the stage of hCM14 were plated on microelectrode arrays (MEAs) containing 120 integrated TiN electrodes (30 μm diameter, 200 μm interelectrode spacing). The MEAs were placed in an incubator with a temperature of 37˚C and 5% CO_2. Two days were given to allow the cardiomyocytes to well attach the MEAs before recording started. Local field potentials at each electrode were collected over a period of 5 min every day in total with a sampling rate of 1 KHz using the MEA2100-HS120 system (Multichannel systems, Reutlingen, Germany). Data analysis was carried out using the MC_DataTool (Multichannel Systems), Origin (OriginLab Corporation) and Matlab (MathWorks). Data shown are based on three independent hESC-CM preparations.

Mass spectrometry-based metabolic measurements

The experiments were performed as described (Krall et al., 2016). Briefly, cells were seeded in 6-well plates, so that the final cell count at the time of metabolite extraction was about $7*10^5$ and this was even across all cell lines. To extract intracellular metabolites, cells were briefly rinsed with cold 150 mM ammonium acetate (pH 7.3), followed by the addition of 1 ml cold 80% MeOH on dry ice. Cell scrapers were used to detach cells, and the cell suspension was transferred into Eppendorf tubes. Extracted metabolites were transferred into glass vials and dried down under vacuum. For the LC-MS-based analysis, the samples were resuspended in 70% acetonitrile and 50 ml were injected onto a Luna NH2 column (150 mm x 2 mm, Phenomenex). Separation was achieved using A) 5 mM NH_4AcO (pH 9.9) and B) ACN. The gradient started with 15% A) going to 90% A) over 18 min, followed by an isocratic step for 9 min and reversal to the initial 15% A) for 7 min. Metabolites were quantified with TraceFinder 3.3 using accurate mass measurements ($\leq$ 3 ppm) and retention times of pure standards. Data analysis was performed using the statistical language R.

Gene expression analysis by quantitative reverse-transcriptase PCR

RNA was extracted from the tissue or the cells cultured with a specific concentration of glucose together with or without titrated metabolic pathway inhibitors using the Direct-zol RNA miniprep kit (Zymo research). RNA was reverse-transcribed into complementary DNA using the qScript cDNA synthesis kit (Quanta Biosciences). Quantitative reverse-transcriptase PCR was performed using Viia7 (Applied Biosystems/ThermoFisher). In Figures 1B, 2B and 4C–E, each bar represents the average of biological duplicates with at least three independent wells, each of which is triplicated for qPCR reaction. The relative mRNA level is normalized to the expression level of 25 mM glucose without any chemicals. Forward and reverse primer sequences are as follows:

GAPDH forward: TTGAGGTCAATGAAGGGGTC;
GAPDH reverse: GAAGGTGAAGGTCGGAGTCA;
TNNT2 forward: CAGAGCGGAAAAGTGGGAAGA;
TNNT2 reverse: TCGTTGATCCTGTTTCGGAGA;
NKX2-5 forward: GTTGTCCGCCTCTGTCTTCT;
NKX2-5 reverse: TCTATCCACGTGCCTACAGC;
PPARGC1A forward: GGTGCCTTCAGTTCACTCTCA;
and PPARGC1A reverse: AACCAGAGCAG- CACACTCGAT.

^{18}F-FDG measurement by g-counter

^{18}F-FDG was obtained from the UCLA Department of Nuclear Medicine. Warmed pregnant mice or pups were injected intravenously or intraperitoneally, respectively, with ~90 microCi (~3.33 MBq) of ^{18}F-FDG. After 2 hr, the mice were sacrificed. Preliminary experiments suggested that 2 hr was suffi- ciently long for ^{18}F-FDG to reach maximum accumulation in each organ and embryo. Fetal or neona- tal hearts were separated from the other tissue (carcass), and the mass and radioactivity in both the hearts and the carcasses were measured using a standard balance and a Wizard 3' automatic gamma counter (Perkin Elmer), respectively. The radioactivity levels in the pup carcasses were higher than the detection limit of the gamma counter, so the expected gamma counter values for the pup car- casses were calculated on the basis of the decay-corrected injected dose of ^{18}F-FDG and known conversion values between microCi and CPM on the gamma counter. To calculate the 'Normalized FDG accumulation', radioactive accumulation in each heart was divided by heart weight and then further divided by the total radioactivity in each embryo or pup. This last normalization is to account for differences in ^{18}F-FDG injected dose and accessibility to the embryos and pups. Averages and standard errors of the mean (SEM) were calculated, and the values were normalized such that E10.5 embryo FDG accumulation was set to 100.

Immunostaining

Mouse embryos were isolated in cold PBS and fixed in 4% PFA for 1~2 hr, followed by equilibration in 30% sucrose in PBS solution overnight. The tissues were placed in 1:1 30% sucrose/OCT (Tissue-Tek, Electron Microscopy Sciences) solution for 1–2 hr, then in 100% OCT compound for 1 hr at 4˚C, and embedded in 100% OCT compound, carefully oriented in Cryomolds (Ted Pella). The blocks were immediately frozen on dry ice with isopropanol and stored at -80˚C. The sections were cut 5 mm with a Leica CM3050 S cryostat. The following primary and secondary antibodies were used: α- actinin (mouse, 1:200, Sigma-Aldrich), Phospho-Histone 3 (rabbit, 1:250, Millipore), as well as Alexa Fluor 488 (green)- and Alexa Fluor 594 (red)-conjugated secondary antibodies specific to the appropriate species, which were used (1:500; ThermoFisher) for fluorescent staining. Sections were mounted with antifade mounting medium with

DAPI (ThermoFisher), and analyzed by using AxioImager D1 (Carl Zeiss Microimaging, Inc).

Statistical analysis

ANOVA and Student’s t-test were used to determine whether any statistically significant difference exists among independent groups.

References

Arshi A, Nakashima Y, Nakano H, Eaimkhong S, Evseenko D, Reed J, Stieg AZ, Gimzewski JK, Nakano A. 2013. Rigid microenvironments promote cardiac differentiation of mouse and human embryonic stem cells. Science and Technology of Advanced Materials 14:025003. DOI: 10.1088/1468-6996/14/2/025003, PMID: 24311969

Barber AJ, Antonetti DA, Kern TS, Reiter CE, Soans RS, Krady JK, Levison SW, Gardner TW, Bronson SK. 2005. The Ins2Akita mouse as a model of early retinal complications in diabetes. Investigative Opthalmology & Visual Science 46:2210–2218. DOI: 10.1167/iovs.04-1340, PMID: 15914643

Brickner ME, Hillis LD, Lange RA. 2000. Congenital heart disease in adults. First of two parts. The New England Journal of Medicine 342:256–263. DOI: 10.1056/NEJM200001273420407, PMID: 10648769

Carey BW, Finley LW, Cross JR, Allis CD, Thompson CB. 2015. Intracellular a-ketoglutarate maintains the pluripotency of embryonic stem cells. Nature 518:413–416. DOI: 10.1038/nature13981, PMID: 25487152

Centers for Disease Control. 1990. Perinatal mortality and congenital malformations in infants born to women with insulin-dependent diabetes mellitus–United States, Canada, and Europe, 1940-1988. MMWR. Morbidity and Mortality Weekly Report 39:363–365. PMID: 2111001

Cox SJ, Gunberg DL. 1972. Metabolite utilization by isolated embryonic rat hearts *in vitro*. Journal of Embryology and Experimental Morphology 28:235–245. PMID: 4642990

Crespo FL, Sobrado VR, Gomez L, Cervera AM, McCreath KJ. 2010. Mitochondrial reactive oxygen species mediate cardiomyocyte formation from embryonic stem cells in high glucose. Stem Cells 28:1132–1142. DOI: 10.1002/stem.441, PMID: 20506541

Drawnel FM, Boccardo S, Prummer M, Delobel F, Graff A, Weber M, Ge´ rard R, Badi L, Kam-Thong T, Bu L, Jiang X, Hoflack JC, Kiialainen A, Jeworutzki E, Aoyama N, Carlson C, Burcin M, Gromo G, Boehringer M, Stahlberg H, et al. 2014. Disease modeling and phenotypic drug screening for diabetic cardiomyopathy using human induced pluripotent stem cells. Cell Reports 9:810–820. DOI: 10.1016/j.celrep.2014.09.055, PMID: 25437537

Fahed AC, Gelb BD, Seidman JG, Seidman CE. 2013. Genetics of congenital heart disease: the glass half empty. Circulation Research 112:707–720. DOI: 10.1161/CIRCRESAHA.112.300853, PMID: 23410880

Fujita H, Haseyama T, Kayo T, Nozaki J, Wada Y, Ito S, Koizumi A. 2001. Increased expression of glutathione S-transferase in renal proximal tubules in the early stages of diabetes: a study of type-2 diabetes in the Akita mouse model. Nephron Experimental Nephrology 9:380–386. DOI: 10.1159/000052636, PMID: 11701997

Gabbay-Benziv R, Reece EA, Wang F, Yang P. 2015. Birth defects in pregestational diabetes: Defect range, glycemic threshold and pathogenesis. World Journal of Diabetes 6:481–488. DOI: 10.4239/wjd. v6.i3.481, PMID: 25897357

Gaspar JA, Doss MX, Hengstler JG, Cadenas C, Hescheler J, Sachinidis A. 2014. Unique metabolic features of stem cells, cardiomyocytes, and their progenitors. Circulation Research 114:1346–1360. DOI: 10.1161/CIRCRESAHA.113.302021, PMID: 24723659

Gelb B, Brueckner M, Chung W, Goldmuntz E, Kaltman J, Kaski JP, Kim R, Kline J, Mercer-Rosa L, Porter G, Roberts A, Rosenberg E, Seiden H, Seidman C, Sleeper L, Tennstedt S, Kaltman J, Schramm C, Burns K, Pearson G, et al. 2013. The Congenital Heart Disease Genetic Network Study: rationale, design, and early results. Circulation Research 112:698–706. DOI: 10.1161/CIRCRESAHA.111.300297, PMID: 23410879

Haase A, Olmer R, Schwanke K, Wunderlich S, Merkert S, Hess C, Zweigerdt R, Gruh I, Meyer J, Wagner S, Maier LS, Han DW, Glage S, Miller K, Fischer P, Scho¨ ler HR, Martin U. 2009. Generation of induced pluripotent stem cells from human cord blood. Cell Stem Cell 5:434–441. DOI: 10.1016/j.stem.2009.08.021, PMID: 19796623

Harris JM, Esain V, Frechette GM, Harris LJ, Cox AG, Cortes M, Garnaas MK, Carroll KJ, Cutting CC, Khan T, Elks PM, Renshaw SA, Dickinson BC, Chang CJ, Murphy MP, Paw BH, Vander Heiden MG, Goessling W, North TE. 2013. Glucose metabolism impacts the spatiotemporal onset and magnitude of HSC induction *in vivo*. Blood 121:2483–2493. DOI: 10.1182/blood-2012-12-471201, PMID: 23341543

Huebsch N, Loskill P, Mandegar MA, Marks NC, Sheehan AS, Ma Z, Mathur A, Nguyen TN, Yoo JC, Judge LM, Spencer CI, Chukka AC, Russell CR, So PL, Conklin BR, Healy KE. 2015. Automated video-based analysis of contractility and calcium flux in human-induced pluripotent stem cell-derived cardiomyocytes cultured over different spatial scales. Tissue Engineering Part C: Methods 21:467–479. DOI: 10.1089/ten.tec.2014.0283, PMID: 25333967

John SA, Ottolia M, Weiss JN, Ribalet B. 2008. Dynamic modulation of intracellular glucose imaged in single cells using a FRET-based glucose nanosensor. Pflu¨gers Archiv - European Journal of Physiology 456:307–322. DOI: 10.1007/s00424-007-0395-z, PMID: 18071748

Krall AS, Xu S, Graeber TG, Braas D, Christofk HR. 2016. Asparagine promotes cancer cell proliferation through use as an amino acid exchange factor. Nature Communications 7:11457. DOI: 10.1038/ ncomms11457, PMID: 27126896

Linker W, Lo¨ ffler M, Schneider F. 1985. Uridine, but not cytidine can sustain growth of Ehrlich ascites tumor cells in glucose-deprived medium with altered proliferation kinetics. European Journal of Cell Biology 36:176–181. PMID: 3996430

Ma J, Guo L, Fiene SJ, Anson BD, Thomson JA, Kamp TJ, Kolaja KL, Swanson BJ, January CT. 2011. High purity human-induced pluripotent stem cell-derived cardiomyocytes: electrophysiological properties of action potentials and ionic currents. AJP: Heart and Circulatory Physiology 301:H2006–H2017. DOI: 10.1152/ajpheart.00694.2011, PMID: 21890694

Mabbott NA, Baillie JK, Brown H, Freeman TC, Hume DA. 2013. An expression atlas of human primary cells: inference of gene function from coexpression networks. BMC Genomics 14:632. DOI: https://doi.org/10.1186/ 1471-2164-14-632, PMID: 24053356

Mackler B, Grace R, Duncan HM. 1971. Studies of mitochondrial development during embryogenesis in the rat. Archives of Biochemistry and Biophysics 144:603–610. DOI: 10.1016/0003-9861(71)90367-5, PMID: 4328160

Makinde AO, Kantor PF, Lopaschuk GD. 1998. Maturation of fatty acid and carbohydrate metabolism in the newborn heart. Molecular and Cellular Biochemistry 188:49–56. DOI: 10.1023/A: 1006860104840, PMID: 9823010

Minami I, Yamada K, Otsuji TG, Yamamoto T, Shen Y, Otsuka S, Kadota S, Morone N, Barve M, Asai Y, Tenkova- Heuser T, Heuser JE, Uesugi M, Aiba K, Nakatsuji N. 2012. A small molecule that promotes cardiac differentiation of human pluripotent stem cells under defined, cytokine- and xeno-free conditions. Cell Reports 2:1448–1460. DOI: 10.1016/j.celrep.2012.09.015, PMID: 23103164

Oburoglu L, Tardito S, Fritz V, de Barros SC, Merida P, Craveiro M, Mamede J, Cretenet G, Mongellaz C, An X, Klysz D, Touhami J, Boyer-Clavel M, Battini JL, Dardalhon V, Zimmermann VS, Mohandas N, Gottlieb E, Sitbon M, Kinet S, et al. 2014. Glucose and glutamine metabolism regulate human hematopoietic stem cell lineage specification. Cell Stem Cell 15:169–184. DOI: 10.1016/j.stem.2014.06.002, PMID: 24953180

Paige SL, Thomas S, Stoick-Cooper CL, Wang H, Maves L, Sandstrom R, Pabon L, Reinecke H, Pratt G, Keller G, Moon RT, Stamatoyannopoulos J, Murry CE. 2012. A temporal chromatin signature in human embryonic stem cells identifies regulators of cardiac development. Cell 151:221–232. DOI: 10.1016/j.cell.2012. 08.027, PMID: 22981225

Reece EA, Homko CJ, Wu YK. 1996. Multifactorial basis of the syndrome of diabetic embryopathy. Teratology 54:171–182. DOI: 10.1002/(SICI)1096-9926(199610)54:4<171::AID-TERA1>3.0.CO;2-4, PMID: 9122886

Reichard P, Canellakis ZN, Canellakis ES. 1960. Regulatory mechanisms in the synthesis of deoxyribonucleic acid *in vitro*. Biochimica et Biophysica Acta 41:558–559. DOI: 10.1016/0006-3002(60)90067-6, PMID: 14437039

Ruijtenberg S, van den Heuvel S. 2016. Coordinating cell proliferation and differentiation: Antagonism between cell cycle regulators and cell type-specific gene expression. Cell Cycle 15:196–212. DOI: 10.1080/15384101.2015.1120925, PMID: 26825227

San Mart´ın A, Ceballo S, Ruminot I, Lerchundi R, Frommer WB, Barros LF. 2013. A genetically encoded FRET lactate sensor and its use to detect the Warburg effect in single cancer cells. PLoS One 8:e57712. DOI: 10.1371/journal.pone.0057712, PMID: 23469056

Shimizu H, Schredelseker J, Huang J, Lu K, Naghdi S, Lu F, Franklin S, Fiji HDG, Wang K, Zhu H, Tian C, Lin B, Nakano H, Ehrlich A, Nakai J, Stieg AZ, Gimzewski JK, Nakano A, Goldhaber JI, Vondriska TM, et al. 2015. Mitochondrial Ca2+ uptake by the voltage-dependent anion channel 2 regulates cardiac rhythmicity. eLife 4: e04801. DOI: 10.7554/eLife.04801, PMID: 25588501

Shiraki N, Shiraki Y, Tsuyama T, Obata F, Miura M, Nagae G, Aburatani H, Kume K, Endo F, Kume S. 2014. Methionine metabolism regulates maintenance and differentiation of human pluripotent stem cells. Cell Metabolism 19:780–794. DOI: 10.1016/j.cmet.2014.03.017, PMID: 24746804

Shyh-Chang N, Locasale JW, Lyssiotis CA, Zheng Y, Teo RY, Ratanasirintrawoot S, Zhang J, Onder T, Unternaehrer JJ, Zhu H, Asara JM, Daley GQ, Cantley LC. 2013. Influence of threonine metabolism on S-adenosylmethionine and histone methylation. Science 339:222–226. DOI: 10.1126/science. 1226603, PMID: 23118012

Simeone RM, Devine OJ, Marcinkevage JA, Gilboa SM, Razzaghi H, Bardenheier BH, Sharma AJ, Honein MA. 2015. Diabetes and congenital heart defects: a systematic review, meta-analysis, and modeling project. American Journal of Preventive Medicine 48:195–204. DOI: 10.1016/j.amepre.2014.09.002, PMID: 25326416

Su AI, Wiltshire T, Batalov S, Lapp H, Ching KA, Block D, Zhang J, Soden R, Hayakawa M, Kreiman G, Cooke MP, Walker JR, Hogenesch JB. 2004. A gene atlas of the mouse and human protein-encoding transcriptomes. PNAS 101:6062–6067. DOI: 10.1073/pnas.0400782101, PMID: 15075390

Subramanian A, Tamayo P, Mootha VK, Mukherjee S, Ebert BL, Gillette MA, Paulovich A, Pomeroy SL, Golub TR, Lander ES, Mesirov JP. 2005. Gene set enrichment analysis: a knowledge-based approach for interpreting genome-wide expression profiles. PNAS 102:15545–15550. DOI: 10.1073/pnas.0506580102, PMID: 16199517

Tennant DA, Dura´n RV, Gottlieb E. 2010. Targeting metabolic transformation for cancer therapy. Nature Reviews Cancer 10:267–277. DOI: 10.1038/nrc2817, PMID: 20300106

Tohyama S, Hattori F, Sano M, Hishiki T, Nagahata Y, Matsuura T, Hashimoto H, Suzuki T, Yamashita H, Satoh Y, Egashira T, Seki T, Muraoka N, Yamakawa H, Ohgino Y, Tanaka T, Yoichi M, Yuasa S, Murata M, Suematsu M, et al. 2013. Distinct metabolic flow enables large-scale purification of mouse and human pluripotent stem cell- derived cardiomyocytes. Cell Stem Cell 12:127–137. DOI: 10.1016/j.stem.2012.09.013, PMID: 23168164

Tohyama S, Fujita J, Hishiki T, Matsuura T, Hattori F, Ohno R, Kanazawa H, Seki T, Nakajima K, Kishino Y, Okada M, Hirano A, Kuroda T, Yasuda S, Sato Y, Yuasa S, Sano M, Suematsu M, Fukuda K. 2016. Glutamine oxidation is indispensable for survival of human pluripotent stem cells. Cell Metabolism 23:663–674. DOI: 10.1016/j.cmet.2016.03.001, PMID: 27050306

Vander Heiden MG, Cantley LC, Thompson CB. 2009. Understanding the Warburg effect: the metabolic requirements of cell proliferation. Science 324:1029–1033. DOI: 10.1126/science.1160809, PMID: 19460998

Vander Heiden MG. 2011. Targeting cancer metabolism: a therapeutic window opens. Nature Reviews Drug Discovery 10:671–684. DOI: 10.1038/nrd3504, PMID: 21878982

Wamstad JA, Alexander JM, Truty RM, Shrikumar A, Li F, Eilertson KE, Ding H, Wylie JN, Pico AR, Capra JA, Erwin G, Kattman SJ, Keller GM, Srivastava D, Levine SS, Pollard KS, Holloway AK, Boyer LA, Bruneau BG. 2012. Dynamic and coordinated epigenetic regulation of developmental transitions in the cardiac lineage. Cell 151:206–220. DOI: 10.1016/j.cell.2012.07.035, PMID: 22981692

Wang J, Takeuchi T, Tanaka S, Kubo SK, Kayo T, Lu D, Takata K, Koizumi A, Izumi T. 1999. A mutation in the insulin 2 gene induces diabetes with severe pancreatic beta-cell dysfunction in the Mody mouse. Journal of Clinical Investigation 103:27–37. DOI: 10.1172/JCI4431, PMID: 9884331

Wang J, Alexander P, Wu L, Hammer R, Cleaver O, McKnight SL. 2009. Dependence of mouse embryonic stem cells on threonine catabolism. Science 325:435–439. DOI: 10.1126/science.1173288, PMID: 195 89965

Warshaw JB, Terry ML. 1970. Cellular energy metabolism during fetal development. II. Fatty acid oxidation by the developing heart. The Journal of Cell Biology 44:354–360. DOI: 10.1083/jcb.44.2.354, PMID: 5415033

Xeros N. 1962. Deoxyriboside control and synchronization of mitosis. Nature 194:682–683. DOI: 10.1038/194682a0, PMID: 14008663

Yaguchi M, Nagashima K, Izumi T, Okamoto K. 2003. Neuropathological study of C57BL/6Akita mouse, type 2 diabetic model: enhanced expression of alphaB-crystallin in oligodendrocytes. Neuropathology 23:44–50. DOI: 10.1046/j.1440-1789.2003.00475.x, PMID: 12722925

Yang X, Rodriguez M, Pabon L, Fischer KA, Reinecke H, Regnier M, Sniadecki NJ, Ruohola-Baker H, Murry CE. 2014. Tri-iodo-l-thyronine promotes the maturation of human cardiomyocytes-derived from induced pluripotent stem cells. Journal of Molecular and Cellular Cardiology 72:296–304. DOI: 10.1016/j.yjmcc.2014.04.005, PMID: 24735830

Yogev Y, Visser GH. 2009. Obesity, gestational diabetes and pregnancy outcome. Seminars in Fetal and Neonatal Medicine 14:77–84. DOI: 10.1016/j.siny.2008.09.002, PMID: 18926784

Yoshioka M, Kayo T, Ikeda T, Koizumi A. 1997. A novel locus, Mody4, distal to D7Mit189 on chromosome 7 determines early-onset NIDDM in nonobese C57BL/6 (Akita) mutant mice. Diabetes 46:887–894. DOI: 10.2337/diab.46.5.887, PMID: 9133560

Young CS, Hicks MR, Ermolova NV, Nakano H, Jan M, Younesi S, Karumbayaram S, Kumagai-Cresse C, Wang D, Zack JA, Kohn DB, Nakano A, Nelson SF, Miceli MC, Spencer MJ, Pyle AD. 2016. A single CRISPR-Cas9 deletion strategy that targets the majority of DMD patients restores dystrophin function in hiPSC-derived muscle cells. Cell Stem Cell 18:533–540. DOI: 10.1016/j.stem.2016.01.021, PMID: 26877224

Zhang J, Wilson GF, Soerens AG, Koonce CH, Yu J, Palecek SP, Thomson JA, Kamp TJ. 2009. Functional cardiomyocytes derived from human induced pluripotent stem cells. Circulation Research 104:e30–e41. DOI: 10.1161/CIRCRESAHA.108.192237, PMID: 19213953

Zhu H, Scharnhorst KS, Stieg AZ, Gimzewski JK, Minami I, Nakatsuji N, Nakano H, Nakano A. 2017. Two dimensional electrophysiological characterization of human pluripotent stem cell-derived cardiomyocyte system. Scientific Reports 7:43210. DOI: 10.1038/srep43210, PMID: 28266620

Chapter 3. Nanoscale Neuromorphic Networks and Criticality: A Perspective

Abstract

Numerous studies suggest critical dynamics may play a role in information processing and task performance in biological systems. However, studying critical dynamics in these systems can be challenging due to many confounding biological variables that limit access to the physical processes underpinning critical dynamics. Here we offer a perspective on the use of abiotic, neuromorphic nanowire networks as a means to investigate critical dynamics in complex adaptive systems. Neuromorphic nanowire networks are composed of metallic nanowires and possess metal-insulator-metal junctions. These networks self-assemble into a highly interconnected, variable-density structure and exhibit nonlinear electrical switching properties and information processing capabilities. We highlight key dynamical characteristics observed in neuromorphic nanowire networks, including persistent fluctuations in conductivity with power law distributions, hysteresis, chaotic attractor dynamics, and avalanche criticality. We posit that neuromorphic nanowire networks can function effectively as tunable abiotic physical systems for studying critical dynamics and leveraging criticality for computation.

Background

Criticality in nature

Nature is awash with complex systems that exhibit behavior which collectively extends beyond the predicted behavior of the system's individual components [1-3].

This is an example of emergent behavior, or properties which cannot be predicted by extrapolation from a system's individual components alone. Rather, the system's state evolves through the interactions of its components [4-5]. Numerous studies have devoted considerable effort to elucidating the mechanisms underlying such complex dynamical systems [3, 6-8]. One potential mechanism that has emerged as a candidate for describing complex behavior is criticality. The concept of criticality refers to a system poised at the point between ordered and disordered states (a "critical point"), analogous to a phase transition [9]. Such systems exhibit long-range spatio-temporal interactions over many scales [9]. Scale-invariant phenomena can be represented in the form of power-law (Pareto) probability distributions, $f(x) \propto x^{-\beta}$, where β is a positive real number [10-13]. Furthermore, the tuning of some parameter that controls or governs the system (e.g. temperature, strain) -- whether driven by the system intrinsically or by an external agent -- can direct the system away from the critical point and into sub- or supercritical regimes [9, 14-17]. In addition, it has been suggested that a system operates optimally when poised at its critical state [9, 18-20].

In nature, numerous abiotic and biotic systems are suspected to exhibit critical dynamics. Evidence of power-law distributions in abiotic phenomena include the dynamics of arrays of magnetic dipoles, cellular automata, earthquake size and frequency, forest fire propagation, atmospheric flows, climate fluctuations, word frequency, wealth distribution, economic systems, and solar flares [14-15, 21-28]. Similarly, power-law distributions are observed in a variety of biotic phenomena including evolutionary ecology, gene networks, morphology, animal collective movement (e.g. flocks of birds), mitochondrial networks in the heart, and neural systems, among others [13, 29-39].

Criteria for criticality

The use of power laws as the sole criterion for determining whether a system demonstrates criticality has been challenged previously [40-41]. The criteria for determining whether or not a system demonstrates criticality are sometimes misunderstood or loosely applied. In certain fields, studies have been published professing that a system exhibits critical or self-organized critical (SOC) dynamics based solely on the exhibition of a power-law distribution. Such work sometimes overlooks non-critical phenomena that are capable of producing power-law distributions. Prominent examples include successive fractionation, multiplicative noise, randomly-terminated exponential processes, preferential attachment, and the typing of random words [42-46]. Therefore, power-law relationships alone are insufficient to conclusively demonstrate that a system is critical.

Criticisms of criticality necessitated the establishment of specific criteria to define a critical system. Physicists and neuroscientists have contributed significantly to this effort by developing a robust set of criteria that critical systems should meet, including:

a) Power-law relationships, $p(x) \propto x^{-\beta}$, between order parameter, control parameter and size of system.
b) Finite size scaling of correlation length and order parameter susceptibility (i.e. distribution cut-offs diverge with system size).
c) Mathematical relationships between power-law exponents for different parameters in a dynamical system [42, 47].
d) Evidence of shape (data) collapse: multiple phenomena or events across

different scales exhibiting self-similarity (e.g. event duration) [47].

e) Tunability: the ability of a system state to be regulated by a control parameter that drives the system into sub- or supercritical regimes, resulting in non-critical dynamics [42].

These requirements, among others, for critical systems have provided focus for experimental tests of criticality in a variety of systems. [42].

Criticality in neuronal systems

Few potentially critical biological systems have received more attention than the brain's cortical neuronal system. Experimental and theoretical studies over the last few decades provide support for the argument that the brain demonstrates critical dynamics [10, 39, 42, 48-49]. Studies of *in vitro* neurons and cortical tissue slices have demonstrated statistically robust power-law distributions in neuronal spiking events, called 'avalanches', in both duration and size of the event [10, 39, 42, 48-49]. After re-scaling avalanche size and duration, the resulting distributions exhibit a shape collapse, where avalanches of different durations converge onto a universal scaling function [47]. Additionally, *in vivo* functional magnetic resonance imaging (fMRI) studies of the human brain provide evidence that the brain may exhibit critical dynamics [50-51]. Computational modeling data from one such study reasonably predicted the patterns of activity in specific regions of the brain when it is in or near a critical state [48]. Other studies showed how critical dynamics were lost in abnormal neural conditions, such as epileptic seizures, in rats and humans. [52-54].

Several studies provide evidence that the brain's performance in operations such as information storage and transmission is optimal when the brain is at or near a critical point [51, 55-57, 58-60]. However, studying the brain for evidence of criticality as a mechanism for its information processing prowess is an inherently challenging task. Our perspective is that an abiotic system that demonstrates both information processing capabilities and diverse nonlinear dynamics could provide new insights into critical systems. The utilization of a tunable abiotic system would also allow for control over available parameter space, material composition, and network topology, as well as more extensive measurement and analysis methodologies. In our view, neuromorphic networks are a suitable system for advancing the understanding of critical dynamics in neuronal and other biological systems.

Nanoscale neuromorphic networks

General characteristics of physical neuromorphic networks

The first synthetic, brain-inspired computer, the perceptron, was developed in 1958 by Frank Rosenblatt at Cornell University and the United States Office of Naval Research [61]. The perceptron was conceived in an attempt to mimic biological information processing systems and perform difficult tasks such as image recognition [61-62]. Although this technology failed to achieve the task in its era, the notion of brain-inspired computational systems endured. In 1990, Carver Mead introduced the concept of neuromorphic engineering to describe systems specifically engineered to mimic features of the brain, including co-localized processing and memory [63-65]. Since then, many neuromorphic computational systems have been developed, including atomic switch networks [65-84].

Atomic switch networks are biologically-inspired, abiotic, physical systems composed of highly interconnected networks of nanoionic devices called ‘atomic switches’ [66]. Atomic switches are functionally akin to information-retaining nonlinear circuit elements which exhibit memory-resistive (memristive) switching and quantized conductance in addition to short- and long-term memory elements [66]. Such memristive circuit elements retain information, or memory, of their previous states. Memristive switching is achieved via the formation or degradation of nanometer-scale conductive filaments between structural elements, which arise from voltage- or current-driven ionic migration and reduction/oxidation processes [85]. The memory effect is governed by the size of the formed filament [67]. The ability to tune the conductance of a memristive (atomic) switch via filament formation/degradation is considered analogous to the adaptive strength of synaptic connections between neurons [67], making them an inorganic synaptic analog. Memristive (atomic) switches, functioning as conductance-based inorganic synapses, can form from nanoscale structures that self-assemble into complex networks [68-70]. Various combinations of conductive and insulating materials can be used to produce these networks, including silver, polyvinylpyrrolidone (PVP), sulfur, iodine, and selenide, among others [69-78]. Memristive switch networks of nanoparticles or nanowires, as shown in Figure 1A-C, previously demonstrated emergent behavior that isolated atomic switches do not, including spatially distributed memory and recurrent dynamics [70,79].

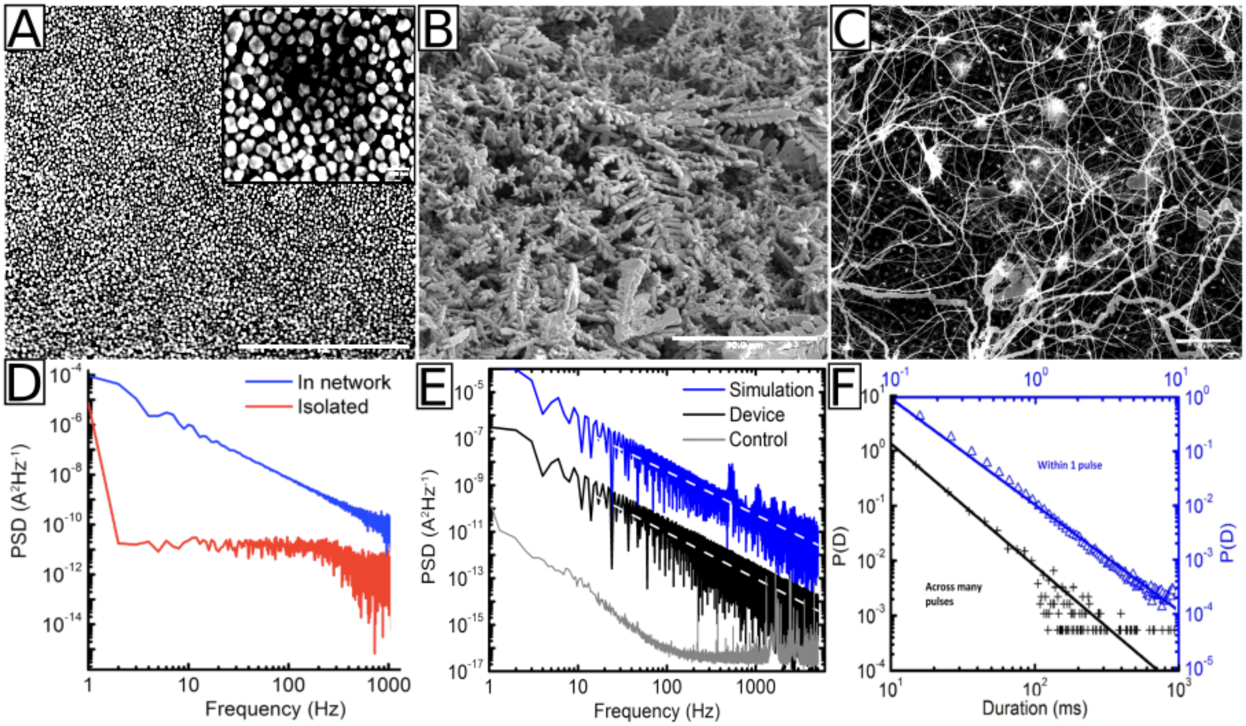

Figure 1. Network morphology and power-law distributions in silver nanoparticle or silver sulfide (Ag_2S) nanowire networks. Top row: scanning electron microscope (SEM) images of different types of networks. A) nanoparticle thin-film network (scale bar = 5 μm, insert = 200 nm), B) dendritic or fractal network (scale bar = 30 μm), C) high-density, seed-patterned nanowire network (scale bar = 50 μm). Bottom row: power-law relationships in memristive (atomic) switches and atomic switch networks. D) power spectral density (PSD) of simulated data for a single atomic switch (red) compared to multiple atomic switches embedded in a network (blue), E) comparison of power-law distributions between PSD plots of a purely ohmic network with no atomic switch (gray), and experimental (black) and simulated (blue) atomic switch networks, F) probability distribution of temporally metastable conduction states over single (blue) and multiple (black) signal pulses. Partially adapted from [72, 80-81].

Nanowire networks

Nanowire-based atomic switch networks (Figure 1B-C) rely on interactions between network elements. However, nanowire networks differ from nanoparticle networks (Figure 1A) in their morphology and connectivity. Nanowire networks can be tuned to control for nanowire thickness, extent of branching, and regional nanowire density [86]. Nanowire networks also exhibit higher levels of connectivity than nanoparticle networks. Each nanowire has the potential to engage in multiple connections with other wires elsewhere in the network, generating long-range connections between wires that would not otherwise interact and enabling recurrent connectivity loops. In contrast, nanoparticle networks rely upon nearest-neighbor interactions. Furthermore, nanowire connections are regulated by the amount of activity experienced by the nanowire-nanowire junction [70]. The high density of atomic switches, functioning as synthetic synapses, in nanowire networks (~10^8 synthetic synapses per square centimeter) further reinforces their structural similarity to synaptic networks between neurons in the brain, e.g. in the neocortex [81]. In addition to synaptic behavior similarities, nanowire networks have demonstrated fractal geometries, power-law behavior (Figure 1D-F), memory, and long-range spatio-temporal correlations [87]. Importantly, the neuromorphic properties of nanowire networks are observed for different materials [71], suggesting their dynamics and information processing capacity are robust to variations in the atomic switch junctions.

Information processing

The intrinsic complexity and interconnectivity of neuromorphic networks have demonstrated a means of distributed computation in materio, which refers to a phenomenon in which the physical changes in the network are capable of performing computational tasks [88-91]. These properties can be harnessed by treating the network as a dynamic reservoir capable of mapping input signals into higher dimensions for complex computational tasks. This is achieved through a technique called reservoir computing (RC), a modification of recurrent neural network frameworks. RC enables the use of a simple readout mechanism from the network which can be employed to map the higher dimension outputs onto a desired task [91-94]. This method is advantageous in that it only requires weighting and manipulation of the output layer, greatly reducing the training cost and improving power efficiency in contrast to conventional computing architectures. Consequently, neuromorphic networks have been extensively explored as a suitable substrate for RC and have successfully realized high fidelity, low power implementation of both simple and complex tasks, including logic tasks, T-maze tests, speech recognition and associative memory among others [95-99].

Simulation-based studies also lend support to the experimental data, demonstrating several information processing and learning tasks implemented in the reservoir computing framework, including chaotic time series prediction, memory capacity, transfer learning, and multitask learning [99-104]. Indeed, one study reported that neuromorphic nanowire networks prepared in an edge-of-chaos state (i.e. a phase transition between stable and unstable dynamics) perform better in tasks of greater computational complexity [105]. A similar result was found in another study using spiking neuromorphic networks prepared in a critical state [106]. Information dynamics (e.g. transfer entropy) has also been found to be maximized when nanowire networks transition from a quiescent to an active phase [102, 107-108]. Task performance, combined with other network properties demonstrate that nanowire networks can perform reservoir computation and other information processing paradigms. Simulations of these networks suggest their optimal performance may arise from operating at a critical regime [74, 109, 95]. Our perspective is that this makes neuromorphic nanowire networks a unique physical system for studying critical dynamics.

Critical dynamics in nanowire networks

Characteristics of criticality have been observed in both Ag_2S and Ag-PVP nanowire networks. Experimental measurements as well as theoretical and simulation studies revealed persistent current fluctuations with a power-law power spectral density (PSD) over several decades in frequency [73, 77, 80-81, 110]. However, as mentioned earlier, power-law relationships, while necessary, are not sufficient to designate a system critical.

Recent studies found evidence for avalanche criticality in Ag-PVP nanowire networks [105]. It is our perspective that evidence for avalanche criticality should also exist in other types of neuromorphic nanowire networks. To test this, we considered a silver selenide (Ag_2Se) nanowire network. Silver selenide nanowire networks can be synthesized by drop-casting nanowires onto a microelectrode array (MEA). Figure 2 shows images of an MEA and the resulting drop-cast network. The highly inhomogeneous morphology of the nanowire network, as seen in Figure 2 (right panel), specifically those regions of higher density and varying degrees of interconnectivity, bears some structural similarity to the neuropil of the biological neocortex [81].

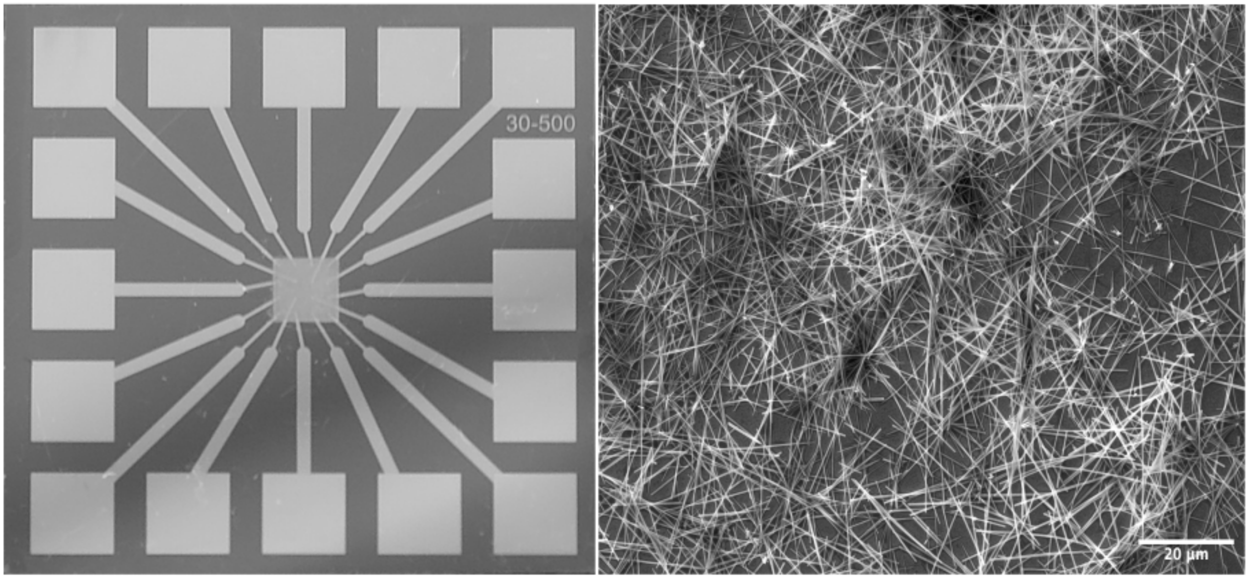

Figure 2. Optical image of MEA (left panel) and scanning electron microscopy (SEM) image of Ag_2Se network (right panel). Microelectrode arrays allow stimulation of the nanowire networks via outer contact electrodes. The networks are grown or drop-cast on the inner electrode (left panel, center). The SEM image (right panel) demonstrates variable density and interconnectivity of nanowires in the network. Scale bar in right panel: 20 µm.

Figure 3 shows current-voltage (*I*-*V*) phase diagrams acquired over many cycles of a 1 Hz triangular input wave. Several observations can be made. Firstly, each cycle forms a closed bipolar hysteresis loop pinched at the centre. This nonlinear (non-Ohmic) electrical response is a key characteristic of memristive devices and reflects their memory property - i.e. the current state *I*(*t*), *V*(*t*) depends on the history of states prior to *t* [111-114]. In this network, individual nanowire-nanowire intersections are memristive atomic switch junctions. Figure 3 indicates that, collectively, these junctions act like a single memristive element. A second observation from Figure 3A and B is that some cycles exhibit fluctuations and hard switching (i.e. a very sharp increase or decrease in *I*). Switching events are associated with abrupt resistance changes at individual junctions, attributable to the formation/degradation of conductive filaments. A third observation is that each *I*-*V* cycle deviates slightly from previous cycles. Indeed, no two trajectories completely coincide. Similar chaotic attractor dynamics was previously observed in memristor devices and memristive networks of Ag-PVP nanowires [105, 115]. Note, however, that the trajectories do not diverge sufficiently to qualify as chaotic. Their confinement to a localized region of phase-space instead suggests chaotic attractor dynamics. Such dynamics may be useful for computation as outputs *I*(*t*) for each AC cycle represent separable features and the collective attractor dynamics suggest solutions converge to local stable states [116-117]. Further investigation is warranted to determine (e.g. via Lyapunov exponent analysis) if these trajectories are consistent with the edge-of-chaos state, or the state where the maximal Lyapunov exponent is approximately zero. This state has been purported to be optimal for information processing [118-120]. Hochstetter et al. showed that Ag-PVP nanowire networks tuned into an edge-of-chaos state performed better on reservoir learning tasks with higher computational complexity [105].

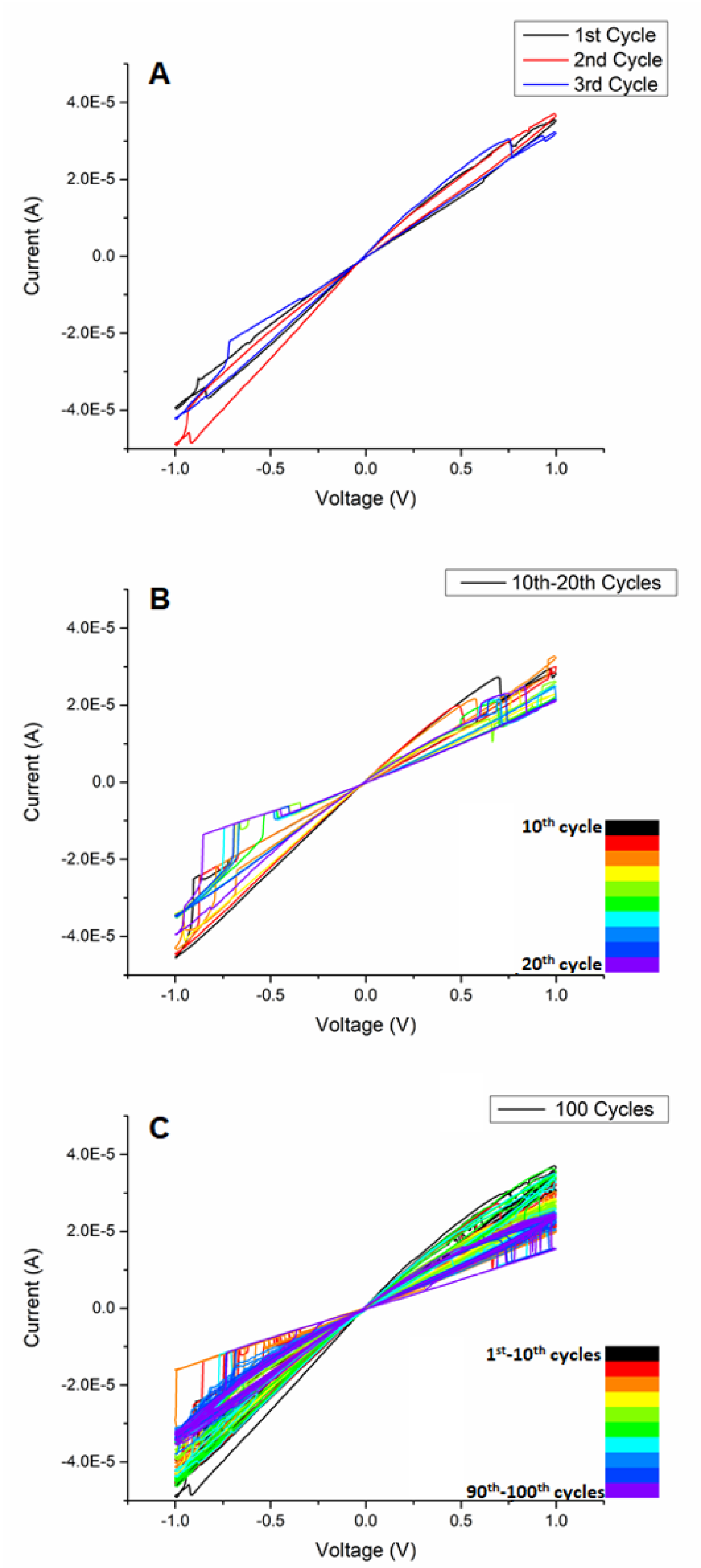
A
1st Cycle
2nd Cycle
3rd Cycle
Current (A)
4.0E-5
2.0E-5
0.0
-2.0E-5
-4.0E-5
-1.0
-0.5
0.0
0.5
1.0
Voltage (V)
B
10th-20th Cycles
10th cycle
20th cycle
Current (A)
4.0E-5
2.0E-5
0.0
-2.0E-5
-4.0E-5
-1.0
-0.5
0.0
0.5
1.0
Voltage (V)
C
100 Cycles
1st-10th cycles
90th-100th cycles
Current (A)
4.0E-5
2.0E-5
0.0
-2.0E-5
-4.0E-5
-1.0
-0.5
0.0
0.5
1.0
Voltage (V)

Figure 3: Current-voltage (I-V) phase diagrams generated by AC triangular input at 1 Hz and +/- 1 V amplitude. Diagrams show nonlinear hysteresis response, resistive switching and fluctuations, as well as chaotic attractor dynamics with increasing number of cycles: A) cycles 1-3; B) cycles 10-20; C) cycles 1-100.

When driven by a DC bias, fluctuations and switching events in Ag_2Se nanowire networks were observed to persist on timescales of many hours, as shown in Figure 4. The magnified insert in Figure 4A reveals many events where changes in $I(t)$ exceed a defined threshold (5%) over the course of a few minutes. The PSD in Figure 4B exhibits a distinctive power-law shape, $x^{-\beta}$, with more low-frequency power potentially indicative of temporal correlations or other collective effects.

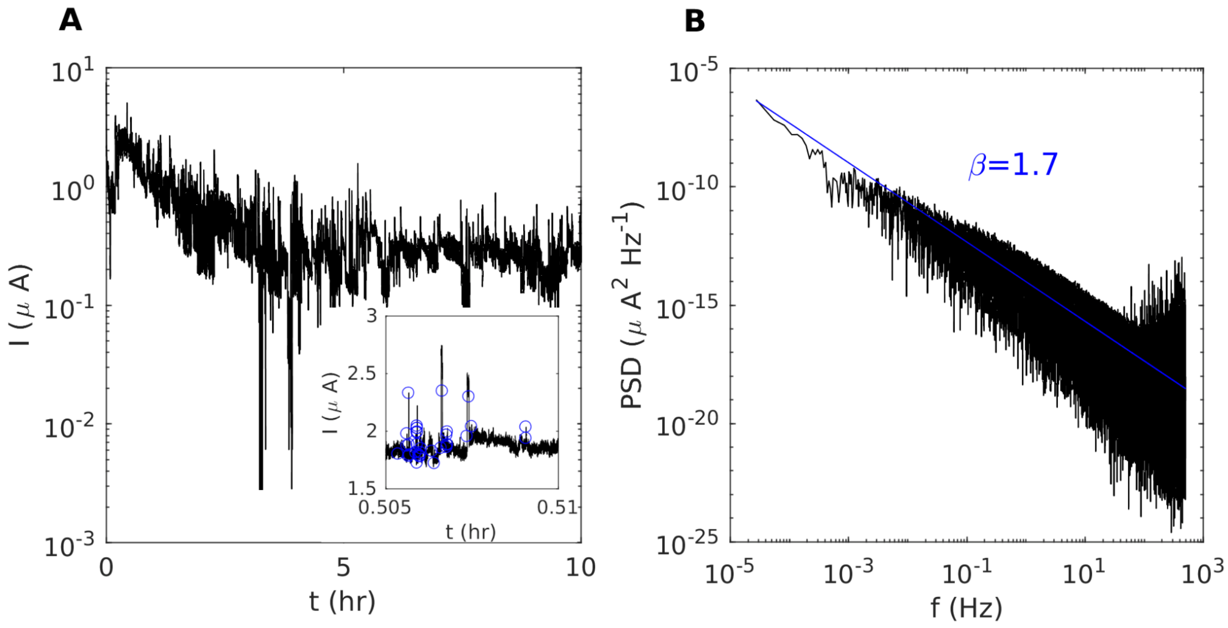

Figure 4: Current time-series and power spectral density plots of Ag_2Se nanowire networks. A) Current time-series, I(t), measured under 5 V DC bias for 10 hrs showing persistent fluctuations and switching events; inset shows a 3 min zoom-in, with circles

(blue) highlighting events where |ΔI/I| exceeds 5%. B) Corresponding power-spectral density, PSD, and power-law fit (blue).

Figure 5 shows avalanche statistics determined from the $I(t)$ data in Figure 4A. The exponents of Maximum Likelihood (ML) power-law fits to $P(S)$ and $P(T)$ are $\tau_S = 1.89 \pm 0.02$ and $\tau_T = 2.12 \pm 0.04$, respectively. The exponent of $<S(T)>$ is $\gamma = 1.23 \pm 0.04$, which is consistent with that predicted by the crackling noise dynamical scaling relation $(\tau_T - 1)/(\tau_S - 1) = 1.26 \pm 0.05$, within uncertainties, thus confirming avalanche criticality [121]. The critical exponent $\gamma = 1.23$ differs from the PSD exponent $\beta = 1.7$, which reflects the inhomogeneous nature of nanowire networks. In homogeneous many-body systems, the mean field approximation (e.g. random field Ising model) predicts a relation between γ and β [122].The critical exponents found for avalanches in Ag_2Se nanowire networks differ from those in Ag-PVP nanowire networks ($\tau_S = 2.1$ and $\tau_T = 2.3$) [105] and Sn nanoparticle networks ($\tau_S = 2.0$ and $\tau_T = 2.6$) [84], which adhere to the crackling noise scaling relation with $\gamma = 1.2$ and 1.6, respectively. Conversely, it was reported that Sn nanoparticle networks demonstrate critical exponents inconsistent with the crackling noise scaling relation [123]. Different critical exponents may indicate different universality classes for these neuromorphic systems. Another possibility is that they exhibit "quasi-criticality", which predicts departure from a single critical point defining a universality class along a line of (τ_S, τ_T) pairs that approximately obey a dynamical scaling relation [124]. Experimental measurements of Ag_2Se networks conducted over a much longer duration than shown in Fig. 4A (up to 72 hrs) exhibited avalanches with varying critical exponents during different epochs (data not shown here). This could be interpreted as quasi-criticality. Further investigation is warranted to continue exploring this idea.

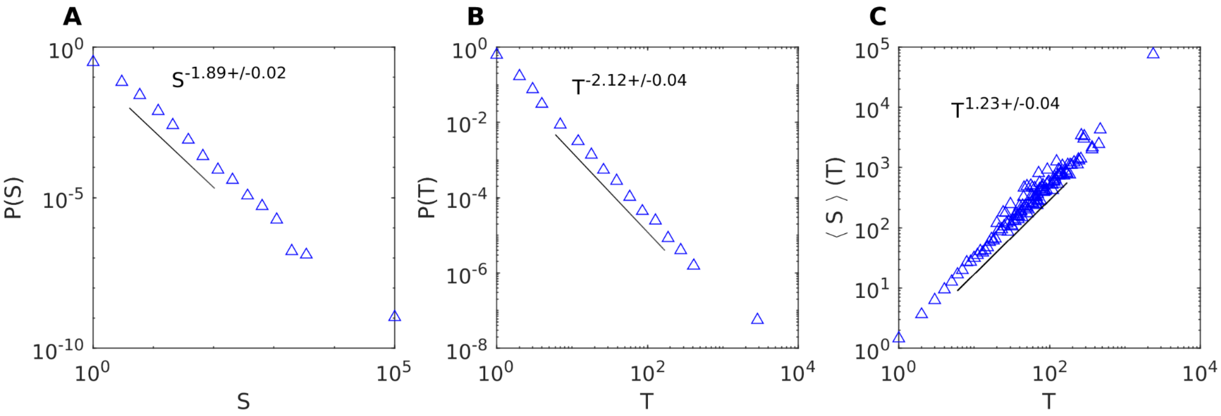

Figure 5: Probability distributions (blue triangles, logarithmically binned) and maximum likelihood power-law fits (black) of avalanche events from I(t) data in Figure 4A. A) avalanche size, S; B) avalanche duration, T. C) Average size, <S>, as a function of T, with power-law fit (black).

Summary

In this perspective, we proposed that neuromorphic networks represent a unique abiotic physical system for studying criticality. We reviewed existing evidence for critical or critical-like dynamics in such systems and tested this proposition further with new experiments on silver selenide nanowire networks. This neuromorphic system was found to exhibit avalanche criticality in addition to hysteresis, persistent fluctuations with a power-law distribution, and chaotic attractor dynamics. Many studies have already demonstrated the information processing capabilities of a variety of in materio neuromorphic networks. What remains to be revealed is how the neuromorphic dynamical properties determine computational abilities. This would provide proof-of-concept credibility for neuromorphic networks as a physical abiotic model system for investigating the role of critical dynamics in information processing and computational task performance.

Outlook

Future Work: Criticality and Neuromorphic Networks

This perspective on neuromorphic networks and criticality provided support for the claim that such networks exhibit characteristics of critical systems. One area prime for future investigation is whether neuromorphic nanowire networks demonstrate optimal information processing capabilities at or near a critical regime.

Studies in simulation have shown that information processing systems perform reservoir computation optimally when operating at or near a critical state [107-108]. To date, this phenomenon remains unexplored in physical neuromorphic systems such as nanowire networks despite their successful implementation into RC frameworks. Our outlook on future studies of critical systems is that new insights are to be gained by investigating how neuromorphic networks perform in a variety of computational tasks when in quasi-critical, critical and non-critical states. As neuromorphic nanowire networks are stimulus driven systems, an important goal is to demonstrate tunability between quasi-critical, critical and non-critical states. Demonstrating improved information processing performance at or near criticality, would justify using these networks as an abiotic physical model to study critical dynamics in the brain.

Neuromorphic networks could enable a new AI “computer” where the training knowledge is resident in the physical structure of the nanowire network. The information in the system can adapt based on real time interactions with the environment, exhibiting emergent human-like cognition. As machine learning and artificial intelligence (AI) proliferate, computers are asked to engage in a larger array of tasks previously reserved for humans (e.g. driving, medical diagnoses, financial markets, warfare), certain distinctions between the brain and computer are expected to increasingly blur. Systems explicitly designed to mimic processes previously relegated to the human domain will need to become more brain-like (i.e. more neuromorphic) in order to achieve an ever-growing list of ambitious operations. To effectively develop such computationally intelligent matter, we need to better understand those attributes crucial to conferring the brain with its various capabilities. Criticality is one such potential attribute and its role in both the brain and abiotic physical systems must be understood in order to develop next-generation technologies for machine intelligence.

References

1. Brown J H, Gupta V K, Li B, Milne B T, Restrepo C and West G B 2002 The fractal nature of nature: power laws, ecological complexity and biodiversity *Philos. Trans. R. Soc. B* **357(1421)** 619-626. DOI: 10.1098/rstb.2001.0993
2. Arthur W B 1999 Complexity and the Economy *Science* **284(5411)** 107-109. DOI: 10.1126/science.284.5411.107
3. Foote R 2007 Mathematics and Complex Systems *Science* **318(5849)** 410-412. DOI: 10.1126/science.1141754
4. Li Z, Sim C and Hean Low M 2006 A Survey of Emergent Behavior and Its Impacts in Agent-based Systems *IEEE Int. Conf. Industr. Inform.* DOI: 10.1109/INDIN.2006.275846
5. O'Connor T 1994 Emergent Properties *Am. Philos. Q.* **31(2)** 91-104.
6. Weng G 1999 Complexity in Biological Signaling Systems *Science* **284(5411)** 92-96.

DOI: 10.1126/science.284.5411.92

7. Pham V D, Repain V, Chacon C, Bellec A, Girard Y, Rousset S, Abad E, Dappe Y J, Smogunov A and Lagoute J 2017 Tuning the Electronic and Dynamical Properties of a Molecule by Atom Trapping Chemistry *ACS Nano* **11(11)** 10742-10749. DOI: 10.1021/acsnano.7b05235
8. Sujith R I and Unni V R 2020 Dynamical systems and complex systems theory to study unsteady combustion *Proc. Combust. Inst.* **38(3)** 3445-3462. DOI: 10.1016/j.proci.2020.07.081
9. Cocchi L, Gollo L L, Zalesky A and Breakspear M 2017 Criticality in the brain: A synthesis of neurobiology, models and cognition *Prog. Neurobiol.* **158** 132-152. DOI: 10.1016/j.pneurobio.2017.07.002
10. Plenz D 2013 The Critical Brain *Physics* **6(47)**. DOI: 10.1103/physics.6.47
11. Pareto V 1897 Cours d’Economique Politique, vol. 2 (1897). DOI: 10.1177/000271629700900314
12. Manual of Political Economy (New York: Augustus M. Kelly, 1971). Translated from Manuale d’Economia Politica (1906)
13. Solé R V, Manrubia S C, Benton M, Kauffman S and Bak P 1999 Criticality and scaling in evolutionary ecology *Trends Ecol. Evol.* **14(4)** 156–160. DOI: 10.1016/S0169-5347(98)01518-3
14. Bak P, Tang C and Wiesenfeld K 1987 Self-organized criticality: An explanation of 1/f Noise *Phys. Rev. Lett.* **59(4)** 381-384. DOI: 10.1103/PhysRevLett.59.381
15. Bak P, Tang C and Wiesenfeld K 1988 Self-organized criticality *Phys. Rev. A* **38(1)** 364-374. DOI: 10.1103/PhysRevA.38.364

16. McFaul L W, Wright W J, Sickle J and Dahmen K A 2019 Force oscillations distort avalanche shapes *Mater. Res. Lett.* **7(12)** 496-502. DOI: 10.1080/21663831.2019.1659437
17. Denisov D V, Lőrincz K A, Wright W J, Hufnagel T C, Nawano A, Gu X, Uhl J T, Dahmen K A and Schall P 2017 Universal slip dynamics in metallic glasses and granular matter – linking frictional weakening with inertial effects *Sci. Rep.* **7(1)** 43376. DOI: 10.1038/srep43376
18. Shew W L and Plenz D 2012 The Functional Benefits of Criticality in the Cortex *Neuroscientist* **19(1)** 88–100. DOI: 10.1177/1073858412445487
19. Crutchfield J P and Young K 1990 Computation at the onset of chaos *SFI Studies in the Sciences of Complexity (Entropy, Complexity, and the Physics of Information vol 8)* ed W Zurek (Reading, MA: Addison-Wesley) p 223-269.
20. Akar F G, Aon M A, Tomaselli G F and O'Rourke B 2005 The mitochondrial origin of postischemic arrhythmias *J. Clin. Invest.* **115(12)** 3527-3535. DOI: 10.1172/JCI25371
21. Bak P and Tang C 1989 Earthquakes as a self-organized critical phenomenon *J. Geophys. Res. Solid Earth* **94(B11)** 15635-15637. DOI: 10.1029/JB094IB11P15635
22. Malamud B D, Morein G and Turcotte D L 1998 Forest Fires: An Example of Self-Organized Critical Behavior *Science* **281(5384)** 1840-1842. DOI: 10.1126/science.281.5384.1840
23. Smyth W D, Nash J D and Moum J N 2019 Self-organized criticality in geophysical turbulence *Sci. Rep.* **9(1)** 3747. DOI: 10.1038/s41598-019-39869-w
24. Dănilă B, Harko T and Mocanu G 2015 Self-organized criticality in a two-dimensional

cellular automaton model of a magnetic flux tube with background flow *Mon. Notices Royal Astron. Soc.* **453(3)** 2983–2992.

25. Rind D 1999 Complexity and Climate *Science* **284(5411)** 105-107. DOI: 10.1126/science.284.5411.105
26. Zipf G K 1936 The Psychobiology of Language (London, UK: Routledge)
27. Zipf G K 1949 Human Behavior and the Principle of Least Effort. (Cambridge, MA: Addison-Wesley)
28. Piantadosi S T 2014 Zipf's word frequency law in natural language: A critical review and future directions *Psychon. Bull. Rev.* **21(5)** 1112-1130. DOI: 10.3758/s13423-014-0585-6
29. Muñoz M A 2018 Colloquium: Criticality and dynamical scaling in living systems *Reviews of Modern Physics* **90** 031001. DOI: 10.1103/RevModPhys.90.031001
30. Kauffman S A 1993 The Origins of Order: Self Organization and Selection in Evolution (New York, NY: Oxford University Press)
31. Kaneko K 2012 Evolution of Robustness and Plasticity under Environmental Fluctuation: Formulation in Terms of Phenotypic Variances *J. Stat. Phys.* **148(4)** 687-705. DOI: 10.1007/s10955-012-0563-1
32. Torres-Sosa C, Huang S and Aldana M 2012 Criticality is an Emergent Property of Genetic Networks that Exhibit Evolvability *PLoS Comput. Biol.* **8(9)** e1002669. DOI: 10.1371/journal.pcbi.1002669
33. Ribeiro T L, Chialvo D R and Plenz D Scale-Free Dynamics in Animal Groups and Brain Networks *Front. Cyst. Neurosci.* **14** DOI: 10.3389/fnsys.2020.591210
34. Aon M A, Cortassa S and O'Rourke B 2004 Percolation and criticality in a

mitochondrial network *Proc. Natl. Acad. Sci. U.S.A.* **101(13)** 4447-4452. DOI: 10.1073/pnas.0307156101

35. Kurz F T, Derungs T, Aon M A, O'Rourke B and Armoundas A A 2015 Mitochondrial Networks in Cardiac Myocytes Reveal Dynamic Coupling Behavior *Biophys. J.* **108(8)** 1922-1933. DOI: 10.1016/j.bpj.2015.01.040
36. Kiyono K, Struzik Z R, Aoyagi N, Sakata S, Hayano J and Yamamoto Y 2004 Critical Scale Invariance in a Healthy Human Heart Rate *Phys. Rev. Lett.* **93** 178103. DOI: 10.1103/PhysRevLett.93.178103
37. Nivala M, Ko C Y, Nivala M, Weiss J N and Qu Z 2012 Criticality in Intracellular Calcium Signaling in Cardiac Myocytes *Biophys. J.* **102(11)** 2433-2442. DOI: 10.1016/j.bpj.2012.05.001
38. Kiyono K, Struzik Z R, Aoyagi N and Yamamoto Y 2006 Multiscale Probability Density Function Analysis: Non-Gaussian and Scale-Invariant Fluctuations of Healthy Human Heart Rate *IEEE Trans. Biomed. Eng.* **53(1)** 95-102. DOI: 10.1109/TBME.2005.859804
39. Beggs J M and Plenz D 2003 Neuronal Avalanches in Neocortical Circuits *J. Neurosci.* **23(35)** 11167-11177. DOI: 10.1523/jneurosci.23-35-11167.2003
40. Stumpf M P H and Porter M A 2012 Critical Truths About Power Laws *Science* **335(6069)** 665-666. DOI: 10.1126/science.1216142
41. Toubal J and Destexhe A 2017 Power-law statistics and universal scaling in the absence of criticality *Phys. Rev. E* **95** 012413. DOI: 10.1103/PhysRevE.95.012413
42. Beggs J M and Timme N 2012 Being Critical of Criticality in the Brain *Front. Physiol.* **3** 163. DOI: 10.3389/fphys.2012.00163

43. Mitzenmacher M 2004 A Brief History of Generative Models for Power Law and Lognormal Distributions *Internet Math.* **1(2)** 226-251. DOI: 10.1080/15427951.2004.10129088
44. Sornette D 1998 Multiplicative processes and power laws *Phys. Rev. E* **57(4)** 4811-4813. DOI: 10.1103/PhysRevE.57.4811
45. Reed W J and Hughes B D 2002 From gene families and genera to incomes and internet file sizes: Why power laws are so common in nature *Phys. Review E* **66** 067103. DOI: 10.1103/PhysRevE.66.067103
46. Chialvo D R 2010 Emergent complex neural dynamics *Nat. Phys.* **6** 744-750. DOI: 10.1038/nphys1803
47. Friedman N, Ito S, Brinkan B A W, Shimono M, Lee DeVille R E, Dahmen K A, Beggs J M and Butler T C 2012 Universal Critical Dynamics in High Resolution Neuronal Avalanche Data *Phys. Rev. Lett.* **108** 208102. DOI: 10.1103/PhysRevLett.108.208102
48. Haimovici A, Tagliazucchi E, Balenzuela P and Chialvo D R 2013 Brain Organization into Resting State Networks Emerges at Criticality on a Model of the Human Connectome *Phys. Rev. Lett.* **110** 178101. DOI: 10.1103/PhysRevLett.110.178101
49. Petermann T, Thiagarajan T C, Lebedev M A, Nicolelis M A, Chialvo D R and Plenz D 2009 Spontaneous cortical activity in awake monkeys composed of neuronal avalanches *Proc. Natl. Acad. Sci*. **106(37)** 15921-15926 DOI: 10.1073/pnas.0904089106
50. Tagliazucchi E, Balenzuela P, Fraiman D and Chialvo D R 2012 Criticality in Large-Scale Brain fMRI Dynamics Unveiled by a Novel Point Process Analysis

Front. Physiol. **3** 15. DOI: 10.3389/fphys.2012.00015

51. Ezaki T, Fonseca dos Reis E, Watanabe T, Sakaki M and Masuda N 2020 Closer to critical resting-state neural dynamics in individuals with higher fluid intelligence *Commun. Biol.* **3** 52. DOI: 10.1038/s42003-020-0774-y
52. Rundle J B, Klein W, Gross S and Turcotte D L 1995 Boltzmann Fluctuations in Numerical Simulations of Nonequilibrium Lattice Threshold Systems *Phys. Rev. Lett.* **75(8)** 1658-1661. DOI: 10.1103/PhysRevLett.75.1658
53. Meisel C, Storch A, Hallmeyer-Elgner S, Bullmore E and Gross T 2012 Failure of Adaptive Self-Organized Criticality during Epileoptic Seizure Attacks *PLoS Comput. Biol.* **8(1)** e1002312. DOI: 10.1371/journal.pcbi.1002312
54. Hobbs J P, Smith J L and Beggs J M 2010 Aberrant Neuronal Avalanches in Cortical Tissue Removed From Juvenile Epilepsy Patients *J. Neurophysiol.* **27(6)** 380-386. DOI: 10.1097/WNP.0b013e3181fdf8d3
55. Meisel C, Bailey K, Achermann P and Plenz D 2017 Decline of long-range temporal correlations in the human brain during sustained wakefulness *Sci. Rep.* **7** 11825. DOI: 10.1038/s41598-017-12140-w
56. Torres J J and Marro J 2015 Brain Performance versus Phase Transitions *Sci. Rep.* **5** 12216. DOI: 10.1038/srep12216
57. Daffertshofer A, Ton R, Kringelbach M L, Woolrich M and Deco G 2018 Distinct criticality of phase and amplitude dynamics in the resting brain *NeuroImage* **180** 442-447. DOI: 10.1016/j.neuroimage.2018.03.002
58. Haldeman C and Beggs J M 2005 Critical Branching Captures Activity in Living Neural Networks and Maximizes the Number of Metastable States *Phys. Rev. Lett.*

94(5) 058101. DOI: 10.1103/PhysRevLett.94.058101

59. Shew W L, Yang H, Yu S, Roy R and Plenz D 2011 Information Capacity and Transmission Are Maximized in Balanced Cortical Networks with Neuronal Avalanches *J. Neurosci.* **31(1)** 55-63 DOI: 10.1523/JNEUROSCI.4637-10.2011
60. Shriki O and Yellin D 2016 Optimal Information Representation and Criticality in an Adaptive Sensory Recurrent Neuronal Network *PLoS Comput. Biol.* **12(2)** e1004698 DOI: 10.1371/journal.pcbi.1004698
61. Rosenblatt F 1960 Perceptron Simulation Experiments *Proc. IRE* **48(3)** 301–309. DOI:10.1109/jrproc.1960.287598
62. Rosenblatt F 1958 The perceptron: A probabilistic model for information storage and organization in the brain *Psychol. Rev.* **65(6)** 386–408. DOI:10.1037/h0042519
63. Mead C 1990 Neuromorphic electronic systems *Proc. IEEE* **78(10)** 1629-1636. DOI: 10.1109/5.58356.
64. Mead C 2020 How we created neuromorphic engineering *Nat. Electron.* **3** 434-435. DOI: 10.1038/s41928-020-0448-2
65. Schuman C D, Potok T E, Patton R M, Birdwell J D, Dean M E, Rose G S and Plank J S 2017 A Survey of Neuromorphic Computing and Neural Networks in Hardware *arXiv*:1705.06963v1
66. Hino T, Hasegawa T, Terabe K, Tsuruoka T, Nayak A, Ohno T and Aono M 2011 Atomic switches: atomic-movement-controlled nanodevices for new types of computing *Sci. Technol. Adv. Mater.* **12(1)** 013003. DOI: 10.1088/1468-6996/12/1/013003
67. Nayak A, Ohno T, Tsuruoka T, Terabe K, Hasegawa T, Gimzewski J K and Aono M

2012 Controlling the Synaptic Plasticity of a Cu2S Gap-Type Atomic Switch *Adv. Funct. Mater.* **22(17)** 3606-3613. DOI: 10.1002/adfm.201200640

68. Ohno T, Hasegawa T, Tsuruoka T, Terabe K, Gimzewski J K and Aono M 2011 Short-term plasticity and long-term potentiation mimicked in single inorganic synapses *Nat. Mater.* **10(8)** 591-595. DOI: 10.1038/nmat3054
69. Stieg A Z, Avizienis A V, Sillin H O, Martin-Olmos C, Aono M and Gimzewski J K 2011 Emergent Criticality in Complex Turing B-Type Atomic Switch Networks *Adv. Mater.* **24(2)** 286-293. DOI: 10.1002/adma.201103053
70. Avizienis A V, Sillin H O, Martin-Olmos C, Shieh H H, Aono M, Stieg A Z and Gimzewski J K 2012 Neuromorphic Atomic Switch Networks *PLoS ONE* **7(8)** e42772. DOI: 10.1371/journal.pone.0042772
71. Kuncic Z and Nakayama T 2021 Neuromorphic nanowire networks: principles, progress and future prospects for neuro-inspired information processing. *Adv. Phys. X* **6(1)** 1894234. DOI: 10.1080/23746149.2021.1894234
72. Sandouk E J, Gimzewski J K and Stieg A Z 2015 Multistate resistive switching in silver nanoparticle films *Sci. Technol. Adv. Mater.* **16(4)** 045004. DOI: 10.1088/1468-6996/16/4/045004
73. Scharnhorst K S, Carbajal J P, Aguilera R C, Sandouk E J, Aono M, Stieg A Z and Gimzewski J K 2018 Atomic switch networks as complex adaptive systems *Jpn. J. Appl. Phys.* **57(3S2)** 03ED02. DOI: 10.7567/JJAP.57.03ED02
74. Lilak S, Woods W, Scharnhorst K, Dunham C, Teuscher C, Stieg A Z and Gimzewski J K 2021 Spoken Digit Classification by In-Materio Reservoir Computing With Neuromorphic Atomic Switch Network *Front. Nanotechnol.* **3** 675792. DOI:

10.3389/fnano.2021.675792

75. Kotooka T, Lilak S, Stieg A, Gimzewski J, Sugiyama N, Tanaka Y, Tamukoh H, Usami Y and Tanaka H 2021 Ag2Se Nanowire Network as an Effective In-Materio Reservoir Computing Device *Research Square Preprint* DOI: 10.21203/rs.3.rs-322405/v1
76. Fostner S and Brown S A 2015 Neuromorphic behavior in percolating nanoparticle films *Phys. Rev. E* **92** 052134. DOI: 10.1103/PhysRevE.92.052134
77. Diaz-Alvarez A, Higuchi R, Sanz-Leon P, Marcus I, Shingaya Y, Stieg A Z, Gimzewski J K, Kuncic Z and Nakayama T 2019 Emergent dynamics of neuromorphic nanowire networks *Sci. Rep.* **9** 14920. DOI: 10.1038/s41598-019-51330-6
78. Milano G, Pedretti G, Fretto M, Boarino L, Benfenati F, Ielmini D, Valov I, Ricciardi C 2020 Brain-Inspired Structural Plasticity through Reweighting and Rewiring in Multi-Terminal Self-Organizing Memristive Nanowire Networks *Adv. Intell. Syst.* **2(8)** 2000096. DOI: 10.1002/aisy.202000096
79. Kuncic Z, Marcus I, Sanz-Leon P, Higuchi R, Shingaya Y, Li M, Stieg A, Gimzewski J, Aono M and Nakayama T 2018 Emergent brain-like complexity from nanowire atomic switch networks: Towards neuromorphic synthetic intelligence *2018 IEEE 18th Int. Conf. Nanotechnol.* DOI: 10.1109/NANO.2018.8626236
80. Stieg A Z, Avizienis A V, Sillin H O, Martin-Olmos C, Lam M, Aono M and Gimzewski J K 2013 Self-organized atomic switch networks *Jpn. J. Appl. Phys.* **53(1S)** 01AA02. DOI: 10.7567/JJAP.53.01AA02
81. Stieg A Z, Avizienis A V, Sillin H O, Aguilera R, Shieh H, Martin-Olmos C, Sandouk E

J, Aono M and Gimzewski J K 2014 Self-organization and Emergence of Dynamical Structures in Neuromorphic Atomic Switch Networks *Memristor Netw.* ed A Adamatzky and L Chua (Switzerland: Springer International Publishing) p 173-209. DOI: 10.1007/978-3-319-02630-5_10

82. Shirai S, Acharya S K, Bose S K, Mallinson J B, Galli E, Pike M D, Arnold M D, Brown S A 2020 Long-range temporal correlations in scale-free neuromorphic networks *Netw. Neurosci.* **4(2)** 432-447. DOI: 10.1162/netn_a_00128
83. Bose S K, Mallinson J B, Gazoni R M and Brown S A 2017 Stable Self-Assembled Atomic-Switch Networks for Neuromorphic Applications *IEEE T. Electron Dev.* **64(12)** 5194-5201. DOI: 10.1109/TED.2017.2766063
84. Mallinson J B, Shirai S, Acharya S K, Bose S K, Galli E and Brown S A 2019 Avalanches and criticality in self-organized nanoscale networks *Sci. Adv.* **5(11)** eaaw8438. DOI: 10.1126/sciadv.aaw8438
85. Yang J J, Strukov D B and Stewart D R 2013 Memristive devices for computing *Nat. Nanotechnol.* **8(1)** 13-24. DOI: 10.1038/nnano.2012.240
86. Demis E C, Aguilera R, Sillin H O, Scharnhorst K, Sandouk E J, Aono M, Stieg A Z and Gimzewski J K 2015 Atomic switch networks--nanoarchitectonic design of a complex system for natural computing *Nanotechnol.* **26** 204003. DOI: 10.1088/0957-4484/26/20/204003
87. Loeffler A, Zhu R, Hochstetter J, Li M, Fu K, Diaz-Alvarez A, Nakayama T, Shine J M and Kuncic Z 2020 Topological Properties of Neuromorphic Nanowire Networks *Front. Neurosci.* **14** 184. DOI: 10.3389/fnins.2020.00184
88. Kaspar C, Ravoo B J, van der Wiel W G, Wegner S V and Pernice W H P 2021 The

rise of intelligent matter *Nature* **594** 345-355. DOI: 10.1038/s41586-021-03453-y

89. Miller J F, Harding S L and Tufte G 2014 Evolution-in-materio: evolving computation in materials *Evol. Intel.* **7** 49-67. DOI: 10.1007/s12065-014-0106-6
90. Miller J F and Downing K 2002 Evolution in materio: looking beyond the silicon box *Proc. NASA/DoD Conference on Evolvable Hardware* DOI: 10.1109/EH.2002.1029882
91. Dale M, Miller J F and Stepney S 2017 Reservoir Computing as a Model for In-Materio Computing. In: Adamatzky A. (eds) Advances in Unconventional Computing. Emergence, Complexity and Computation **(22)** Springer, Cham. DOI: 10.1007/978-3-319-33924-5_22
92. Lukoševičius M and Jaeger H 2008 Reservoir computing approaches to recurrent neural network training *Comput. Sci. Rev.* **3(3)** 127-149. DOI: 10.1016/j.cosrev.2009.03.005
93. Tanaka, G et al 2019 Recent advances in physical reservoir computing: A review *Neural Netw.* **115** 100-123. DOI: 10.1016/j.neunet.2019.03.005
94. Lukoševičius M, Jaeger H and Schrauwen, B 2012 Reservoir Computing Trends *Künstl. Intell.* **26** 365-371. DOI: 10.1007/s13218-012-0204-5
95. Sillin H O, Aguilera R, Shieh H, Avizienis A V, Aono M, Stieg A Z and Gimzewski J K 2013 A theoretical and experimental study of neuromorphic atomic switch networks for reservoir computing *Nanotechnology* **24(38)** 384004. DOI: 10.1088/0957-4484/24/38/384004
96. Katumba A et al 2018 Neuromorphic Computing Based on Silicon Photonics and Reservoir Computing *IEEE J. Sel. Top. Quantum Electron.* **24(6)** DOI:

10.1109/JSTQE.2018.2821843

97. Donati E et al 2018 Processing EMG signals using reservoir computing on an event-based neuromorphic system *IEEE BioCAS* 18328127 DOI: 10.1109/BIOCAS.2018.8584674

98. Gupta S, Chakraborty S and Thakur C S 2021 Neuromorphic Time-Multiplexed Reservoir Computing With On-the-Fly Weight Generation for Edge Devices *IEEE Trans. Neural Netw. Learn. Syst.* DOI: 10.1109/TNNLS.2021.3085165

99. Fu K, Zhu R, Loeffler A, Hochstetter J, Diaz-Alvarez A, Stieg A Z, Gimzewski J K, Nakayama T and Kuncic Z 2020 Reservoir Computing with Neuromemristive Nanowire Networks IEEE IJCNN DOI: 10.1109/IJCNN48605.2020.9207727

100. Loeffler A, Rhu R, Hochstetter J, Diaz-Alvarez A, Nakayama T, Shine J M and Kuncic Z 2021 Modularity and Multitasking in Neuro-memristive Reservoir Networks *Neuromorph. Comp. Eng.* (under review)

101. Zhu R et al. 2021 MNIST classification using Neuromorphic Nanowire Networks *ICONS*

102. Zhu R, Hochstetter J, Loeffler A, Diaz-Alvarez A, Nakayama T, Lizier J T and Kuncic Z 2021 Information dynamics in neuromorphic nanowire networks *Sci. Rep.* **11** 13047. DOI: 10.1038/s41598-021-92170-7

103. Zhu R, Hochstetter J, Loeffler A, Diaz-Alvarez A, Stieg A Z, Gimzewski J K, Nakayama T and Kuncic Z 2020 Harnessing adaptive dynamics in neuro-memristive nanowire networks for transfer learning *IEEE ICRC* DOI: 10.1109/ICRC2020.2020.00007

104. Kuncic Z et al. 2020 Neuromorphic Information Processing with Nanowire

Networks *IEEE ISCAS* DOI: 10.1109/ISCAS45731.2020.9181034

105. HochstetterJ, Zhu R, Loeffler A, Diaz-Alvarez A, Nakayama T and Kuncic Z. 2021. Avalanches and edge-of-chaos learning in neuromorphic nanowire networks. *Nat. Commun.* **12** 4008. DOI: 10.1038/s41467-021-24260-z

106. Cramer B, Stöckel D, Kreft M, Wibral M, Schemmel J, Meier K and Priesemann V 2020 Control of criticality and computation in spiking neuromorphic networks with plasticity *Nat. Commun.* **11** 2853. DOI: 10.1038/s41467-020-16548-3

107. Snyder D, Goudarzi A and Teuscher C Computational capabilities of random automata networks for reservoir computing 2013 *Phys. Rev. E.* **87** 042808. DOI: 10.1103/PhysRevE.87.042808

108. Goudarzi A, Teuscher C, Gulbahce N and Rohl T 2012 Emergent Criticality through Adaptive Information Processing in Boolean Networks *Phys. Rev. Lett.* **108** 128702. DOI: 10.1103/PhysRevLett.108.128702

109. Scharnhorst K, Woods W, Teuscher C, Stieg A Z and Gimzewski J K 2017 Non-temporal logic performance of an atomic switch network *IEEE Int. Symp. Nano.* 133-138. DOI: 10.1109/NANOARCH.2017.8053728

110. O'Callaghan C, Rocha C G, Niosi F, Manning H G, Boland J J and Ferreira M S 2018 Collective capacitive and memristive responses in random nanowire networks: Emergence of critical connectivity pathways *J. Appl. Phys.* **124(15)** 152118. DOI: 10.1063/1.5037817

111. Chua L 1971 Memristor-The Missing Circuit Element *IEEE Trans. Circuit Theory* **18(5)** 507–519. DOI: 10.1109/TCT.1971.1083337

112. Chua L 2011 Resistance switching memories are memristors *Appl. Phys. A*

102(4) 765–783. DOI: 10.1007/s00339-011-6264-9

113. Yang J J, Pickett M D, Li X, Ohlberg D A, Stewart D R and Williams R S 2008 Memristive switching mechanism for metal/oxide/metal nanodevices *Nature Nanotech* **3(7)** 429–433. DOI: 10.1038/nnano.2008.160

114. Pershin Y V and Di Ventra M 2011 Memory effects in complex materials and nanoscale systems *Adv. Phys.* **60(2)** 145–227. DOI: 10.1080/00018732.2010.544961

115. Chua L 2013 Memristor, hodgkin-huxley, and edge of chaos *Nanotechnology* **24(38)** 383001. DOI: 10.1088/0957-4484/24/38/383001

116. Hopfield J J 1982 Neural networks and physical systems with emergent collective computational abilities *Proc. Natl. Acad. Sci.* **79(8)** 2554-2558. DOI: 10.1073/pnas.79.8.2554

117. Maass W, Natschläger T and Markham H 2002 A model for real-time computation in generic neural microcircuits. *NIPS* **229**. DOI: 10.5555/2968618.2968647

118. Langton C G 1990 Computation at the edge of chaos: Phase transitions and emergent computation *Physica D* **42(1-3)**12–37. DOI: 10.1016/0167-2789(90)90064-V

119. Bertschinger N and Natschläger T 2004 Real-Time Computation at the Edge of Chaos in Recurrent Neural Networks *Neural Comput.* **16(7)** 1413–1436. DOI: 10.1162/089976604323057443

120. Boedecker J, Obst O, Lizier J T, Mayer N M and Asada M 2012 Information processing in echo state networks at the edge of chaos *Theory Biosci* **131(3)**

205–213. DOI: 10.1007/s12064-011-0146-8

121. Sethna J P, Dahmen K A and Myers C R 2001 Crackling noise *Nature* **410** 242–250. DOI: 10.1038/35065675

122. Kuntz M C and Sethna J P 2000 Noise in disordered systems: The power spectrum and dynamic exponents in avalanche models Phys Rev B 62 11699 DOI: 10.1103/PhysRevB.62.11699

123. Pike M D et al. 2020 Atomic Scale Dynamics Drive Brain-Like Avalanches in Percolating Nanostructured Networks *Nano Lett.* **20(5)** 3935-3942. DOI: 10.1021/acs.nanolett.0c01096

124. Fosque L J, Williams-Garcia R V, Beggs J M and Ortiz G 2021 Evidence for Quasicritical Brain Dynamics *Phys. Rev. Lett.* **126** 098101. DOI: 10.1103/PhysRevLett.126.098101

Chapter 4. Pacemaker translocations and power laws in 2D stem cell-derived cardiomyocyte cultures.

Abstract

Power laws are of interest to several scientific disciplines because they can provide important information about the underlying dynamics (e.g. scale invariance and self-similarity) of a given system. Because power laws are of increasing interest to the cardiac sciences as potential indicators of cardiac dysfunction, it is essential that rigorous, standardized analytical methods are employed in the evaluation of power laws. This study compares the methods currently used in the fields of condensed matter physics, geoscience, neuroscience, and cardiology in order to provide a robust analytical framework for evaluating power laws in stem cell-derived cardiomyocyte cultures. One potential power law-obeying phenomenon observed in these cultures is pacemaker translocations, or the spatial and temporal instability of the pacemaker region, in a 2D cell culture. Power law analysis of translocation data was performed using increasingly rigorous methods in order to illustrate how differences in analytical robustness can result in misleading power law interpretations. Non-robust methods concluded that pacemaker translocations adhere to a power law while robust methods convincingly demonstrated that they obey a doubly truncated power law. The results of this study highlight the importance of employing comprehensive methods during power law analysis of cardiomyocyte cultures.

Introduction

Recent investigations of human induced pluripotent and embryonic stem cell-derived cardiomyocytes (hiPSC-CM and hESC-CM, respectively) have shone significant light on numerous factors contributing to the development of the heart [1-6]. However, the mechanisms underlying the full maturation of cardiomyocytes to robust adult phenotypes remain unknown [1, 7-8]. Phenotypic traits which have thus far failed to match those in adult cardiomyocytes include electrical impulse propagation, mechanical properties including sarcomere length and contractility, cell morphology, and gene expression [1, 9-11]. Additionally, some studies have suggested that defective cardiomyocyte development may play a role in a number of disease states such as cardiomyopathy and late myocardial dysfunction [2, 12-13]. The inability to mature beyond the late fetal phenotype stage considerably limits applications for stem cell-derived cardiomyocytes in drug screening, disease modeling, and regenerative medicine [1-2, 7, 14-15].

Among the mechanisms which must be understood in the context of cardiomyocyte development is the establishment of pacemaker cells. These pacemaker cells are responsible for maintaining the rhythmic beating of all cells in the cardiomyocyte syncytium by means of action potential generation [16-17]. The heart has a dedicated region of pacemaker cells, known as the sinoatrial node (SAN), that is responsible for maintaining a consistent beat rhythm throughout the lifetime of the organism [1, 18]. Many types of arrhythmias result from the disruption of rhythm-maintaining electrical impulses in the SAN, throwing the system into disarray [2, 19]. Although SAN is responsible for initiating heartbeat in the postnatal heart in physiological condition, all cardiomyocytes in the early embryonic heart are capable of generating autonomic beats. The pacemaker cells are specialized during mid-gestational stages. *In vitro* differentiation of hESC-CMs/hiPSC-CMs recapitulates this process [20]. Understanding how pacemaker regions arise and the role of pacemaker instability during cardiomyocyte maturation could provide insight into the development of the SAN and would help in furthering the current understanding of arrhythmias.

Difficulty in elucidating the mechanisms responsible for pacemaker development may be partially attributed to gaps in knowledge about the underlying interactions between cells in the cardiomyocyte culture (i.e. interactions within the cardiomyocyte network). Information in the form of environmental, physical, genomic, and chemical cues concerning the establishment of specialized cellular structures (e.g. intercalated discs) and functional roles (e.g. pacemaker cells, late fetal proliferating cells, ventricular conduction system-like cells) needs to be transmitted to the cardiomyocytes within the network [2, 21-24]. Insight into cardiomyocyte network dynamics and the processes responsible for information transfer may be attainable through the analysis of observable network characteristics (e.g. beat rate, pacemaker behavior, and biomechanical properties) for adherence to power laws.

Power laws – probability distributions of the form $p(x) \propto x^{-\alpha}$ – are of interest to several scientific fields because they provide important information about the dynamics of the system, e.g. long-range correlations, scale invariance, and self-similarity [25-27]. Several studies have explored whether power laws apply to cardiac systems, particularly in the context of tissue or cellular dysfunction, e.g. mitochondrial oxidative stress and arrhythmias [28-32]. Prior studies demonstrated power law behavior in investigations of heart (beat) rate variability, calcium load, and contractile stress in cardiomyocytes [33-37]. Several studies have shown that aberrant cardiac systems exhibit a discernible change in the exponent of the power law measured for heart rate variability, which describes small variations in the interval between heart beats, in patients with myocardial infarction and coronary heart disease, and in heart transplant patients [29, 38-41]. Other studies focused on power laws as they relate to the mitochondrial network and the effect of oxidative stress on both the network and the dependent cardiac myocytes.

While intriguing, the applied methodologies in these studies fail to meet the standards defined in other fields, including: condensed matter physics, geology, and neuroscience, where power law analysis is more established [42-45]. In these fields, power laws are typically evaluated through a combination of methods, including: 1) calculation of the power law exponent, α, via maximum likelihood estimation (MLE), 2) statistical assessments of how well the data fit to a proposed distribution using the Kolmogorov-Smirnov goodness-of-fit test, 3) log-likelihood ratio tests between power law (Equation 1), exponential (Equation 2), and other heavy-tailed distributions (i.e. distributions in which the tail probability decays polynomially rather than exponentially), including log-normal (Equation 3), Weibull (stretched exponential, Equation 4), doubly truncated power law (Equation 5), and other candidate distributions to determine which demonstrates the superior fit to the data [42, 46-48].

$$f(x) = x^{-\alpha} \tag{1}$$

$$f(x) = e^{-\lambda x} \tag{2}$$

$$f(x) = \frac{1}{x} \star exp\left[\frac{(ln(x)-\mu)^2}{2\sigma^2}\right] \tag{3}$$

$$f(x) = (x\lambda)^{\beta-1} \star e^{-(\lambda x)^{\beta}} \qquad (4)$$

$$f(x) = x^{-\alpha} \star e^{-\lambda x} \qquad (5)$$

For the power law distribution (Equation 1), α represents the power law exponent. In the exponential distribution (Equation 2), λ represents the rate parameter and is used to indicate the rate of decay. For the log-normal distribution (Equation 3), μ represents the expected value (i.e. mean) and σ represents the standard deviation of the natural logarithm of the variable, x. In the Weibull, or stretched exponential, distribution (Equation 4), λ again represents the rate parameter and β represents the stretching parameter. Finally, for the case of the doubly truncated power law distribution (Equation 5), α and λ are as previously defined in the power law and exponential functions.

In contrast, most, if not all, power law assessments performed in the cardiac science community employed relatively straightforward logarithmic plots of two parameters, e.g. size x and number of events of size x, against each other (i.e. $\log_{10}(y)$ vs $\log_{10}(x)$), accompanied by linear regression of the data. The underlying logic of this method is that if the data fit well to a line on a log-log plot, then the data must obey a power law, because a power law produces a straight line on logarithmic axes [49-51]. However, this is not always true and there could be other, superior descriptors of the data, e.g. exponential distributions or one of the aforementioned heavy-tailed distributions, that this method seldom considers. Consequently, this methodology must be considered incomplete.

This study seeks to demonstrate how analysis conducted using the incomplete methods described above can lead to misleading or contradictory interpretations for a system that demonstrates heavy-tailed, potentially power law behavior. A thorough comparison is made using more robust, established techniques, including: MLE to calculate the (suspected) power law's exponent and log-likelihood ratio tests to engage in comparisons between alternative distributions to which the data could belong [42, 52]. This analysis is applied to the quiescent (stable) period between pacemaker translocations, defined here as the spatial instability and subsequent relocation of the pacemaker region across consecutive beats, as observed in stem cell-derived cardiomyocyte cultures. Pacemaker translocations were observed previously but were not examined in detail [8]. The quiescent periods between pacemaker translocations are suspected to obey a power law due to their superficial similarity to a known power law-obeying system: the inter-burst (or inter-event) interval between neuronal action potential spiking events observed in neuronal cultures [53-54]. Pacemaker translocation quiescent periods are investigated electrophysiologically using two-dimensional monolayers of stem cell-derived cardiomyocytes plated onto microelectrode arrays (MEAs). This experimental design provides the requisite spatiotemporal information essential for the analysis of pacemaker translocation quiescent periods in order to determine whether they constitute a power law-adhering phenomenon.

Materials and methods

Cell cultures and microelectrode array measurements

Human ESCs were grown and differentiated in a chemically defined condition as previously described [8, 55-56]. Usage of all the human embryonic stem cell lines is approved by the UCLA Embryonic Stem Cell Research Oversight (ESCRO) Committee and the Institutional Review Boards (IRB) (approval #2009-006-04). Differentiation efficiency is checked periodically by flow cytometry and maintained around 80-90%. Thus, the contamination of non-cardiomyocytes is minimal with these differentiation methods. Two weeks after differentiation, cardiomyocytes were plated, without performing any extra purification step, as two-dimensional monolayers on matrigel-coated (Corning #354277), commercially available microelectrode arrays (MEAs) containing 120 integrated TiN electrodes. All electrodes were 30 μm in diameter with an interelectrode spacing of 200 μm (Multichannel Systems, Reutlingen, Germany). The MEAs were placed in an incubator set to a temperature of 37 °C and gas flow of 5% CO_2. The cell cultures were given a minimum of 24 hours to ensure the cardiomyocytes were well-attached to each MEA. Local field potentials at each electrode were recorded over an average period of 19.5 minutes, up to twice daily, with a sampling rate of 1 KHz using the MEA2100-HS120 system (Multichannel Systems, Reutlingen, Germany). The full data acquisition yielded 30 MEA recordings across 3 distinct cardiomyocyte cell cultures.

Computational tools

A custom developed, graphical user interface-based (GUI) Python program, in combination with the powerlaw Python library, was used to conduct the analysis [48]. The program is written for Python 3.8 or above and utilizes a variety of freely available Python libraries, including NumPy, SciPy, Pandas, Matplotlib, Seaborn, Numba, and Statsmodels, among others. The GUI was constructed using PyQt5. The complete code of the GUI program will be made available in a publicly accessible repository.

Beat detection and pacemaker determination

Beat detection was achieved using the findpeaks function in the SciPy signal processing (scipy.signal) Python library. The key parameters used to identify the peak corresponding to the R-wave in the field potential signal were minimum peak height (electrical amplitude) and minimum peak distance (the allowed spacing between peaks, represented in this case as some time interval). A signal-to-noise ratio in excess of 3:1 was enforced for all potential signals. Furthermore, the detected beats were manually inspected to ensure that the data set parameters correctly identified the R-wave peak for each beat recorded by each electrode. This was done to ensure that the findpeaks function worked as expected.

The pacemaker region of each beat was calculated by identifying the time associated with each R-wave peak recorded for each electrode. Time points were then scaled on a per-beat basis by subtracting the minimum raw time from each time point across all viable electrodes in the beat window. This was done to ensure each beat had a true “zero” value across the array and thereby standardize the data for visualization via heatmap. Therefore, being the progenitor of the electrical impulse directing a rhythmic beat across a culture, the pacemaker region, or closest proxy for the region, in the array corresponds to the “zero” time point of the given beat.

Pacemaker translocation algorithm

Pacemaker translocations were detected by monitoring the movement of the pacemaker region across subsequent beats. If the pacemaker region, while moving from one location to another, exceeds a distance threshold (500 μm), then a ‘clock’ is engaged that counts the number of beats and the duration that the pacemaker region remains in this new location. If the location changes again, the ‘clock’ is stopped, the number of beats and duration are stored in a list, and the ‘clock’ is reset for the new position. This process is repeated for each detected pacemaker region of each beat over the full length of the MEA recording. At the end of the calculation, the first recorded event is dropped from the list due to uncertainty regarding how long the pacemaker was in the region prior to the start of the recording. Likewise, the end of the recording does not contribute to an event designation and is similarly not considered. The algorithm was applied both manually through visual inspection and computationally in Python in order to ensure agreement of results.

Power law analysis and distribution comparisons

Simple or incomplete power law analysis consisted of log-log plots of one variable, X, corresponding to the quiescent period length (the number of beats between translocation events), and Y, corresponding to the number of translocation events (events with a quiescent period of size X). Only events whose quiescent period length occurred more than once ($Y > 1$) were considered for analysis. This was done in part to eliminate potential outliers within a limited data set. The data were then evaluated using either linear regression or nonlinear least squares fitting of the data to a power law function of the form $F(x) = Ax^{-\alpha}$, where A is a normalization constant and α is the power law exponent. Statistical assessment of the resultant fit, e.g. correlation coefficients and goodness-of-fit metrics, were generated programmatically using established statistical methods in combination with the statsmodels Python library.

Robust power law analysis was performed in accordance with previously described methods and the powerlaw Python library [42, 48]. Visualization was achieved using histograms of pacemaker translocation data and fitting multiple heavy-tailed probability density functions (PDFs), including exponential, power law, log-normal, and Weibull distributions, to the data. Calculation of the power law exponent was achieved using the MLE approach implemented in powerlaw's Fit method with the optional method argument 'discrete' set to True. Log-log plots of both PDFs and complementary cumulative distribution functions (CCDFs) were produced using two methods within the powerlaw library (denoted as object.distribution.plot_pdf() and object.distribution.plot_ccdf() in the library's code) for qualitative comparisons of empirical data-to-distribution fitting. Finally, comparisons between these probability distributions, as well as the doubly truncated power law distribution, were performed using powerlaw's distribution compare method (denoted as distribution_compare() in the library's code) with the optional method argument normalized ratio (denoted as normalized_ratio in the powerlaw documentation) set to True. The doubly truncated power law distribution uses an optional argument, x_{max}, to define the exponential cutoff. For this experiment, $x_{max} = 150$.

Results

Assessment of cardiomyocyte culture viability on MEAs

Microelectrode arrays were used to record cardiomyocyte local field potentials (hereafter called field potentials), which are extracellular electrical signals generated in part by transient imbalances in ion concentrations in the intercellular space [57-59]. These field potentials resemble, but are not equivalent to, electrocardiogram recordings, preventing analysis of P, Q, and S waves. The field potentials were analyzed for each channel (electrode) of each 120 electrode MEA, shown in Figure 1A, across all recordings. These data represent 3 unique cultures of two-dimensional (2D) stem cell-derived cardiomyocyte monolayers, as shown in Figure 1B. The use of 2D monolayers allows for the acquisition of spatially defined information and is further complemented by the precisely-manufactured electrode configuration of the recording field of the MEA. Each recording was visually inspected to validate peak detection methodology for their respective peak amplitude and distance parameters. Except in cases of extreme noise or faulty channels (e.g. due to poor cell-electrode contact, heterogeneous composition of the adhesion layer (Matrigel), or physical degradation of the electrode), peak detection performed as expected. Some representative field potential examples with annotated R-wave-like peaks (red x) and beat amplitude (vertical arrow line, gray) are shown in Figure 1C. The average beat rate (beats per minute, bpm) across all datasets was 36.64 bpm with a standard deviation of 14.48 bpm.

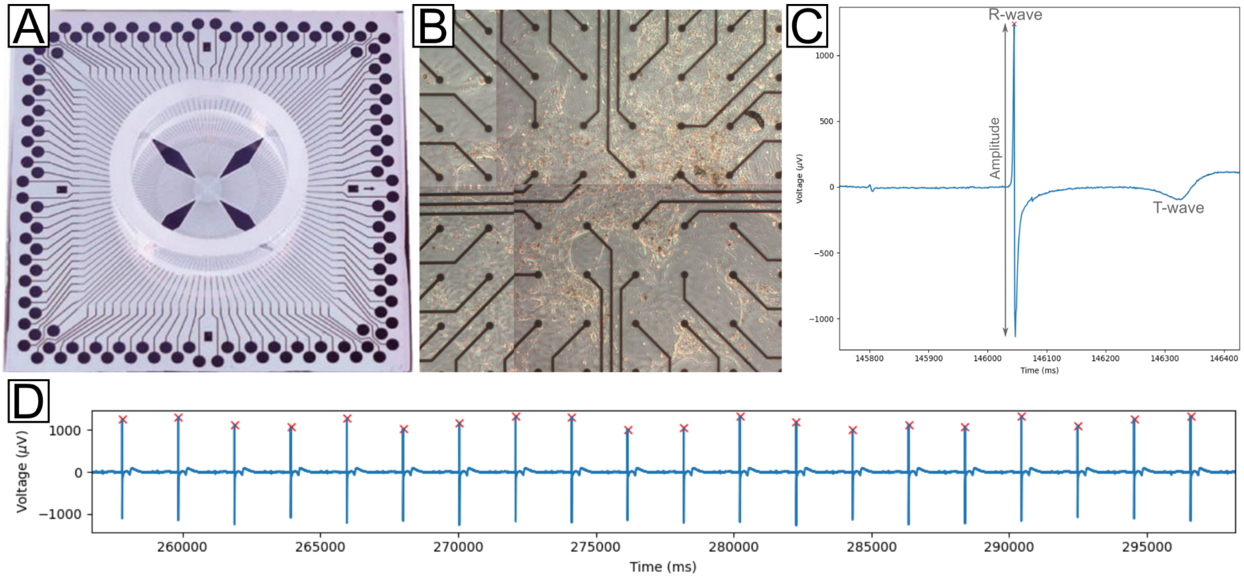

Figure 1. Representative MEA device, culture and field potential signals. A) 120 electrode MEA with TiN electrodes. B) Cardiomyocyte culture on a 120 electrode MEA. C) Field potential showing three beats. Beat amplitude is indicated with a vertical arrow

line in red. D) Extended view of field potentials for one electrode across a 45 second interval. In both C and D, R-wave-like field potential peaks, as detected by the findpeaks algorithm, are marked with a red X.

Detection of pacemaker translocations

Beat occurrence times were calculated, normalized to a global maximum, and examined for each beat. These calculations yielded values for the time lag, t_{lag}, which is the time taken from when a beat is first detected (pacemaker region, $t_{lag} = 0$ ms) until the last detected peak of the beat ($t_{lag} = t$). Time lag values were assessed for each beat in each recording via heatmap in order to view pacemaker regions within the electrode array, as shown in Figure 2. Comparisons between the field potentials and heatmap were consistent: as t_{lag} increased from the minimum (dark blue) to maximum (dark red), there was an observable shift in the field potential relative to $t_{lag} = 0$ ms. Electrodes which did not exhibit detectable beat activity or experienced excessive noise were omitted and color-coded white. Cursory examinations of field potentials across electrodes failed to reveal any noteworthy changes in signal morphology. Pacemaker regions were observed as frequently lacking a fixed location. The pacemaker region demonstrated instability and moved at least twice in 21 of 30 recordings, while the remaining 9 recordings did not. The movement of the pacemaker region from one location to another is referred to as a pacemaker translocation. Examples of two such translocations are illustrated in Figure 3.

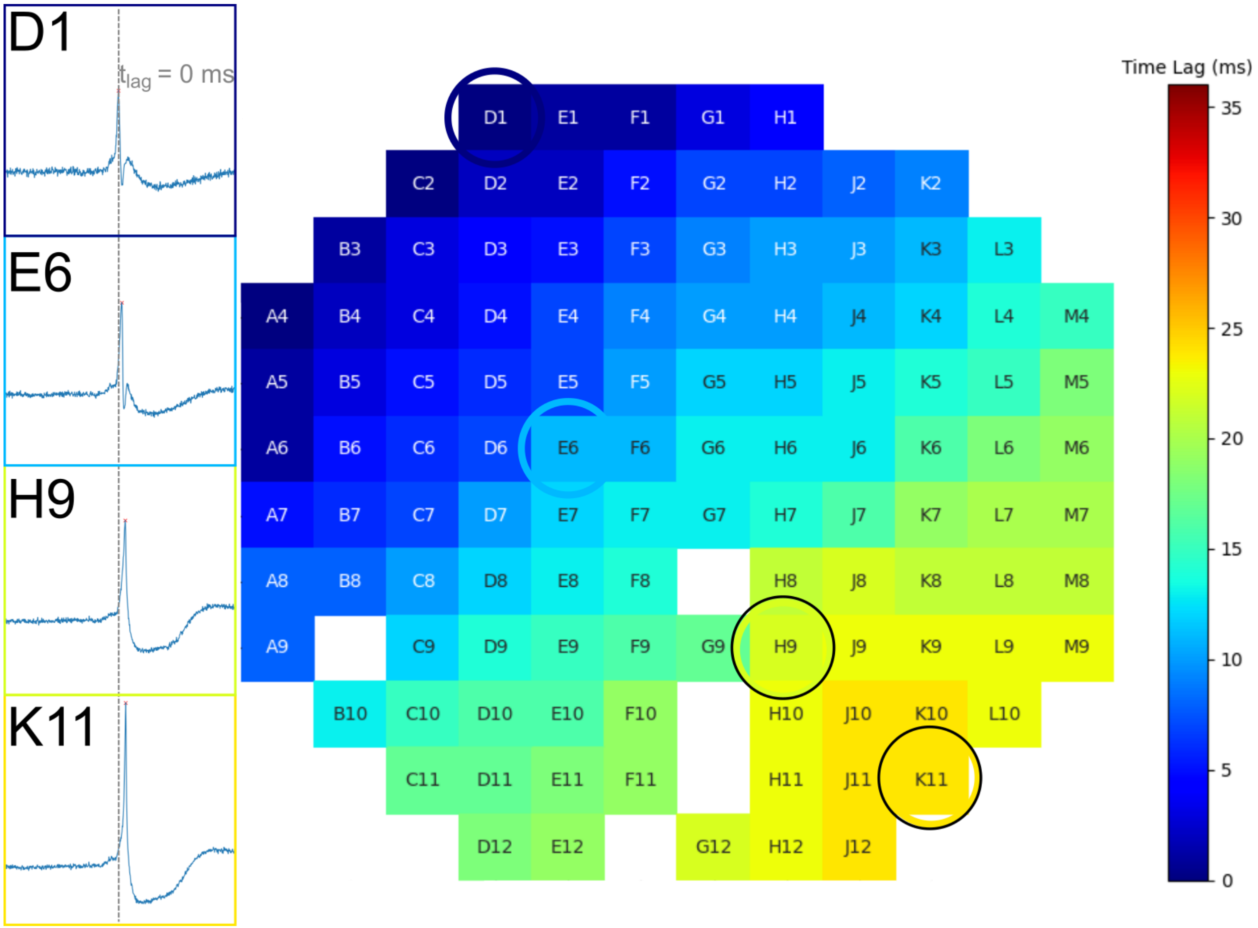

Figure 2. Field potentials of electrodes in four different regions of the pacemaker map. The pacemaker region is near electrode D1, which has a recorded normalized time lag of t_{lag} = 0 ms. Electrodes further from the pacemaker exhibit a shift to the right of the t_{lag} = 0 ms time point (dashed, vertical line) and show how the time at which the signal is detected increases with increasing distance away from the pacemaker region. This shift is correlated with the heatmap time lag values. White squares indicate electrodes that were excluded from analysis due to insufficient signal.

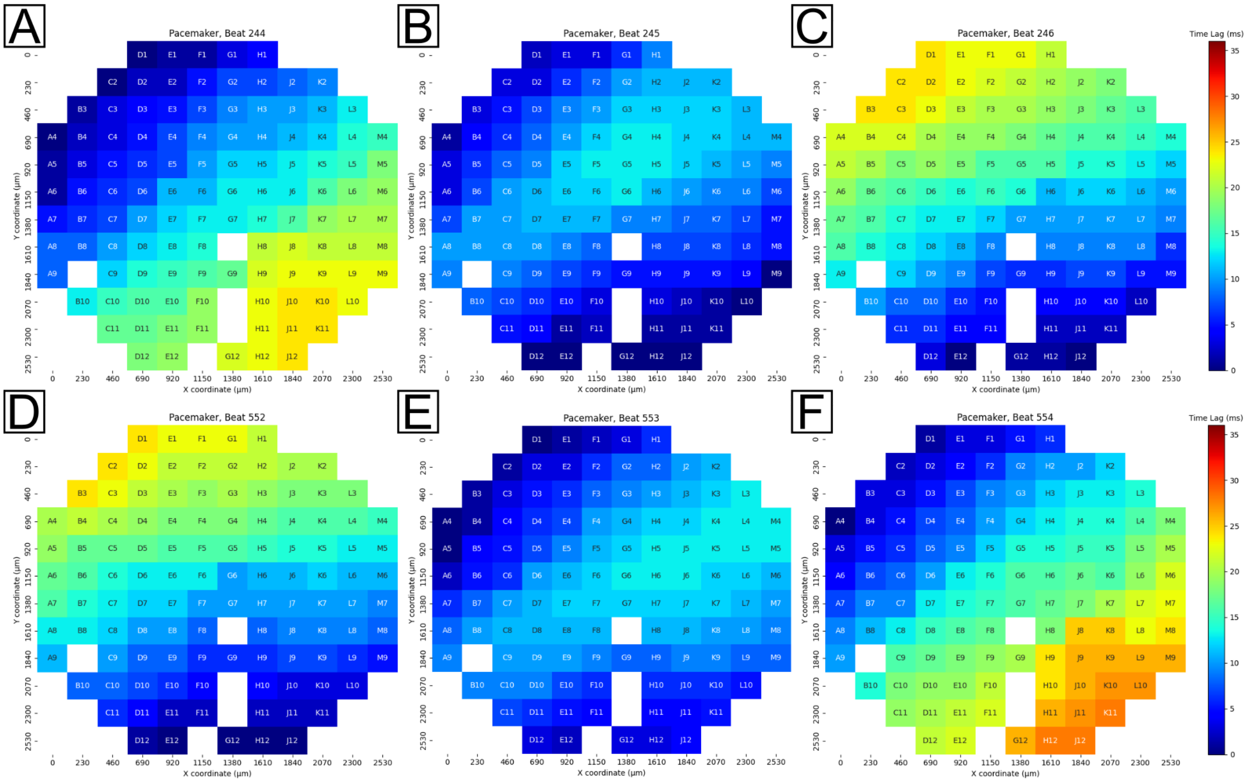

Figure 3. Example pacemaker translocations observed in one recording of a 120 electrode MEA. Color bar is normalized from the lowest time lag (0 milliseconds, dark blue) to highest time lag (35 milliseconds, dark red) in the full recording. Top row: the pacemaker region translocates from the top-left corner of the array (A) to a temporary regime positioned simultaneously in the top-left and bottom-right corners (B) before stabilizing in the bottom-right corner of the array (C). Bottom row: another translocation event observed in the same recording over 300 beats later that follows a similar pattern as A-C. The pacemaker is stable in the bottom-right (D) until translocating to a temporary regime positioned simultaneously in the top-left and bottom-right corners (E) before settling in the top-left corner of the array (F).

Figure 3A shows the pacemaker region situated closest to the upper left quadrant (dark blue) of the MEA during beat 244. The next beat, 245, is shown in Figure

3B and was observed in a state of flux as the pacemaker region translocated, or moved, from the upper left quadrant to the lower right quadrant (dark blue regions in each respective quadrant, lighter blue in between). The pacemaker region subsequently settled in the lower right quadrant in beat 246, as shown in Figure 3C. This region remained in a stable location from beat 247 to beat 249, which strongly indicated that the translocation phenomenon was due to conditions in the culture (i.e. caused by the cells) and not due to the equipment or analysis program. A second translocation with a clear transitional state is shown from the same recording approximately 308 beats later in Figs 3D-F. Additional translocations were detected between the translocations depicted in Figure 3, although they are not shown here.

Non-robust power law analysis of pacemaker translocation quiescent periods

The quiescent period, or the time (measured in beats) between pacemaker translocation events, was calculated using the pacemaker translocation algorithm described earlier. The number of occurrences of a given quiescent period (referred to here as the number of events) were subsequently calculated. The plots shown in Figure 4 constitute the non-robust or “incomplete” analysis of the data. First, a log-log plot of the number of events (y) vs the quiescent period (x) was generated from the data. Linear regression was then applied to the data to produce the plot shown in Figure 4A. On logarithmic axes, the fitted line (black) represents a power law with calculated values for the power law exponent, $\alpha = -1.539$, and goodness-of-fit, $R^2 = 0.955$. Additional analysis was performed using nonlinear least squares to fit the data to a power law function, as shown in Figure 4B. Here, the calculations yielded $\alpha = -1.951$ and $R^2 =$

0.995. Finally, the nonlinear least squares fit was plotted on logarithmic axes to produce the plot shown in Figure 4C.

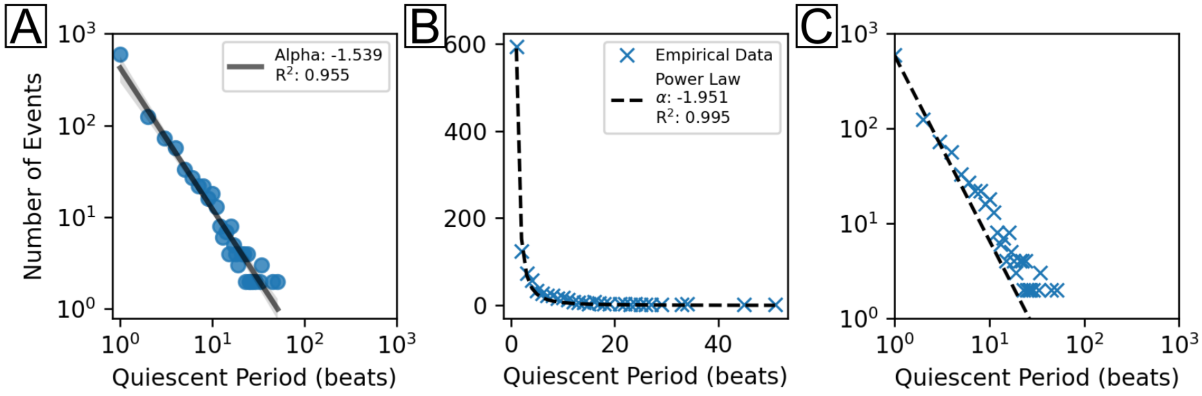

Figure 4. Non-robust power law analysis. A) $\log_{10}(y)$ vs $\log_{10}(x)$ (scatterplot, blue), where y is the number of events and x is the quiescent period between translocations as measured in the number of beats between. Linear regression of the data (solid line, black) yielded α = -1.539 and R^2 = 0.955. The confidence interval (0.95) of the linear regression fit is shown in gray shading. Number of unique data points, N: 30. B) Nonlinear least squares fit to a power law function (dashed, black) with the calculated α = -1.951 and R^2 = 0.995. C) Log-log axis visualization of B.

Robust power law analysis of pacemaker translocation quiescent periods

A robust approach to power law analysis is demonstrated in Figure 5. Figure 5A provides a qualitative assessment using a histogram of the data and probability distribution curves (blue: power law, red: exponential, yellow: log-normal, green: Weibull) to demonstrate how well the data adhere to each distribution. Here, it is observed that the power law is an inferior fit to the data compared to the Weibull distribution, as judged by the distance between the data and distribution curve. Next, log-log plots of the PDF vs quiescent period and the complementary cumulative distribution function (CCDF) vs quiescent period for each distribution were generated. The interpretation is relatively straightforward: the closer a distribution curve is to the empirical curve, the better the fit between data and distribution. Figure 5B shows the log-log plot of the PDF vs quiescent period for the empirical data (black) and all candidate distributions: power law (blue), log-normal (yellow), exponential (red), and Weibull (green). Table 1 summarizes the parameters calculated for each distribution. The minimum cutoff value, x_{min}, was calculated by the powerlaw library ($x_{min} = 1$) as the value which yields an optimal power law fit and is required in order to avoid undefined behavior in power law analysis. Through the first decade, the data adhere reasonably well to power law, log-normal, and Weibull distributions but do not follow the exponential distribution. Between the first and second decades, the tail of the data appears to deviate from a power law and instead demonstrates a closer fit to either a log-normal or Weibull distribution. Similarly, Figure 5C shows the CCDF vs quiescent period for the empirical data and all candidate distributions. Here, the deviation of the data from power law behavior is made more explicit as judged by the growing distance between the empirical curve and the power law fit as they diverge at the tail. Notably, the empirical data approaches a vertical limit or asymptote in a manner similar to the exponential distribution as it terminates. A vertical asymptote can be an indication of an exponentially truncated, or doubly truncated, power law. This distribution is evaluated later in the final phase of analysis.

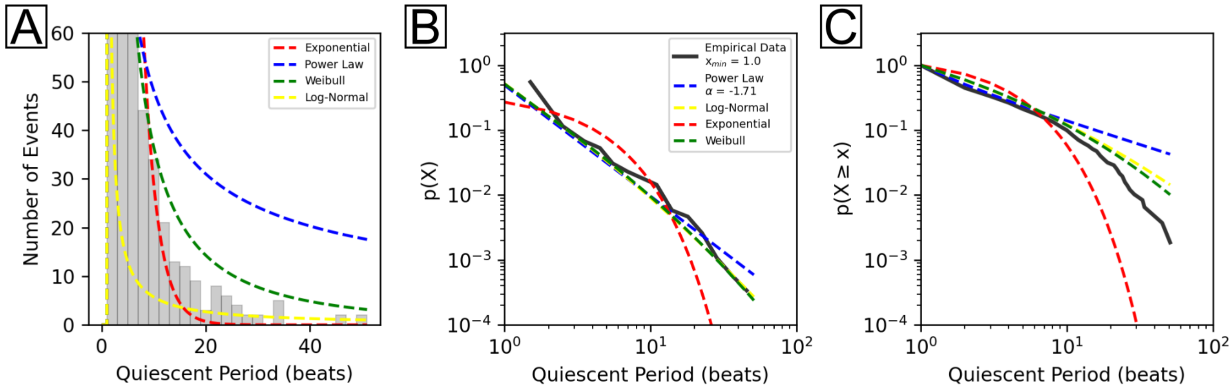

Figure 5. Comparisons between heavy-tailed probability distributions. A) Histograms and fitted PDFs of power law (blue, solid), log-normal (yellow, dashed line), exponential (red, dashed line), and Weibull (green, dashed line) probability distributions for all quiescent periods. B) Empirical data (black, solid line) plot overlaid with PDFs of power law (blue, dashed line), log-normal (yellow, dashed line), exponential (red, dashed line) and Weibull (green, dashed line) distributions. C) Empirical data plot overlaid with complementary cumulative distribution functions (CCDFs) of power law, log-normal, exponential, and Weibull distributions. The empirical x_{min}, or minimum cutoff value, value was determined algorithmically by the powerlaw library. Calculated parameters for each distribution are summarized in Table 1.

Table 1. Summary of calculated parameters for each distribution.

	Distribution				
Parameter	Power Law	Doubly Truncated Power Law	Log-Normal	Exponential	Weibull
α	1.814^a	1.583^a	N/A	N/A	N/A
x_{min}	1.0	1.0	1.0	1.0	1.0
μ	N/A	N/A	2.363^a	N/A	N/A

σ	N/A	N/A	2.252	N/A	N/A
λ	N/A	0.032	N/A	0.315	83.884
β	N/A	N/A	N/A	N/A	0.238

[a]Value represents the magnitude and omits the sign (which is negative).

The final phase of analysis engaged in comparisons between candidate distributions using the powerlaw library's distribution comparison function (distribution_compare()). In each comparison, either a power law or doubly truncated power law distribution was selected as the first distribution (numerator) and the alternative heavy-tailed distribution (log-normal, exponential, Weibull) was used for the second distribution (denominator). Log-likelihood ratios (LLRs) and p-values to assess significance of the ratio's sign were calculated by the powerlaw library. If the sign is positive, the first distribution is the more likely fit, and if the sign is negative, the second distribution is the more likely fit. All p-values were compared to the 0.05 significance level ($p \leq 0.05$). A complete summary of the distribution comparison outputs are shown in Table 2.

Table 2. Log-likelihood ratio (LLR) comparisons between distributions.

	Distribution	
Parameter	Power Law	Doubly Truncated Power Law
	vs. Log-Normal	
LLR	-4.043	3.806
p-value*	5.271×10^{-5}	1.412×10^{-4}
	vs. Exponential	
LLR	8.888	10.544

p-value*	$6.194x10^{-19}$	$5.422x10^{-26}$
	vs. Weibull	
LLR	-3.909	3.881
p-value*	$9.268x10^{-5}$	$1.041x10^{-4}$
	vs. Doubly Truncated Power Law	vs. Power Law
LLR	-4.049	4.049
p-value*	$4.720x10^{-8}$	$4.720x10^{-8}$

*p-values denote the statistical significance of the sign of the LLR. Significance level: 0.05.

Discussion

Power laws in cardiological systems

One can intuitively surmise that as cardiomyocytes mature, they would exhibit less pacemaker region volatility and more consistent beating. These attributes would be congruous with the establishment of a stable or even permanent pacemaker region such as the sinoatrial node in the heart. Pacemaker instability is already known to be detrimental to heart function: severe abnormalities in pacemaker function necessitate the surgical implantation of electrical devices to maintain heart rhythm [60-62]. Thus, identifying the mechanisms for and improving understanding of pacemaker abnormalities in cardiomyocytes could provide insight into problems afflicting the sinoatrial node of the heart.

Previous studies have shown that there is significant diagnostic power to be found in power law exponents. Investigations of heart rate variability (HRV, also referred to as beat rate variability or BRV), defined as small variations in the interval between heart beats, reported differences in power law exponents between healthy, functional tissue and abnormal tissues, e.g. following myocardial infarction or transplant [28, 38-41]. These studies suggest that power law exponents may hold strong predictive power in diagnosing heart abnormalities. However, the use of power laws as diagnostic tools can only be effective if optimal, comprehensive methodologies are applied.

Suboptimal or incomplete methods lead to misleading interpretations of power law behavior

Suboptimal and optimal power law analysis were performed as shown in Figure 4 and Figure 5, respectively. Figure 4 utilized linear regression of log(y) vs log(x) (Figure 4A) and nonlinear least squares of y vs x on regular (Figure 4B) and logarithmic (Figure 4C) axes. While these methods demonstrated good fits to the data (R^2 = 0.955 and 0.995), they were problematic for two key reasons: 1) they did not adequately consider power laws as probability distributions of the form $p(x) \propto x^{-\alpha}$ [63-64] and 2) they lacked consideration for power law alternatives, e.g. exponential, log-normal and Weibull distributions. These deficiencies were rectified using the methods in Figure 5. Here, qualitative assessments of the fit between data and distributions were conducted using three methods: 1) histogram and PDF curve fits of the quiescent period (Figure 5A), 2) log-log of the PDF (Figure 5B) vs quiescent period, and 3) log-log of the CCDF (Figure 5C) vs quiescent period.

Figure 5A shows that there is a large gap between the data and the power law fit (blue curve), contradicting the results of Figure 4. Rather, the Weibull distribution (green curve) is, qualitatively, a far better candidate than any of the distributions considered to this point. Thus, the histogram serves as an effective estimation, but is not the preferred qualitative method. Instead, the preferred qualitative assessment for power laws is the log-log plot of the PDF (or, better still, the CCDF) vs event size, as in Figs 5B and 5C. Figure 5B shows that the PDF of the empirical data fits poorly to the power law PDF for most values. The CCDF in Figure 5C shows that the empirical data adhere better to a Weibull distribution (in agreement with Figure 5A) than power law after the first decade. Finally, the gradual decay of the CCDF tail suggests that the data approach a vertical limit or asymptote which could correspond to a maximum cutoff value for the system [48]. Together, these results: 1) thoroughly contradict the interpretation from Figure 4 that the data obey a power law and 2) indicate the data may fit to another power law alternative: the doubly-truncated power law distribution, which is discussed next.

Pacemaker translocations obey a doubly-truncated power law

All power laws are at a minimum singularly truncated, i.e. there is always a minimum value, x_{min} ($x_{min} > 0$), for which power law distributions are valid and, at worst, values below x_{min} could produce undefined behavior. Here, x_{min} was determined algorithmically by the powerlaw library as previously described [48]. In addition to the lower bound, systems may possess an upper bound, x_{max}. The upper bound reflects some natural limitation(s) of the system, e.g. the number of available nodes within a network that is confined to a specific geometric size. This upper bound must be given unique consideration for each system. For a cardiac system, a plausible upper bound is the maximum capacity for the number of beats that a heart (or cardiomyocyte culture) will beat in its lifetime. This is a logical suspicion: because the cardiomyocyte culture cannot beat indefinitely, there could never be a pacemaker translocation quiescent period of infinite length. Under these conditions, it is reasonable to consider truncating the power law at a maximum value using an exponential cutoff. This gives rise to the doubly truncated power law distribution [48, 65-66]. Evidence to support this interpretation in this experiment was provided by the asymptotic tail in Figure 5C. Furthermore, many of the power laws observed in nature are in fact doubly, rather than singularly, truncated [43, 67]. Thus, consideration of a doubly truncated power law distribution is quite reasonable.

Comparisons between power law, doubly truncated power law, exponential, log-normal, and Weibull distributions using log-likelihood ratio (LLR) tests (Table 2) reveal that a power law is disfavored for all cases except the exponential distribution (exponential: LLR = 8.888, log-normal: LLR = -4.043, Weibull: LLR = -3.909, doubly-truncated power law: LLR = -4.049; $p < 0.05$). This result is in agreement with the qualitative assessment from Figure 5 that the power law is a poor descriptor of the data. Equivalent comparisons between doubly truncated power law and alternative distributions favors the doubly truncated power law in all cases (exponential: LLR = 10.544, log-normal: LLR = 3.806, Weibull: LLR = 3.881). Overall, both the robust qualitative and quantitative methods provide strong evidence that pacemaker translocations adhere better to a doubly-truncated power law than any of the heavy-tailed distributions considered here.

Doubly truncated power law exponent indicates potential for a critical system

The doubly truncated power law exponent ($\alpha = -1.583$), calculated using MLE methods, from Table 2 presents a particularly intriguing possibility: that pacemaker translocations could represent a critical system. Critical systems are systems that demonstrate scale invariant spatiotemporal dynamics, long-range correlations, self-similarity (fractal structures), and power laws, among other features [45, 68-73]. These systems operate at or near a critical point between subcritical (“ordered”) and supercritical (“disordered”) configurations, analogous to the critical point separating phases of matter in a phase diagram. At the critical point, the system dynamics are markedly different from either the subcritical or supercritical states, leading to the emergence of new properties [72]. Critical dynamics have been observed in both abiotic systems, (e.g. word frequency, earthquake intensity and wildfire frequency) and biotic systems (e.g. animal migration patterns, neurons and the brain) [45, 70, 72-73]. Importantly, many of these critical systems demonstrated a power law exponent of $\alpha = -1.5$, which differs by only ~5.5% from the α calculated in this study.

If pacemaker translocations constitute a critical system, then critical dynamics would represent one potential mechanism underpinning the stabilization of the pacemaker region. Suspected critical systems, e.g. neuronal cultures, have demonstrated optimal information exchange between cooperative units when operating at or near criticality [66, 69, 74-79]. Cardiomyocyte cultures could utilize critical dynamics to determine the optimal location for the pacemaker region to reside. In the cardiomyocyte network, information concerning which cells will become pacemaker cells needs to be conveyed throughout the network across great distances. Operating at or near a critical regime could enable the cardiomyocyte network to maximize signal transduction (i.e. communication of information regarding cellular conditions), ensuring that all cardiomyocytes in the network are in active contact with one another [79-81]. Maximized communication between cardiomyocytes could allow the cells to share structural, local environmental, and genetic information across the entire culture at great distances and speed, which could help determine an optimal region in the culture for the establishment of pacemaker cells. Thus, critical dynamics may play a crucial role in determining the ideal pacemaker region in the cardiomyocyte culture.

Conclusion

Pacemaker translocations were observed in 21 of 30 cardiomyocyte MEA recordings. A cursory analysis of these translocations using non-robust methods revealed a potential power law relationship between the quiescent period and the number of quiescent periods of a given length. Unfortunately, these techniques are insufficient for assessing power law behavior, partly because they do not represent power laws accurately as probability distributions. More robust methods were subsequently employed to evaluate the data against several probability distributions, including power law, doubly truncated power law, exponential, log-normal, and Weibull. Application of these methods failed to support the interpretation that the data uniquely obey a power law distribution. However, the evidence shows that the data exhibit superior fit to a doubly truncated power law with $\alpha = -1.583$. These findings demonstrate that 1) misleading conclusions are likely if less robust or incomplete methods are applied to power law analysis of cardiological phenomena, 2) pacemaker translocations obey a doubly truncated power law distribution, and 3) indicate the potential for critical dynamics in the establishment of the pacemaker region in cardiomyocyte cultures.

References

1. Karbassi E, Fenix A, Marchiano S, Muraoka N, Nakamura K, Yang X, et al. Cardiomyocyte maturation: advances in knowledge and implications for regenerative medicine. Nat Rev Cardiol. 2020;17: 341-359. doi: 10.1038/ s41569-019-0331-x.

2. Guo Y, Pu WT. Cardiomyocyte maturation: New phase in development. Circ Res. 2020;126: 1086-1106. doi: 10.1161/CIRCRESAHA.119.315862.
3. Breckwoldt K, Letuffe-Brenière D, Mannhardt I, Schulze T, Ulmer B, Werner T, et al. Differentiation of cardiomyocytes and generation of human engineered heart tissue. Nat Protoc. 2017;12: 1177–1197. doi: 10.1038/nprot.2017.033.
4. Lian X, Hsiao C, Wilson G, Zhu K, Hazeltine LB, Azarin SM, et al. Cardiac differentiation of jPSCs via Wnt Signaling. Proc Natl Acad Sci. 2012;109: E1848-E1857. doi: 10.1073/pnas.1200250109
5. Maguire EM, Xiao Q, Xu Q. Differentiation and Application of Induced Pluripotent Stem Cell-Derived Vascular Smooth Muscle Cells. Arterioscler Thromb Vasc Biol. 2017;37: 2026–2037. doi: 10.1161/ATVBAHA.117.309196
6. Xiaojun L, Xiaoping B, Abraham A, Jialu L, Yue W, Dong W, et al. Efficient differentiation of human pluripotent stem cells to endothelial progenitors via small-molecule activation of Wnt signaling. Stem Cell Rep. 2014;3: 804-16. doi: 10.1016/j.stemcr.2014.09.005.
7. Ahmed RE, Anzai T, Chanthra N, Uosaki H. A brief review of current maturation methods for human induced pluripotent stem cells-derived cardiomyocytes. Front Cell Dev Biol. 2020;8: 178. doi: 10.3389/fcell.2020.00178.
8. Zhu H, Scharnhorst KS, Stieg AZ, Gimzewski JK, Minami I, Nakatsuji N, et al. Two dimensional electrophysiological characterization of human pluripotent stem cell-derived cardiomyocyte system. Sci Rep. 2017;7: 43210, doi: 10.1038/srep43210.

9. Kannan S, Kwon C. Regulation of cardiomyocyte maturation during critical perinatal window. J Physiol. 2018;598: 2941-2956. doi: 10.1113/JP276754.

10. Koivumäki JT, Naumenko N, Tuomainen T, Takalo J, Oksanen M, Puttonen KA, et al. Structural immaturity of human iPSC-derived cardiomyocytes: in silico investigation of effects on function and disease modeling. Front Physiol. 2018;9: 80. doi: 10.3389/fphys.2018.00080.

11. Funakoshi S, Fernandes I, Mastikhina O, Wilkinson D, Tran T, Dhahri W, et al. Generation of mature compact ventricular cardiomyocytes from human pluripotent stem cells. Nat Commun. 2021;12: 3155, doi: 10.1038/s41467-021-23329-z

12. Lausten PG, Russell SJ, Cui L, Entingh-Pearsall A, Holzenberger M, Liao R, et al. Essential role of insulin and insulin-like growth factor 1 receptor signaling in cardiac development and function. Mol Cell Biol. 2007;27: 1649-1665. doi: 10.1128/MCB.01110-06.

13. Guo Y, VanDusen NJ, Zhang L, Gu W, Sethi I, Guatimosim S, et al. Analysis of cardiac myocyte maturation using CASAAV, a platform for rapid dissection of cardiac myocyte gene function *in vivo*. Circ Res. 2017;120: 1874-1888. doi: 10.1161/CIRCRESAHA.116.310283.

14. Alcon A, Cagavi Bozkulak E, Qyang Y. Regenerating functional heart tissue for myocardial repair. Cell Mol Life Sci. 2012;69: 2635–2656. doi: 10.1007/s00018-012-0942-4.

15. Scuderi GJ, Butcher J. Naturally Engineered Maturation of Cardiomyocytes. Cell Front Cell Dev Biol. 2017;5: 50. doi: 10.3389/fcell.2017.00050.

16. Wiese C, Gireskamp T, Airik R, Mommersteeg MTM, Gardiwal A, de Gier-de Vries C, et al. Formation of the sinus node head and differentiation of sinus node myocardium are independently regulated by Tbx18 and Tbx3. Circ Res. 2008;104: 388-397. doi: 10.1161/CIRCRESAHA.108.187062.
17. Burkhard S, van Eif V, Garric L, Christoffels VM, Bakkers J. On the evolution of the cardiac pacemaker. J Cardiovasc Dev Dis. 2017;4: 4. doi: 10.3390/jcdd4020004.
18. Opthof, T. The Mammalian Sinoatrial Node. Cardiovasc Drugs Ther. 1988;1: 573-597. doi: 10.1007/BF02125744.
19. Kiuchi S, Usami A, Shimoyama T, Otsuka F, Yamaguchi S, Nakamura T, et al. Cardiac pacemaker cells generate cardiomyocytes from fibroblasts in long-term cultures. Sci Rep. 2019;9: 15174. doi: 10.1038/s41598-019-51001-6.
20. Mangoni ME and Nargeot J. Genesis and regulation of the heart automaticity. Physiol Rev. 2008; 88:919-82. doi: 10.1152/physrev.00018.2007.
21. Chakraborty S, Yutzey KE. Tbx20 regulation of cardiac cell proliferation and lineage specialization during embryonic and fetal development *in vivo*. Dev Biol. 2012;363: 234-246. doi: 10.1016/j.ydbio.2011.12.034
22. Yutzey KE. Cardiomyocyte proliferation: teaching an old dogma new tricks. Circ Res. 2017;120: 627–629. doi: 10.1161/CIRCRESAHA.116.310058
23. Ribeiro da Silva A, Neri EA, Turaça LT, Dariolli R, Fonseca-Alaniz MH, Santos-Miranda A, et al. NOTCH1 is critical for fibroblast-mediated induction of cardiomyocyte specialization into ventricular conduction system-like cells *in vitro*. Sci Rep. 2020;10. doi: 10.1038/s41598-020-73159-0

24. Mandla R, Jung C, Vedantham V. Transcriptional and Epigenetic Landscape of Cardiac Pacemaker Cells: Insights Into Cellular Specialization in the Sinoatrial Node. Front Physiol. 2021;12. doi: 10.3389/fphys.2021.712666
25. Stanley HE, Buldyrev SV, Goldberger AL, Havlin S, Peng C-K, Simmons M. Long-range power law correlations in condensed matter physics and biophysics. Physica A: Stat Mech Appl. 1993;200: 4-24. doi: 10.1016/0378-4371(93)90500-4
26. Stanley HE, Amaral LAN, Gopikrishnan P, Ivanov PC, Keitt TH, Plerou V. Scale invariance and universality: organizing principles in complex systems. Physica A: Stat Mech Appl. 2000;281: 60-68. doi: 10.1016/S0378-4371(00)00195-3
27. Gisiger, T. Scale invariance in biology: coincidence or footprint of a universal mechanism? Biol Rev. 2001;76: 161-209. doi: 10.1017/S1464793101005607
28. Bigger JT, Steinman RC, Rolnitzky LM, Fleiss JL, Albrecht P, Cohen RJ. Powerlaw behavior of RR-interval variability in healthy middle-aged persons, patients with recent acute myocardial infarction, and patients with heart transplants. Circulation. 1996;93: 2142–2151.
29. Aon MA, Cortassa S, O'Rourke B. Percolation and criticality in a mitochondrial network. Proc Natl Acad Sci. 2004;101:4447-4452. doi: 10.1073pnas.0307156101.
30. Akar FG, Aon MA, Tomaselli GF, O'Rourke B. The mitochondrial origin of postischemic arrhythmias. J Clin Invest. 2005;115: 3527-3535. doi: 10.1172/JCI25371.
31. Aon MA, Cortassa S, Akar FG, O'Rourke B. Mitochondrial criticality: a new concept at the turning point of life or death. Biochim Biophys Acta. 2006;1762: 232-240. doi: 10.1016/j.bbadis.2005.06.008.

32. Vetter L, Cortassa S, O'Rourke B, Armoundas AA, Bedja D, Jende JME, et al. Diabetes increases the vulnerability of the cardiac mitochondrial network to criticality. Front Physiol. 2020;11: 175. doi: 10.3389/fphys.2020.00175.
33. Kiyono K, Struzik ZR, Aoyagi N, Sakata S, Hayano J, Yamamoto Y. Critical scale invariance in a healthy human heart rate. Phys Rev Lett. 2004;93: 178103. doi: 10.1103/PhysRevLett.93.178103.
34. Nivala M, Ko CY, Nivala M, Weiss JN, Qu Z. Criticality in intracellular calcium signaling in cardiac myocytes. Biophys J. 2012;102: 2433-2442. doi: 10.1016/j.bpj.2012.05.001.
35. Mandel Y, Weissman A, Schick R, Barad L, Novak A, Meiry G, et al. Human embryonic and induced pluripotent stem cell-derived cardiomyocytes exhibit beat rate variability and power-law behavior. Circulation. 2012;125: 883-893. doi: 10.1161/CIRCULATIONAHA.111.045146.
36. Kim J, Kuusela J, Aalto-Setala K, Rasanen E. Short- and long-range correlations in beat rate variability of human pluripotent-stem-cell-derived cardiomyocytes. Comput Cardiol. 2017;44. doi: 10.22489/CinC.2017.207-155
37. Wang X, Wang L, Dou W, Huang Z, Zhao Q, Mahli M, et al. Electrical impedance-based contractile stress measurement of human iPSC-cardiomyocytes. Biosens Bioelectron. 2020;166: 112399. doi: 10.1016/j.bios.2020.112399
38. Huikuri HV, Mäkikallio TH, Juhani Airaksinen KE, Seppänen T, Puukka P, Räihä IJ, et al. Power-law relationship of heart rate variability as a predictor of mortality in the elderly. Circulation. 1998;97: 2031-2036. doi: 10.1161/01.CIR.97.20.2031.

39. Jokinen V, Syvänne M, Mäkikallio TH, Juhani Airaksinen KE, Huikuri HV. Temporal age-related changes in spectral, fractal and complexity characteristics of heart rate variability. Clin Physiol. 2008;21: 273-281. doi: 10.1046/j.1365-2281.2001.00326.x.
40. Kemuriyama T, Ohta H, Sato Y, Maruyama S, Tandai-Hiruma M, Kato K, et al. A power-law distribution of inter-spike intervals in renal sympathetic nerve activity in salt-sensitive hypertension-induced chronic heart failure. Biosystems. 2010;101: 144-147. doi: 10.1016/j.biosystems.2010.06.002.
41. Kucera JP. What makes the heart rhythm so intricate? Heart Rhythm. 2014;11: 1220-1221. doi: 10.1016/j.hrthm.2014.04.013.
42. Clauset A, Shalizi CR, Newman MEJ. Power-law distributions in empirical data. SIAM Rev. 2009;51: 661-703. doi: 10.1137/070710111.
43. Marshall N, Timme NM, Bennett N, Ripp M, Lautzenhiser E, Beggs JM. Analysis of power laws, shape collapses, and neural complexity: new techniques and MATLAB support via the NCC toolbox. Front Physiol. 2016;7: 250. doi: 10.3389/fphys.2016.00250.
44. Corral A, González A. Power law size distributions in geoscience revisited. Earth Space Sci. 2019;6: 673-697. doi: 10.1029/2018EA000479.
45. Dunham CS, Lilak S, Hochstetter J, Loeffler A, Zhu R, Chase C, et al. 2021. Nanoscale neuromorphic networks and criticality: a perspective. J Phys Complex. 2021;2: 042001. doi: 10.1088/2632-072X/ac3ad3.
46. Goldstein ML, Morris SA, Yen GG. Problems with fitting to the power-law distribution. Eur Phys J B. 2004;41: 255-258. doi: 10.1140/epjb/e2004-00316-5.

47. van Beek P. Backtracking search algorithms. In: Rossi F, van Beek P, Walsh T, editors. Foundations of Artificial Intelligence, Handbook of Constraint Programming. Elsevier Science; 2006. doi: 10.1016/S1574-6526(12)70002-0.
48. Alstott J, Bullmore E, Plenz D. powerlaw: A Python package for analysis of heavy-tailed distributions. PLoS One. 2014;9: e85777. doi: 10.1371/journal.pone.0085777.
49. Clark RM, Cox SJD, Laslett GM. Generalizations of power-law distributions applicable to sampled fault-trace lengths: model choice, parameter estimation, and caveats. Geophys J Int. 1999;136: 357-372. doi: 10.1046/j.1365-246X.1999.00728.x.
50. van der Hofstad R. Random Graphs and Complex Networks, vol 1. Cambridge University Press; 2017.
51. Chen B, Ma C, Krajewski WF, Wang P, Ren F. Logarithmic transformation and peak-discharge power-law analysis. Hydrol Res. 2020;51: 65-76. doi: 10.2166/nh.2019.108.
52. Hanel R, Corominas-Murtra B, Liu B, Thurner S. Fitting power-laws in empirical data with estimators that work for all exponents. PLoS One. 2017;12: e0170920. doi: 10.1371/journal.pone.0170920.
53. Bellay T, Klaus A, Seshadri S, Plenz D. Irregular spiking of pyramidal neurons organizes as scale-invariant neuronal avalanches in the awake state. eLife. 2015;07224. doi: 10.7554/eLife.07224.
54. Lombardi F, Herrmann HJ, Plenz D, de Arcangelis L. Temporal correlations in neuronal avalanche occurrence. Sci Rep. 2016;6: 24690. doi: 10.1038/srep24690.

55. Minami I, Yamada K, Otsuji TG, Yamamoto T, Shen Y, Otsuka S, et al. A small molecule that promotes cardiac differentiation of human pluripotent stem cells under defined, cytokine- and xeno-free conditions. Cell Rep. 2012;2: 1448-1460. doi: 10.1016/j.celrep.2012.09.015.
56. Nakano H, Minami I, Braas D, Pappoe H, Wu X, Sagadevan A, et al. Glucose inhibits cardiac muscle maturation through nucleotide biosynthesis. eLife. 2017;6: e29330. doi: 10.7554/eLife.29330.
57. Klauke N, Smith GL, Cooper J. Extracellular recordings of field potentials from single cardiomyocytes. Biophys J. 2006;91: 2543-2551. doi: 10.1529/biophysj.106.085183.
58. van Meer BJ, Tertoolen LGJ, Mummery CL. Concise review: measuring physiological responses of human pluripotent stem cell derived cardiomyocytes to drugs and disease. Stem Cells. 2016;34: 2008–2015. doi: 10.1002/stem.2403.
59. Stangherlin A, Watson JL, Wong DCS, Barbiero S, Aiwei Z, Seinkmane E, et al. Compensatory ion transport buffers daily protein rhythms to regulate osmotic balance and cellular physiology. Nat Commun. 2021;12: 6035. doi: 10.1038/s41467-021-25942-4.
60. Zipes DP, Festoff B, Schaal SF, Cox C, Sealy WC, Wallace AG. Treatment of Ventricular Arrhythmia by Permanent Atrial Pacemaker and Cardiac Sympathectomy. Annals of Internal Medicine. 1968; doi: 10.7326/0003-4819-68-3-591.
61. Kay GN, Ellenbogen KA, Giudici M, Redfield MM, Jenkins LS, Mianulli M, et al. 1998. The Ablate and Pace Trial: A Prospective Study of Catheter Ablation of the AV Conduction System and Permanent Pacemaker Implantation for Treatment of Atrial

Fibrillation. J Interv Card Electrophysiol. 1998; 2: 121-135. doi: 10.1023/A:1009795330454.

62. Jennifer MS, Cortez D. Pearson marrow-pancreas syndrome with cardiac conduction abnormality necessitating prophylactic pacemaker implantation. Ann Noninvasive Electrocardiol. 2019; 25: e12681. doi:10.1111/anec.12681.
63. Pareto, V. Cours d'Economie Politique vol. 2. 1st ed. Lausanne: Université de Lausanne; 1897. pp. 426.
64. Pareto, V. Manual of Political Economy. Reprint. New English Translation ed. Translated by AS Schwier and AN Page. New York: Augustus M Kelly; 1971. pp. 504.
65. Deluca A, Corral A. Fitting and goodness-of-fit test of non-truncated and truncated power law distributions. Acta Geophys. 2013;61: 1351-1394. doi: 10.2478/s11600-013-0154-9.
66. Cocchi L, Gollo LL, Zalesky A, Breakspear M. Criticality in the brain: a synthesis of neurobiology, models and cognition. Prog Neurobiol. 2017;158: 132-152. doi: 10.1016/j.pneurobio.2017.07.002.
67. Navas-Portella V, Serra I, Corral A, Vives E. Increasing power-law range in avalanche amplitude and energy distributions. Phys Rev E. 2018;97: 022134. doi: 10.1103/PhysRevE.97.022134.
68. Paczuski M, Maslov S, Bak P. Avalanche dynamics in evolution, growth, and depinning models. Phys Rev E. 1996;53: 414–443. doi: 10.1103/PhysRevE.53.414.
69. Beggs J, Plenz D. Neuronal Avalanches in Neocortical Circuits. J Neurosci. 2003;23: 11167-11177. doi: 10.1523/jneurosci.23-35-11167.2003.

70. Beggs JM, Timme N. Being critical of criticality in the brain. Front Physiol. 2012;3: 163. doi: 10.3389/fphys.2012.00163.
71. Hesse J, Gross T. Self-organized criticality as a fundamental property of neural systems. Front Syst Neurosci. 2014;8: 166. doi: 10.3389/fnsys.2014.00166.
72. Muñoz MA. Colloquium: Criticality and dynamical scaling in living systems. Rev Mod Phys. 2018;90: 031001. doi: 10.1103/RevModPhys.90.031001.
73. Roli A, Marco V, Alessandro F, Roberto S. Dynamical criticality: overview and open questions. J Syst Sci Complex. 2018;31: 647-663. doi: 10.1007/s11424-017-6117-5.
74. Haldeman C, Beggs JM. Critical branching captures activity in living neural networks and maximizes the number of metastable states. Phys Rev Lett. 2005; 94: 058101. doi: 10.1103/PhysRevLett.94.058101.
75. Vanni F, Luković M, Grigolini P. Criticality and transmission of information in a swarm of cooperative units. Phys Rev Lett. 2011;107: 078103, doi: 10.1103/PhysRevLett.107.078103.
76. Shew WL, Plenz D. The functional benefits of criticality in the cortex. Neuroscientist. 2013;19: 88-100. doi: 10.1177/1073858412445487.
77. Gollo LG, Kinouchi S, Copelli M. Single-neuron criticality optimizes analog dendritic computation. Sci Rep. 2013;3: 3222., doi: 10.1038/srep03222.
78. Ma Z, Turrigiano GG, Wessel R, Hengen KB. Cortical circuit dynamics are homeostatically tuned to criticality *in vivo*. Neuron. 2019;104: 655-665. doi: 10.1016/j.neuron.2019.08.031.
79. Meijers M, Ito S, Rein ten Wolde P. Behavior of information flow near criticality. Phys Rev E. 2021;103: L010102. doi: 10.1103/PhysRevE.103.L010102.

80. Vázquez-Rodríguez B, Avena-Koenigsberger A, Sporns O, Griffa A. Stochastic resonance at criticality in a network model of the human cortex. Sci Rep. 2017;7: 13020. doi: 10.1038/s41598-017-13400-5.
81. Ashikaga H, Asgari-Targhi A. Locating order-disorder phase transition in a cardiac system. Sci Rep. 2018;8: 1967. doi: 10.1038/s41598-018-20109-6.

Chapter 5. Cardio PyMEA: A user-friendly, open-source Python application for cardiomyocyte microelectrode array analysis

Abstract

Open source analytical software for the analysis of electrophysiological cardiomyocyte data offers a variety of new functionalities to complement closed-source, proprietary tools. Here, we present the Cardio PyMEA application, a free, modifiable, and open source program for the analysis of microelectrode array (MEA) data obtained from cardiomyocyte cultures. Major software capabilities include: beat detection; pacemaker origin estimation; beat amplitude and interval; local activation time, upstroke velocity, and conduction velocity; analysis of cardiomyocyte property-distance relationships; and robust power law analysis of pacemaker spatiotemporal instability. Cardio PyMEA was written entirely in Python 3 to provide an accessible, integrated workflow that possesses a user-friendly graphical user interface (GUI) written in PyQt5 to allow for performant, cross-platform utilization. This application makes use of object-oriented programming (OOP) principles to facilitate the relatively straightforward incorporation of custom functionalities, e.g. power law analysis, that suit the needs of the user. Cardio PyMEA is available as an open source application under the terms of the GNU General Public License (GPL). The source code for Cardio PyMEA can be downloaded from Github at the following repository: https://github.com/csdunhamUC/cardio_pymea.

Introduction

Cardiomyocyte cell cultures, particularly human embryonic and induced pluripotent stem cell-derived cardiomyocytes (hESC-CM and hiPSC-CM, respectively), are of significant interest for their potential to serve as model systems for studying a wide range of phenomena [1-2]. Potential applications of hESC-CMs and hiPSC-CMs in scientific and industrial environments include: pharmacological drug screening, disease modeling, cardiac development and maturation, and regenerative medicine [3-11]. However, the utility of these cultures is often limited by their immature nature [12]. Currently, insufficient knowledge exists to enable these cells to fully achieve adult phenotype maturity *in vitro* [8, 10, 13]. This maturity deficiency limits our capacity to study disease states, including cardiomyopathy and late myocardial dysfunction, which may be linked to defective cardiomyocyte development in humans [9, 14-16]. The inability to induce maturation of stem cell-derived cardiomyocytes beyond the late fetal stage imposes limitations to their applications to disease modeling, drug screening, and regenerative medicine initiatives [4, 7, 8-10].

In recent years, microelectrode arrays (MEAs) became a popular tool for use in the study of cardiomyocyte cultures [13, 17-18]. Microelectrode arrays enable spatiotemporal analysis of cardiomyocyte field potentials, which are extracellular electrical potentials generated by the cells in the culture. Microelectrode arrays also confer the ability to perform controlled stimulation and pacing experiments of cardiomyocyte cultures using a variety of input waveforms [19-20]. Concurrent with the increase in MEA-oriented cardiomyocyte analysis was the academic development of purpose-built MEA software with graphical user interfaces (GUIs) [17-18, 21-22]. These software applications enabled a wider audience to analyze electrophysiological cardiomyocyte data with open-access tools offering enhanced functionality beyond that offered by proprietary software released by the MEA system manufacturers. Each program offers a unique feature that provides value to electrophysiological cardiomyocyte analysis, e.g. new methods for determining the T-wave endpoints and for calculating conduction velocity.

Although powerful and incredibly helpful for cardiomyocyte analysis, there is one significant hurdle that merits consideration. Most, if not all, previously released open source cardiomyocyte analysis tools were written in MATLAB, a licensed programming language developed by MathWorks (Natick, MA) for engineers and scientists [23]. Despite its relative maturity, MATLAB's licensing can impose both financial barriers and accessibility constraints on continued application development. Such costs and constraints can pose significant challenges to research communities [24]. The Python programming language overcomes these hindrances thanks to its free and open source nature. Thus, the financial barrier inherent to developing MATLAB-based cardiomyocyte tools can be overcome by developing Python-based tools instead. This perspective motivated the development of a new MEA analysis application: Cardio PyMEA.

Cardio PyMEA is a free and open source software application (FOSS) written in Python for the analysis of MEA recordings of cardiomyocyte cell cultures. It was designed with a user-friendly GUI to allow scientific programmers and non-programmers alike to engage in robust electrophysiological analysis of MEA data. Because Cardio PyMEA allows the end user to readily adjust analysis parameters, the software is capable of analyzing noisy data sets that demonstrate incompatibility with automated algorithms and applications. In addition to calculating common cardiomyocyte parameters (e.g. pacemaker origin, local activation time, conduction velocity, etc.), Cardio PyMEA offers unique features such as property-distance relationship analysis and power law analysis. The latter is particularly useful for its applications in understanding cardiomyocyte culture system dynamics [25].

Unlike most commercial systems, which are fixed in capabilities, Cardio PyMEA was developed to facilitate relatively easy extensibility thanks to its utilization of object oriented programming principles. This makes the addition of new GUI elements (e.g. additional plotting windows) and new calculations (e.g. machine learning techniques) comparatively straightforward to achieve. Here, Cardio PyMEA is presented using real data acquired from MEA recordings of hESC-CM and hIPSC-CM cell cultures to demonstrate its utility in cardiomyocyte characterization and analysis, and its potential for continued development.

Materials and methods

Cell cultures and microelectrode array measurements

Human ESCs were grown and differentiated in a chemically defined condition as previously described [13, 26-27]. Usage of all human embryonic stem cell lines is approved by the UCLA Embryonic Stem Cell Research Oversight (ESCRO) Committee and the Institutional Review Boards (IRB) (approval #2009-006-04). After differentiation, cardiomyocytes were plated as two-dimensional monolayers on matrigel-coated (Corning #354277), commercially available microelectrode arrays (MEAs) containing 120 integrated TiN electrodes. These electrodes were 30 μm in diameter and were manufactured with an interelectrode spacing of 200 μm (Multichannel Systems, Reutlingen, Germany). Following plating, the MEAs were placed in an incubator set to 37 °C with a gas flow of 5% CO_2. The cell cultures were given no less than 24 hours to ensure the cardiomyocytes adhered well to each MEA.

Software requirements

Cardio PyMEA is written for Python 3.8 or above and utilizes several freely available, actively maintained Python libraries. These libraries include NumPy, SciPy, Pandas, Matplotlib, Seaborn, and Numba, among others. The GUI was constructed using PyQt5. The complete source code and the dependency (pip) requirements file ("requirements.txt") for Cardio PyMEA are available on Github at the following link: https://github.com/csdunhamUC/cardio_pymea.

Using Cardio PyMEA

The preferred way to launch Cardio PyMEA is through the terminal of your chosen operating system. The central file used to run and operate Cardio PyMEA is 'analysisGUI.py'. This file contains the code for the various graphical windows, import function, MEA dictionary, and other functions. Alternatively, for users less inclined toward operating Cardio PyMEA from a terminal, executable files (made using PyInstaller) for Linux, MacOS, and Windows 10 can be accessed from the DataDryad repository.

The main window of Cardio PyMEA, shown in Fig 1, consists of a traditional menu navigation system anchored around the central plotting window that, after calculations, will display heatmaps of the time lag (pacemaker), local activation time (LAT), upstroke velocity (dV/dt), and conduction velocity (CV). To import MEA data, the user can click on 'File' → 'Import Data' and select an appropriate MC_Data-derived *.txt file. The expected format of MEA data is discussed in the next section. Once the data is imported, the user can run the beat detection by selecting ‘Calculations’ → ‘Find Beats’, choosing whether to apply any smoothing filters, and then clicking the button to execute. After this step, the user can choose among the various calculations of interest, including ‘All’ to perform the calculations for pacemaker, LAT, maximal upstroke velocity (dV/dt_{max}), CV, beat amplitude, and beat interval properties. This workflow is summarized by the flowchart in Fig 2.

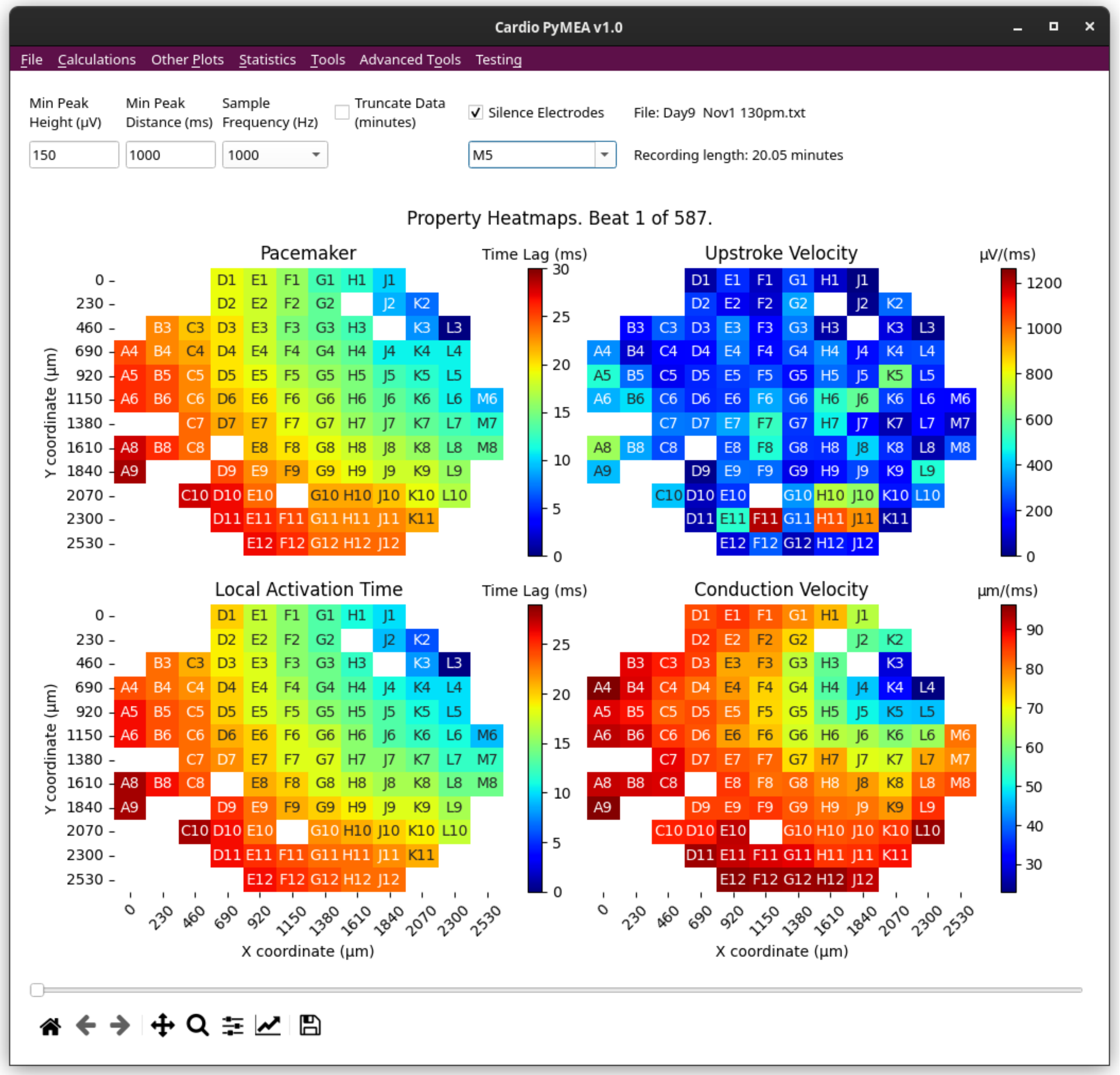

Min Peak Height (µV): 150

Min Peak Distance (ms): 1000

Sample Frequency (Hz): 1000

☐ Truncate Data (minutes)

☑ Silence Electrodes: M5

File: Day9 Nov1 130pm.txt

Recording length: 20.05 minutes

Fig 1. Main window of Cardio PyMEA graphical user interface. All of the user's interactions with Cardio PyMEA stem from this window. The user can utilize the various drop-down menu options to import data, perform calculations, and perform statistical analysis.

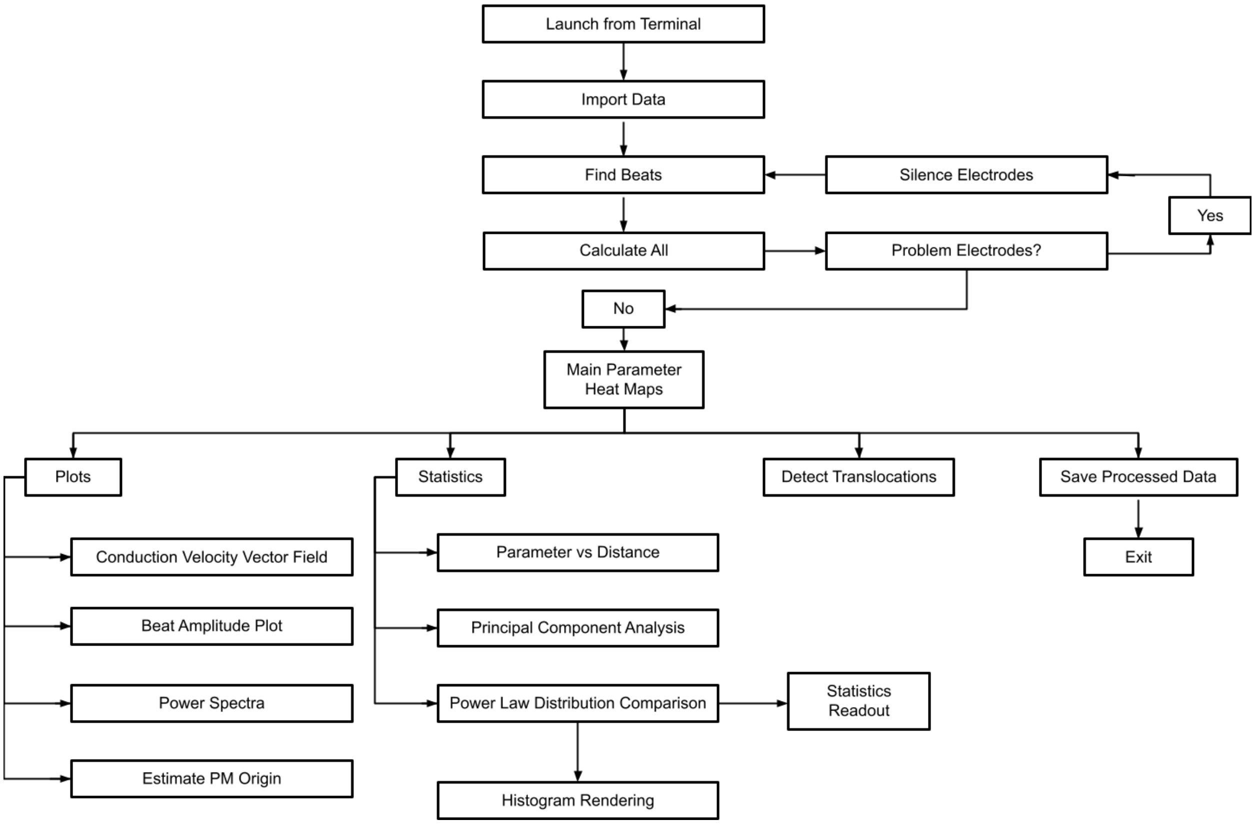

Fig 2. Operational flowchart for using Cardio PyMEA. This flowchart illustrates how Cardio PyMEA can be operated in order to analyze cardiomyocyte MEA data.

Input data format and geometric configuration of MEAs

Cardio PyMEA was designed to utilize data obtained from Multichannel Systems' MC_Rack MEA recording software and the MC_Data conversion tool. The *.mcd files produced by MC_Rack must be converted to ASCII (*.txt) files using MC_Data. Cardio PyMEA expects that the resulting *.txt file should be organized column-wise, beginning with the time, t, in milliseconds (or fractions of milliseconds for sample frequencies > 1KHz), followed by electrode names with their measured voltages (in microvolts). For example, when using a 120 electrode MEA recording with a sample frequency of 1000 Hz, the first column of the *.txt data file is expected to correspond to the time, t, in milliseconds. The second is expected to correspond to the electrode F7. This electrode is designated as channel 1 (electrode 1) in the manufacturer's MEA channel schematic. Each subsequent electrode is expected to adhere to this schematic. As a result, Cardio PyMEA expects that the *.mcd to *.txt conversion proceeds with 'All' electrodes selected in the conversion wizard window.

Cardio PyMEA's design allows for the relatively easy expansion of other MEA geometries due to its object-oriented nature. The ElectrodeConfig class (a template for creating an object; in this case, an electrode configuration variable) houses information for the MEA configurations that a researcher may choose to employ. Currently, Cardio PyMEA recognizes both 60 and 120 electrode MEAs from Multichannel Systems with 30 μm diameters and 200 μm interelectrode spacings. Other configurations can be added in a straightforward manner by creating new class attributes (a variable that belongs to the class) for the other systems in the ElectrodeConfig class.

All MEA data used in Cardio PyMEA requires geometric coordinates and labeling for the electrodes in the array. The schematic used in Cardio PyMEA arbitrarily positions the coordinate map origin (i.e. the coordinate (0, 0)) in the top-left corner of the array. A schematic illustrating the expected geometries is shown in Fig 3. Electrode coordinates are assigned manually to each electrode and are housed in a Python dictionary for each respective MEA configuration (i.e. each ElectrodeConfig attribute).

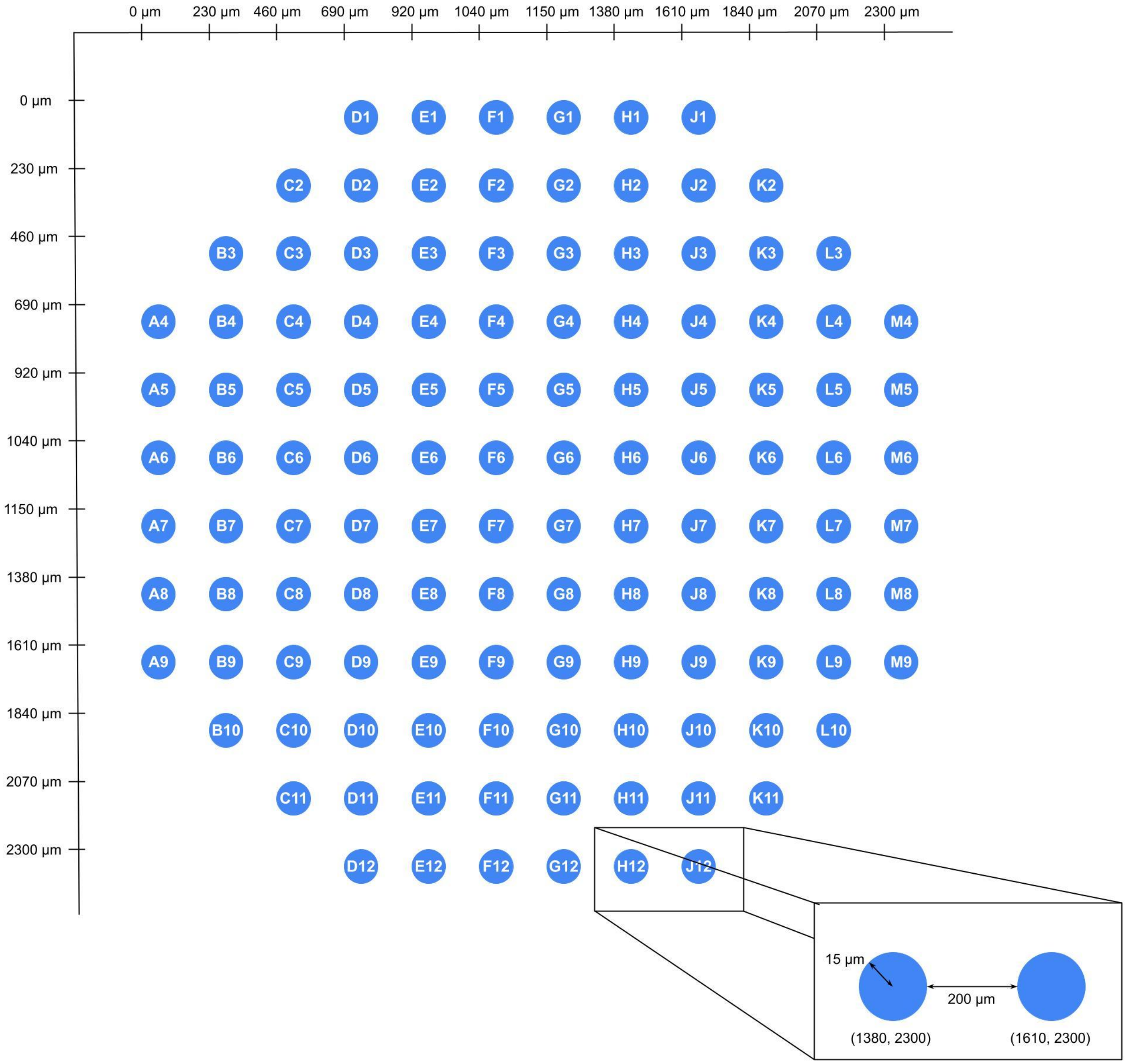

Fig 3. Representative schematic of the geometric configuration used for a 120 electrode MEA. This coordinate system shown here was devised using an interelectrode spacing of 200 µm and electrode diameter of 30 µm.

Cardio PyMEA calculation methods and functions

One of the strengths of Cardio PyMEA is that it houses a wide variety of calculations used in the analysis of cardiomyocyte MEA data. These functions and calculations include: automated electrode exclusion algorithm, manual electrode silencing, pacemaker, LAT, dV/dt_{max}, CV, field potential duration (FPD), beat amplitude, beat interval, and pacemaker translocations (instances in which the spatial configuration of the pacemaker region becomes unstable and translocates, or moves, to another area of the MEA over time). A complete description and representative example of each calculation output follows.

Beat detection

Cardiomyocyte beats, identified in MEAs as the most prominent peak of the field potential, are calculated by Cardio PyMEA using the `findpeaks` function contained in the SciPy library. First, users enter their designed peak height (minimum signal amplitude, in microvolts) and peak distance (minimum separation between peaks, in milliseconds) into the appropriate fields in the GUI. Alternatively, users may proceed using the default parameters. Next, beat detection can be performed by selecting 'Calculations' from Cardio PyMEA's menu bar and choosing 'Find Beats'. This action opens the 'Find Beats Results' window, shown in Fig 4. The user can next choose whether to filter the signal using low-pass, high-pass, or bandpass Butterworth filters, or use the raw (unfiltered) signal. Finally, the user clicks the 'Find Beats' button, which begins the calculation using the given parameters. Two plots are subsequently generated to show the MEA's signal trace of voltage (μV) vs time (ms). The left-side plot shows a single beat for a single electrode. This view can be adjusted by using sliders marked with 'Beat' and 'Electrode', respectively. The right-side plot shows a condensed view of field potentials for all electrodes at the selected beat. These plots can be further manipulated using the provided navigation toolbar. Finally, these plots can be saved as *.png files by clicking the ‘Save’ (disk) icon in the navigation toolbar.

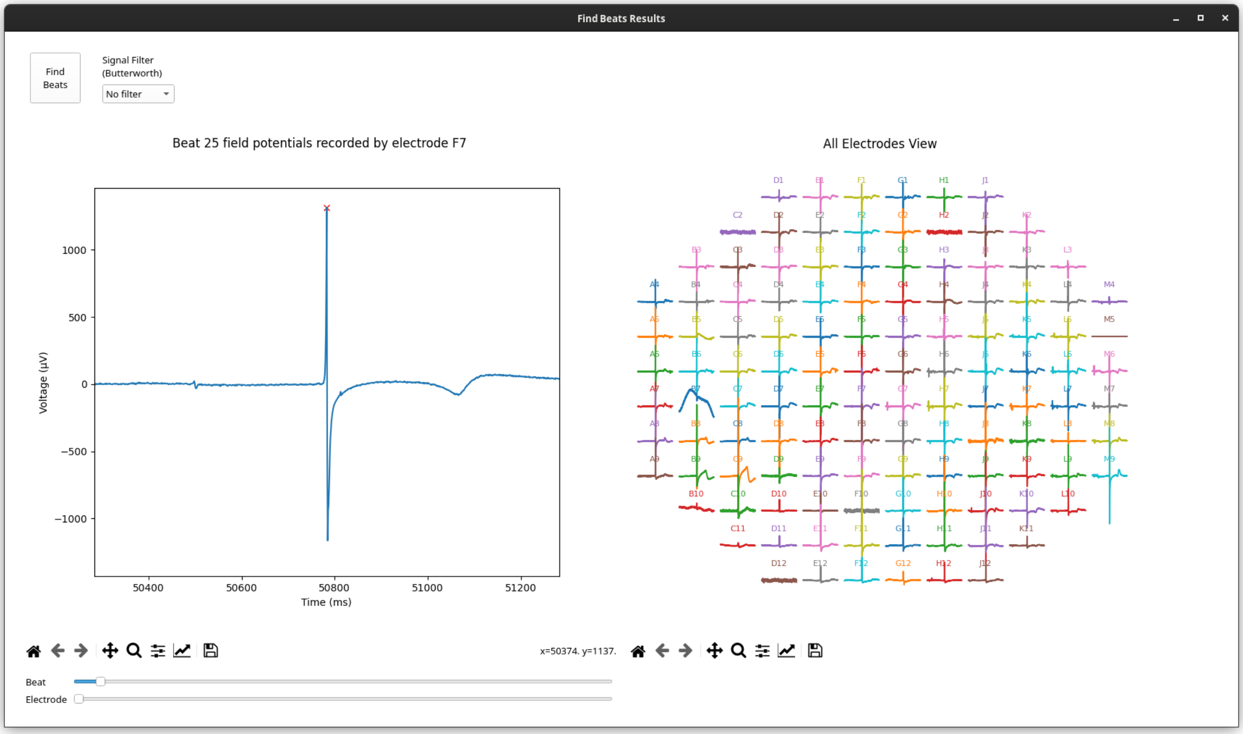
Signal Filter (Butterworth): No filter

Fig 4. ‘Find Beats Results’ window. The left plot shows an individual beat for the electrode specified by the window slider. The sliders below the plot control which beat and/or electrode is plotted. The right plot shows the full MEA for a specified beat and is controlled by the same ‘Beat’ slider as the left plot.

Automated electrode exclusion

Electrodes with an atypical beat count, as measured in comparison to other electrodes, may negatively affect the calculations performed by Cardio PyMEA (e.g. by producing vectors and matrices of different dimensions, requiring interpolation or other data pre-processing to resolve). To rectify this, Cardio PyMEA utilizes an automated electrode exclusion process. After determining the number of beats in a data set using the beat detection algorithm described previously, Cardio PyMEA calculates the beat count mode across the data set for each electrode. Following this calculation, Cardio PyMEA automatically excludes those electrodes whose beat counts vary from the beat count mode.

Manual electrode silencing

It is possible for electrodes to pass the automated electrode exclusion process yet still exhibit unusual signal characteristics, e.g. inverted field potential peaks. These problematic electrodes can be seen qualitatively in either the ‘Find Beats Results’ plots or in property heatmaps, where they contradict the behavior of their neighbors during certain beats. Electrodes demonstrating atypical or erratic behavior (e.g. abnormally high time lag values) can be manually silenced by selecting the check-box labeled ‘Silence Electrodes’ in the top right corner of the main window. Once checked, the user can choose which electrode(s) to silence from the drop-down menu. After choosing which electrodes to silence, ‘Find Beats’ must be executed again to complete the exclusion. Once this operation is performed, data from the manually excluded electrodes will no longer be included for analysis. Electrode exclusion can be reversed by simply de-selecting the silenced electrode(s) and executing ‘Find Beats’ again.

Time lag (pacemaker) calculation and origin estimation

For each electrode in the MEA, Cardio PyMEA records the time at which the field potential peak of an individual beat is detected. Cardio PyMEA then compares these values to determine the point of origin of the pacemaker signal. The lowest time value (i.e. earliest electrode to detect a signal during a beat) is determined to correspond to the pacemaker region. To normalize the data, Cardio PyMEA subtracts the field potential peak time recorded across all other electrodes from the earliest time recorded at the pacemaker, as shown in Fig 5A. This means that the pacemaker electrode is the one with the lowest time lag value, and in the normalized data, corresponds to the electrode with a time lag value of 0 ms. This method is repeated for each beat and yields the time lag (pacemaker) value: the time elapsed between the earliest signal detected and the time signal is detected at another electrode in the array. Cardio PyMEA uses the normalized time lags to render a color-coded heat map which is spatially defined by the geometry of the MEA. Electrodes colored dark blue indicate the location of the pacemaker (minimum time lag), while dark red indicates electrodes with the highest time lag farthest from the pacemaker (maximum time lag).

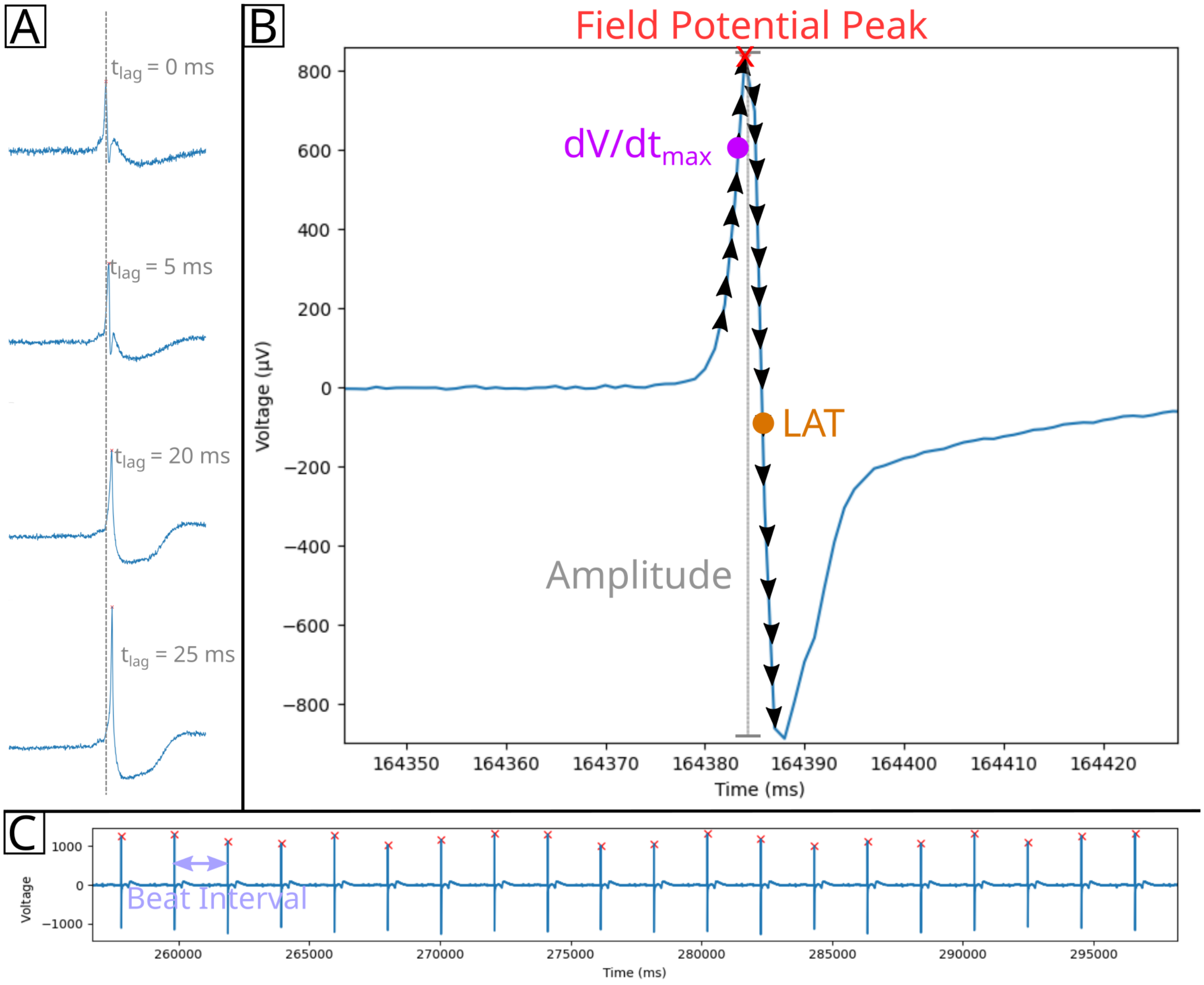

Fig 5. Diagram of cardiomyocyte field potential property calculations. A) Time lag (t_{lag}, pacemaker) calculation. The field potential peak for each electrode is calculated, then the peak with the minimum time is normalized to 0 ms. This process is applied to all electrodes to yield normalized time lag values for the given beat. B) Amplitude (gray vertical line), dV/dt_{max}, and LAT can be calculated from the field potential signal. Black arrows indicate derivative calculations along points prior to or after the field potential peak (red x). The maximum positive (dV/dt_{max}, magenta circle) and negative (LAT, orange circle) derivatives are identified and used in calculating dV/dt_{max} and LAT,

respectively. C) Beat intervals are calculated by determining the time between field potential peaks.

To access this operation, select ‘Calculations’ → ‘Pacemaker’ from the main window menu bar. A new window will open that displays the pacemaker heat map for the first beat detected in the data set. The x and y axes provide the 2D coordinates of each electrode. The slider at the bottom of the window is used to toggle between heat maps for all beats detected in the given data set.

The coordinates of the pacemaker origin can also be estimated by Cardio PyMEA. First, the estimation employs a contour plot to determine the wave front of the pacemaker data. The process is designed to favor the contour line that contains the most data points for model fitting. Next, Cardio PyMEA uses nonlinear least squares to estimate the coordinates of the center (h, k) and the radius (r) for a circle defined by the equation

$$r = sqrt[(x - h)^2 + (y - k)^2]$$

The radius parameter, r, is bound within the geometry of the MEA during the fitting process. This measure is taken to ensure that the center of the circle, (h, k), does not reside outside of the culture region of the MEA. Ultimately, the calculated coordinate (h, k) represents the estimated location of the pacemaker origin.

To access this operation, select ‘Other Plots’ → ‘Estimated Pacemaker Origin’ from the main window menu bar. A new window will open that depicts a contour map. This contour map indicates the estimated origin of the pacemaker for a single beat. The slider at the bottom of the window can be used to change which beat is displayed. The orange dot at the center of the rendered circle denotes the estimated origin of the pacemaker signal, while the blue dots at the edge of the circle represent the values from the wave front that were used during fitting.

Local activation time calculation

The LAT is calculated by finding the maximal negative intrinsicoid deflection (the maximum negative derivative (-dV/dt) to the right of the field potential peak in a given beat). For every electrode, Cardio PyMEA calculates the derivative (slope) of the field potential signal, beginning from the peak and moving to the right, for each beat in the data set, as shown in Fig 5B. These calculated LAT values are normalized in a similar manner to the time lag values for the pacemaker calculations. Using the calculated LATs, Cardio PyMEA renders a heatmap for qualitative data analysis.

To access this operation, select ‘Calculations’ → ‘Local Activation Time’ from the main window menu bar. A new window will open that displays the LAT heatmap. This heat map uses a color scheme that is identical to the pacemaker heat map: dark blue indicates the minimum, normalized LAT, while dark red indicates the maximum, normalized LAT in the full recording. The x and y coordinates represent the position of the specified electrode in the MEA system. The slider at the bottom of the window can be used to change which beat is displayed.

Maximum upstroke velocity calculation

The maximum upstroke velocity (dV/dt_{max}) refers to the maximum slope to the left of the field potential peak, as shown in Fig 5B. Cardio PyMEA calculates the derivative, using a backward finite difference method, of the time series data to the left of the field potential peak (i.e. preceding the peak) for each electrode and each beat. Finally, Cardio PyMEA normalizes the heatmap color gradient to the observed global minimum and maximum dV/dt_{max} values.

To access this operation, select ‘Calculations’ → ‘Upstroke Velocity’ from the main window menu bar. A new window will open that displays a heat map for the dV/dt_{max} data of each electrode for the specified beat. The legend to the right describes the color coding: dark blue corresponds to the observed minimum, while dark red corresponds to the observed maximum. The slider along the bottom enables users to toggle between data for each individual beat.

Beat amplitude and beat interval calculations

Beat amplitude refers to the voltage magnitude of the primary peak (R-wave-like peak) of the field potential for a detected beat. Because these potentials encompass both positive and negative peaks, the beat amplitude calculation in Cardio PyMEA identifies both the positive and negative field potential signals at the location of the R-wave-like peak when determining the overall magnitude of the beat [19]. This is indicated in Fig 5B. The beat interval is calculated by identifying the time that Beat A occurred and subtracting that value from the time that Beat B occurred. This difference reflects the interval between the beats and is shown in Fig 5C. Beat intervals are calculated this way for all beats in the recording. Cardio PyMEA uses data from the LAT calculation to compute these differences and generate beat intervals.

Conduction velocity calculation

Conduction velocity is defined as the speed and direction of the propagation of an electrochemical signal or impulse along a pathway in a network of cells. Conduction velocity is calculated in a straightforward manner by determining the distance between any two electrodes and dividing this distance by the change in local activation time (ΔLAT) recorded at the electrodes, i.e.: (electrode distance)/ΔLAT. This is Cardio PyMEA's default CV calculation method for 2 reasons: 1) it is a simple, computationally efficient calculation and 2) the precise geometry of the MEAs provides a uniform map that ensures consistent, reasonable results across cultures. This method is similar to one used in a previous study [13].

Field potential duration calculation

Cardio PyMEA uses previously described methods to calculate the FPD [28]. Here, the R-wave is analogous to the field potential peak and the T-wave endpoint is determined using the method from Vázquez-Seisdedos et al [28]. A brief summary of this method follows. First, the T-wave is identified using a peak finding algorithm akin to the R-wave. Second, the maximum first derivative of the field potential signal between the T-wave peak and baseline is identified. Using the location (i.e. time or x-value) of the maximum derivative as a fixed point, along with an arbitrary location 50-200 ms past the T-wave peak, the algorithm fits a trapezoid with a mobile point to the two fixed points. Optimizing the maximum area of the trapezoid yields the T-wave endpoint [28]. The length of time (in milliseconds) between the R-wave and T-wave endpoint constitutes the FPD. In addition to calculating the FPD, Cardio PyMEA will generate a plot that can be cycled through each beat and each electrode using the slider at the bottom of the window. This window also facilitates visual confirmation of the T-wave endpoint in the user's data.

Pacemaker translocation detection algorithm

Pacemaker translocations were identified through monitoring the movement of the pacemaker region across subsequent beats. Provided that this movement (translocation) exceeds a distance threshold (500 µm), a timer is engaged to count the number of beats, along with the time interval, that the pacemaker region is stable in the new location. This period of stability is referred to as a “quiescent period” (i.e. the pacemaker is stable, or tranquil, and does not move during this time). If the location of the pacemaker region changes again in a manner that exceeds the distance threshold, the timer is stopped, the quiescent period (in beats and recording time) is stored in a list, and the timer is reset for the new position. The process repeats for each detected pacemaker region of each beat over the full MEA recording. Once the calculation concludes, the first recorded quiescent period is excluded from the list. This is done to remove potential artifacts induced by the uncertainty surrounding the true duration of the quiescent period of the pacemaker region. Similarly, the end of the recording does not contribute to a translocation (“event”) designation or quiescent period. The algorithm was verified manually through visual inspection and computationally in Python in order to ensure agreement of results.

Statistical analyses unique to Cardio PyMEA

Statistical analysis of cardiomyocyte culture data can take a variety of forms. Cardio PyMEA output data can be saved as a spreadsheet file (*.xlsx format) via the save data function (described in an upcoming section) for further analysis by the user. Additionally, Cardio PyMEA provides two types of statistical assessment that are unique to the software in the realm of cardiomyocyte analysis: 1) analysis of property-distance relationships and 2) analysis of power law behavior in pacemaker translocations.

Property-distance relationship analysis

Property-distance relationships (also referred to here as ‘Property vs Distance’) can be evaluated to assess whether pacemaker time lag, LAT, upstroke velocity, and/or CV exhibit correlations with the distance from the estimated pacemaker origin. The user can perform a simple elimination of outliers by designating a number of standard deviations (‘Sigma’) from the mean. Any values outside of the range specified by the (number of standard deviations * Sigma) operation are excluded from the analysis.

To access this operation, select ‘Statistics’ → ‘Property vs Distance’. Using this function, plots for each property versus distance from the pacemaker region are produced. Either linear (pacemaker, LAT, dV/dt_{max}) or nonlinear (CV) regression is applied to obtain a goodness-of-fit metric, R^2. The top 10 R^2 values for each property, and their associated beats, are shown in a text box on the right side of the window.

Power law analysis and distribution comparisons

Power laws are heavy-tailed probability distributions of the form $P(X) \propto x^{-\alpha}$. Demonstration of power law relationships between measurable properties in the system of interest, along with the calculated value of the power law exponent, α, can provide unique information regarding the underlying properties of a complex system. These properties may include scale-free dynamics, fractal geometries, and long-range spatiotemporal correlations, among others [29-31]. The analysis of power laws is particularly important in the study of cardiac systems because power law exponents could also provide diagnostic value. Previous studies in patients with myocardial infarction, coronary heart disease, and heart transplants showed that the value of α

measured for heart rate variability (small variations in the beat interval between heart beats) differed significantly from healthy patients [32-36]. Therefore, analysis of power laws in cardiomyocyte cultures could provide unique and invaluable insight into the underlying culture conditions and system dynamics.

Power law analysis in Cardio PyMEA relies upon several functions contained within the powerlaw Python library [37]. Cardio PyMEA uses the `distribution_compare` method from powerlaw (with the normalized_ratio parameter set to True) to compare how well a given data set adheres to other, similarly heavy-tailed, probability distributions [37]. This method calculates the log-likelihood ratios (LLRs) and p-values in order to compare distributions and determine the significance of the results. If the LLR is positive, then the first distribution (power law) is the best fit; if the LLR is negative, then the second distribution tested is a better fit. This allows users to determine if the data robustly demonstrate power law behavior, or if another, similarly heavy-tailed distribution serves as a superior descriptor of the data.

Cardio PyMEA also provides a qualitative assessment of the data, rendering a histogram superimposed with probability distribution curves fit to the entered data (default: power law, log-normal, stretched exponential). The user can specify the number of bins used in the histogram or rely upon automated methods (e.g. Sturges' Rule) to determine the number of bins for them [38]. To access these functions, users first must detect any translocations in the data set using 'Tools' → 'Detect Translocations' and then select 'Statistics' → 'Power Law Distribution Comparison' from the menu bar. Subsequently, a new window will open that displays qualitative plots and quantitative evaluations for power law, exponential, log-normal, Weibull, and doubly truncated power law probability distributions.

Saving data

Cardio PyMEA allows the user to save their processed data for each calculated parameter set. These data include values for: pacemaker, LAT, dV/dt_{max}, CV, beat amplitude, beat interval, and property vs distance statistics. The save function writes the data to a single, multi-tab spreadsheet (*.xlsx) file. The file can be opened in FOSS spreadsheet software, e.g. LibreOffice Calc, or through licensed software, e.g. Microsoft Excel. To access this operation, select 'File' → 'Save Processed Data' from the main window's menu bar. The file name can be inputted and saved to the user's chosen directory.

Batch analysis

Cardio PyMEA affords batch processing of pacemaker translocation data to simplify power law analysis for large numbers of MEA recordings. The user simply needs to add their file information to the batch file spreadsheet (included in the repository). Once the batch file is ready, the user will navigate to 'File' → 'Batch' and select their spreadsheet (*.xlsx) batch file. At that point, Cardio PyMEA will detect and compile pacemaker translocations for all files in the batch. Power law analysis can then be performed using the batched data, which Cardio PyMEA will recognize and require no additional work on the part of the user.

Results and discussion

Cardio PyMEA grants users flexibility via parameter control during cardiomyocyte analysis

Cardio PyMEA was tested using 30 MEA recordings across 3 distinct differentiations. Cardiomyocytes demonstrated good adhesion to the MEAs (Figs 6A and 6B). The beat detection algorithm was successful in identifying beats from the field potential signals without the need for signal filtering (Fig 6C). The beat detection algorithm was validated manually for each MEA and performed well under varying levels of noise, as shown in Figs 6D-F. Faulty electrodes, whether due to cell culture conditions (e.g. non-uniform spread of the culture), heterogeneous Matrigel application causing depressed local signal detection, or electrode degradation as a result of prolonged MEA usage, were excluded by the automated electrode exclusion algorithm. The excluded electrodes were deemed appropriate upon manual review, thus validating the algorithmic choices. The remaining electrodes demonstrated sufficient signal for all subsequent analyses. Successful cultures typically had only a few electrodes excluded from the analysis. The average beat rate (beats per minute, bpm) across all datasets was 36.64 bpm with a standard deviation of 14.48 bpm.

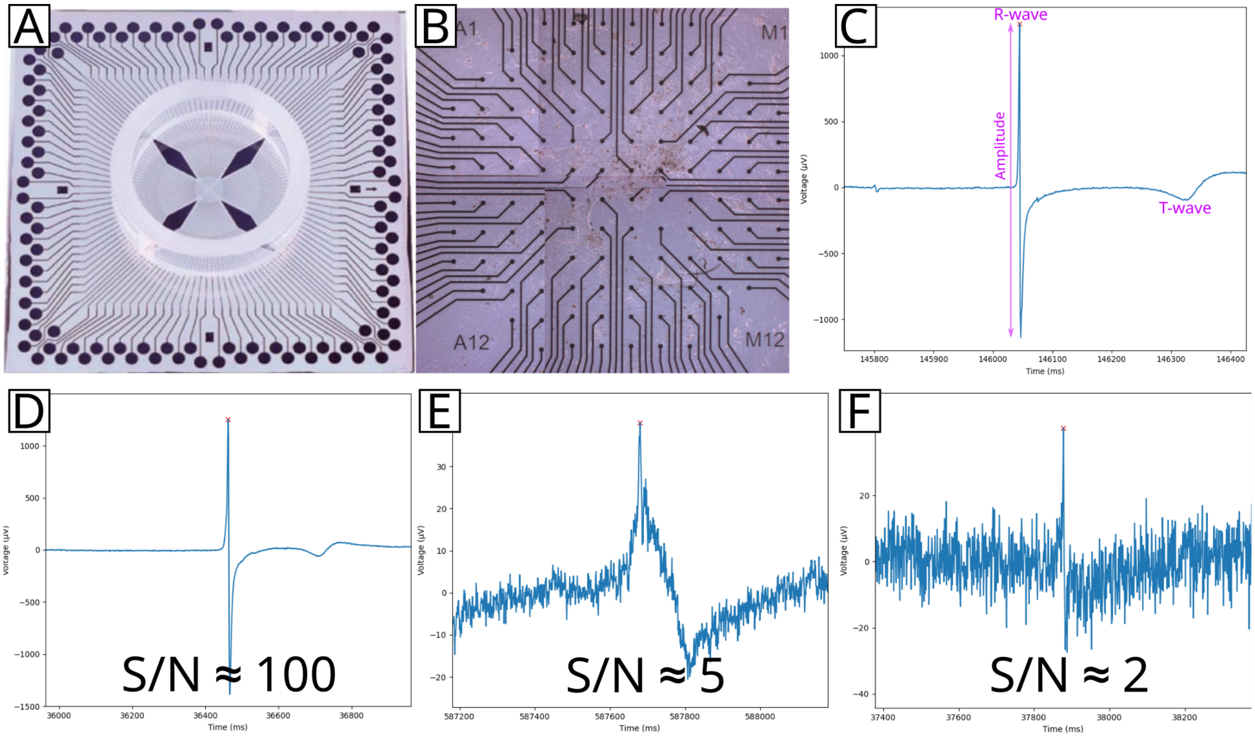

Fig 6. Beat detection results for an MEA-plated cardiomyocyte culture. An individual 120 electrode MEA (A) was plated with cardiomyocytes (B). Field potentials were recorded (C) and analyzed to determine the R-wave-like peak, beat amplitude, T-wave endpoint, and other features. These field potentials showed varying levels of noise, ranging from clean (D) to moderately (E) or significantly (F) noisy, as indicated by the decreasing signal-to-noise (S/N) ratios. Beat detection was performed for all field potentials across all MEAs.

Cardio PyMEA demonstrated effective performance under noisy conditions thanks to its utilization of user-provided parameter inputs. User-defined thresholds of beat amplitude and distance provide flexibility in analyzing noisy datasets, even under low signal-to-noise (S/N) conditions (Figs 6E-F). Successful beat detection enables the analysis of a variety of cardiomyocyte culture properties, including: pacemaker time lag, LAT, upstroke velocity, CV, FPD, and beat amplitude and interval. Local activation time, which is associated with the time of maximum sodium conductance in the myocardium, is a requisite property for analyzing cardiac conduction velocity and serves as another metric for assessing pacemaker activity. The maximum decrease in field potential voltage is generally accepted as the activation time for a beat [39]. Maximum upstroke velocity is associated with the peak influx of sodium and calcium ions during the action potential and presents another property useful for evaluating cardiomyocyte maturity [40]. Finally, beat amplitude and interval are widely known to serve as indicators of cardiomyocyte maturity.

Cardio PyMEA provides effective calculation and estimation of pacemaker regions in 2D cardiomyocyte cultures

Cardio PyMEA successfully generated per-beat, spatial heatmaps of time lag (pacemaker) activity across the MEA culture, as shown in Figs 7A-C. Pacemaker heatmaps were evaluated across dozens of beats and multiple MEAs. Subsequent analysis of the time lag wave front propagation using the pacemaker origin estimation tool revealed the most likely signal origin for the given data (Figs 7D-F). Identification of the pacemaker region in the culture could have practical implications for MEA stimulation experiments, e.g. by providing information regarding which electrode(s) to use for stimulation of a spatially-constrained system [41]. These results demonstrate Cardio PyMEA's ability to produce spatially defined heatmaps of pacemaker activity and determine a logical point-of-origin for the active pacemaker region within the culture.

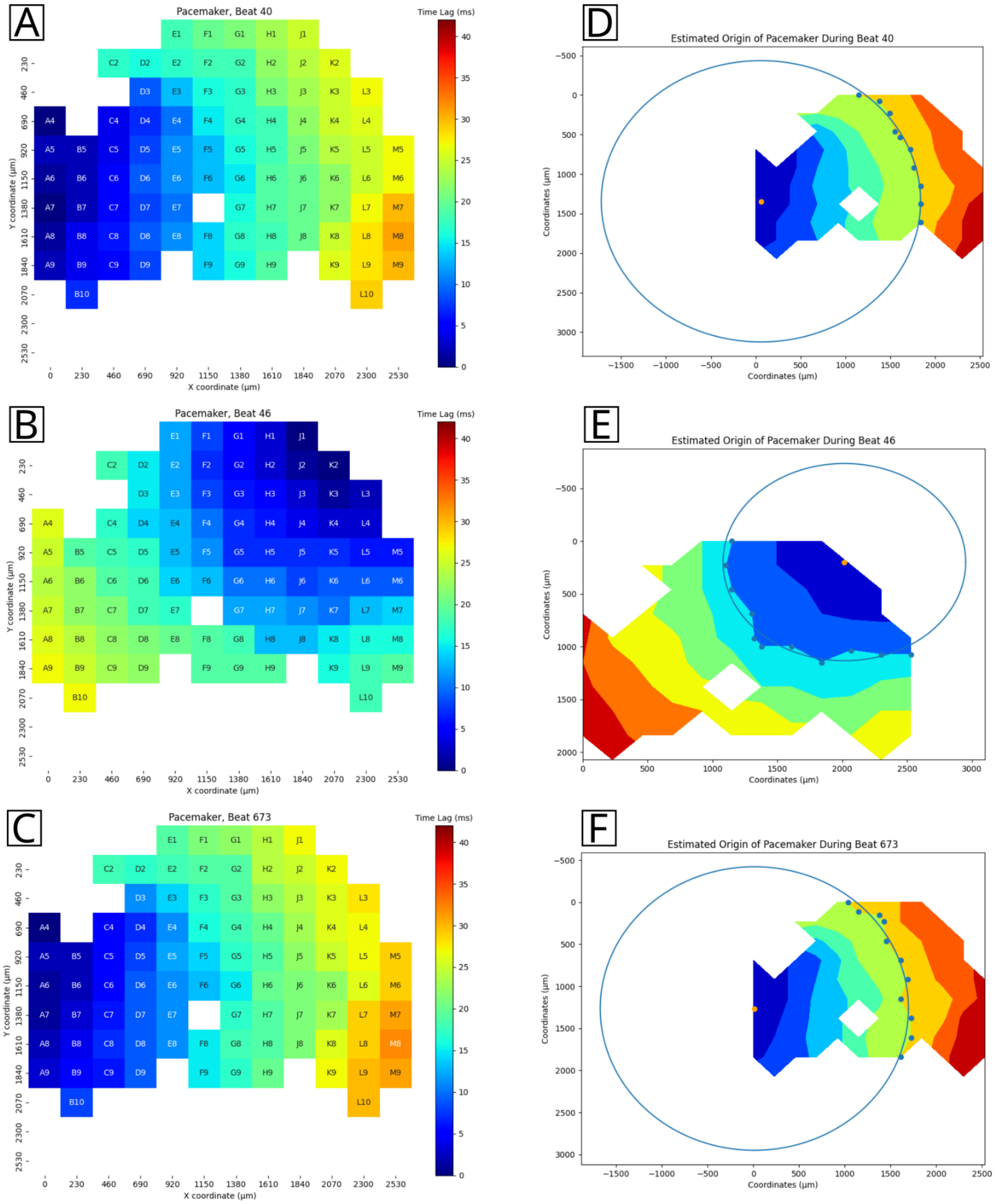

Fig 7. Pacemaker analysis output. A-C: representative pacemaker heatmap, spatially defined by the MEA coordinate system. D-F: estimated pacemaker location for the given

data based on the time lag propagation wavefront. The estimated origin is indicated by an orange dot.

Cardio PyMEA provides unique statistical tools for assessing cardiomyocyte maturation

During natural heart formation in the early embryo, all cardiomyocytes develop autonomic contraction and possess pacemaker characteristics. During the mid-gestational stages, working myocardium diversifies and acquires characteristic phenotypes including decreased automaticity, higher CV, and higher contractility [42]. If the stem cell-derived cardiogenesis recapitulates embryonic heart formation, one could hypothesize that cells distant from the pacemaking cells on an MEA present an increase in CV and field potential magnitude. To investigate this possible distance dependency of cardiomyocyte properties, Cardio PyMEA provides a unique function to analyze changes in property values with distance (i.e. property-distance relationships). Several plots were constructed tracking the correlations between a) pacemaker time lag, b) LAT, c) dV/dt_{max}, and d) CV and distance from the pacemaker region, both on a per-beat basis and averaged across all beats in the dataset. An example output is provided in Fig 8 and yields a mean $R^2 = 0.898$ for conduction velocity versus distance, suggesting that a relationship exists, based on good fitting between these two properties, for the given cardiomyocyte culture. These data suggest that the electrophysiological activity of *in vitro* stem cell-derived cardiomyocyte cultures may reflect early events during the lineage diversification and maturation of cardiac conduction system and working myocardium.

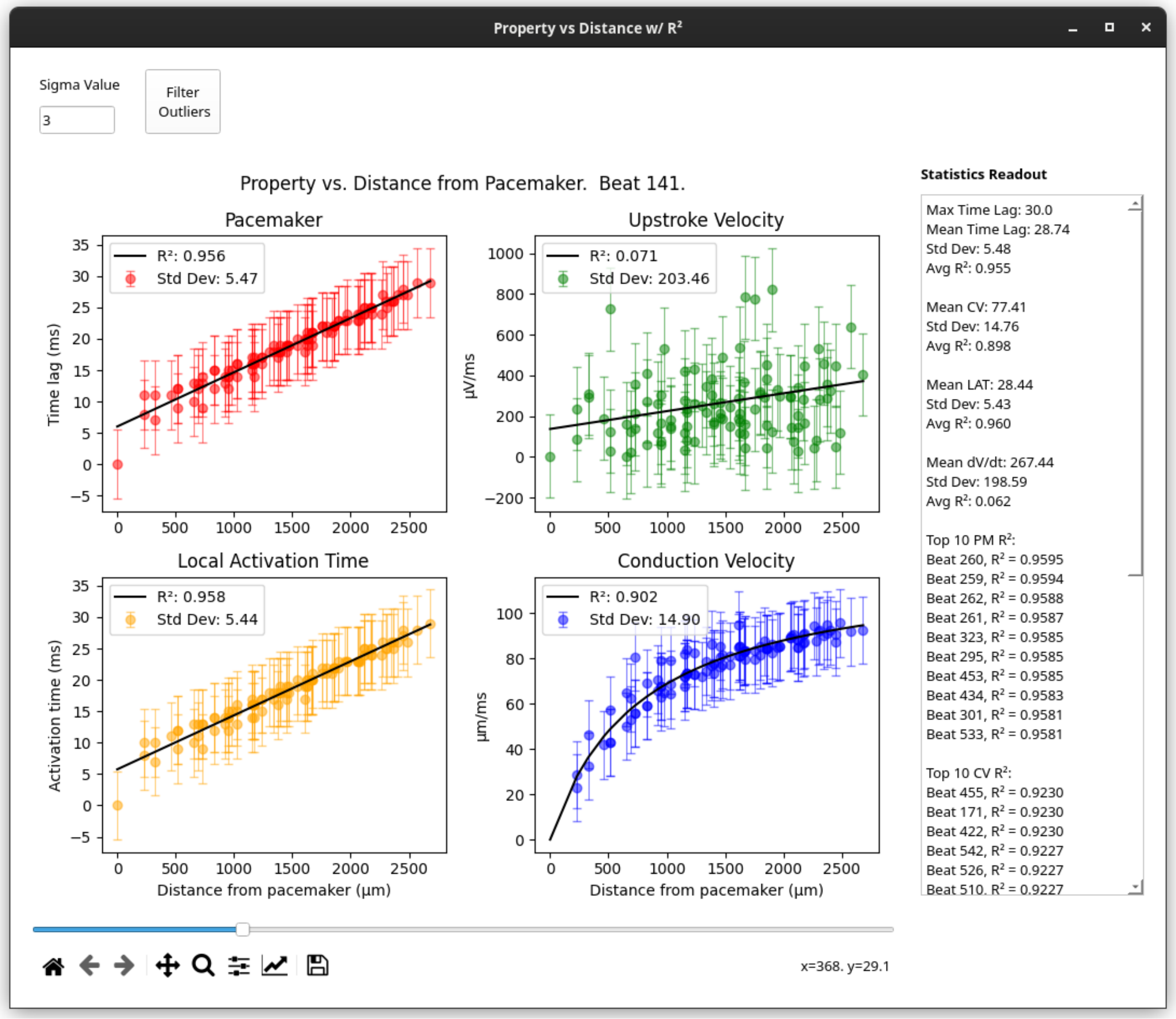

Sigma Value: 3

```
Max Time Lag: 30.0
Mean Time Lag: 28.74
Std Dev: 5.48
Avg R²: 0.955

Mean CV: 77.41
Std Dev: 14.76
Avg R²: 0.898

Mean LAT: 28.44
Std Dev: 5.43
Avg R²: 0.960

Mean dV/dt: 267.44
Std Dev: 198.59
Avg R²: 0.062

Top 10 PM R²:
Beat 260, R² = 0.9595
Beat 259, R² = 0.9594
Beat 262, R² = 0.9588
Beat 261, R² = 0.9587
Beat 323, R² = 0.9585
Beat 295, R² = 0.9585
Beat 453, R² = 0.9585
Beat 434, R² = 0.9583
Beat 301, R² = 0.9581
Beat 533, R² = 0.9581

Top 10 CV R²:
Beat 455, R² = 0.9230
Beat 171, R² = 0.9230
Beat 422, R² = 0.9230
Beat 542, R² = 0.9227
Beat 526, R² = 0.9227
Beat 510, R² = 0.9227
```

Fig 8. 'Property vs Distance with R^2' window. Representative plots of each property versus distance from the pacemaker. Statistical quantities, such as average time lag and conduction velocity, as well as top R^2 values, are presented in the 'Statistics Readout' text box on the right side of the window.

Cardio PyMEA provides unique tools for and simplifies the analysis of pacemaker translocations for power law behavior

A unique feature provided by Cardio PyMEA is the ability to investigate the quiescent period between pacemaker translocations in two-dimensional cardiomyocyte cultures as a potential power law-obeying phenomenon. Here, Cardio PyMEA was used in combination with the powerlaw Python library to evaluate pacemaker translocations [25, 37]. The justifications for these comparisons were based on their conceptual similarity to neuronal avalanche inter-burst (also sometimes referred to as inter-event) intervals, or IBI [43-44].

Cardio PyMEA simplifies power law analysis of cardiomyocyte cultures by effectively wrapping a graphical user interface over the powerlaw Python library, allowing the user to easily select from several input parameters [37]. Furthermore, the user can choose to evaluate power law behavior at both the individual recording level and in large batches (e.g. 30 or more) of recordings. The software outputs not only graphical representations of the data, as shown in Fig 9, but also a quantitative summary (in a separate text box below the plot) of distribution parameters and log-likelihood ratio (LLR) comparisons between each heavy-tailed distribution considered.

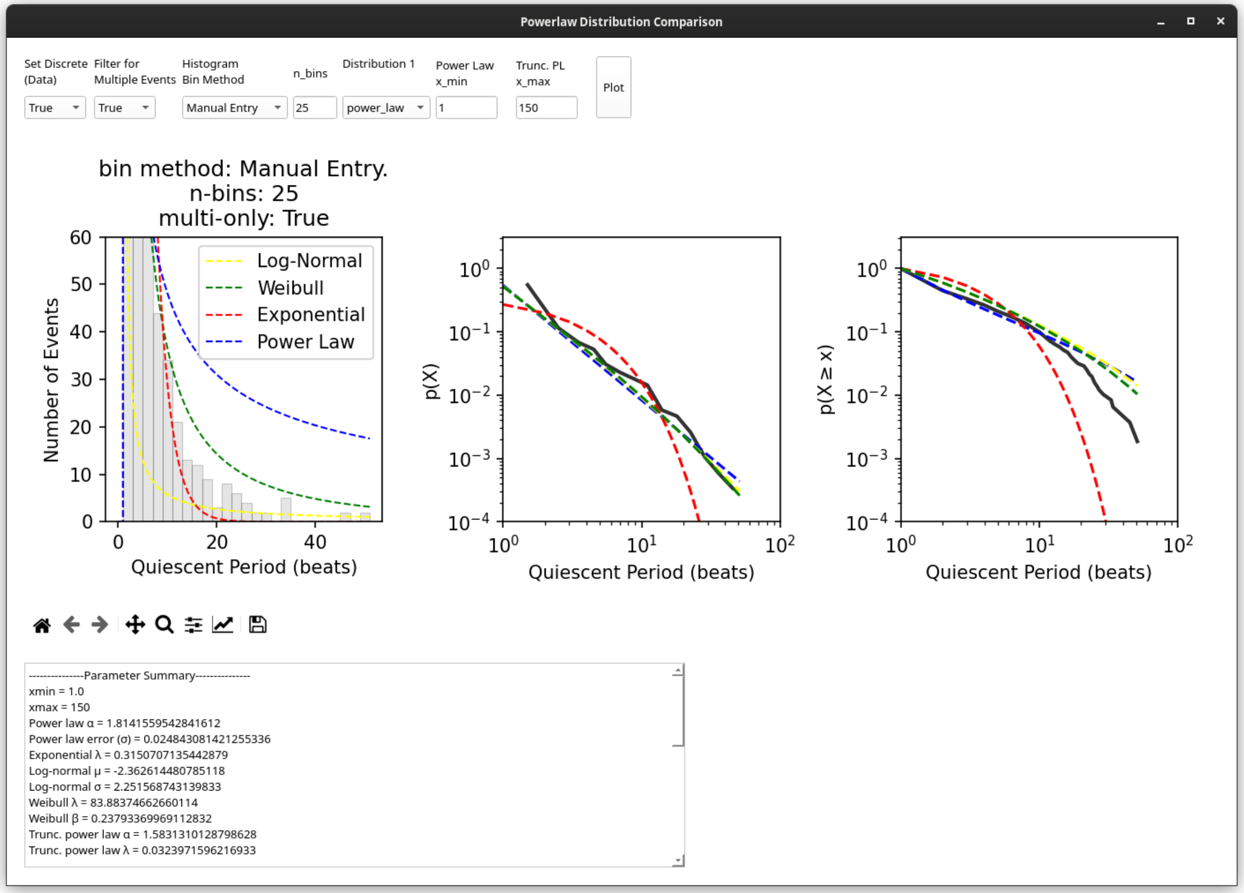

Powerlaw Distribution Comparison

Set Discrete (Data): True
Filter for Multiple Events: True
Histogram Bin Method: Manual Entry
n_bins: 25
Distribution 1: power_law
Power Law x_min: 1
Trunc. PL x_max: 150

```
---------------Parameter Summary---------------
xmin = 1.0
xmax = 150
Power law α = 1.8141559542841612
Power law error (σ) = 0.024843081421255336
Exponential λ = 0.3150707135442879
Log-normal μ = -2.362614480785118
Log-normal σ = 2.251568743139833
Weibull λ = 83.88374662660114
Weibull β = 0.23793369969112832
Trunc. power law α = 1.5831310128798628
Trunc. power law λ = 0.0323971596216933
```

Fig 9. 'Powerlaw Distribution Comparison' window. The results of power law analysis, both qualitative (plots) and quantitative (numerical output, text box below plots) are presented in this window of the application. The user can adjust a variety of parameters, as necessary, and execute their analysis by clicking 'Plot'. The power law plot was adapted from [25].

Using Cardio PyMEA's power law analysis integration and pacemaker translocation detection tool revealed that, while pacemaker translocations do not necessarily follow a general power law distribution, they do convincingly obey a doubly truncated power law distribution (i.e. a power law with an exponentially-defined maximum, or cutoff, value that captures finite-size effects within the system) with a power law exponent of $\alpha = -1.583$ [25]. Several known power law-obeying systems demonstrate a similar exponent of with ɑ = -1.5 and many are categorized as critical systems. Some suspected critical systems, e.g. neuronal cultures, exhibit optimal performance (e.g. maximized information exchange between individual units within the system) when the system is operating at or near a critical point [45-47]. The value for ɑ calculated from pacemaker translocations suggests that critical dynamics may play a role in maximizing information transfer between cardiomyocytes within the culture and facilitate the identification of an optimal pacemaker region of the culture [25]. Thus, Cardio PyMEA facilitates and greatly simplifies power law analysis of cardiomyocyte cultures in order to help elucidate potential mechanisms governing cardiomyocyte system dynamics. Furthermore, thanks to Cardio PyMEA's extensible design philosophy, it would be quite feasible to further adapt the software for power law analysis of other observable phenomena in cardiomyocyte networks. Such work could constitute a future development goal.

Cardio PyMEA helps democratize computational tools for cardiomyocyte analysis

A key aim underlying Cardio PyMEA's development was to provide both a free-to-use and free-to-edit computational tool for cardiomyocyte MEA analysis. Most, if not all, previously released, free-to-use cardiomyocyte MEA analysis applications are written in MATLAB. Although these programs can be distributed freely, any efforts to edit and execute the underlying source code require a MATLAB license. This presents a potentially high barrier-to-entry in the form of operational costs, particularly at the academic tier for smaller institutions, that can be burdensome for researchers [24].

Thus, it became clear that achieving the elimination of these barriers to accessibility and development would require writing Cardio PyMEA in Python.

Python is an established, mature, and robust programming language known for its accessibility to those new to computer programming and its ubiquity in data science and machine learning applications. It provides a minimal barrier to entry, requiring only a computer and an internet connection. Python enjoys widespread community support via online resources which provide abundant resources for fledgling and senior programmers alike [48].

Cardio PyMEA leverages the aforementioned characteristics of Python to provide a cardiomyocyte MEA analysis tool suitable for continued development and refinement. The software’s GUI was written using PyQt5 and adheres to a basic object-oriented programming paradigm that, with a modest background, is simple enough for a novice programmer to grasp and modify. In fact, Cardio PyMEA was designed in such a way that undergraduate students with no or modest programming experience could (and, in fact, did) successfully contribute new functionalities to the software. Therefore, Cardio PyMEA should prove suitable as an ongoing developmental platform and help to further democratize analytical tools for cardiomyocyte MEA data analysis.

Conclusion and outlook

Cardio PyMEA is an open-source software designed to facilitate the analysis of microelectrode array data obtained for cardiomyocyte cultures. It provides an easy-to-use graphical user interface to allow non-programmers to carry out analysis of MEA data and, because of its object oriented nature, can be readily modified to accommodate additional MEA geometries and configurations. Calculations for several cardiomyocyte properties were successfully executed using Cardio PyMEA, including time lag, local activation time, upstroke and conduction velocities, beat amplitude, and beat interval, among others. Cardio PyMEA is readily extensible and provides users with two built-in analytical techniques for the assessment of property-distance correlations and the observance of power laws in pacemaker translocations.

Choosing to write Cardio PyMEA in Python presented clear benefits in the form of open access, extensibility, and ease of use. However, there are some drawbacks inherent to this choice that merit a brief discussion. Among the more significant issues inherent to Python application development is the global interpreter lock (GIL). When executing a Python script or program, the interpreter occupies one – and only one – computational thread on the host machine's CPU. This causes the GUI's widgets (e.g. the file dialog box) to temporarily "freeze" during the execution of a function call, such as a calculation or plotting operation, until the operation has completed. As a consequence of this GIL, the user may experience some minor performance issues during the operation of the program in the form of windows freezing, accompanied by a request to wait for the program to complete its task. One way this issue could be remedied is through extensive revisions to the code to enact multithreaded operations – a non-trivial exercise, but one which may take place at a later date.

Another opportunity for improvement, in select cases, is input/output and calculation speed. Python is known to be a relatively slow programming language, particularly compared to C and C++. Loading files is one of the more time-intensive operations performed by Cardio PyMEA, particularly for *.txt files exceeding 500 megabytes in size. For example, on Linux kernel 5.16, the import operation for a file of size 1.9GB (e.g. a 20 minute long, 120 electrode MEA recording) can take ~45 seconds. Although our development was limited to *.txt file inputs as a result of MC_Data file outputs, it may be possible to incorporate a conversion tool into Cardio PyMEA that yields hierarchical data format HDF5 files for subsequent loading operations. Use of HDF5 input files has the potential to further improve data load times and partially alleviate data storage requirements [49].

Additionally, improvements to graphing performance may be possible by exchanging function calls to the Matplotlib and Seaborn plotting libraries for equivalents in PyQtGraph. PyQtGraph can demonstrate superior speed compared to the aforementioned libraries [50]. Many calculations in Cardio PyMEA were optimized through the use of libraries like NumPy and Numba, which utilize C-based operations, to perform similarly to analogous calculations in other, faster programming languages. Further optimization should be possible with additional development.

Beyond performance improvements, we expect to see Cardio PyMEA acquire new features and functionalities over time. One area that may be primed for expanded development is comparative analysis of MEAs. Implementation of comparative methods, in which two separate recording files are loaded and analyzed in parallel, may provide significant workflow improvements over the current paradigm. Ultimately, Cardio PyMEA's potential is bound only by the imagination of its contributors and evolution of the Python programming language.

References

1. Zhang W, Kong CW, Tong MH, Chooi WH, Huang N, Li RA, et al. Maturation of human embryonic stem cell-derived cardiomyocytes (hESC-CMs) in 3D collagen matrix: effects of niche cell supplementation and mechanical stimulation. Acta Biomater. 2017;49: 204-217. doi: 10.1016/j.actbio.2016.11.058
2. Cho S, Lee C, Skylar-Scott MA, Heilshorn SC, Wu JC. Reconstructing the heart using iPSCs: engineering strategies and applications. J Mol Cell Cardiol. 2021;157: 56-65. doi: 10.1016/j.yjmcc.2021.04.006
3. Cao F, Wagner RA, Wilson KD, Xie X, Fu J, Drukker M, et al. Transcriptional and functional profiling of human embryonic stem cell-derived cardiomyocytes. PLoS ONE. 2008;3(10): e3474. doi: 10.1371/journal.pone.0003474
4. Alcon A, Cagavi Bozkulak E, Qyang Y. Regenerating functional heart tissue for myocardial repair. Cell Mol Life Sci. 2012;69: 2635–2656. doi: 10.1007/s00018-012-0942-4.
5. Wang G, McCain ML, Yang L, He A, Pasqualini FS, Agarwal A, et al. Modeling the mitochondrial cardiomyopathy of Barth syndrome with induced pluripotent stem cell and heart-on-chip technologies. Nat Med. 2014;20: 616-623. doi: 10.1038/nm.3545.
6. Hinson JT, Chopra A, Lowe A, Sheng CC, Gupta RM, Kuppusamy R, et al. Integrative analysis of PRKAG2 cardiomyopathy iPS and microtissue models identifies AMPK as a regulator of metabolism, survival, and fibrosis. Cell Rep. 2016;17(12): 3292-3304. doi: 10.1016/j.celrep.2016.11.066
7. Scuderi GJ, Butcher J. Naturally Engineered Maturation of Cardiomyocytes. Cell Front Cell Dev Biol. 2017;5: 50. doi: 10.3389/fcell.2017.00050.
8. Karbassi E, Fenix A, Marchiano S, Muraoka N, Nakamura K, Yang X, et al. Cardiomyocyte maturation: advances in knowledge and implications for regenerative medicine. Nat Rev Cardiol. 2020;17: 341-359. doi: 10.1038/ s41569-019-0331-x.
9. Guo Y, Pu WT. Cardiomyocyte maturation: New phase in development. Circ Res. 2020;126: 1086-1106. doi: 10.1161/CIRCRESAHA.119.315862.
10. Ahmed RE, Anzai T, Chanthra N, Uosaki H. A brief review of current maturation methods for human induced pluripotent stem cells-derived cardiomyocytes. Front Cell Dev Biol. 2020;8: 178. doi: 10.3389/fcell.2020.00178.
11. Thomas D, Shenoy S, Sayed N. Building multi-dimensional induced pluripotent stem cells-based model platforms to assess cardiotoxicity in cancer therapies. Front Pharmacol. 2021;12: 607364. doi: 10.3389/fphar.2021.607364.
12. Jonsson MKB, Vos MA, Mirams GR, Duker G, Sartipy P, de Boer TP, et al. Application of human stem cell-derived cardiomyocytes in safety pharmacology requires caution beyond hERG. J Mol Cell Cardiol. 2012;52(5): 998-1008. doi: 10.1016/j.yjmcc.2012.02.002.
13. Zhu H, Scharnhorst KS, Stieg AZ, Gimzewski JK, Minami I, Nakatsuji N, et al. Two dimensional electrophysiological characterization of human pluripotent stem

cell-derived cardiomyocyte system. Sci Rep. 2017;7: 43210, doi: 10.1038/srep43210.

14. Hinson JT, Chopra A, Nafissi N, Polacheck WJ, Benson CG, Swist S, et al. Titin mutations in iPS cells define sarcomere insufficiency as a cause of dilated cardiomyopathy. Science. 2015;349(6251): 982-986. doi: 10.1126/science.aaa5458.
15. Lausten PG, Russell SJ, Cui L, Entingh-Pearsall A, Holzenberger M, Liao R, et al. Essential role of insulin and insulin-like growth factor 1 receptor signaling in cardiac development and function. Mol Cell Biol. 2007;27: 1649-1665. doi: 10.1128/MCB.01110-06.
16. Guo Y, VanDusen NJ, Zhang L, Gu W, Sethi I, Guatimosim S, et al. Analysis of cardiac myocyte maturation using CASAAV, a platform for rapid dissection of cardiac myocyte gene function *in vivo*. Circ Res. 2017;120: 1874-1888. doi: 10.1161/CIRCRESAHA.116.310283.
17. Pradhapan P, Kuusela J, Viik J, Aalto-Setälä K, Hyttinen J. Cardiomyocyte MEA Data Analysis (CardioMDA) – A Novel Field Potential Data Analysis Software for Pluripotent Stem Cell Derived Cardiomyocytes. PLoS ONE. 2013;8(9): e73637. doi: 10.1371/journal.pone.0073637
18. Georgiadis V, Stephanou A, Townsend PA, Jackson TR. MultiElec: A MATLAB Based Application for MEA Data Analysis. PLoS ONE. 2015;10(6): e0129389. doi: 10.1371/journal.pone.0129389
19. Hayes HB, Nicolini AM, Arrowood CA, Chvatal SA, Wolfson DW, Cho HC, et al. Novel method for action potential measurements from intact cardiac monolayers with multiwell microelectrode array technology. Sci Rep. 2019;9: 11893. doi: 10.1038/s41598-019-48174-5
20. Park JS, Grijalva SI, Jung D, Li S, Junek GV, Chi T, et al. Intracellular cardiomyocytes potential recording by planar electrode array and fibroblasts co-culturing on multi-modal CMOS chip. Biosens Bioelectron. 2019;144: 111626. doi: 10.1016/j.bios.2019.111626
21. Tomek J, Burton RAB, Bub G. Ccoffinn: Automated Wave Tracking in Cultured Cardiac Monolayers. Biophys J. 2016; 111(8): 1595-1599. doi: 10.1016/j.bpj.2016.08.049
22. O'Shea C, Holmes AP, Yu TY, Winter J, Wells SP, Correia J, et al. ElectroMap: High-throughput open-source software for analysis and mapping of cardiac electrophysiology. Sci Rep. 2019;9: 1389. doi: 10.1038/s41598-018-38263-2
23. What is MATLAB? [Internet]. Natick (MA): MathWorks (US); [reviewed 2022 Mar 2; cited 2022 Mar 2]. Available from: https://www.mathworks.com/discovery/what-is-matlab.html
24. Research evaluation needs to change with the times. Nature. 2022;601. doi: 10.1038/d41586-022-00056-z

25. Dunham CS, Mackenzie ME, Nakano H, Kim AR, Juda MB, Nakano A, et al. Pacemaker translocations and power laws in 2D stem cell-derived cardiomyocyte cultures. PLoS ONE. 2022;17(3): e0263976. doi: 10.1371/journal.pone.0263976
26. Minami I, Yamada K, Otsuji TG, Yamamoto T, Shen Y, Otsuka S, et al. A small molecule that promotes cardiac differentiation of human pluripotent stem cells under defined, cytokine- and xeno-free conditions. Cell Rep. 2012;2: 1448-1460. doi: 10.1016/j.celrep.2012.09.015.
27. Nakano H, Minami I, Braas D, Pappoe H, Wu X, Sagadevan A, et al. Glucose inhibits cardiac muscle maturation through nucleotide biosynthesis. eLife. 2017;6: e29330. doi: 10.7554/eLife.29330.
28. Vázquez-Seisdedos CR, Neto JE, Marañón Reyes EJ, Klautau A, Limão de Oliveira, RC. New approach for T-wave end detection on electrocardiogram: performance in noisy conditions. Biomed Eng Online. 2011;10: 77, doi: 10.1186/1475-925X-10-77
29. Stanley HE, Buldyrev SV, Goldberger AL, Havlin S, Peng C-K, Simmons M. Long-range power law correlations in condensed matter physics and biophysics. Physica A: Stat Mech Appl. 1993;200: 4-24. doi: 10.1016/0378-4371(93)90500-4
30. Stanley HE, Amaral LAN, Gopikrishnan P, Ivanov PC, Keitt TH, Plerou V. Scale invariance and universality: organizing principles in complex systems. Physica A: Stat Mech Appl. 2000;281: 60-68. doi: 10.1016/S0378-4371(00)00195-3
31. Gisiger, T. Scale invariance in biology: coincidence or footprint of a universal mechanism? Biol Rev. 2001;76: 161-209. doi: 10.1017/S1464793101005607
32. Bigger JT, Steinman RC, Rolnitzky LM, Fleiss JL, Albrecht P, Cohen RJ. Powerlaw behavior of RR-interval variability in healthy middle-aged persons, patients with recent acute myocardial infarction, and patients with heart transplants. Circulation. 1996;93: 2142–2151. pmid:8925583
33. Huikuri HV, Mäkikallio TH, Juhani Airaksinen KE, Seppänen T, Puukka P, Räihä IJ, et al. Power-law relationship of heart rate variability as a predictor of mortality in the elderly. Circulation. 1998;97: 2031-2036. doi: 10.1161/01.CIR.97.20.2031.
34. Jokinen V, Syvänne M, Mäkikallio TH, Juhani Airaksinen KE, Huikuri HV. Temporal age-related changes in spectral, fractal and complexity characteristics of heart rate variability. Clin Physiol. 2008;21: 273-281. doi: 10.1046/j.1365-2281.2001.00326.x.
35. Kemuriyama T, Ohta H, Sato Y, Maruyama S, Tandai-Hiruma M, Kato K, et al. A power-law distribution of inter-spike intervals in renal sympathetic nerve activity in salt-sensitive hypertension-induced chronic heart failure. Biosystems. 2010;101: 144-147. doi: 10.1016/j.biosystems.2010.06.002.
36. Kucera JP. What makes the heart rhythm so intricate? Heart Rhythm. 2014;11: 1220-1221. doi: 10.1016/j.hrthm.2014.04.013.
37. Alstott J, Bullmore E, Plenz D. powerlaw: A Python package for analysis of heavy-tailed distributions. PLoS ONE. 2014;9: e85777. doi: 10.1371/journal.pone.0085777.

38. Scott DW. Sturges' rule. Wiley Interdiscip Rev Comput Stat. 2009;1: 303-306. doi: 10.1002/wics.35
39. Cantwell CD, Roney CH, Ng FS, Siggers JH, Sherwin SJ, Peters NS. Techniques for automated local activation time annotation and conduction velocity estimation in cardiac mapping. Comput Biol Med. 2015;65: 229-242. doi: 10.1016/j.compbiomed.2015.04.027.
40. Cohen IS, Datyner NB, Gintant GA, Mulrine NK, Pennefather P. A note on the relation of maximum upstroke velocity to peak inward current recorded by the voltage clamp. Circ Res. 1985: 57(3): 482-484. doi: 10.1161/01.RES.57.3.482
41. Natarajan A, Stancescu M, Dhir V, Armstrong C, Sommerhage F, Hickman JJ, et al. Patterned cardiomyocytes on microelectrode arrays as a functional, high information content drug screening platform. Biomaterials. 2011;32(18): 4267-4274. doi: 10.1016/j.biomaterials.2010.12.022
42. Christoffels VM, Burch JBE, Moorman AFM. Architectural plan for the heart: early patterning and delineation of the chambers and the nodes. Trends Cardiovasc Med. 2004;14(8): 301-307. doi: 10.1016/j.tcm.2004.09.002.
43. Bellay T, Klaus A, Seshadri S, Plenz D. Irregular spiking of pyramidal neurons organizes as scale-invariant neuronal avalanches in the awake state. eLife. 2015;07224. doi: 10.7554/eLife.07224.
44. Lombardi F, Herrmann HJ, Plenz D, de Arcangelis L. Temporal correlations in neuronal avalanche occurrence. Sci Rep. 2016;6: 24690. doi: 10.1038/srep24690.
45. Beggs J, Plenz D. Neuronal Avalanches in Neocortical Circuits. J Neurosci. 2003;23: 11167–11177. pmid:14657176
46. Dunham CS, Lilak S, Hochstetter J, Loeffler A, Zhu R, Chase C, et al. 2021. Nanoscale neuromorphic networks and criticality: a perspective. J Phys Complex. 2021;2: 042001.
47. Meijers M, Ito S, Rein ten Wolde P. Behavior of information flow near criticality. Phys Rev E. 2021;103: L010102. pmid:33601642
48. Perkel J. Programming: Pick up Python. Nature. 2015; 518: 125–126. doi: 10.1038/518125a
49. Collette A. Python and HDF5 [Internet]. Sebastopol (CA): O'Reilly Media, Inc (US); [reviewed 2022 Apr 17; cited 2022 Apr 18]. Available from: https://www.oreilly.com/library/view/python-and-hdf5/9781491944981/ch01.html
50. PyQtGraph [Internet]. PyQtGraph; [reviewed 2022 Apr 17; cited 2022 Apr 18]. Available from: https://www.pyqtgraph.org

Chapter 6. Optimizing Methods for ICP-MS Analysis of Mercury in Fish: An Upper-division Chemistry Laboratory

Abstract

Food safety is a prominent field that many analytical chemists aspire to practice due to its every-day relevance and clear practical applications. One of the most important aspects of food safety science is the detection and regulation of mercury (Hg) in food, e.g., fish products, due to mercury’s potency as a debilitating and frequently lethal neurotoxin. The stringent standards and practices for the analysis of Hg in fish, as implemented by institutions such as the Food and Drug Administration (FDA), require both highly skilled analytical chemists and sensitive quantitative techniques, e.g., inductively coupled plasma mass spectrometry (ICP-MS). These needs inspired the development of an upper-division, undergraduate analytical chemistry experiment that is explicitly designed to teach students how to properly quantify mercury in commercial fish products via ICP-MS analysis. In this hands-on laboratory exercise, students were taught how to use a standard reference material (SRM) for method validation and to understand how different matrices can affect the accuracy of the analysis. Students also learned how to optimize ICP-MS instrument parameters such as kinetic energy discrimination (KED) voltage. Students worked in small groups and across lab sections to analyze their data and to identify the best parameter set for their experimental conditions. This lab exercise provides a rigorous, practical, and challenging experience

for aspiring analytical chemists and can be readily adapted to the needs and interests of any institution with access to an ICP-MS instrument.

Graphical abstract

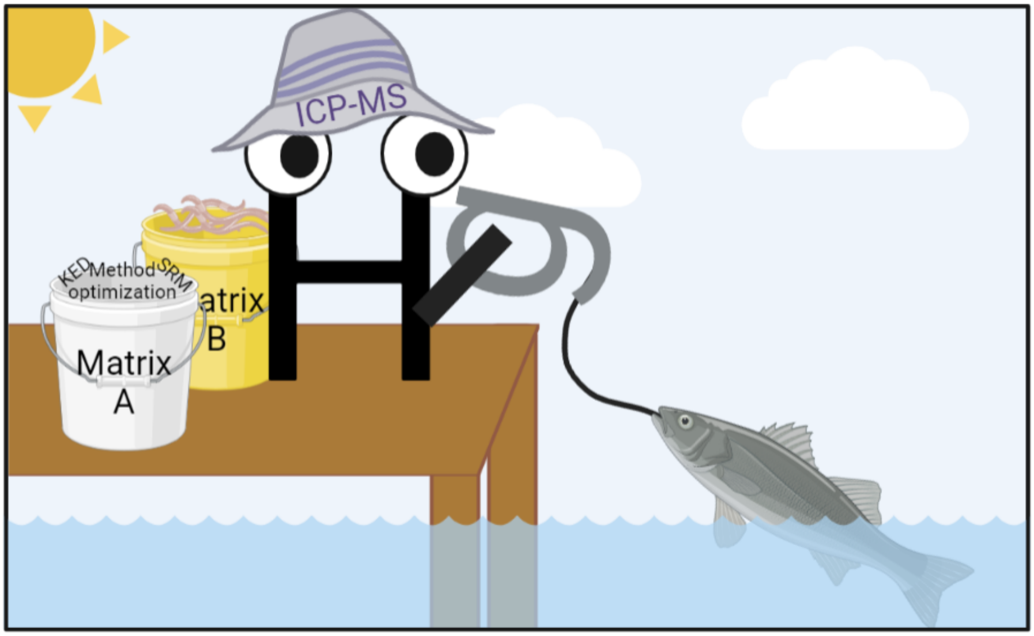

Introduction

Government regulatory bodies such as the Food and Drug Administration (FDA) and the Environmental Protection Agency (EPA) routinely oversee the administration and enforcement of regulations governing hazardous compounds that can enter the food supply. Screening mercury (Hg) in commercial fish products is of particular importance because seafood is the main source of this toxin for the general public[1]. Mercury toxicity can lead to brain damage including psychological disturbance, impaired hearing, loss of sight, ataxia, loss of motor control, and general debilitation[2]. Moreover, mercury exposure during the embryonic phase can lead to severe abnormalities in psychomotor development[3].

Thus, the FDA closely monitors Hg levels in commercial fish, provides guidelines on its consumption, and prohibits the sale of fish that have methylmercury levels higher than an action level of 1 ppm[4-8]. Action levels represent the limit at which the FDA will take legal action to remove products from the market. The FDA regularly updates the elemental analysis manual for food and related products and inductively coupled plasma-mass spectrometry (ICP-MS) is one of the primary methods for the quantification of Hg in fish[9].

ICP-MS is a sensitive tool for elemental quantification with diverse applications, e.g., environmental sample analysis, water quality control, and food analysis[10-13]. This technique utilizes a plasma to achieve ionization and atomization of molecular species into their elemental components and is well suited for sensitive quantitative analysis, as it can detect analytes at concentrations well into the parts-per-trillion (ppt) range[14]. These traits make ICP-MS a particularly powerful technique for trace metal analysis in commercial products.

The prevalence of ICP-MS in real-world analytical chemistry applications has led to a number of proposed student lab exercises using ICP-MS over the last decade[15-19]. Such protocols are of great pedagogical benefit and introduce students to foundational concepts of ICP-MS and the practical application of the technique. However, important analytical chemistry concepts such as matrix effects on the accuracy of the ICP-MS analysis and parameter optimization process via the usage of a standard reference material (SRM) have not been extensively explored in previously published student-led

ICP-MS experiments[16-19]. Here, we introduce a hands-on lab exercise for an upper-division, undergraduate analytical chemistry course that mimics industry- and government-level ICP-MS protocols.

This undergraduate lab exercise was tested during the Winter 2020 quarter and fully implemented during the Winter 2022 quarter at the University of California, Los Angeles (UCLA) for a chemical instrumentation/analytical chemistry class. Students were tasked with optimizing experimental and instrument parameters with fish samples that were digested with two different acid matrices, Matrix A (1.62% HNO_3 and 0.34% H_2O_2) or Matrix B (1.62% HNO_3,0.21% HCl, and 0.34% H_2O_2).

Furthermore, students were introduced to the concept of kinetic energy discrimination (KED) as a means of suppressing polyatomic interfering species[20]. Polyatomic interference is caused by polyatomic species that are isobaric with the target element. KED takes advantage of the fact that isobaric polyatomic species will lose more kinetic energy relative to the target ions as they travel through a cell filled with a non-reactive gas such as helium (Figure 1).

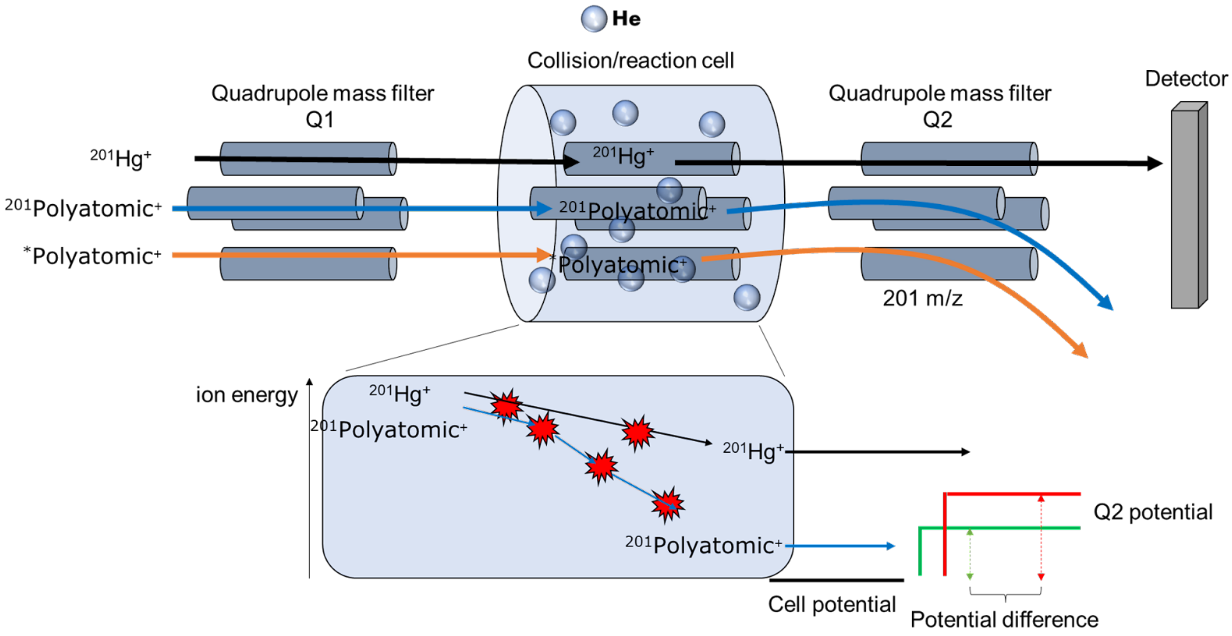

Figure 1. Polyatomic interference (or isobaric interference) can be attenuated via kinetic energy discrimination. In a single-quadrupole mode, Quadrupole 1 (Q1) is set to let ions of all m/z pass through. The target element ($^{201}Hg^{+}$), polyatomic species with the same m/z (^{201}Polyatomic^{+}), and other ions are introduced into the collision/reaction cell. In no gas mode (not shown), all ions travel unhindered to quadrupole 2 (Q2) and ions with the target m/z value (201 m/z) are selected by Q2. In helium mode, the collision/reaction cell is filled with helium. Polyatomic species that can potentially cause isobaric interference will undergo more collisions with helium compared to $^{201}Hg^{+}$. The resulting kinetic energy discrepancy can be taken advantage of to filter out ^{201}Polyatomic^{+} by setting up a potential energy barrier, the magnitude of which can be manipulated by adjusting the potential difference between the collision/reaction cell and Q2.

The SRM 1947 (Lake Michigan Fish Tissue)[21] from the National Institute of Standards and Technology (NIST) was used for method validation. Students analyzed each sample/matrix combination across multiple lab periods and several KED voltages were investigated for each lab section. Students pooled their data together into a centralized cloud repository for analysis. Using their data, students determined an optimal matrix and KED for their analysis. Finally, students used the data from their most optimal run to assess the safety of the fish sample for potential human consumption.

Experimental procedure

Reagents

Hydrochloric acid (37%, ≥99.999% trace metal grade, Sigma-Aldrich, Cat. no. 339253), nitric acid (70%, ≥99.999% trace metal grade, Sigma-Aldrich, Cat. no. 225711), hydrogen peroxide 30% (trace metal grade, Sigma-Aldrich, Cat. no. 95321), and water (high performance liquid chromatography (HPLC)-grade, Fisher, Cat. no. W9-1) were used to generate matrices for digestion and analysis. Scandium stock solution (100 µg/mL, 7% HNO_3, Inorganic Ventures, part no. CGSC10-125ML) and Yttrium stock solution (100 µg/mL, 2% HNO_3, Inorganic Ventures, part no. MSY-100PPM-125ML) were diluted to 8 ng/mL and 4 ng/mL, respectively, with either Matrix A (1.62% HNO_3 and 0.34% H_2O_2) or Matrix B (1.62% HNO_3, 0.21% HCl, and 0.34% H_2O_2) to generate internal standard (ISTD) solutions. Mercury standard (10 µg/mL, 5% HNO_3, Agilent, part no. 5190-8575) was diluted with either Matrix A or Matrix B to generate a 10 ng/mL stock solution, which was used to make calibration solutions. ICP-MS tuning solution (10 mg/mL Ce, Co, Li, Mg, Tl, and Y, Agilent, part no. 5190-0465) was diluted to 1 µg/L with 2% HNO_3 to conduct instrument warm-up and auto-tuning. SRM 1947 (Lake Michigan Fish Tissue, certification date 9/3/2020, expiration date 12/31/2026) was purchased from NIST.[21] Canned tuna (Skipjack tuna in water)was purchased from local supermarkets. Following digestion (see the Microwave Digestion & Sample Preparation section for details), the samples were stored in acid-resistant Nalgene™ Narrow-Mouth Bottles Made of Teflon™ PFA (Fisher, Cat. no. DS1630-0001).

Microwave digestion and sample preparation

All samples were digested via microwave digestion. Microwave digestion was performed at the ICP-MS facility within the UC Center for Environmental Implications of Nanotechnology at UCLA. Samples (method blank, SRM, fish) were measured into clean Teflon vessels for acid digestion. The digestion was carried out using either a mixture of 4 mL 70% HNO_3, 2 mL 30% H_2O_2, and 1 mL H_2O, or 4 mL 70% HNO_3, 2 mL 30% H_2O_2, and 1 mL 37% HCl at 190°C for 20 minutes in a microwave digestion system (Titan MPS, PerkinElmer). Once the samples were cooled to room temperature, they were subsequently diluted to the final volume of 50 mL by adding filtered deionized water.

ICP-MS instrument parameters

An 8800 ICP-MS QQQ ICP-MS system (Agilent) equipped with an SPS 4 Autosampler (Agilent) was used for the experiment. MassHunter Workstation 4.1 software (Agilent) was used to control the system and to process the data. The key parameters for ICP-MS are listed in Table 1 and were consistent throughout all experiments.

Table 1. Instrument parameters.

RF Power	1550 W	*Nebulizer Pump*	0.10 revolutions per second
RF Matching	1.80 V	*S/C Temp*	2 °C
Sampling Depth	8.0 mm	*Gas Switch*	Dilution Gas
Carrier Gas	1.00 L/min	*Makeup/Dilution Gas*	0.20 L/min
Option Gas	0.0%		

Teaching methods

Students were instructed on the fundamental concepts of quantitative analytical chemistry and specific aspects of ICP-MS (instrumentation, application) during the lecture and assigned reading components of the course. For the laboratory exercise, students were provided with the experimental protocol. The handling of mercury samples described in this protocol was approved by and in accordance with UCLA Environmental Health and Safety (EH&S) guidelines.

The lab experiment was conducted over two, four-hour lab sections within the same week. Students worked in groups of 3-4 to carry out this experiment. At the beginning of each lab section, students were briefed on the experimental protocol and were instructed on how to use a serological- and micro-pipette. The 10 µg/mL mercury standard from Agilent was always handled by teaching assistants (TAs) for the safety of the students.

Lab Period 1: The first lab period uses Matrix A to construct calibration curves and analyze samples. Conical tubes (15 mL and 50 mL) were rinsed as described in the protocol. The TAs prepared the 10 ng/mL working stock, from which students generated their calibration curves through serial dilutions. Water was then used to dilute the method blank, SRM, and fish sample 3.5-fold to the appropriate matrix composition. Once samples were prepared, they were loaded into the autosampler of the ICP-MS instrument for subsequent measurements. The overall class was composed of 3 separate sections; each section was assigned their own KED value (ranging from 0-12 V). Students then compiled their raw data into a central data repository to analyze the KED effects.

Lab Period 2: The second lab period repeated the procedures followed during lab period 1, except Matrix B was used to construct calibration curves and analyze samples. After all data were collected, students were asked to calculate the percent error of the average SRM concentrations (Equation (1)). Students first validated the method by checking whether the percent error calculated from Equation 1 is within ±10%. Then, students determined the combination of matrix, gas mode, and KED voltage that yielded the most accurate results based on SRM error (%).

*Equation (1): ((expected [SRM] - observed [SRM])/expected [SRM])*100*

Finally, students used this combination of parameters to calculate the concentration of mercury in the fish sample and describe its relevance to reported FDA values of mercury in fish.

Hazards

Students should always wear protective goggles, gloves, and lab coats during the experiment. 70% HNO_3 and 37% HCl used for mercury extraction are caustic and should be handled with care. The calibration solutions that contain HNO_3, HCl, and mercury should be generated with care in a well-ventilated fume hood and should be discarded following data acquisition. Finally, it is recommended that the autosampler chamber be ventilated during and after the experiment so that any vapor build-up containing mercury is minimized.

Results and discussion

The 42 students participating in the class had no prior or limited analytical chemistry lab experience. The students were divided into groups of 3-4 students. Each group performed the experiment on a rotating basis throughout the 10-week quarter. Each “Lab Period 1” began with a TA-guided question-and-answer session to ensure students worked through the pre-lab exercises, followed by guided inquiry and discussion of container preparation (i.e., the rinse protocol), sample preparation, calibration curve preparation, and kinetic energy discrimination. All students participated in preparing calibration curves and sample dilutions for Matrix A using both serological- and micro-pipettes. Students calculated the calibration curve concentrations in the pre-lab assignment. The generation of the calibration curve stock solution was handled by the TAs to minimize hazard exposure to undergraduate students. After the completion of solution preparation, students vortexed all containers and inserted their samples into the autosampler. Next, students were instructed on how to use the instrument software and received guidance on basic principles of sample batch design. The final batch parameters were approved by the TAs before batch submission to the instrument queue for analysis. Representative calibration curves, produced by the MassHunter software using student data, are shown in Figure 2.

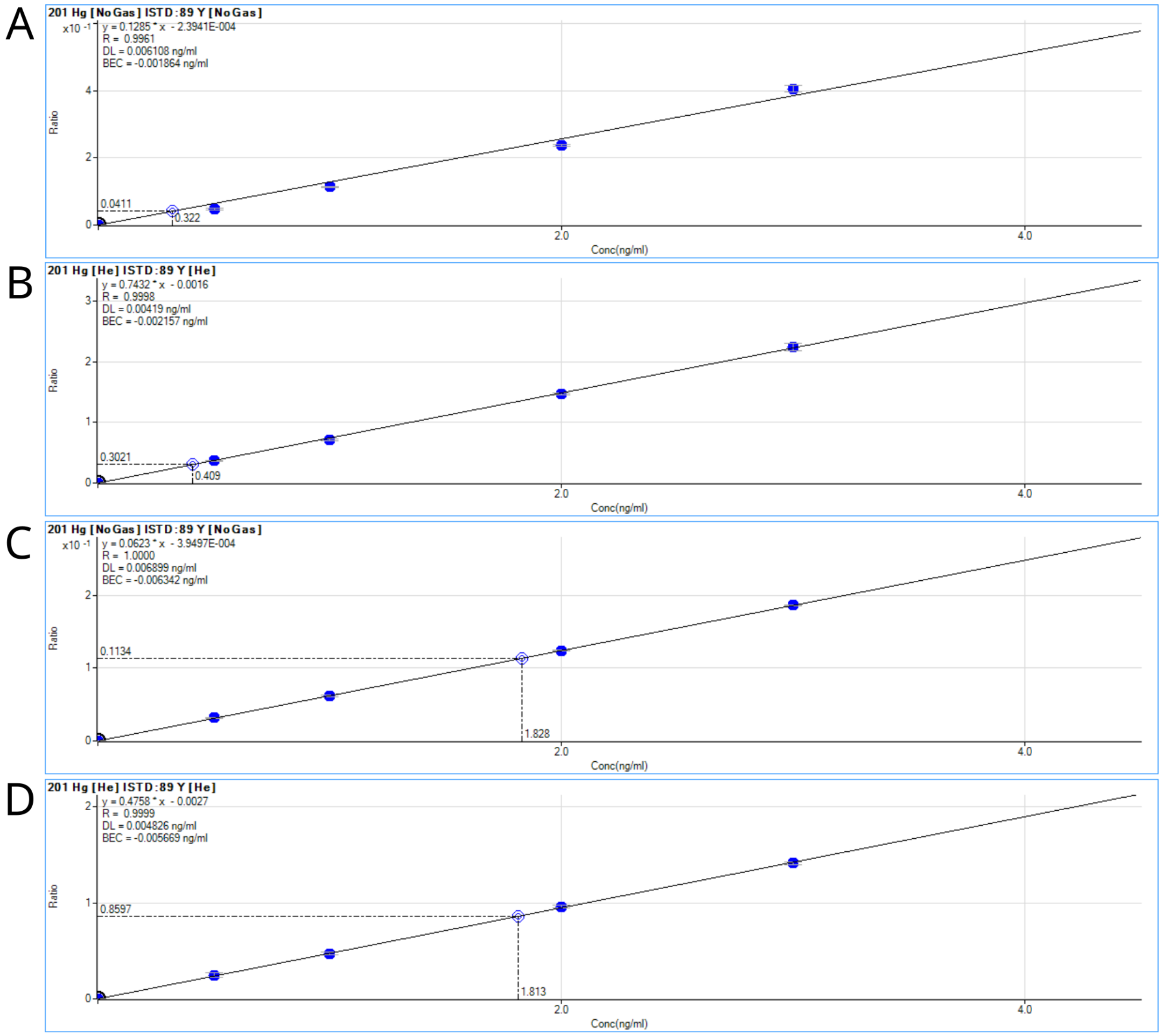

Figure 2. Calibration curves produced from student data. The y-axis is expressed as the ratio between analyte signal (Hg) to internal standard (Y). A) Matrix A in no gas mode, B) Matrix A in helium mode, C) Matrix B in no gas mode, and D) Matrix B in helium mode. Overall linearity was excellent with R^2 values ranging from 0.980 to 1.000.

During “Lab Period 2”, following sample preparation and batch submission to the queue, students engaged in a TA-led discussion over data analysis. Students examined data collected during the previous lab period by both themselves and the groups in other lab sections. By checking whether the percent error of the average SRM concentration is within ±10%, students first validated the method. Sample and SRM masses from the microwave digestion were provided in a shared README file. Using this data, students calculated the expected mercury concentration for the SRM in each matrix and compared these values to the acquired data. Students were asked to determine which matrix performed better in combination with other parameters by comparing expected and observed SRM mercury concentrations. Then, students assessed which KED voltage is the most optimal by comparing the datasets from several different KED voltages (e.g., 0V, 2V, 6V). For the final phase of the experiment, students were asked to use the data obtained from the optimal method to evaluate whether their fish sample would be safe to consume according to FDA guidelines.

Educational outcomes for this exercise were assessed through a combination of pre- and post-lab surveys and a written lab report assignment. All students were provided with a short list of questions to address in their report concerning method validation and optimization, results, and interpretation. Students from all groups determined that Matrix B, with its hydrochloric acid component, serves as a superior matrix for mercury analysis. Students determined that the choice in optimal gas mode could vary based on the applied KED. In many cases, students found that the no gas mode and helium gas mode with a KED of 6V to be the optimal method based on SRM error (%) (See Teaching Methods section). An example of parameter optimization work as performed by the students is shown in Table 2.

Table 2. Student-generated summary of data for determining the optimal parameter combination.

Matrix	*Mode*	*KED (V)*	*Fish (ng/mL)*	*Mean SRM (ng/mL)*	*SRM within ±10% of expected value?*	*Y/N*
A	No Gas	0V	0.180	2.140	21.64	NO
A	He Gas	0V	0.179	2.060	17.12	NO
A	No Gas	2V	0.180	2.051	16.60	NO
A	He Gas	2V	0.179	1.873	6.453	YES
A	No Gas	6V	0.194	2.233	26.93	NO
A	He Gas	6V	0.230	2.024	15.03	NO
B	No Gas	0V	0.284	1.959	7.423	YES
B	He Gas	0V	0.274	1.912	4.849	YES
B	No Gas	2V	0.266	1.976	8.367	YES
B	He Gas	2V	0.280	1.955	7.236	YES
B	No Gas	6V	0.268	1.852	1.589	YES
B	He Gas	6V	0.237	1.784	-2.147	YES

General Reflections

Surveys were administered prior to and after the conclusion of the lab exercise to gauge the educational benefits of the class. Students were asked to rate their understanding on a scale of 1-10, 10 being the greatest understanding. The surveys assessed students' general understanding of ICP-MS, how a SRM is used for method verification, polyatomic interference, the purpose of using different gas modes, and the application of KED (Figure 3). The students' understanding increased after the lab in all areas. The class also resulted in the students feeling more confident in their ability to explain the concept of KED to a colleague. In the post-lab survey, there was an additional question that asked, "Did this lab help to improve your understanding of ICP-MS and undergraduate-level analytical chemistry techniques and data analysis?", to which 98% of students responded "yes".

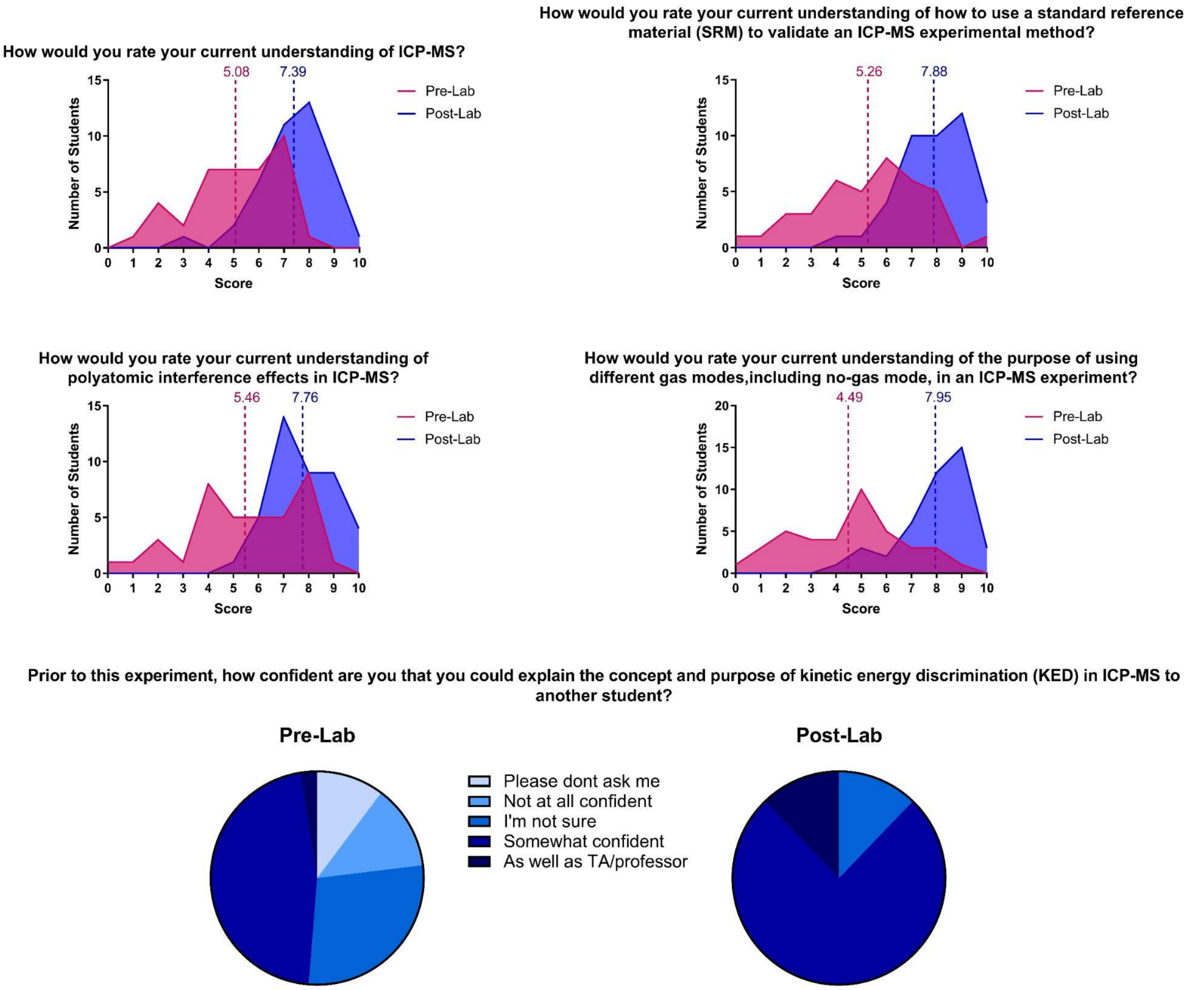

Figure 3. Student responses to pre- and post-lab surveys. The numbers listed above the dashed lines are the mean of the probability distributions.

Our objective in this lab exercise was to use the methodology employed by the FDA to teach advanced method development and parameter optimization skills. Students were able to successfully select the most optimal ICP-MS method by comparing the experimentally determined and expected values of mercury in the SRM. Using this information, students could inform the report reader about whether the fish was safe for human consumption according to FDA standards. Overall, the real-world relevance of the experiment kept students engaged and interested in the lab exercise. Below is an example conclusion from a student lab report.

> “With this study, an accurate measurement was able to be made of store-bought Skipjack tuna. Utilizing varying experimental conditions such as different matrices, KED, and gas modes, an optimal condition was able to be found and used. Matrix B, containing 1.6% HNO3, 0.34% H2O2, and 0.21% HCl, 6V of KED and a No Gas mode yielded the lowest deviations from a NIST-Certified SRM at roughly 1.59%. The concentration of mercury in this sample was found to be roughly 43ppb in comparison the FDA reported 95% confidence intervals of 120ppb to 140ppb. Therefore, this method of analysis can verify that the mercury contents of the store-bought Skipjack tuna is

> within safe ranges for human consumption which is essential due to mercury being a potent toxin in high quantities."

Conclusion

This experiment was successfully incorporated into an analytical chemistry class at UCLA. For this course, mercury concentration determination with ICP-MS was performed on commercial fish samples. However, the lab exercise can be adjusted accordingly to be implemented into any course curriculum that aims to teach the concept of optimizing instrument parameters for measuring real world samples. The utilization of FDA-approved practices introduces students to real-life applications of government-level analytical chemistry techniques for food safety analysis. The class provides students with hands-on practical lab work experience and discussion-focused data interpretation which promotes development of analytical skills essential for aspiring analytical chemists. The pre- and post- lab surveys highlight student growth in ICP-MS data acquisition, method optimization, and data analysis.

References

1. Storelli, M. M., Barone, G., Piscitelli, G. & Marcotrigiano, G. O. Mercury in fish: Concentration vs. fish size and estimates of mercury intake. Food Additives and Contaminants. 24, 1353–1357 (2007).

2. Fernandes Azevedo, B. et al. Toxic effects of mercury on the cardiovascular and central nervous systems. J. Biomed. Biotechnol. 2012, (2012).

3. Storelli, M. M., Giacominelli Stuffler, R., Marcotrigiano, G. O. & Marcotrigian, G. O. Total and methylmercury residues in tuna-fish from the Mediterranean Sea. Food Additives and Contaminants. 19, 715-720 (2002).

4. Mercury Concentrations in Fish from the FDA Monitoring Program (1990-2010) | FDA. https://www.fda.gov/food/metals/mercury-concentrations-fish-fda-monitoring-program-1990-2010. Accession date: 3/26/2022

5. Mercury Levels in Commercial Fish and Shellfish (1990-2012) | FDA. https://www.fda.gov/food/metals-and-your-food/mercury-levels-commercial-fish-and-shellfish-1990-2012. Accession date: 3/26/2022

6. Advice about Eating Fish. | FDA. https://www.fda.gov/food/consumers/advice-about-eating-fish. Accession date: 3/26/2022

7. Public Health Statement: Mercury | ATSDR. https://www.atsdr.cdc.gov/PHS/PHS.asp?id=112&tid=24. Accession date: 3/26/2022

8. Guidance for Industry: Action Levels for Poisonous or Deleterious Substances in Human Food and Animal Feed | FDA.

https://www.fda.gov/regulatory-information/search-fda-guidance-documents/guidance-industry-action-levels-poisonous-or-deleterious-substances-human-food-and-animal-feed. Accession date: 3/26/2022

9. Elemental Analysis Manual for Food and Related Products. Version 1.2 (2020) | FDA. https://www.fda.gov/media/87509/download. Accession date: 3/26/2022

10. Pröfrock, D., Leonhard, P., Wilbur, S. & Prange, A. Sensitive, simultaneous determination of P, S, Cl, Br and I containing pesticides in environmental samples by GC hyphenated with collision-cell ICP-MS. J. Anal. At. Spectrom. 19, 623–631 (2004).

11. Allibone, J., Fatemian, E. & Walker, P. J. Determination of mercury in potable water by ICP-MS using gold as a stabilising agent. J. Anal. At. Spectrom. 14, 235–239 (1999).

12. Nardi, E. P. et al. The use of inductively coupled plasma mass spectrometry (ICP-MS) for the determination of toxic and essential elements in different types of food samples. Food Chem. 112, 727–732 (2009).

13. Maione, C. et al. Comparative study of data mining techniques for the authentication of organic grape juice based on ICP-MS analysis. Expert Syst. Appl. 49, 60–73 (2016).

14. Ammann, A. A. Inductively coupled plasma mass spectrometry (ICP MS): a versatile tool. J. Mass Spectrom. 42, 419–427 (2007).

15. Sanders, J. K. Inductively Coupled Plasma-Mass Spectrometry: Practices and Techniques (Taylor, Howard E.). J. Chem. Educ. 78, 1465 (2001).

16. Donnell, A. M., Nahan, K., Holloway, D. & Vonderheide, A. P. Determination of Arsenic in Sinus Wash and Tap Water by Inductively Coupled Plasma–Mass Spectrometry. J. Chem. Educ. 93, 738–741 (2016).

17. He, P., Colón, L. A. & Aga, D. S. Determination of Total Arsenic and Speciation in Apple Juice by Liquid Chromatography–Inductively Coupled Plasma Mass Spectrometry: An Experiment for the Analytical Chemistry Laboratory. J. Chem. Educ. 93, 1939–1944 (2016).

18. Duedahl-Olesen, L., Holmfred, E., Niklas, A. A., Nielsen, I. K. & Sloth, J. J. Case Study Teaching for Active Learning on Analytical Quality Assurance Concepts in Relation to Food Safety Exposure Assessment. J. Chem. Educ. 98, 3776–3783 (2021).

19. Neu, H. M., Lee, M., Pritts, J. D., Sherman, A. R. & Michel, S. L. J. Seeing the 'Unseeable,' A Student-Led Activity to Identify Metals in Drinking Water. J. Chem. Educ. 97, 3690–3696 (2020).

20. Yamada, N. Kinetic energy discrimination in collision/reaction cell ICP-MS: Theoretical review of principles and limitations. Spectrochimica Acta - Part B Atomic Spectroscopy. 110, 31–44 (2015).

21. SRM 1947 - Lake Michigan Fish Tissue | NIST.

https://www-s.nist.gov/srmors/view_detail.cfm?srm=1947 Accession date: 3/26/2022

Chapter 7. Spoken Digit Classification by In-Materio Reservoir Computing With Neuromorphic Atomic Switch Networks

Abstract

Atomic Switch Networks comprising silver iodide (AgI) junctions, a material previously unexplored as functional memristive elements within highly interconnected nanowire networks, were employed as a neuromorphic substrate for physical Reservoir Computing This new class of ASN-based devices has been physically characterized and utilized to classify spoken digit audio data, demonstrating the utility of substrate-based device architectures where intrinsic material properties can be exploited to perform computation in-materio. This work demonstrates high accuracy in the classification of temporally analyzed Free-Spoken Digit Data These results expand upon the class of viable memristive materials available for the production of functional nanowire networks and bolster the utility of ASN-based devices as unique hardware platforms for neuromorphic computing applications involving memory, adaptation and learning.

Introduction

Speech recognition is a seminal task in the field of artificial intelligence and natural language processing. Typical algorithmic approaches to speech recognition break apart sections of raw speech data and bin them into hidden Markov models manipulating Markov chains. While effective, these approaches are more computationally intensive than some recently developed neural network models, which may prove a more suitable compute framework for handling increasingly larger data sets[1–3]. Artificial Neural Networks (ANNs) have also been a promising avenue for more efficient speech recognition tasks which offer the benefit of being trained for natural language processing and are believed to be a more suitable candidate for handling the varied complexity of each person's unique voice and accent. Implementation of ANNs in modern computing hardware remains computationally burdensome and often requires access to and utilization of high-performance computing clusters. A suitable hardware architecture for local execution of complex tasks such as natural language processing must be able to process dynamic, temporal data in real-time while remaining energy efficient. Memristive materials have been identified as strong candidates for such applications as they offer an opportunity to alleviate the bus latency between memory and processing elements in traditional von Neumann architectures while also performing in-memory computation with reduced power consumption[4]. The nonlinear character of memristors, resulting from the underlying physics of the material itself, is essential for enabling simultaneous storage of data (memory) and performance of complex tasks with it (processing) through a relatively new technique known as evolution in-materio[5–8].

The growing field of evolution in-materio computing has sought to optimize computational architectures via evolutionary (search) algorithms[6,7]. The materials and architectures employed vary with the desired facet of computation, but ideally these materials are computationally and energetically efficient at employing a litany of machine learning based algorithms. Utilizing a single hardware element capable of exhibiting both memory and processing alleviates the burden of busing information between two separate hardware components, reducing latency in computation[3]. The most robust currently known architecture that combines the aforementioned elements is the mammalian brain, which has been both a foundation and inspiration towards the development of architectures which can efficiently process multi-input, chaotic, and/or time-varying (temporal) datasets.

This work focuses on the class of neuromorphic computing devices known as Atomic Switch Networks (ASN), comprising a highly-interconnected network of memristive nanowire junctions as shown schematically in Figure 1. Ongoing efforts to develop memristive hardware for neuromorphic computing include not only ASNs, but also patterned crossbar arrays, and nanoparticle clusters[9–13]. ASN-based devices provide a physical system with structure and functional dynamics reminiscent of the mammalian brain[14–17] that has previously been employed as a computational material for applications in Reservoir Computing (RC)[18–24]. The atomic switch is a nanoscale electroionic element consisting of a Metal-Insulator-Metal (MIM) junction whose properties can be manipulated via a time-dependent input signal[25–28]. Individual atomic switches have been shown to produce memristive, nonlinear responses, exhibiting both short and long-term memory as well as quantized conductance[12,13,29,30]. For electrochemical metallization memristors filament growth is dominated by cation transport through the insulating medium as shown in Figure 1 and has been experimentally observed in-situ[31–33]. These properties render atomic switches and other memristive systems as ideal circuit elements for use within a network architecture that can serve as a dynamic physical reservoir used to solve complex computational tasks, including speech recognition and natural language processing[34,35].

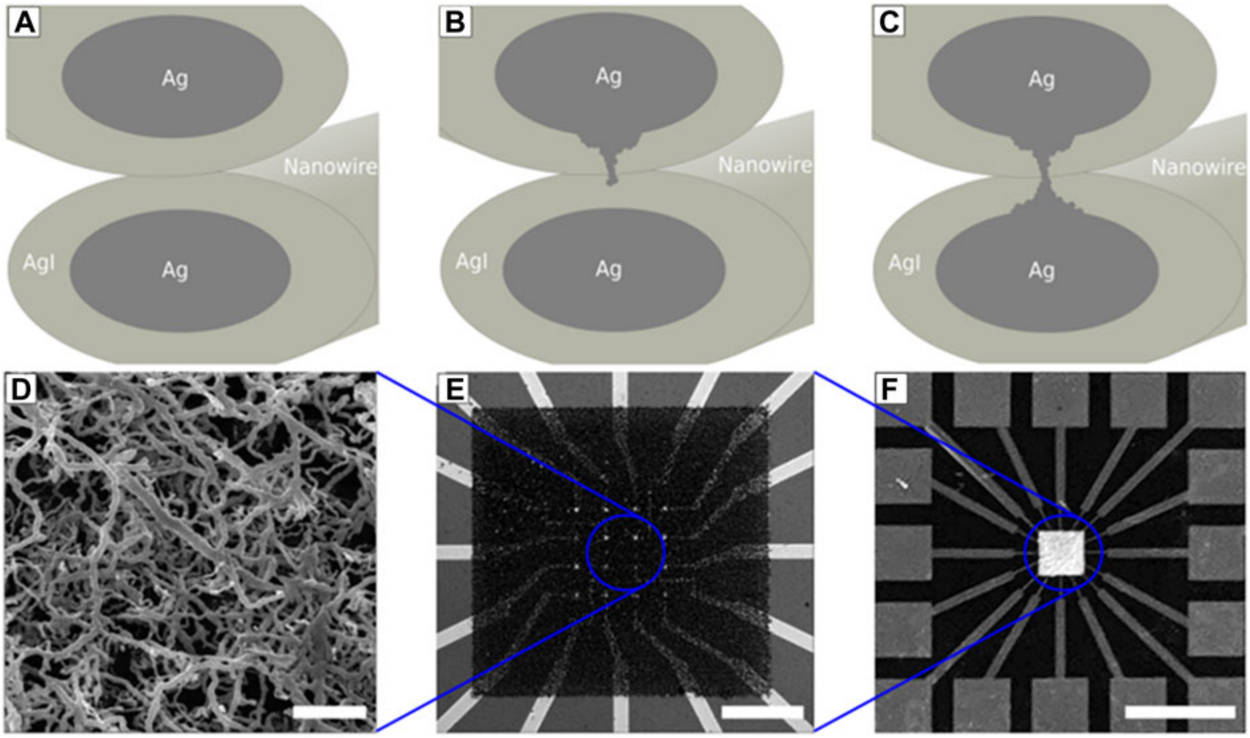

Figure 1. Schematic diagram of an AgI-based ASN device, from nanowire junction to chip. (A) initial high resistance state of the system. (B) filament formation process under an applied bias (C) completed silver filament short circuits between overlapping nanowires (low resistance state). Yellow-gray represents AgI. Dark-gray represents Ag. Filament formation occurs as a gapless junction between Ag nanowires. (D) SEM image of the interconnected nanowire (scale bar = 20 um). (E) Optical image of microelectrode array at center of the ASN device (scale bar = 360 um). (F) Optical image of a complete 16-electrode ASN device (scale bar = 5 mm).

RC provides a framework for computing complex functions using a dynamical system as a ‘reservoir’[18,36–38]. The RC framework is ideal for the processing of dynamic, temporal real-time signals and can be used in many of the same situations as recurrent feed-forward neural networks. RC also offers advantages such as fault-tolerance and the capacity for learning[38,39]. Passing a time varying input through a dynamic reservoir produces a higher dimensional representation of the signal through nonlinear transformation, where different points on the reservoir are measured and linearly combined to reproduce an arbitrary output signal as shown in Figure 2. Training is only performed on the linear readout coefficients (voltage readouts are shown in Figure 3 demonstrating a reproducible response over time); the reservoir dynamics themselves are generally considered fixed. Limiting training to the weights between the reservoir and output layer alleviates the need to use gradient-descent based methods, greatly minimizing the associated computational burden.

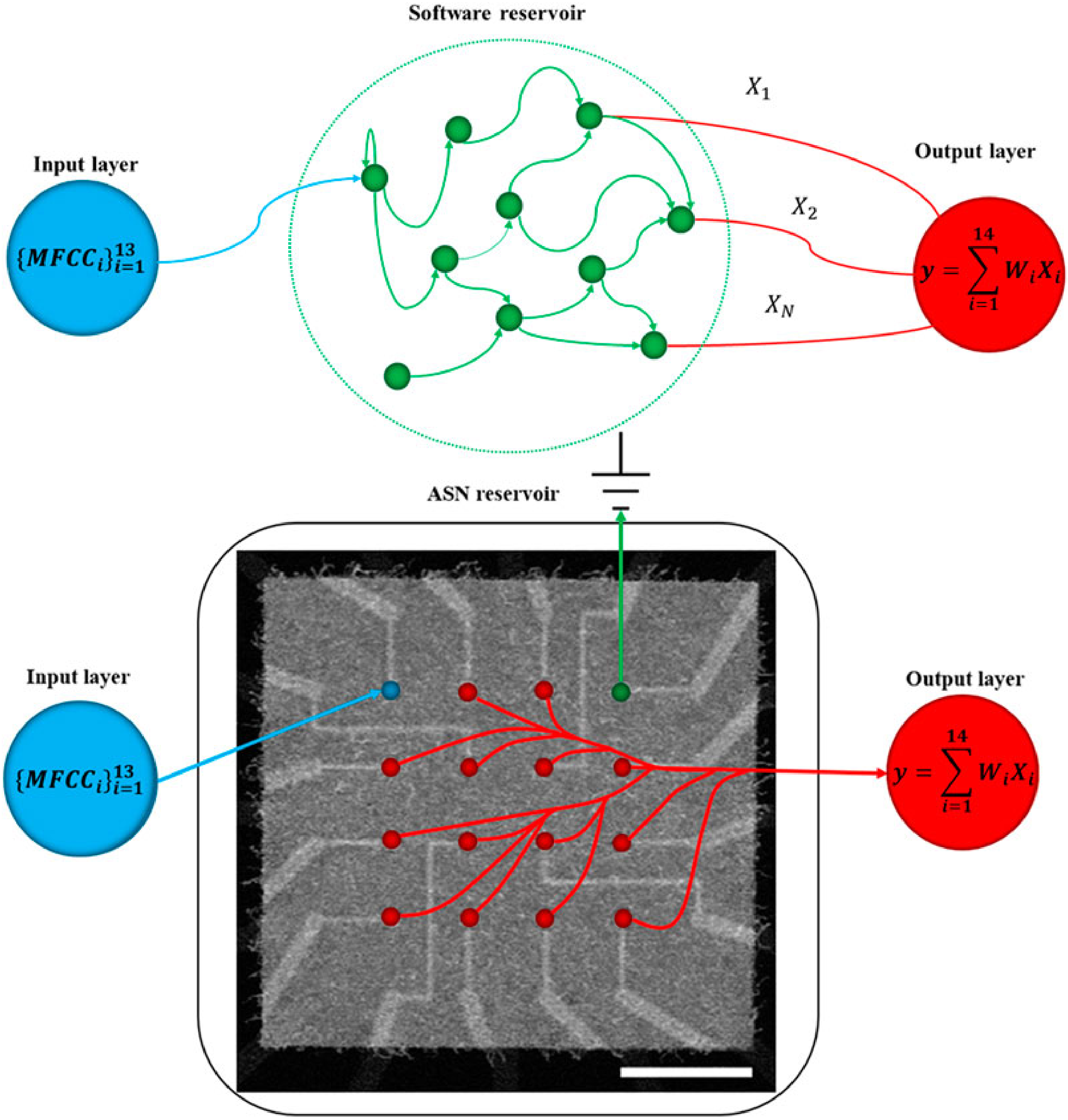

Figure 2. Overview of reservoir computation schematics. A traditional software-based reservoir (top) is contrasted with the ASN acting as an in-materio reservoir (bottom), in which 13 MFCC's are sequentially delivered to the ASN in the form of a time-varying voltage to a single electrode. Utilizing physical nodes enables hardware acceleration at a lower power cost. Simultaneous, real-time voltage

measurements are carried out at each of the remaining 14 electrodes and provided to an output layer for regression analysis.

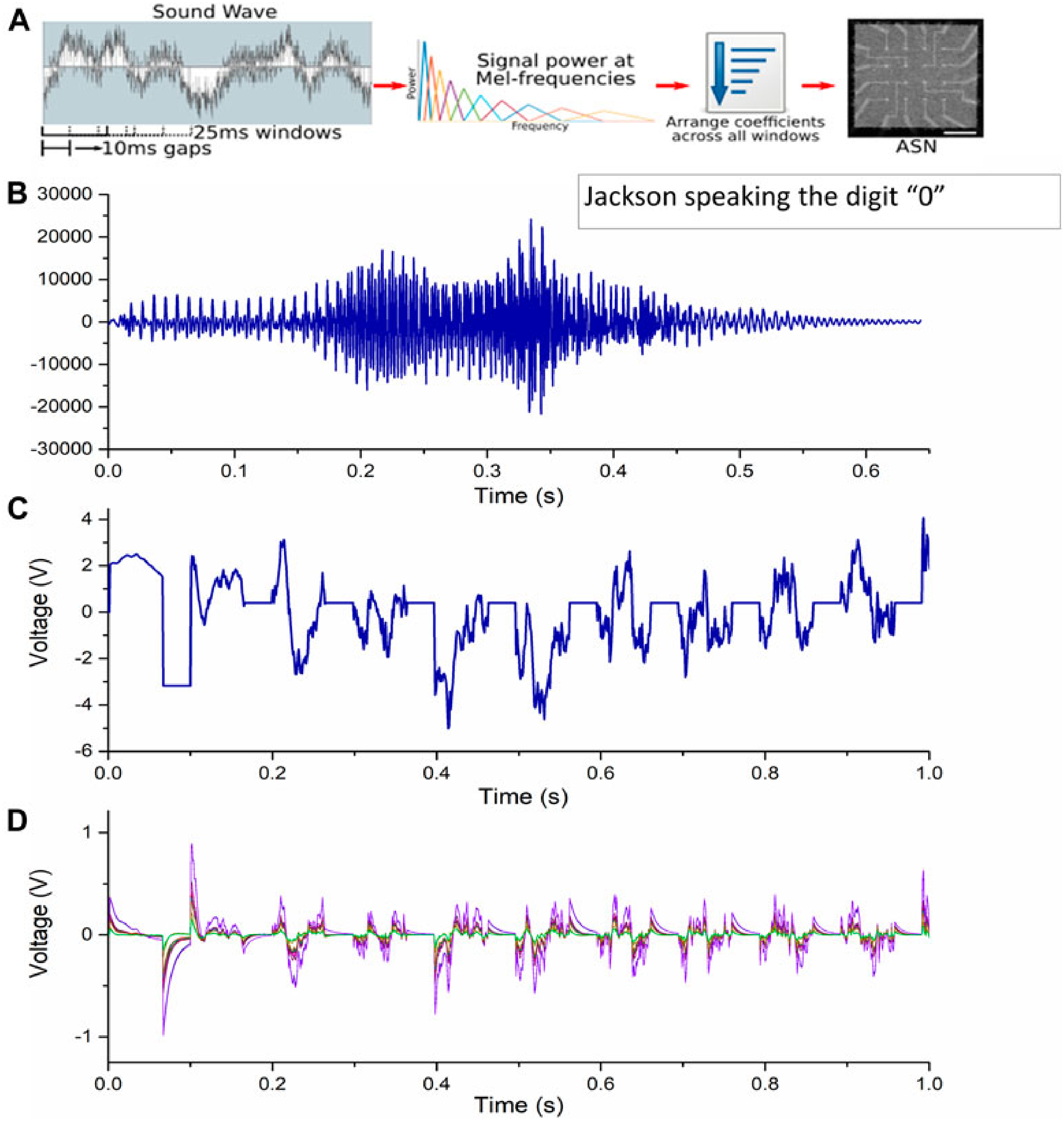

Figure 3. Method workflow schematic. (A) The workflow for RC-based speech recognition using ASN-based devices involved encoding and separation of raw audio data - spoken digits - data into overlapping windows, each of which was converted into

13 MFCCs. Individual MFCCs were arranged to minimize input thrashing and then delivered as input voltage to a single electrode of the ASN device. Output data, in the form of voltage traces, was collected at all remaining electrodes. (B) The raw FSDD audio signal of “Jackson” speaking the digit zero and its subsequent conversion to a voltage signal (C). The resultant 14 voltage recordings and their unique responses are overlaid in (D).

As an alternative to simulation-driven RC, in-materio RC leverages material complexity for computational purposes[40–43]. Whereas early implementations of RC simply utilized a body of a liquid acting as the dynamic reservoir, more recent works harnessed the intrinsic properties of complex physical systems, including ASNs, as the basis for a computation[20,22,24,36,44]. Software RC has historically been demonstrated as a suitable method for a litany of complex tasks including pattern classification, signal generation and temporal based logic tasks[42]. Hardware based approaches to RC commonly leverage photonic interactions or memristor dynamics, though photonic systems aren’t performing computations in-materio in contrast to memristors[42,45]. In-materio approaches to traditional RC have recently garnered attention as potential candidates to accelerate compute times while achieving higher power efficiency. Recent in-materio studies have demonstrated high accuracy in time-series analysis[9,35], handwritten digit identification [46] and biosignal processing[47].

Computational neural models such as the perceptron and support vector machine can also be used as reservoirs; however, long convergence times can be a drawback depending on the task. Material-based reservoirs have the benefit of efficiently performing these tasks in-situ, enabling low-power, on-chip computing[48–50].

This alternative approach offers the opportunity to employ neural networks and machine learning algorithms offline, without the need to access servers, clusters and other high-performance computing infrastructures.

ASNs have been shown to represent a uniquely suitable class of materials for implementation of hardware-based RC, namely complex network architectures with the requisite material complexity[15,39,51]. These self-organized systems offer a unique opportunity to produce highly-interconnected memristive networks, where a density of atomic switch junctions of up to 10^8/cm[30] has been previously reported. The fabrication scheme, based on electroless deposition, produces a diverse ensemble of silver nanowires with varying lengths, widths and thereby junction dimensions. This structural diversity in the material substrate imparts a distribution of operational characteristics that improves the capacity to perform non-linear transformations of input signals.

Herein, we report the use of a new memristive material, silver iodide (AgI), as the functional element in the ASN framework[13,52,53]. Silver iodide can be robustly prepared in a brief vapor phase reaction of iodine vapor with silver nanowires at room temperature in contrast to the lengthy formation times at elevated temperatures of previously reported silver sulfides. This promising material provides voltage-controlled resistance in both the bulk and when integrated into crossbar architectures, rendering it suitable as a memristive material for RC applications which require non-linear transformations and quantized conductance states[39]. This work expands the catalog of investigated ASN materials by fabricating and testing AgI for non-linear, temporal computation through the classification of spoken digits.

Methods

Device fabrication

The substrate for ASN devices, a multielectrode array enabling spatiotemporal stimulation and monitoring, was fabricated using standard thermally oxidized (500 nm) silicon wafers as the base substrate. A 16-electrode grid of Pt (150 nm) was patterned by photolithography and deposited using a negative photoresist (AZ NLOF 2020) onto a Cr or Ti wetting layer (5 nm). Liftoff was induced overnight in N-methyl-2-pyrrolidone (NMP) at 60°C. Point contact electrodes were prepared using a patterned insulating layer of SU-8 (400 nm) which was soft baked (90°C), exposed to UV, post exposure baked (90°C), developed for 3 min, and hard baked at 180°C for 30 min. An array of copper (300 nm) seed sites with 5 x 5 µm spacing in a grid were patterned onto inner point contact electrodes and deposited onto AZ NLOF 2020 via metal evaporation at 3 nm/s followed by lift-off overnight in NMP (60°C). The resultant device platforms consist of a stack of Si/SiO2/Cr/Pt-electrodes/SU-8/Cu-posts and were stored in an inert atmosphere until bottom-up silver nanoarchitecture construction[37,54].

This substrate was placed into a 50 mM solution of silver nitrate ($AgNO_3$) for 30-60 minutes. Silver nanowires formed through an electroless deposition reaction involving the reduction of silver and the oxidation of copper through the following reaction:

The ordered copper posts (5x5 µm) directed a density-controlled formation of interconnected silver nanowires, whereby each ASN exhibited a unique structure determined by the bottom-up fabrication of metal cations. Subsequent silver iodide was formed in a nitrogen purged and sealed glass chamber with the ASN chip suspended over a small iodine pellet. Two different experimental techniques, one under ambient conditions (5 minutes exposure time) and the other with added heat (30 °C, 2-3 minutes exposure time) were employed with both techniques successfully iodizing the silver nanowires.

UV-Vis and XPS samples were prepared using transparent silver thin films (20 nm). These films were deposited on glass cover slides via a silver target in a Hummer 6.2 sputter system at 15 mA from Anatech Ltd (Hayward, CA, USA) under an argon vacuum environment (80 mtorr).

Material characterization

Optical and scanning electron microscopy (SEM) were used to characterize the as-fabricated structure of the nanowire network. SEM images were acquired using the JEOL JSM-7500F. X-Ray photoelectron (XPS) and UV-VIS spectroscopy were employed using transparent Ag thin film substrates with Ag as a control. Absorbance spectra of thin films were collected using the HP 8453 spectrophotometer. XPS spectra were obtained on an AXIS Ultra DLD XPS instrument from Kratos Analytical. The X-ray source was Al K at 1486.6 eV. Survey (1200 eV) and high-resolution scans were integrated over 4 and 16 sweeps, respectively.

Electrical characterization

Characterization of ASN devices involves the spatially-defined stimulation and monitoring of electrical activity throughout the network in the form of current and voltage traces. All input-output signals were generated/acquired using a purpose-built software package developed in Labview in conjunction with dedicated hardware manufactured by National Instruments. A data acquisition card (DAQ) (model PXIe-6368) was used to deliver input signals routed through a shielded connector box (model SCB-68A) to the ASN device. A source measurement unit (model PXIe-4141) was used to measure current flow through the ASN at user-selected electrodes, where acquired and applied signals were routed using a 16x32 switch matrix terminal block (model TB-2642B). Voltage traces were simultaneously monitored at all 16 electrodes using the DAQ card. All components were housed in a National Instruments chassis (model PXIe-1078) with an embedded controller.

Prior to any FSDD output signals, each ASN was driven through an initialization (activation) process in which the electrodes were sequentially stimulated with 7 Hz triangle waves. This process was repeated with increasing voltages (0.01-1 V) to realize switching patterns within the network. The switch matrix was employed in conjunction with the DAQ to calculate the resistance of every electrode combination prior to and after initialization, where successful activation was characterized by a sharp reduction in the network-wide parallel resistance as compared to the virgin metal system. Current-voltage and voltage-voltage measurements utilized triangle wave outputs from the DAQ card. The FSDD signal outputs were also produced by the DAQ card at selected electrode locations via the switch matrix.

Reservoir computing

The AgI ASN’s were evaluated for their potential RC applications through three different tests: non-temporal logic operations, temporal logic operations and recall of previous inputs and spoken digit classification. The non-linear XOR task was chosen for all logic operations and the assessment of the network's temporal properties.

Spoken digit classification was implemented in AgI ASN devices via RC using the FSDD. The task was not performed using raw audio data, but rather using Mel-Frequency Cepstrum Coefficients (MFCCs) of the data, similar to previously reported techniques. Each 8 kHz wave-format sound file from the FSDD was zero-padded up to 1 second of recording length and then converted into MFCCs using the “python_speech_features” Python package. Mel-frequency cepstrum is a short-term power spectrum of the sound waves, using a linear cosine transform of a log power spectrum and is a nonlinear mel scale of frequency that approximates the human auditory response better than standard linear spacing of frequency components.

Default settings were used, resulting in an array of MFCCs where each 25 ms window of signal was parameterized by 13 MFCCs. Windows were offset by 10 ms, resulting in 1287 total coefficients. To reduce device thrashing, the resulting MFCC array was flattened and fed to the network one at a time. The entire temporal sequence of the lowest-frequency coefficient was passed first, then the next-lowest-frequency coefficient’s values, and so on. The resulting 1287 Hz signal (shown in Figure 2) was sent to an input electrode, 14 electrodes were measured, and another electrode was grounded. Both the input and 14 read electrodes were recorded at 1 kHz. For RC, the resulting voltage streams were sampled at the end of sub-windows of computation, and the entire collection of sampled recordings was linearly regressed to indicate which digit was spoken (see Figure 3). Twelve unique spoken digit recordings were used, characterized by two speakers, saying three digits, two unique times. The FSDD speakers were ‘Jackson’ and ‘Theo’, the digits spoken were zero, one, or two, and the first two instances of each digit were used. As a baseline, regressions were performed on only the input electrode's voltage reading ("input only" mode) as well as on the full electrode suite of the input electrode and the 14 readout electrodes ("reservoir" mode).

Results and discussion

Material and device characterization

Silver nanowire networks like those shown in Figure 1b were reliably produced based on previously developed protocols. The network functionalization process requires conversion of silver nanowire junctions to silver iodide. The protocol for the formation of silver iodide was validated using UV-Vis and X-ray Photoelectron Spectroscopies (XPS). Figure 4 provides representative visible absorption spectra of as-prepared Ag and AgI thin films. Ag thin films prepared by desktop sputtering exhibited a Surface Plasmon Resonance (SPR), suggesting the presence of silver islands within the film[55]. These results are in line with previous reports which have demonstrated that silver exposed to iodine decreases SPR intensity coupled with a buildup of excitons. An absorbance peak around 420 nm has been previously reported and longer exposure to iodine at ambient temperature yielded a red-shifted maximum, which has been associated with the formation of larger AgI particles[55,56]. XPS results shown in Figure 5 confirmed the presence of characteristic peaks for iodide $3d_{5/2}$ and $3d_{3/2}$ core level energies previously reported in metal iodides at binding energies of 620 and 631 electron volts (eV) which are absent in silver control samples[57]. While both functionalization protocols successfully produced AgI, the heated method was used for all ASN devices due to quicker sublimation of solid iodine.

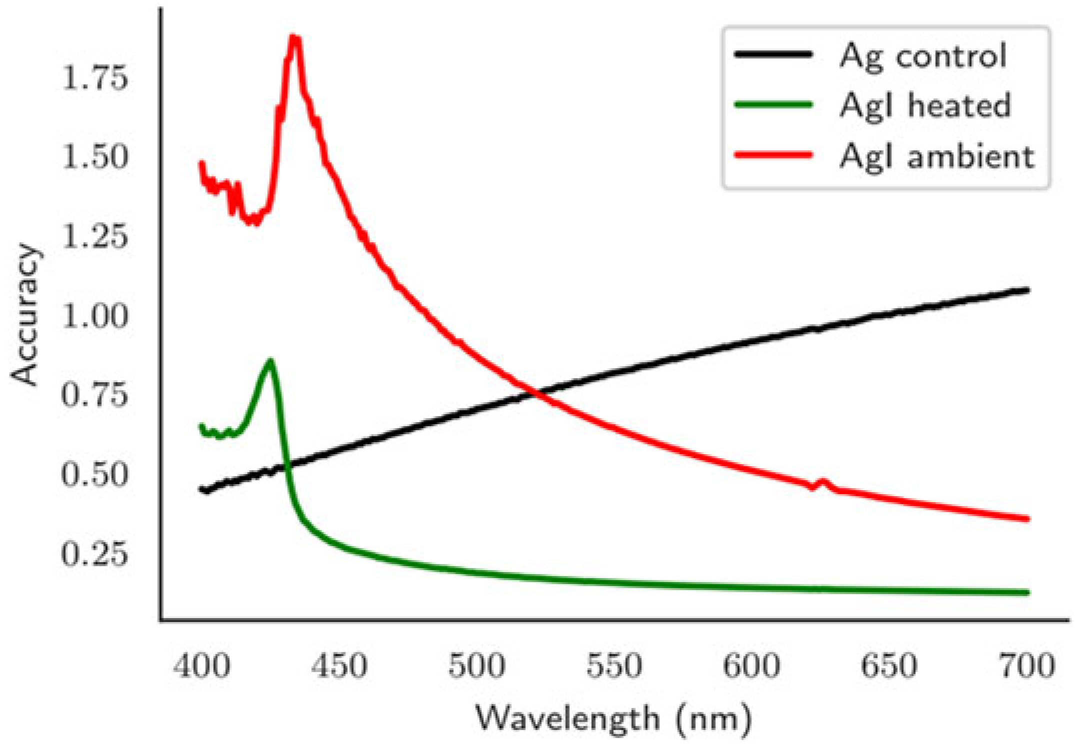

Figure 4. UV-Vis spectra of silver thin films. Spectra shown are before and after iodization under ambient (λ max = 433 nm) and heated to 30°C (λ max = 424 nm). The presence of surface plasmon resonance in the blank silver samples suggests the thin films are discontinuous small islands of metal formed during the sputtering process.

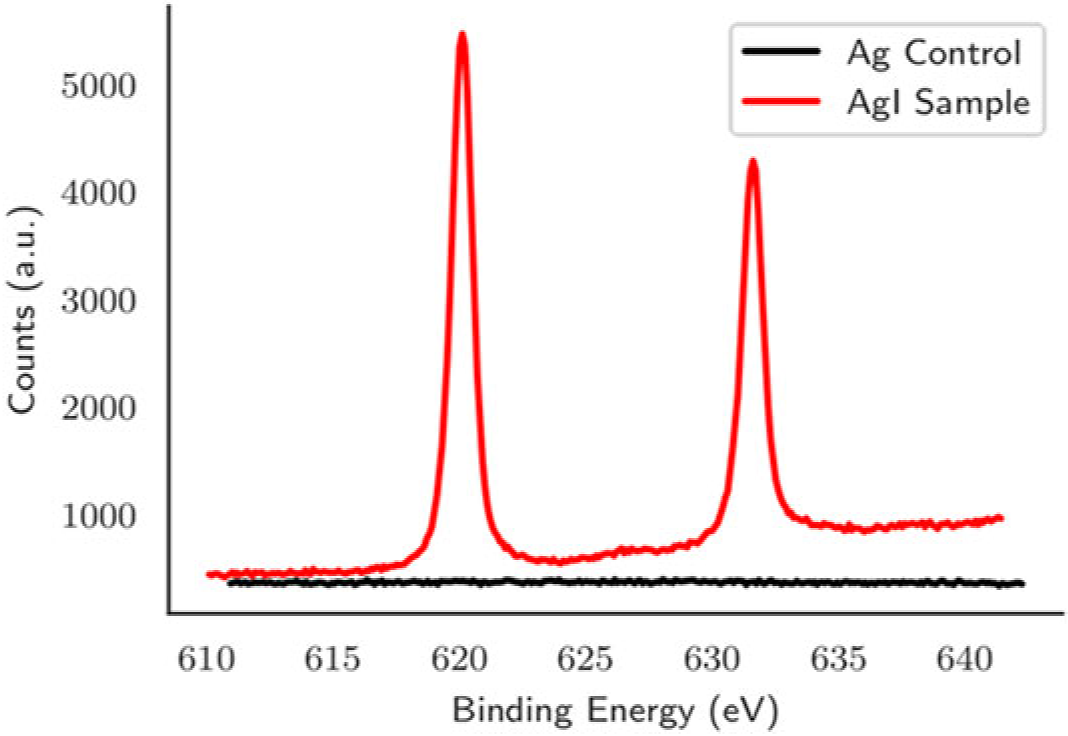

Figure 5. XPS spectra of an AgI-based ASN device. The spectra show the iodine $3d_{5/2}$ and $3d_{3/2}$ core levels in silver-based ASN devices exposed to (sample, red) and not exposed to (control, black) iodization procedures. The two peaks at 620 and 631 eV correspond to the expected I^- bands for $I_{3/d7}$.

To confirm the viability of AgI networks as a physical substrate for in-materio RC, the spatially distributed nonlinear characteristics of the ASN were examined. Voltage traces acquired at each of the 14 measurement electrodes enabled the analysis of Lissajous plots (V-V) as shown in Figure 6. AgI devices demonstrated distributed nonlinear dynamics throughout the entirety of the nanowire network as a consequence of their highly interconnected nature, where a stable and reproducible nonlinear transformation of the input signal was observed. Different switching regimes emerge throughout the network (Figure 6) demonstrating different dynamics dominating spatial regions, suggesting there is a combination of switching dominated (blue, green plots) and capacitance dominated (red, pink) regions distributed throughout the network under an applied bias at any given electrode combination. The switching mechanism for AgI junctions is accepted to arise from the formation of metallic filaments between the insulating material classifying them as electrochemical metallization cells[31–33,58]. The memristive properties of individual AgI junctions have been well characterized by Tappertzhofen et al. and Sánta et al[13,59] and clearly demonstrate pinched hysteresis in their I-V curves. The unique dynamics observed in ASNs are the result of coupled memristive switching events amongst many interconnected junctions, where measurements at a point electrode capture the dynamics of an ensemble of memristive elements rather than a single one. Consequently, Lissajous plots of ASN device operation do not commonly produce the characteristic pinched hysteresis loops associated with individual memristive junctions. This capacity for the non-linear transformation of time-varying signals and temporal datasets renders the AgI nanowire network ideal for the performance RC-based speech recognition tasks.

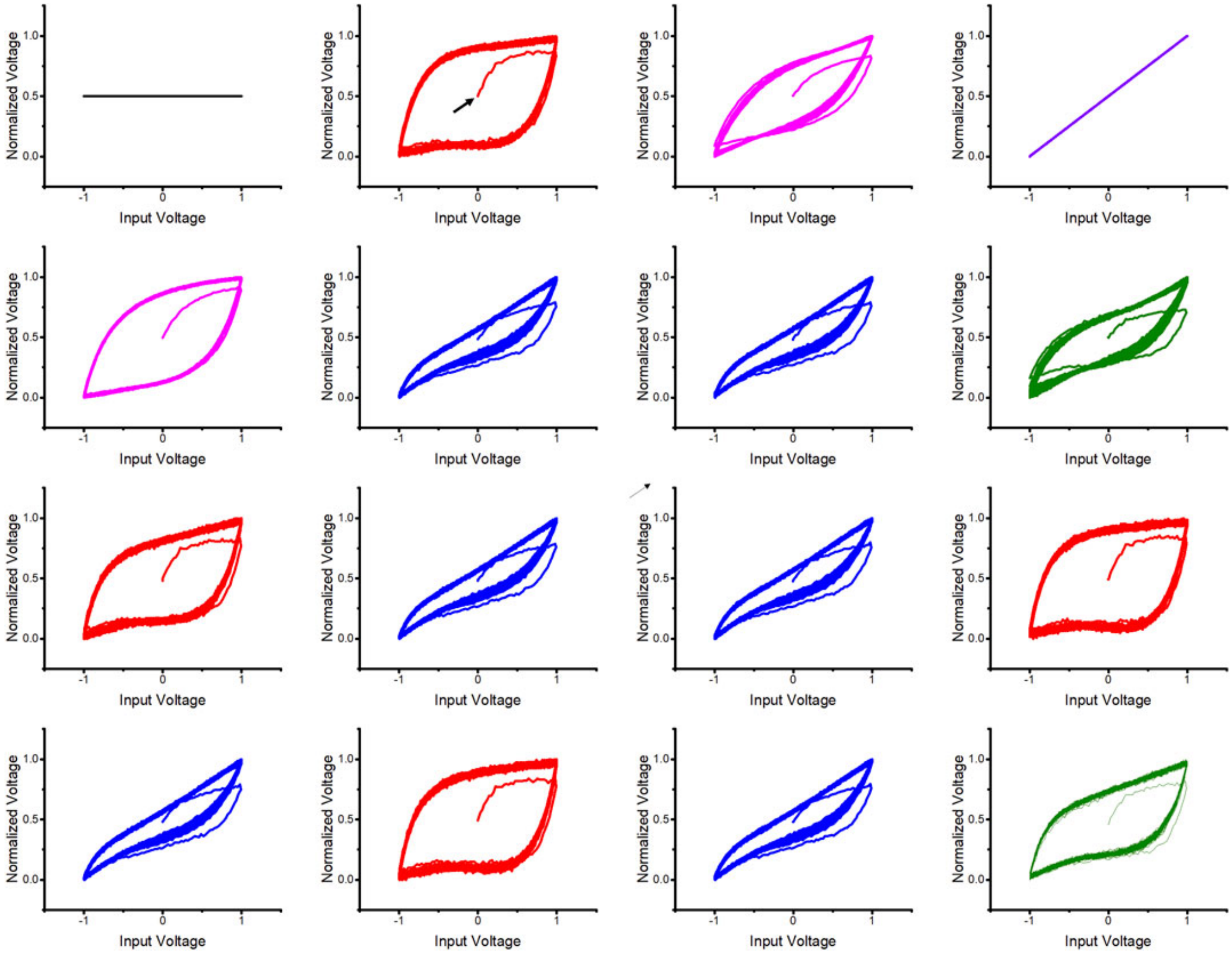

Figure 6. Representative, normalized Lissajous plots of all 16 electrodes in an AgI device. Electrodes were measured simultaneously using a 7 Hz triangle waveform swept from –1 to +1 V over the course of 23 s with the grounded electrode (top left) and input signal (top right) recorded. Different colors correspond to different emergent dynamics spatially distributed throughout the network. The first sweep can be seen in all plots as indicated by the black arrow. The network demonstrated a spatially diverse system with reproducible, non-linear behavior distributed throughout the networks.

AgI ASN-based reservoir computing

AgI nanowire networks were evaluated for their RC potential in spoken digit recognition as shown schematically in Figure 4. To effectively benchmark the value of the nanowire network in the performance of a spoken digit classification task, linear regression was performed in two ways. First, linear regression of the input voltages only - defined as ‘Input Only’-was carried out in the absence of the physical reservoir. Second, the full reservoir system – defined as ‘Reservoir’ - employed regression of both the input signal and all device outputs. Inclusion of the input signal allows the regression to more accurately discern correlations between the transformed output signals and the input itself. FSDD digits encoded as MFCCs and passed to the network as a temporal sequence at 1287 Hz were successfully classified as shown in Figure 7. A sufficient number of training examples were found to stabilize the reservoir’s behavior, and evaluating testing data on only a single array of readout coefficients was found to be valid[60].

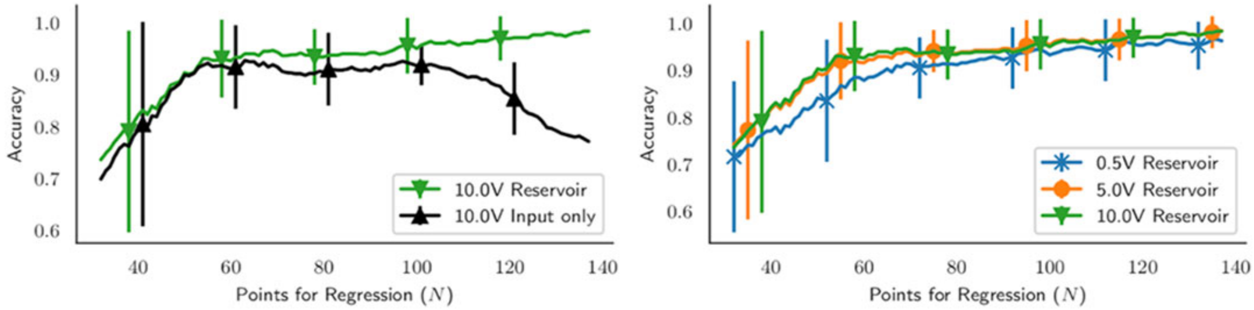

Figure 7. Spoken digit classification task performance. (Left) Performance of the spoken digit classification task using AgI nanowire networks for in-materio RC to tap the temporal sequence of spoken digit MFCCs at N different points and regressing to identify the digit spoken. Mean accuracy and standard deviation clearly shows that the “Reservoir” readout method avoided overfitting and improved task performance as compared to using the “Input Only” mode (Right). The input signal amplitude (voltage) was observed to have minimal impact on accuracy, indicating the potential for maintaining task performance under low-power operation of AgI ASNs.

The target function was regressed by dividing the measured electrode data into *N* segments and using the last data point from each segment; this post-processing of voltage traces is done offline. For the “input only” mode, this means that *N* = 80 used 80 values in the regression. For the “reservoir” mode, this means that *N* = 80 used 80 × 15 = 1200 values in the regression. To determine the accuracy at each *N* value, 12-fold cross-validation was employed using 11 of the audio files as training data and the 12th audio file as testing data. Each file was delivered to the device multiple times on a loop, aggregating far more than twelve tests to compute the accuracy. Nonetheless, there were only 12 unique data streams used. As a result, this problem suffered from significant overfitting, indicated by the “input only” results decreasing in accuracy as more points were used for the regression. This overfitting manifested as significant noise in the accuracy; *N* = 100 might give an accuracy as high as 100%, while *N* = 101 would give an accuracy of 54 %. To account for this, the space of points N tested was divided into windows of size 25, and the average and standard deviation of accuracy within this window is shown in Figure 7. For instance, the mean and standard deviation shown at *N* = 100 indicate the statistics for $N \in \{88, ..., 112\}$. The ASN reservoir also demonstrated highly accurate results across a wide range of input voltages (0.5-10V), suggesting potential utility of these devices for low-power applications.

These results clearly demonstrate the added stability provided by the ASN reservoir, evidenced by consistent accuracy at higher points of regression in the reservoir. The ASN’s robustness and versatility was demonstrated by its capability to discern spoken digits when stimulated by both high and low voltage signals without a significant loss in accuracy. The ASN also provided a moderate benefit in accuracy, even before the input-only lines began overfitting. The lack of overfitting on the reservoir lines could be interpreted as a side-effect of the temporal, non-linear properties of the reservoir. This is corroborated by the fact that the reservoir lines achieved higher accuracy than the input only lines, a phenomenon that could not be achieved without non-linear or temporal behavior. Rather than relying on a stream of individual values, each of which has some noise associated, the reservoir readout mode could rely on 15 such streams. Assuming the noise on each electrode is somewhat independent, averaging these channels could have significantly reduced noise.

Conclusion

Neuromorphic nanowire networks such as the ASN represent a burgeoning class of material architectures whose dynamical nature makes them uniquely suited to serve as physical substrates for hardware-based, in-materio computing. While the ever-increasing demands for computational capacity and complexity continue to challenge even the most advanced computing architectures, dynamical in-memory compute platforms such as the ASN may provide an alternative solution that is scalable, energy-efficient, adaptive, and capable of processing complex, time-varying data without the need for pre-programming or remote intervention. Expanding the catalog of memristive materials amenable to production of ASN-based devices, and thereby the diversity of network dynamics available for task performance, further increases their potential utility as a platform technology for next-generation computing applications. The new AgI-based ASN devices reported here served as a dynamic, memristive reservoir for the nonlinear transformation of temporal data and demonstrated the capacity to reliably classify spoken digits with high accuracy across a wide range of input voltages.

Combined with the relative ease and low cost of the fabrication process, these AgI nanowire networks represent both a new material system that is ripe for future study and an opportunity to further develop the concept of in-materio computing toward real-world applications.

References

1. Deshmukh, A. M. Comparison of Hidden Markov Model and Recurrent Neural Network in Automatic Speech Recognition. *Eur. J. Eng. Res. Sci.* **5**, 958–965 (2020).
2. Schatz, T. & Feldman, N. H. *Neural network vs. HMM speech recognition systems as models of human cross-linguistic phonetic perception*. *Proceedings of the Conference on Cognitive Computational Neuroscience* http://kaldi-asr.org/. (2018).
3. Mustafa, M. K., Allen, T. & Appiah, K. A comparative review of dynamic neural networks and hidden Markov model methods for mobile on-device speech recognition. *Neural Comput. Appl.* **31**, 891–899 (2019).
4. Ielmini, D. & Wong, H. S. P. In-memory computing with resistive switching devices. *Nature Electronics* vol. 1 333–343 (2018).
5. Miller, J. F., Harding, S. L. & Tufte, G. Evolution-in-materio: Evolving computation in materials. *Evolutionary Intelligence* vol. 7 49–67 (2014).
6. Dale, M., Miller, J. F., Stepney, S. & Adamatzky, A. Reservoir Computing as a Model for In-Materio Computing. *Adv. Unconv. Comput. Vol. 1 Theory* **23**, 533–571 (2017).
7. Harding, S. & Miller, J. F. Evolution in Materio. in *Encyclopedia of Complexity and Systems Science* 3220–3233 (Springer New York, 2009). doi:10.1007/978-0-387-30440-3_190.
8. Miller, J. F. & Downing, K. Evolution in materio: Looking beyond the silicon box. in *Proceedings - NASA/DoD Conference on Evolvable Hardware, EH* vols 2002-January 167–176 (Institute of Electrical and Electronics Engineers Inc., 2002).
9. Moon, J. *et al.* Temporal data classification and forecasting using a memristor-based reservoir computing system. *Nat. Electron.* **2**, 480–487 (2019).

10. Du, C. *et al.* Reservoir computing using dynamic memristors for temporal information processing. *Nat. Commun.* **8**, 1–10 (2017).
11. Alibart, F., Zamanidoost, E. & Strukov, D. B. Pattern classification by memristive crossbar circuits using ex situ and in situ training. *Nat. Commun.* **4**, (2013).
12. Sattar, A., Fostner, S. & Brown, S. A. Quantized conductance and switching in percolating nanoparticle films. *Phys. Rev. Lett.* **111**, 136808 (2013).
13. Tappertzhofen, S., Valov, I. & Waser, R. Quantum conductance and switching kinetics of AgI-based microcrossbar cells. *Nanotechnology* **23**, 145703 (2012).
14. Srinivasa, N. N. & Cruz-Albrecht, J. J. Neuromorphic adaptive plastic scalable electronics: analog learning systems. *Pulse, IEEE* **3**, 51–56 (2012).
15. Avizienis, A. V *et al.* Neuromorphic atomic switch networks. *PLoS One* **7**, e42772--e42772 (2012).
16. Türel, Ö., Lee, J. H., Ma, X. & Likharev, K. K. Neuromorphic architectures for nanoelectronic circuits. *Int. J. Circuit Theory Appl.* **32**, 277–302 (2004).
17. Calimera, A., Macii, E. & Poncino, M. The Human Brain Project and neuromorphic computing. *Funct. Neurol.* **28**, 191–196 (2013).
18. Lukoševičius, M. & Jaeger, H. Reservoir computing approaches to recurrent neural network training. *Comput. Sci. Rev.* **3**, 127–149 (2009).
19. Schrauwen, B., Verstraeten, D. & Van Campenhout, J. An overview of reservoir computing: theory, applications and implementations. *Proc. 15th Eur. Symp. Artif. Neural Networks. p. 471-482 2007* 471 (2007).
20. Snyder, D. R., Goudarzi, A. & Teuscher, C. Computational Capabilities of Random Automata Networks for Reservoir Computing. *arXiv.org* (2012).

21. Du, C. *et al.* Reservoir computing using dynamic memristors for temporal information processing. *Nat. Commun.* **8**, 1–10 (2017).

22. Goudarzi, A., Lakin, M. R. & Stefanovic, D. Reservoir Computing Approach to Robust Computation using Unreliable Nanoscale Networks. *arXiv.org* (2014).

23. Sillin, H. O. *et al.* A theoretical and experimental study of neuromorphic atomic switch networks for reservoir computing. *Nanotechnology* **24**, (2013).

24. Fu, K. *et al.* Reservoir Computing with Neuromemristive Nanowire Networks. in *Proceedings of the International Joint Conference on Neural Networks* (Institute of Electrical and Electronics Engineers Inc., 2020). doi:10.1109/IJCNN48605.2020.9207727.

25. Zhu, R. *et al. Harnessing adaptive dynamics in neuro-memristive nanowire networks for transfer learning*.

26. Kuncic, Z. *et al.* Neuromorphic Information Processing with Nanowire Networks. in 1–5 (Institute of Electrical and Electronics Engineers (IEEE), 2020). doi:10.1109/iscas45731.2020.9181034.

27. Manning, H. G. *et al.* Emergence of winner-takes-all connectivity paths in random nanowire networks. *Nat. Commun.* **9**, 1–9 (2018).

28. Manning, H. G., Biswas, S., Holmes, J. D. & Boland, J. J. Nonpolar Resistive Switching in Ag@TiO2 Core-Shell Nanowires. *ACS Appl. Mater. Interfaces* **9**, 38959–38966 (2017).

29. Terabe, K., Hasegawa, T., Nakayama, T. & Aono, M. Quantized conductance atomic switch. *Nature* **433**, 47–50 (2005).

30. Hasegawa, T. *et al.* Learning abilities achieved by a single solid-state atomic switch. *Adv. Mater.* **22**, 1831–1834 (2010).
31. Guo, X., Schindler, C., Menzel, S. & Waser, R. Understanding the switching-off mechanism in Ag+ migration based resistively switching model systems. *Appl. Phys. Lett.* **91**, 133513 (2007).
32. Yang, Y. *et al.* Observation of conducting filament growth in nanoscale resistive memories. *Nat. Commun.* **3**, 1–8 (2012).
33. Sun, W. *et al.* Understanding memristive switching via in situ characterization and device modeling. *Nature Communications* vol. 10 1–13 (2019).
34. Kan, S. *et al.* Simple Reservoir Computing Capitalizing on the Nonlinear Response of Materials: Theory and Physical Implementations. *Phys. Rev. Appl.* **15**, 024030 (2021).
35. Zhong, Y. *et al.* Dynamic memristor-based reservoir computing for high-efficiency temporal signal processing. *Nat. Commun.* **12**, 1–9 (2021).
36. Lukoševičius, M., Jaeger, H. & Schrauwen, B. Reservoir Computing Trends. *KI - Künstliche Intelligenz* **26**, 365–371 (2012).
37. Sillin, H. O. *et al.* A theoretical and experimental study of neuromorphic atomic switch networks for reservoir computing. *Nanotechnology* **24**, (2013).
38. Hashmi, A., Berry, H., Temam, O. & Lipasti, M. Automatic abstraction and fault tolerance in cortical microachitectures. (2011).
39. Stieg, A. Z. *et al.* Self-organized atomic switch networks. *Japanese Journal of Applied Physics* vol. 53 (2014).

40. Konkoli, Z., Nichele, S., Dale, M. & Stepney, S. Reservoir computing with computational matter. in *Natural Computing Series* 269–293 (Springer Verlag, 2018). doi:10.1007/978-3-319-65826-1_14.
41. Teuscher, C. The Weird, the Small, and the Uncontrollable: Redefining the Frontiers of Computing. *Computer (Long. Beach. Calif).* **50**, 52–58 (2017).
42. Tanaka, G. *et al.* Recent advances in physical reservoir computing: A review. *Neural Networks* vol. 115 100–123 (2019).
43. Nakajima, K. Physical reservoir computing-an introductory perspective. *Japanese Journal of Applied Physics* vol. 59 60501 (2020).
44. Lukosevicius, M. Reservoir computing and self-organized neural hierarchies. (2011).
45. Vandoorne, K. *et al.* Photonic reservoir computing: A new approach to optical information processing. in *2010 12th International Conference on Transparent Optical Networks, ICTON 2010* (2010). doi:10.1109/ICTON.2010.5548990.
46. Midya, R. *et al.* Reservoir Computing Using Diffusive Memristors. *Adv. Intell. Syst.* **1**, 1900084 (2019).
47. Kudithipudi, D., Saleh, Q., Merkel, C., Thesing, J. & Wysocki, B. Design and Analysis of a Neuromemristive Reservoir Computing Architecture for Biosignal Processing. *Front. Neurosci.* **9**, 61907 (2016).
48. Bürger, J., Goudarzi, A., Stefanovic, D. & Teuscher, C. Computational capacity and energy consumption of complex resistive switch networks. *AIMS Mater. Sci.* **2**, 530–545 (2015).

49. Kuzum, D., Jeyasingh, R. G. D., Yu, S. & Wong, H.-S. Low-Energy Robust Neuromorphic Computation Using Synaptic Devices. (2012) doi:10.1109/TED.2012.2217146.

50. Loppacher, C. *et al.* Direct Determination of the Energy Required to Operate a Single Molecule Switch. *Phys. Rev. Lett.* **90**, 4 (2003).

51. Nayak, A. *et al.* Rate-Limiting Processes Determining the Switching Time in a Ag2S Atomic Switch. *J. Phys. Chem. Lett.* **1**, 604–608 (2010).

52. Cai, K., Sun, J., Li, B. & Zhou, J. Hysteretic Current-Voltage Characteristics and Memristive Behaviors in AgI Nano-Particles Assembly. *ECS J. Solid State Sci. Technol.* **2**, N6–N10 (2013).

53. Liang, X. F. *et al.* Resistive switching and memory effects of AgI thin film. *J. Phys. D. Appl. Phys.* **40**, 4767–4770 (2007).

54. Demis, E. C. *et al.* Nanoarchitectonic atomic switch networks for unconventional computing. *Jpn. J. Appl. Phys.* **55**, 1102B2 (2016).

55. Bharathi Mohan, D., Sreejith, K. & Sunandana, C. S. Surface plasmon-exciton transition in ultra-thin silver and silver iodide films. *Appl. Phys. B Lasers Opt.* **89**, 59–63 (2007).

56. Gnanavel, M. & Sunandana, C. S. Optical absorption and photoluminescence in ultra thin silver and silver iodide films. in *2008 IEEE PhotonicsGlobal at Singapore, IPGC 2008* (2008). doi:10.1109/IPGC.2008.4781352.

57. Kato, Y. *et al.* Silver Iodide Formation in Methyl Ammonium Lead Iodide Perovskite Solar Cells with Silver Top Electrodes. *Adv. Mater. Interfaces* **2**, (2015).

58. Yang, J. J., Strukov, D. B. & Stewart, D. R. Memristive devices for computing. *Nat. Nanotechnol.* **8**, 13–24 (2013).

59. Sánta, B. *et al.* Nanosecond resistive switching in Ag/AgI/PtIr nanojunctions. *Beilstein J. Nanotechnol.* **11**, 92–100 (2020).

60. Scharnhorst, K., Woods, W., Teuscher, C., Stieg, A. & Gimzewski, J. Non-Temporal logic performance of an atomic switch network. in *Proceedings of the IEEE/ACM International Symposium on Nanoscale Architectures, NANOARCH 2017* 133–138 (Institute of Electrical and Electronics Engineers Inc., 2017). doi:10.1109/NANOARCH.2017.8053728.